High-Force Soft Robots with Applications in Burrowing

A THESIS

SUBMITTED TO THE FACULTY OF THE GRADUATE SCHOOL

OF THE UNIVERSITY OF MINNESOTA

BY

Steven Daniel Thomalla

IN PARTIAL FULFILLMENT

OF THE REQUIREMENTS FOR THE DEGREE OF

DOCTOR OF PHILISOPHY

Advisor

James D. Van de Ven, PhD

May 2022

Acknowledgements

The author would like to thank Prof. Jim Van de Ven and Prof. Art Erdman for all their incredible guidance, support, and mentorship while at the University of Minnesota. The author would also like to sincerely thank the Earl E. Bakken Medical Devices Center for providing the opportunity to experience such a diverse and meaningful time in graduate school and for providing the environment to grow so much as a person. Specifically, the author would like to express gratitude to Art Erdman, Darrin Beekman, John Huss, Marge Hartfel, Paul Rothweiler, and Cara Herbers from the Earl E. Bakken Medical Devices Center (as well as the countless others) for all their trust, support, and mentorship. The author would like to thank all former and current members of the Mechanical Energy and Power Systems laboratory that he was fortunate enough to work with during his PhD experience including Mark Gilbertson, Alex Yuddel, Jeremy Simmons, Gillian McDonald, Anthony Knutsen and many others. The author would like to thank his committee members Prof. Arthur Erdman, Prof. William Durfee, and Prof. Emmanuel Detournay. The author would also like to thank the University of Minnesota Graduate School, the Mechanical Energy and Power Systems Laboratory, the Earl E. Bakken Medical Devices Center, NSF EFRI C3 SoRo, and the Mistletoe Foundation for their financial support. Finally, the author would like to thank all the undergraduate students that spent countless hours helping with experiments, filtering data, writing code, and building actuators during this research project. The author would specifically like to thank Kevin Orpen who contributed to the project in the most incredible way for over two years. The author would also like to thank Junchi Feng and Jack Sonstegard who spent over a year developing experiments and testing actuators in the lab. Finally, the author would also like to thank the other students who assisted with the project including John Thomalla, Jacob Rankin, Christopher Heen, and Ryan Kruchten.

Abstract

Efficient burrowing and tube-traversing systems are needed for installation and inspection of underground infrastructure, search and rescue, and other applications where excavation is undesirable. Hydraulically driven soft robots offer a solution to this problem where the maneuverability of soft robotics and the power density of hydraulic power transmission are both critical. This thesis presents the design, modeling, and manufacturing techniques for developing a multi-segment, hydraulically driven soft robot capable of traversing tubular environments like a burrow.

A new force model was developed to address modeling limitations of the traditionally thin-walled, pneumatically-driven McKibben actuator – a common linear soft actuator. Hydraulic contracting and extending actuators were fabricated, and the new model was experimentally validated against commonly used existing models for both actuator versions. In the contracting McKibben experiments, the overall average error for the new model was 9.1% while the overall average error for three commonly used models were 9.9%, 10.5%, and 10.0%. Similar results were reported in the extending McKibben experiments. While the improvement of the new model over the other models is small, it is expected that the new model will be more accurate for high-pressure actuators with thicker walls that are needed in burrowing applications. One contracting actuator was driven at 13.9 MPa – the highest known pressure to date in literature.

Further testing showed that extending McKibben actuators follow traditional column buckling theory, and it was demonstrated that extending McKibben actuators can develop extension forces greater than the critical buckling load when operating in a constrained environment such as a burrow.

Radially expanding traction actuators were developed to generate the forces needed to anchor the multi-segment robot in the burrow. A new traction force model was developed to predict the generated traction force when actuated in a burrow. Multiple traction actuators were designed, fabricated, and experimentally tested to validate the model. The results of the experiments showed the new model to be a reasonable predictive design tool for the traction actuators.

One extending McKibben and two traction segments were combined into a novel multi-segment robot with internal fluid lines allowing for independent actuation of the robot segments - enabling travel in both the forward and reverse directions. Experimental constraints, performance constraints, and performance objectives of the robot design were selected to ensure the robot could generate the forces and motions for efficient travel. A grid-search was used to study the solution space and select an initial geometry for the multi-segment robot within the constraints and objectives of the design. The extending McKibben segment was 76.2 mm long, had a 50.8 mm outside diameter, a 3.2 mm initial wall thickness, and was built with an initial fiber wrap angle of 80 degrees. When pressurized at 207 kPa, the extender could produce up to 206 N of extension force. The two traction segments had the same outside diameter, wall thickness, and operating pressure as the extending segment. The 114.3 mm long segments were able to produce up to 1043 N of traction force.

The multi-segment robot was tested in two horizontally oriented tubes of varying diameters to simulate a burrow, and it was able to travel in both directions without issues. The robot was also tested in a vertical tube and was able to travel upwards against gravity. These results demonstrate that the contributions in this thesis provide the framework to develop soft robotic solutions for applications like burrowing where large forces and specific motions are required.

Table of Contents

List of Tables

List of Figures

Nomenclature

Table 1: Nomenclature used throughout this thesis

A	cross-sectional area
A_{wall}	area of external wall that the actuator's pressure is being applied to
B	length of single fiber
C_1	constant lumped parameter
C_2	constant lumped parameter
δ	spacing between fibers or actuator displacement
δ_{max}	maximum achievable δ
d	inner diameter
d_i, r_i	initial elastomer outside diameter, radius
D_i	initial outside diameter
D_o	diametric constant
D	current outside diameter
ε	contraction ratio (or strain)
ε_{max}	maximum achievable contraction ratio
E	elastomer Young's modulus
E_{in}	energy required to expand or extend actuator segment
F	contraction force
$F_{anchoring}$	anchoring force radially applied by the actuator
$F_{elastic}$	elastic axial force of elastomer
F_{fibers}	actuator force developed from internal pressure
$F_{friction}$	friction force
F_{normal}	normal force
F_{total}	total actuator force
$F_{traction}$	axial traction force produced by the actuator
γ	angle between fibers measured about origin of radius of curvature
I	smallest area moment of inertia
k	radius of gyration
l	fitting to fitting actuator length
l_{eff}	axial contact length between actuator and external tube
$l_{effective}$	effective column length
l_f	final extended actuator length
l_o, L_o	initial actuator length
L	current actuator length
N_f	total number of fibers wrapped around actuator
n_s	number of spaces between fibers

N, n	# fiber turns around elastomer
σ	elastomer stress
σ_1	actuator hoop stress
σ_a	elastomer axial stress
σ_e	elastomer effective stress
σ_h	elastomer hoop stress
σ_{max}	maximum tensile strength of elastomer
θ_o	initial fiber angle
θ	current fiber angle
θ_{lock}	kinematic lock fiber angle of 54.7 degrees
P	applied fluid pressure
P_{burst}	elastomer bursting pressure
P_{cr}	critical buckling load
$P_{elastic}$	internal pressure required to expand the actuator to a new radius, r_t
$P_{elastic}(V)$	internal pressure required to expand segment to r_f as a function of V
r_{bulge}	radius of curvature of the bulge between fibers
R_i	initial outside radius
R, r	current outside radius
r_f	final actuator outside radius (based on burrow diameter)
r_t	actuator expansion radius
r_o	actuator initial outside radius
S	elastomer Type A durometer
s_{bulge}	bulge arc
S_r	slenderness ratio
SF_{buckle}	safety factor against buckling failure
SF_{burst}	safety factor against burst failure
S_{yc}	compressive yield strength
t	current elastomer wall thickness
t_f	final elastomer wall thickness after expansion
t_k	initial elastomer wall thickness
T	total fiber tension
T_x	fiber tension component in x-direction
T_z	fiber tension component in z-direction
μ_t, μ_s	coefficient of static friction between actuator and tube surface
V	actuator volume
V_1	initial actuator volume
V_2	expanded actuator volume
x	distance over which actuator force is applied

Chapter 1: Introduction

This chapter introduces the field of soft robotics, presents the current state-of-the-art of soft robot technology, and introduces the specific contributions of this thesis to address opportunities within the field. Furthermore, the motivation for this project and detailed background information on the McKibben actuator, a key part of this research, are presented. Finally, an overview of the contents of this thesis, including a proposed multi-segment soft robot design, is provided at the end of this chapter.

1.1 Motivation

There is a need for efficient burrowing and tube-traversing systems for installation and inspection of underground infrastructure, search and rescue robots, and other applications where excavation is undesirable. The recent technological advancements in soft robotics have been introducing novel perspectives for designing soft robots [1], and biomimicry has been used to design innovative soft robots that can crawl, grip objects, and change stiffness [2]. Furthermore, hydraulic power transmission offers unmatched power density and can generate very large forces. High pressure, compact burrowing robot technologies that utilize the benefits of soft robotic actuation and hydraulic power transmission present a new opportunity within the field of soft robotics. The long-term objective of this work is to develop the models and design methodology required to realize high force, compact, soft robots with applications in burrowing

technology capable of traversing many soil substrates and environments. This thesis presents the development of force models, design methodologies, and manufacturing approaches for the development of a novel multi-segment, hydraulically driven soft robot capable of navigating tubular environments like a burrow.

The proposed soft robot consisted of two radially expanding segments connected with an axially extending segment that can be independently actuated to allow the robot to move in a controlled manner through a tubular environment using alternating anchor locomotion as shown in Figure 1.

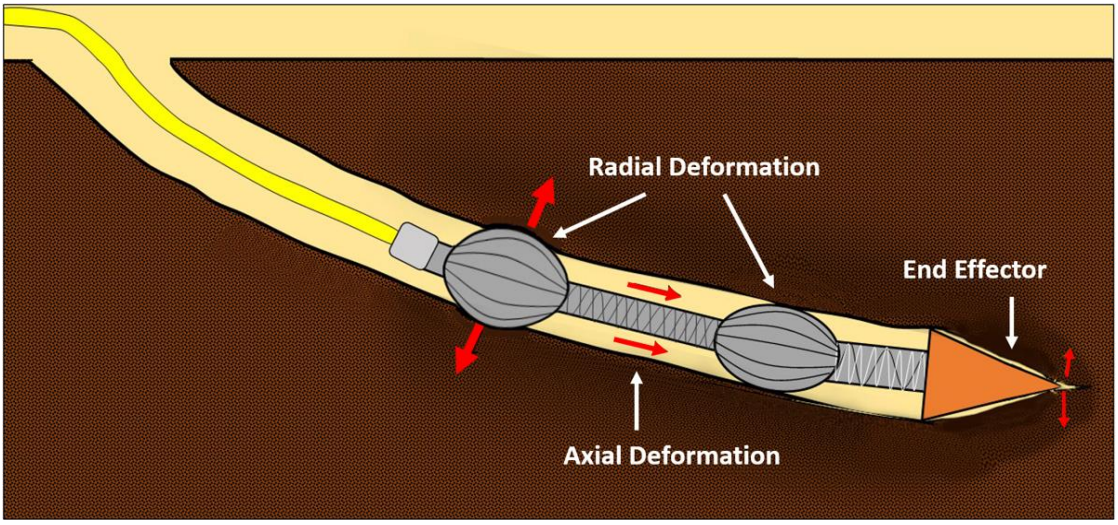

Figure 1: Proposed multi-segment soft robot design utilizing alternating anchoring locomotion to move through a burrow

Trenching is the most common method used for installing, replacing, and repairing the millions of miles of pipelines, sewer systems, irrigation lines, fiber optic cables, electrical lines, geothermal systems, and other similar underground

utilities. However, excavation is inefficient, unsafe, destructive to the environment and biological ecosystems, and not ideal in many sensitive areas [3-5]. Directional boring is a trenchless burrowing method used mostly in dry soils, with a variety of constituents like sand, silt, gravel, clay, or shale, for installing utility lines that utilizes the pushing of a rotary cutting tool long distances underground and removing the soil from the burrow. Directional drilling and boring units require a human operator, are hard to steer, resulting in position error up to one meter at long distances, are large, and expensive all of which limit their number of useful applications [6-8].

Optimized by natural selection, burrowing mechanics and locomotion techniques are exhibited in nature by lizards, worms, moles, gophers, clams, and many other animals to navigate efficiently, which is measured by their metabolic and oxygen consumption rates, through a variety of different soil compositions [9-13]. Several biomimicry based burrowing robotic systems have been investigated to penetrate into specific soils, but there are currently no compact robotic burrowing systems capable of producing the large forces and kinematics required for fast and efficient burrowing for non-invasive utility installation and repair through a variety of different soil substrates [14-18].

Recent developments in the field of soft robots show that high force, hydraulically powered, fiber reinforced soft actuators can produce the necessary forces and kinematics that could be used for efficient burrowing locomotion. The

McKibben actuator, a soft extending and contracting linear actuator, has been studied and shown to be useful for adoption in high force hydraulic systems [19-22]. Hydraulic transmission is unsurpassed in force and power density in comparison to other conventional actuation techniques which makes it a natural choice for compact systems that are used in confined spaces and require high power density [21].

The long-term objective of this work is to develop the framework necessary for developing high force, excavation-free, compact burrowing robot systems capable of precise and efficient burrowing through a variety of soil types commonly found in underground utility installation such as pipes, sewers, or irrigation lines. This will be done by utilizing soft actuators, biomimicry, and the density of hydraulic power transmission. It is hypothesized that such a system, with the ability to push itself into the soil as well as pull itself along using traction/anchoring mechanisms, would be more easily steered than directional boring that is exclusively pushed along within a burrow. Such a system may be useful in rescue operations, anchoring applications, welfare robots, and many other applications [11, 23-25]. Figure 2 shows possible ways that a multi-segment burrowing robot could utilize nature-inspired techniques to realize the long-term objective of efficient, multi-substrate burrowing robot systems. Figure 3 shows a few of the many potential applications of the proposed burrowing technology where excavation of the soil is undesirable.

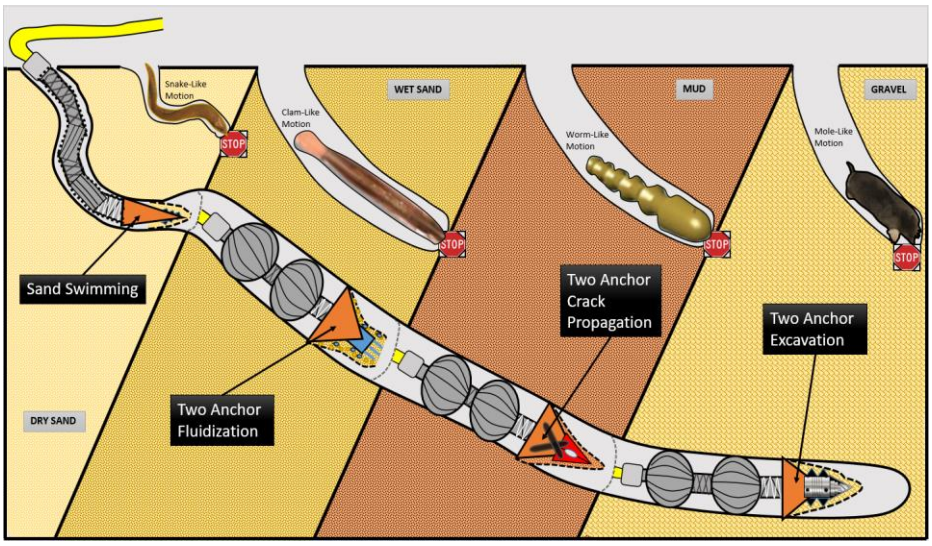

Figure 2: Potential designs of a multi-segment, multi-substrate burrowing robot based on biomimicry

Figure 3: Electrical, irrigation, sewage, and drilling applications

1.2 Background

This section introduces the field of soft robotics, provides an overview of a common soft actuator – the McKibben actuator, reviews burrowing mechanics found in nature, and presents a synopsis of existing burrowing and tube-traversing robots found in literature.

1.2.1 Soft Robotics

Soft robots are comprised of a soft, elastic structure, have a compliant response based on the environment, and can have many degrees of freedom - allowing them to be used to accomplish tasks that rigid robots cannot. Soft robots are a unique subset of robots as illustrated by the robot classification diagram in Figure 4 [26].

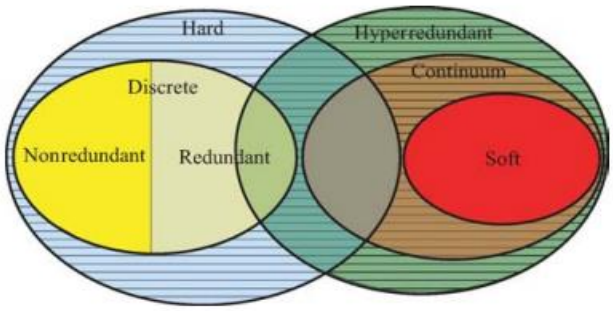

Figure 4: Classification of robots [26]

Soft robots, often found in or inspired by nature, can conform to their environment, navigate in or through confined spaces, and be specifically designed for complex tasks. However, understanding the kinematics and forces generated by soft robots is much more challenging than with hard robots [1].

Nature provides a myriad of biological soft robots ranging from the hydraulically powered connective tissue-reinforced tube feet of starfish to the muscle fiber-reinforced dog tongue as observed in Figure 5 [26].

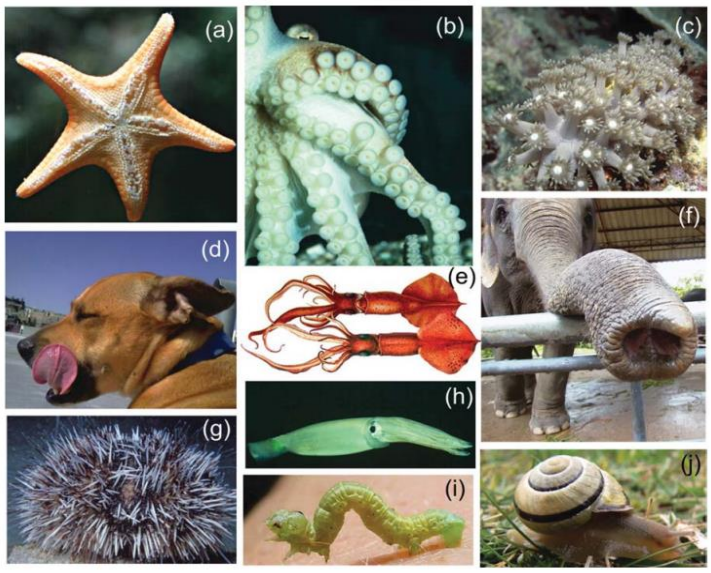

Figure 5: Examples of soft robots in nature: (a) tube feet in starfish, (b) octopus arms, (c) colonial anemone, (d) mammalian tongue, (e) squid, (f) elephant trunk, (g) echinoid, (h) Illex illecebrosus, (i) inchworm, and (j) snail feet. [26]

There are four primary methods for actuation of soft robots including shape memory alloys, dielectrics, cables, and pressurized fluid [27]. Shape memory alloys (SMAs) have been utilized to design soft robots that crawl, climb, and roll using linear and coil springs that simulate biological muscle forces and caterpillar like motion [28-29]. Soft robots that mimic the movement of an octopus have been designed to grasp objects by utilizing cable actuation that applies tensile forces [30], and dielectrics are utilized to rapidly activate elastomers in the presence of an electrical field [31]. However, the most common soft robot

actuation technique in nature and past literature is pressurized fluid. Introducing pressurized fluid volume into an enclosed pressure vessel causes deformation and force generation depending on the composition and characteristics of the elastic vessel material and support structure. It is also possible to combine soft robot actuation techniques. In one study, pressurized fluid actuation was coupled with SMAs that acted as the support structure which caused improvement to the displacement response speed of the actuator [32].

Soft robots that are powered by fluid, either pneumatically or hydraulically, can generally be further classified as fiber-reinforced or fiber-less actuators. Fiber-less actuators have been constructed with custom internal cavities and chambers, commonly known as bellows, that allow for specialized locomotion upon pressurization and are sometimes known as ‘flexible micro-actuators’ [33]. Kota et al. presented the first modeling approaches of fiber-reinforced elastomeric enclosures (FREE actuators), comprised of a hollow elastomer that is reinforced with stiff fibers, that generate specific motions based on their fiber wrap configuration [34-35]. FREE actuators have been designed with various arrangement of fiber families and elastomer geometry to achieve many modes of locomotion including radial expansion and contraction, axial extension and contraction, bending, twisting, and combinations thereof [34-41]. Figure 6 shows an example of a cylindrical FREE actuator consisting of two fiber families at different wrap angles that produces simultaneous contraction and twisting motion when pressurized [37].

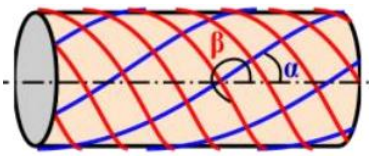

Figure 6: FREE actuator with two families of fibers at different fiber wrap angles [37]

There are many applications and designs of FREE actuators that can be found in literature. One example of a low-pressure hydraulic FREE actuator is an assistive glove designed at Harvard University that can assist a user with bending their fingers as shown in Figure 7 [42].

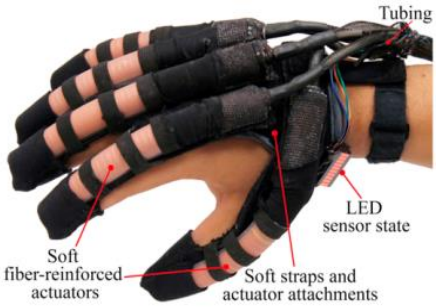

Figure 7*:* FREE actuator-based hand assistive device [42]

FREE actuators can produce many different motions depending on how the fibers are oriented. One FREE actuator was developed to generate extending, bending, and twisting deformation and could generate the complex motion needed to grip objects as shown in Figure 8 [43].

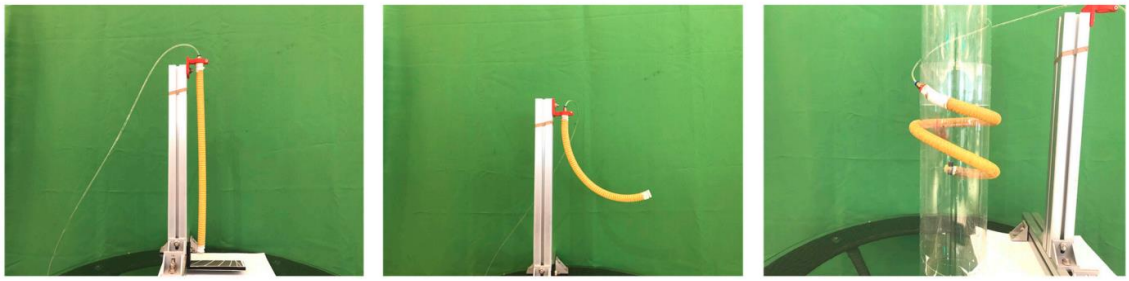

Figure 8: FREE actuator generating complex motions [43]

Many other forms of soft robots have been developed as well. Kanno et al. have developed a pneumatically-driven, spring-reinforced soft actuator capable of producing larger force outputs per cross-sectional area than traditional extending soft actuators like the McKibben actuator shown in Figure 9 [44].

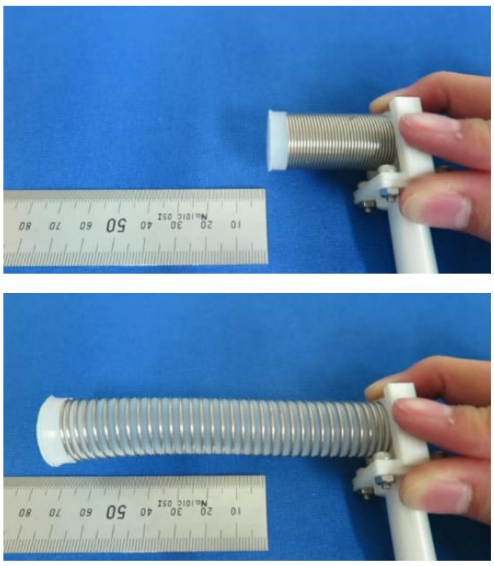

Figure 9: Pneumatic spring-reinforced soft actuator [44]

Another technique for soft robot synthesis has been developed where structural elements are used to replace the inextensible fibers commonly found in

FREE actuators. Kota et al. have developed unique soft actuators with auxetic sleeves that experience unique kinematic behavior by utilizing structural elements on the surface of the soft actuator [45]. The actuator model enables the user to synthesize the actuators to produce contraction, extension, expansion, and bending, all of which can vary along the surface of the actuator both axially and circumferentially. The actuator concept is shown in Figure 10 and shows potential for very specific applications where unique motions and precise deformations are needed.

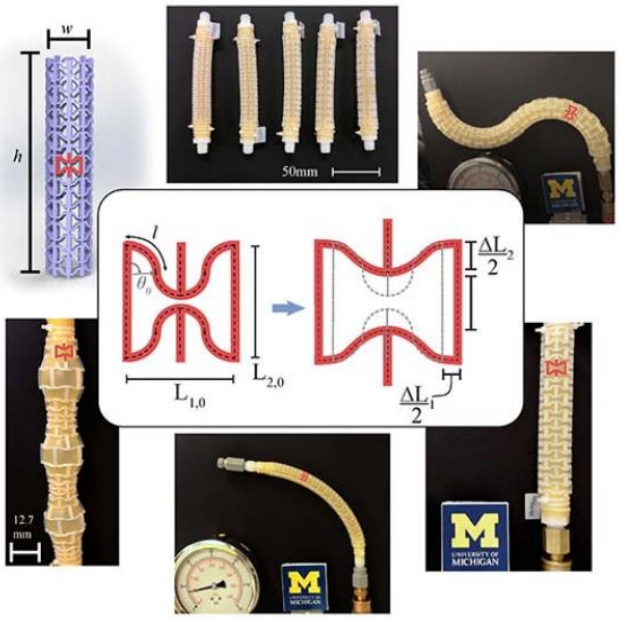

Figure 10: Structural elements used to generate unique soft robot motions [45]

Many other unique examples of soft robots have been presented in literature including pneumatic variable stiffness robotic hands [46], steerable worm-like robots [47], pneumatic pipe traversing robots [48], straight-fiber FREE actuators for generating ballooning motions and radial traction forces [49], and many others. However, the relatively new field of soft robotics has been primarily

limited to low-force, pneumatically-driven applications, and limited research has been conducted on high-force, hydraulic soft robot applications. Hydraulically driven soft robots provide an opportunity to harness the flexibility and customization of soft robotics and the force density of hydraulic power transmission for underground burrowing and similar applications.

1.2.2 The McKibben Actuator

This section introduces one of the most common soft robotic actuators – the McKibben actuator – which will be one of the main focuses of this thesis. An overview of design, failure mechanisms, and applications of the McKibben actuator are presented in this section.

1.2.2.1 Design

McKibben actuators, comprised of an elastomeric tube wrapped in inextensible fibers, were developed in the 1950s and have been used primarily in pneumatic applications. McKibben actuators provide superior force and power density at a lower cost compared to many conventional actuators because of their simple design.

A McKibben actuator is a special case of a FREE actuator where the forward and backward fiber wrap angles are equal and opposite as shown in Figure 11. When fluid is added to the McKibben actuator, the actuator axially

extends or contracts and radially grows or shrinks depending on the fiber wrap angle. The axial force is approximately proportional to the input pressure. Many existing models predict the deformation and force generation of the actuator based on the actuator geometry and fiber wrap angles [34-35, 50-51]. Note that compression of the McKibben actuator can lead to buckling failure.

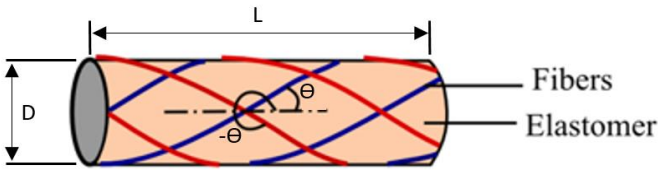

Figure 11: McKibben actuator equal and opposite fiber wrap angles [35]

McKibben actuators are compliant and cost-effective linear actuators that have advantages over many conventional actuators including hydraulic cylinders, air cylinders, and electromagnetic motors with ball screws in terms of force and power density [52-53]. The compact and compliant nature of McKibben actuators, as well as the development of high strength fibers [52], has made it lucrative to explore utilizing these actuators in hydraulic systems where force and power density are critical. Most of the design and modeling work to date on the McKibben actuator is in the pneumatic space, where thin-walled elastomeric enclosures and coarse fiber spacing are used in fabricating the actuators, and therefore, only small forces can be developed [53]. Challenges with pneumatic McKibben actuators are that the compressibility of fluid yields poor position control and lower efficiency when the compressible fluid is vented to the atmosphere [54]. Increasing the operating pressure of the actuator and utilizing

hydraulics addresses these challenges and significantly increases the axial and radial force capability. This introduces a need to design actuators that can withstand larger forces. Specifically, hydraulic McKibben actuators require a thicker walled elastomeric enclosure and closer fiber spacing to resist failure from bursting and robust segment connectors to prevent slipping at high axial forces. Past studies have also analyzed the performance and efficacy of controlling hydraulic McKibben actuators [20, 55], the drive characteristics of the actuator [56], and the effect of the elastomeric material selection on actuator performance [57-58]. While the hydraulic McKibben actuator shows increased force capabilities and better position control than the pneumatic McKibben actuator, further work in refining the design of the mechanical structure and modeling techniques for the hydraulic actuator must be undertaken to enable more uses of the technology. While the majority of McKibben research to date has been based on the pneumatic McKibben, some work on the hydraulic McKibben has been conducted in literature and some examples are presented here.

One extension-type hydraulic McKibben actuator was tested at 2.5 MPa and was able to generate 450 N of extension force without buckling failure [19]. This suggests that hydraulic McKibben actuators may be useful for applications where large extension or penetration forces are more useful than contraction forces. If a contracting McKibben has a fiber angle of 23.5 degrees and a similar extending McKibben has a fiber angle of 67.5 degrees, they produce equal amounts of displacement – just in the opposite direction [19]. One experiment by

Suzumori et al. showed that by combining extending and contracting McKibben actuators with the aforementioned fiber wrap angles in parallel, bending actuators can be developed as shown in Figure 12 [60]. The hydraulic McKibben actuator has also been used in a practical application by driving a robotic hand mechanism at 4 MPa capable of clasping objects with variable force [21].

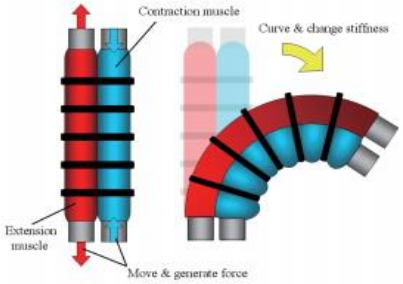

Figure 12: Bending actuator design with McKibben actuators in parallel [60]

Suzumori et al. and Zhang et al. have both developed high force, water powered McKibben actuators by developing custom crimp fittings to withstand the large forces that are developed and utilizing a 2x2 twill pattern braided sheath comprised of high strength fibers [19, 21, 56, 59]. Three-layered tubes have been used to protect the fiber sleeve and reduce burst failure by encasing the fiber sleeve between two rubber tubes and chemically vulcanizing the layers together as shown in Figure 13 [19]. While traditional pneumatic McKibben actuators can only be driven up to 0.7 MPa of pressure, the hydraulic versions have been pressurized up to 7 MPa [19]. By combining the use of high strength fibers, custom crimp fittings, and three-layered tubes to increase the strength of the hydraulic McKibben actuator, it has been estimated that these soft robotic

actuators can withstand pressures up to 30 MPa without failure enabling very large forces to be developed [19].

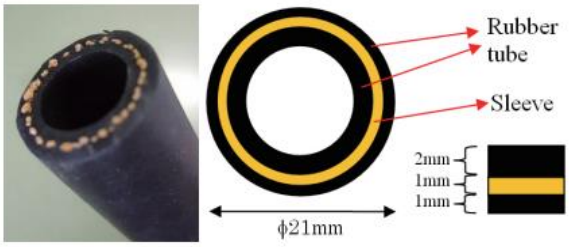

Figure 13: Three-layer tube design [19]

Zhang et al. studied in detail the static characteristics of the hydraulic McKibben actuator as a function of the manufacturing and operating parameters driven at hydraulic pressures up to 6 MPa [61]. Multiple McKibben actuators with off-the-shelf fiber sleeves were studied, and the results of these experiments demonstrated the significant impact of the sleeve's fiber angle and the elastomer wall thickness on the total axial force generated by the hydraulic version of the actuators. Figure 14 and Figure 15 show the design of the contracting McKibben actuators for experiments at hydraulic pressures by Zhang et al. [61].

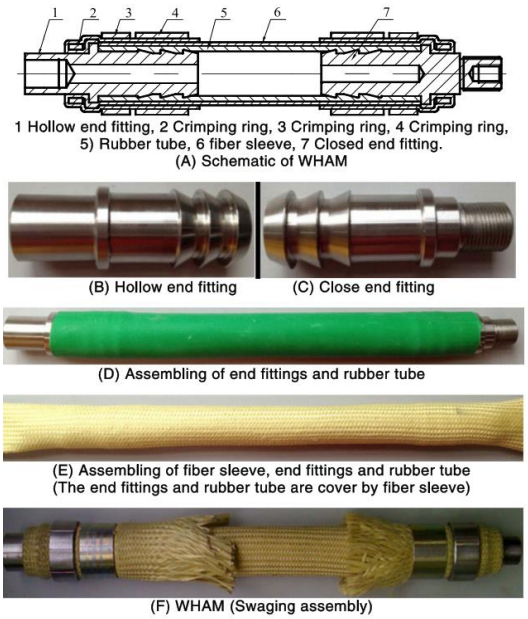

Figure 14: Hydraulic McKibben actuator design [61]

Figure 15: Hydraulic McKibben actuators used in experiments [61]

More recently, Slightam et al. have studied the hydraulic McKibben actuator at pressures up to 14 MPa, and have demonstrated that the actuator can produce up to 6.3 kN of axial force which is very promising for high-force applications such as burrowing [62]. The experiments demonstrated the structural integrity of the hydraulic McKibben actuator at hydraulic pressures and

examined the effectiveness of various McKibben modeling approaches that will be discussed in Chapter 2. Figure 16 shows an image of the experimental set up and McKibben actuators used in this study.

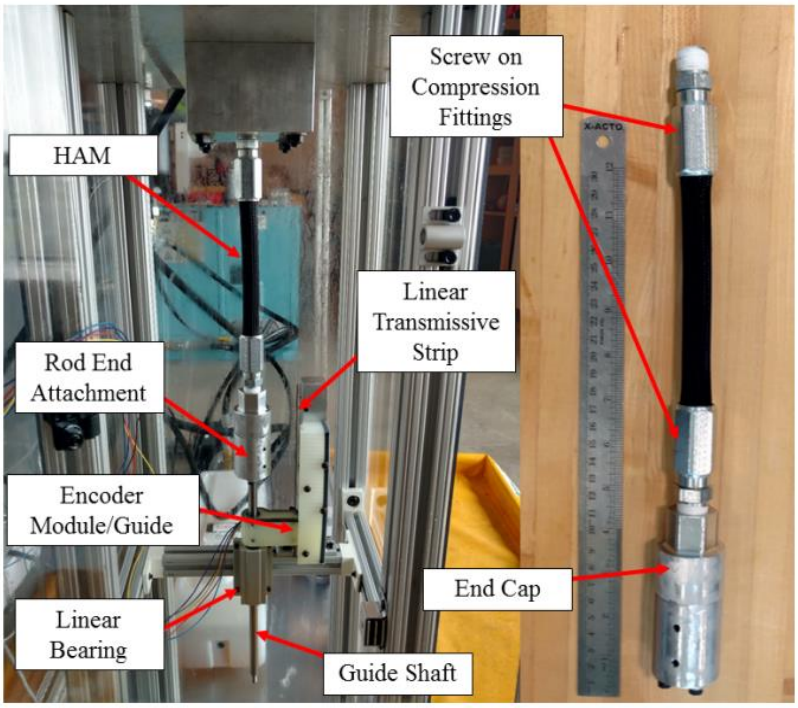

Figure 16: Hydraulic McKibben actuator testing at hydraulic pressures [62]

1.2.2.2 Failure Mechanisms

Previous hydraulic McKibben actuator research has explored challenges in developing high strength fibers and fiber sleeves suitable for preventing actuator bursting [19, 53], developing robust segment connectors to prevent axial slipping [19, 56-59, 63], and developing high strength three-layer tube structures for increased actuator strength and durability [19]. The four most common failure modes of the hydraulic McKibben actuator are the elastomer bursting through the

fiber weave, mechanical fitting failure, tensile fiber failure, and buckling failure. An introduction to these failure modes is provided in this section.

Zhang et al. have extensively studied the mechanical strength and failure modes of hydraulically driven McKibben actuators including the primary failure modes of fitting slippage, fiber sleeve failure, and burst failure [64]. The results from this study demonstrated that the most important factors relating to the strength of the hydraulic McKibben actuator is the fiber sleeve, elastomer, and mechanical fitting design. This work provides considerable insight into how to address the problems associated with designing soft robots for applications at hydraulic pressures. Models to predict fiber stress and failure were developed, depending on fiber weave and orientation, and experimentally validated. Furthermore, models on the impact of the elastomer wall thickness relative to the strength of the actuator were presented and experimentally validated. Finally, a design study and optimization were performed to identify a segment connector structure that best connects the elastomer and the fiber sleeve to prevent slipping. The conclusions from this study on robust hydraulic McKibben design are summarized below.

- In order, the axial force generation capabilities of a McKibben actuator are affected the most by the fiber angle, the fiber material, displacement of the elastomer, and the elastomer wall thickness.

- In order, the actuator's ability to resist burst failure from internal pressure is affected the most by initial fiber angle, the fiber material, the elastomer wall thickness, and the displacement of the elastomer.

- If higher axial forces are needed, a small initial fiber angle should be selected. If higher resistance to burst failure is desired, a larger initial fiber angle and a larger initial elastomer wall thickness should be selected.

- Increasing the area covered by the fiber sleeve prevents the elastomer from slipping with respect to the fiber sleeve.

- Decreasing the ratio of axial displacement of the elastomer to wall thickness deformation of the elastomer reduces the effects of stress concentration near the segment connector structures and reduces the tendencies of the actuator to fail due to segment connector structure slippage.

Fitting Failure

A commonly observed failure mode of hydraulically powered McKibben actuators is slipping of the mechanical fittings that hold the fibers and elastomer together. The actuators can generate large axial forces that must be balanced by the clamping forces of the segment connectors. A barbed crimp fitting is often used on commercial hydraulic hoses. Some past studies have presented custom segment connector structures that share the generated loads between the fiber

sleeve and crimp-elastomer interface to increase the reliability and axial force capability of the hydraulic McKibben actuator as shown in Figure 14 and Figure 15 [61]. These methods require custom segment connector fabrication that must be designed to increase the axial strength of the actuator. Traditional hydraulic hose crimping standards are not able to be used because of the variety of inner diameters, wall thicknesses, and material properties of the elastomers used in McKibben actuator applications. When there are insufficient clamping forces at the segment connector, the fiber sleeve can become loose, the mechanical fittings can slip, or the elastomer can slip away from the segment connectors – all of which result in actuator failure as shown in Figure 17, Figure 18, and Figure 19 respectively [64].

Figure 17: Fiber sleeve loosening [64]

Figure 18: Segment connector slipping [64]

Figure 19: Elastomer slipping out of connector [64]

Fiber and Burst Failure

Another mode of hydraulic McKibben actuator failure is exceeding the strength of the fibers themselves. Failure of the reinforcing fibers causes catastrophic failure of the McKibben actuator as shown in Figure 20 [64].

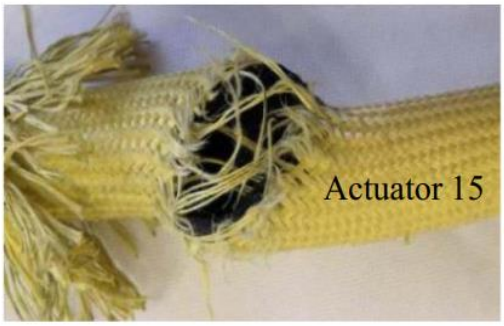

Figure 20: Fiber failure leading to actuator failure [64]

For modeling purposes, high strength fibers, such as aramid or carbon fibers, are generally considered ‘sufficiently strong’ for many applications, and developing an understanding of the limits of the high force McKibben actuator due to the fibers failing in tension is important to entirely understand the failure

criteria of McKibben actuators in high-force applications. The developed fiber tension in the fiber sleeve of a McKibben actuator can be predicted as shown in Figure 21 where T, θ, D, P, and $\mathbf{F}$ represent the fiber tension, fiber angle, inner tube diameter, operating pressure, and external loads respectively [21].

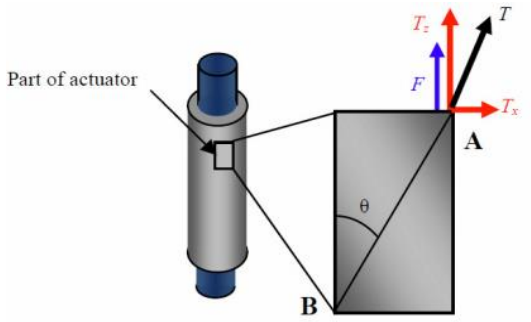

Figure 21: Fiber tension in fiber sleeve [21]

$$T_x = \pi P D^2 \tan(\theta) \tag{1.1}$$

$$T_z = \frac{\pi P D^2}{4} + \mathrm{F} \tag{1.2}$$

The total tension in the fibers must not exceed the strength of the fibers or actuator failure will occur. Some McKibben actuators, such as the one developed by the author in Figure 22, have been custom-wrapped with fibers that are not part of a fiber sleeve resulting in large spaces between the fibers that can lead to burst failure of the elastomer through the fibers.

Figure 22: Custom fiber-wrapped McKibben actuator developed by the author

Burst failure of the elastomer between the fibers has not been studied in prior literature, and a preliminary investigation of this behavior is presented in Chapter 2 of this thesis. Furthermore, elastomer burst failure can occur due to stress concentration near the segment connectors as shown in Figure 23 [64].

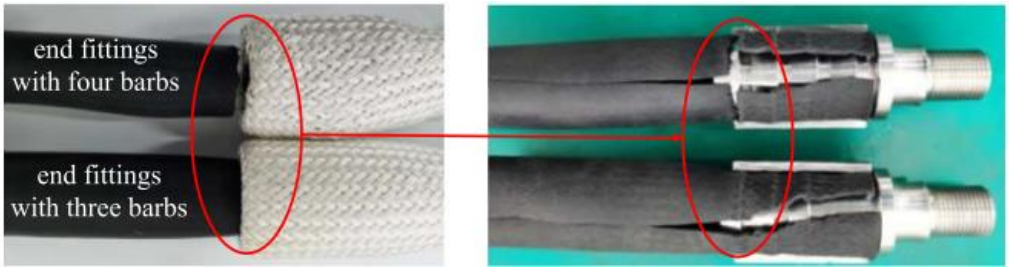

Figure 23: Elastomer burst failure due to stress concentration near the segment connectors [64]

Buckling Failure

Buckling occurs due to the actuator being loaded in compression. Because compliant actuators capable of producing extension forces are needed in burrowing applications that occur in a tube-like environment, an understanding of how buckling impacts the ability to generate large extension forces must be developed. It is hypothesized that short, thick-walled McKibben actuators with a large diameter can better resist buckling than slender actuators, but it is uncertain from literature if Euler beam theory, which will be presented in Chapter 3 of this thesis, applies to McKibben actuators due to the presence of the high strength fiber sleeve and the variable pressure fluid column. Once buckling mechanics are understood, the impact of the tube-like environment will be investigated to determine if and how extension forces can propagate within a constrained, tube-like environment like a burrow. The potential use of an extending McKibben actuator as the middle section of a multi-segment burrowing robot is presented in Figure 24, and an example of a buckled hydraulic McKibben actuator developed by the author is shown in Figure 25. A full investigation of McKibben buckling behavior will be presented in Chapter 3.

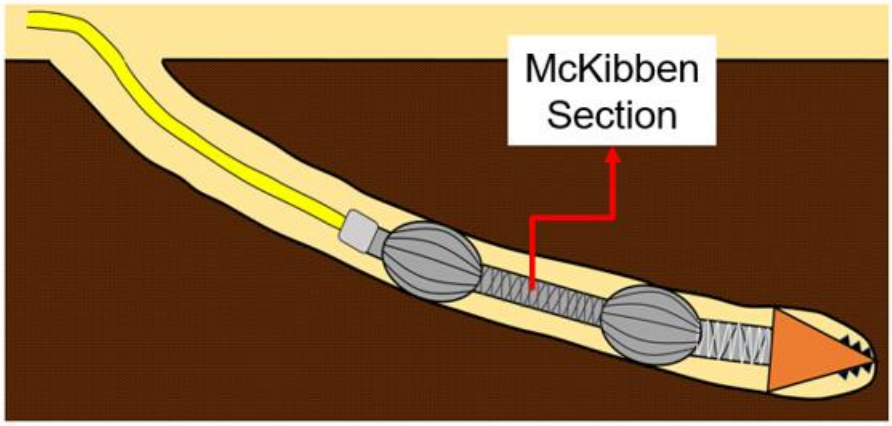

Figure 24: Potential use of an extending McKibben actuator in a multi-segment burrowing robot

Figure 25: Buckling McKibben actuator developed by the author

1.2.2.3 Applications

There has been a myriad of applications of the McKibben actuator in literature with nearly all of them dealing with the pneumatic version of the actuator. One application of the McKibben actuator was presented by Suzumori et al. where multiple thin McKibben actuators were braided together, and the overall combined actuator could create unique locomotion and improved contraction because the individual McKibben actuators could be independently actuated as shown in Figure 26 [65].

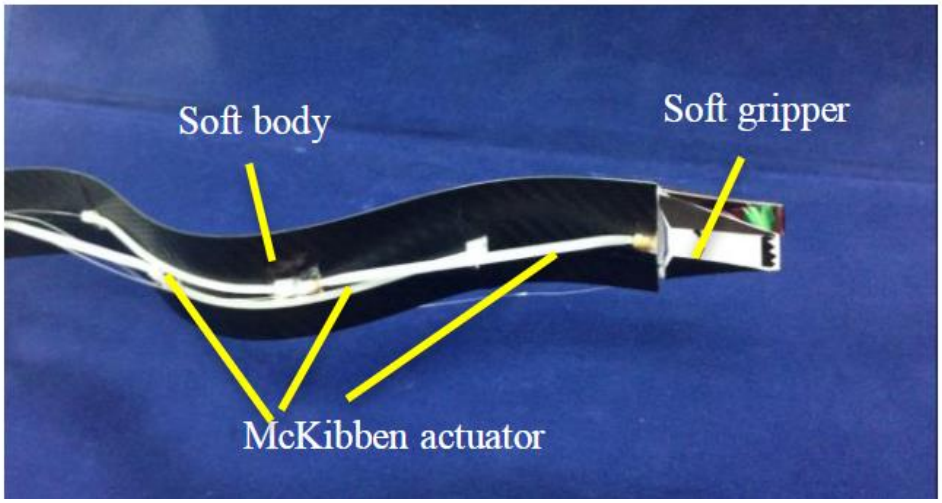

Figure 26: McKibben based soft robot manipulator [65]

Suzumori et al. demonstrated that a trade-off existed between increased contraction ability (~35% increase) and decreased contraction force (10-40% reduction) for the combined McKibben actuator systems [66]. The thin, combined McKibben actuator application was expanded by Suzumori et al. for medical device purposes such as a muscular hand [67], upper body [68], or lower body assistive medical device system as shown in Figure 27 [69].

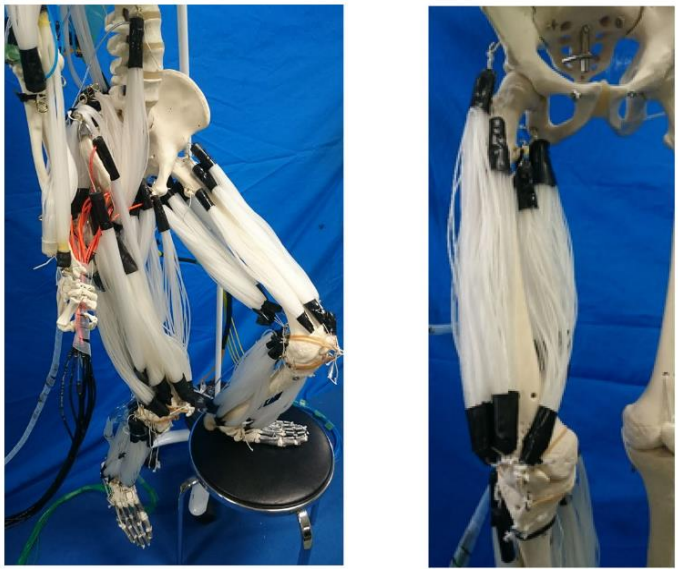

Figure 27: Lower body assistive medical device system based on the thin McKibben actuator [69]

Hammond III et al. have developed a modified version of the pneumatic McKibben actuator that is equipped with radial sensors that enable position and force sensing of the actuator [70]. Two of the actuators were connected in a system to generate antagonistic actuation of a one degree-of-freedom linkage system. The embedded sensors allow for closed loop force and position control of the system without the need of any external sensing equipment. Figure 28 shows the design of the actuator and the placement of the force and position sensors. Figure 29 shows the completed linkage system driven by the McKibben actuator.

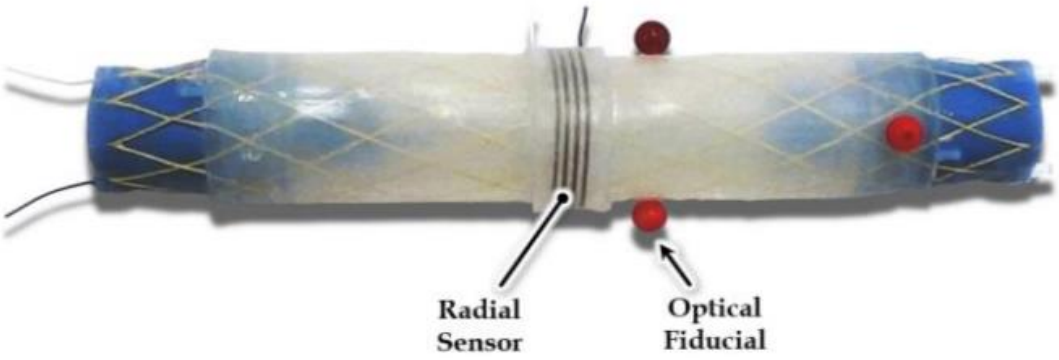

Figure 28: Modified McKibben actuator with force and position sensing [70]

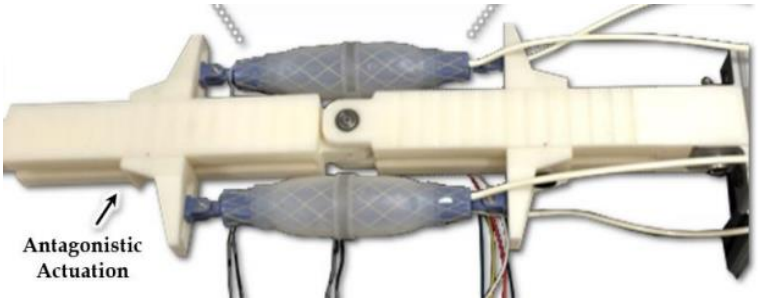

Figure 29: Combined linkage system based on the McKibben actuator [70]

While the majority of McKibben applications are primarily pneumatic, there are some examples of hydraulic McKibben actuators that can be found in literature. For example, Suzumori et al. developed a knee-support device that was based on a four-bar linkage driven by a hydraulic McKibben actuator that emulated the muscles in the knee [71]. The hydraulic McKibben actuator is uniquely beneficial for these types of applications where a large force output and flexibility is needed but large displacement is not. Figure 30 shows a diagram of the hydraulical McKibben driven device at 3 MPa.

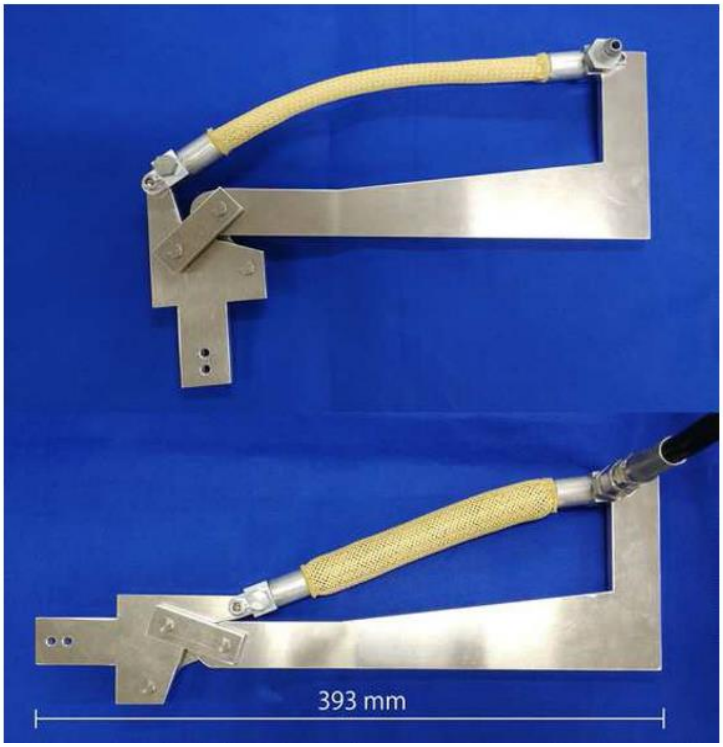

Figure 30: Hydraulic McKibben based knee-support device [71]

There are similar applications of the hydraulic McKibben actuator, such as the shape adaptable hand [59] and underwater manipulator [21], but literature is limited to simple applications of the actuator where its inherent flexibility and ability to generate large forces may not be utilized to their fullest potential. Modeling limitations, design challenges, and lack of the awareness of applications have historically limited development of hydraulic McKibben actuators that may be useful in high-force applications in confined places like burrowing.

1.2.3 Burrowing Mechanics and Systems

Burrowing mechanics in nature have been extensively studied as inspiration for biomimicry-based robots. This section provides an overview of burrowing mechanics found in nature and robot technologies that have been developed to accomplish tasks related to underground burrowing such as soil penetration or traversing a tubular environment like a burrow. While the contributions of this thesis will not include development of a soil penetrating head, a high-level review of soil penetration and existing soil penetrating technologies will be provided.

While burrowing locomotion requires more energy than running, flying, or swimming locomotion, many animals have evolved to be able to burrow efficiently, as defined by their metabolic and oxygen consumption rates, into different substrates in order to survive [12, 72]. A variety of burrowing locomotion techniques have been observed in nature where animals and plants have developed locomotion gaits that are dependent upon the soil mechanics of the substrate as shown in Figure 31 [25]. The mechanics and efficiency of these locomotion gaits and techniques have been studied extensively in prior literature [14, 72-80].

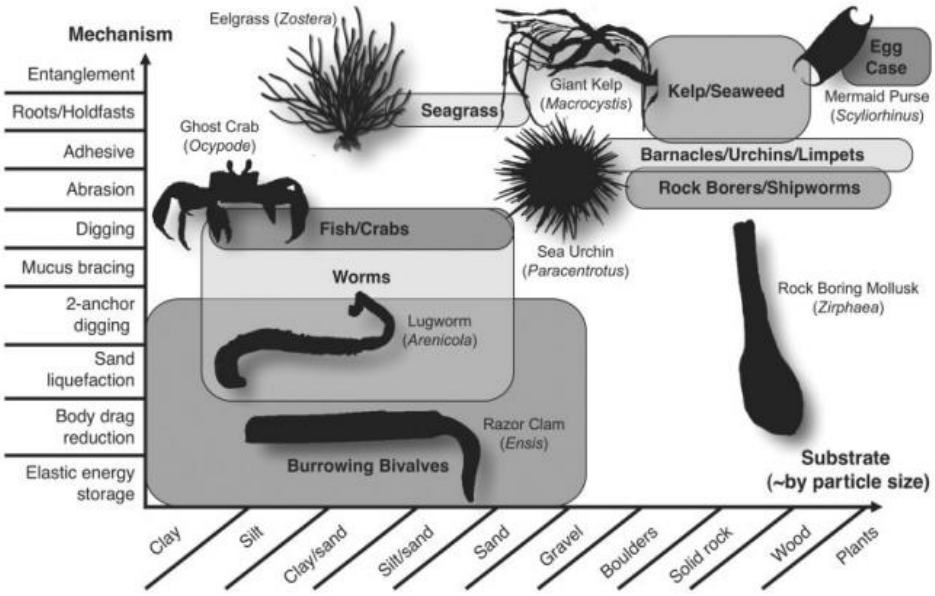

Figure 31: Burrowing and anchoring mechanisms for some animals found in nature [25]

Soils that are composed of granular media (i.e. sandy soils) are home to worms, ants, moles, lizards and other species that burrow into the substrate [81]. Granular soils are characterized by the presence of individual particles that compose the substrate and dictate the soil response through the inter-particle contact forces [9, 82]. Some lizards and snakes have evolved to have shovel-shaped snouts and a counter-sunk lower jaw that allow them to penetrate the soil substrate, and once submerged into the soil, they utilize a locomotion technique known as sand swimming to provide the necessary propulsion forces to burrow. This is done by generating sinusoidal waves up and down the body of the animal [81]. The efficiency of soil penetration is very much affected by the shape of the penetrator [76]. Dimensionless wedge numbers and studies of penetrometer shape have been studied to predict soil deformation [78, 83-84]. Because granular media is not as naturally cohesive as other substrates, it is much more

difficult for the particles to ‘stick together’ and leave a lasting burrow [85-86]. Models of undulatory self-propulsion (sand swimming) have been developed to understand the burrowing kinematics and efficiencies of animals and bio-inspired robots in granular media as well as the drag forces experienced by the burrower depending on the water content in the soil and other physical soil properties [73, 77, 81, 85, 87-89]. Goldman et al. developed a sand swimming robot that used servo motors and a bioinspired, wedge shaped head to mimic the behavior of a sandfish lizard as shown in Figure 32 [81].

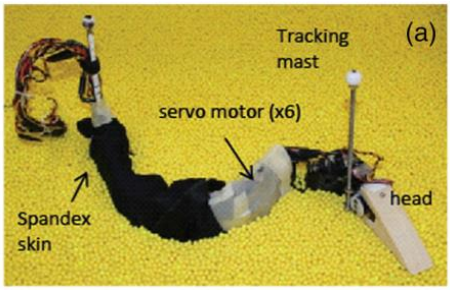

Figure 32: Bioinspired sand swimming robot [81]

Wet or muddy soils are home to many burrowing animals such as clams and worms [90]. These soils are characterized from a continuum perspective rather than a particle-based approach due to the high prevalence of cohesion between particles. Because of the inherent elasticity of wet soils, much different burrowing locomotion techniques are used by animals to navigate through wet soils than sandy soils [91]. Because wet soils are more viscous than dry soils, the ease and efficiency of burrowing in wet soils is greater [11, 85]. Moles, frogs, and spiders have been observed to use a shoveling excavation method to provide

propulsive forces, steer the direction of their burrow, and remove soil from or compact soil in their burrows [11, 92-93].

A class of burrowing techniques that utilize fluid lubricant to reduce friction have been observed in nature. One study confirmed experimentally that using a pneumatically powered, mole-inspired excavation technique to burrow into wet soils that behave elastically was much more efficient than in dry soils, and it is suggested that injecting water into the dry soil will increase the viscosity and cohesion of the initially dry substrate to enable more efficient burrowing [11]. Roots growing into dry soils have been observed to secrete mucus that reduces the root-soil drag to increase penetration efficiency [94-96]. Mazzolai et al. have extensively studied plant root morphology as an inspiration for soft robot design for applications in soil exploration [97]. This work demonstrated that biomimicry of plant roots can be used to increase energy and force efficiency of soil penetration. Figure 33 shows the penetration force, F_z versus the penetration depth, z for several different geometry soil probes.

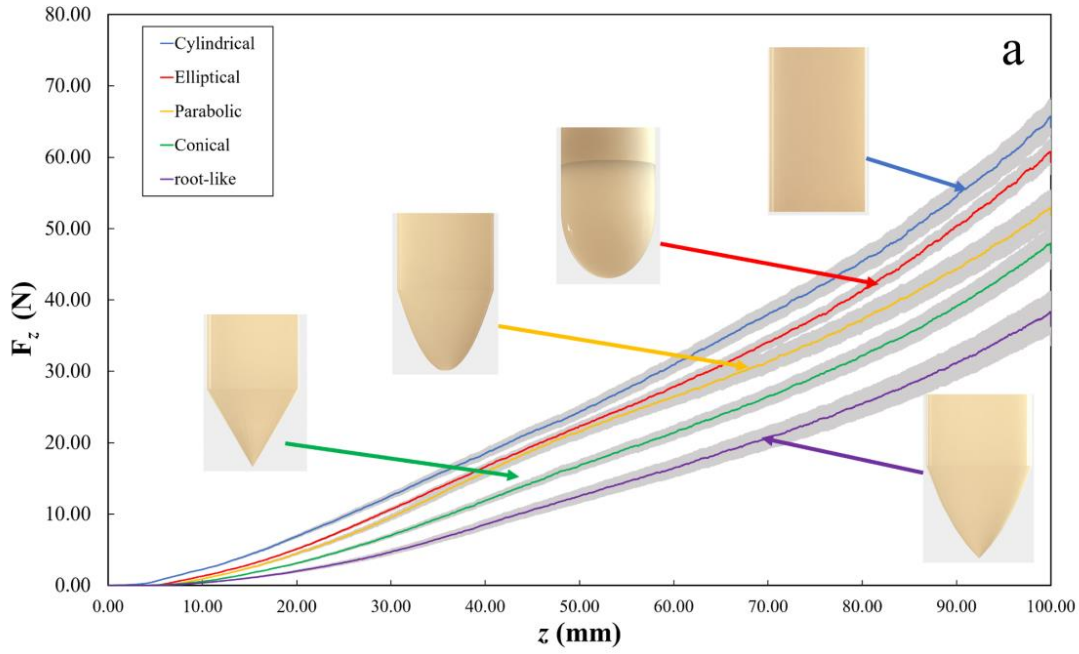

Figure 33: Penetrator geometry study results [97]

Mazzolai et al. also developed a soft probe for soil exploration that was designed to simulate the radial expansion mechanisms of a plant root [98]. Plant roots grow in a particular geometry and rate that limits penetration friction, therefore improving the energy efficiency of the plant root tip penetration process into the soil. The probe tip was designed in the shape of a root tip and was fitted with ball bearings to further reduce frictional forces when penetrating the soil. Experimental probing into soil demonstrated that the radial expansion of the probe tip, along with the rolling bearings in the probe tip, reduced the overall penetration energy by 13.02% and overall penetration force by 13.40%. These experiments demonstrate the considerable impact that friction has on penetration efficiency as well as how crack propagation and biomimicry can be used in soil to improve energy efficiency. The soft robotic probe is shown in Figure 34.

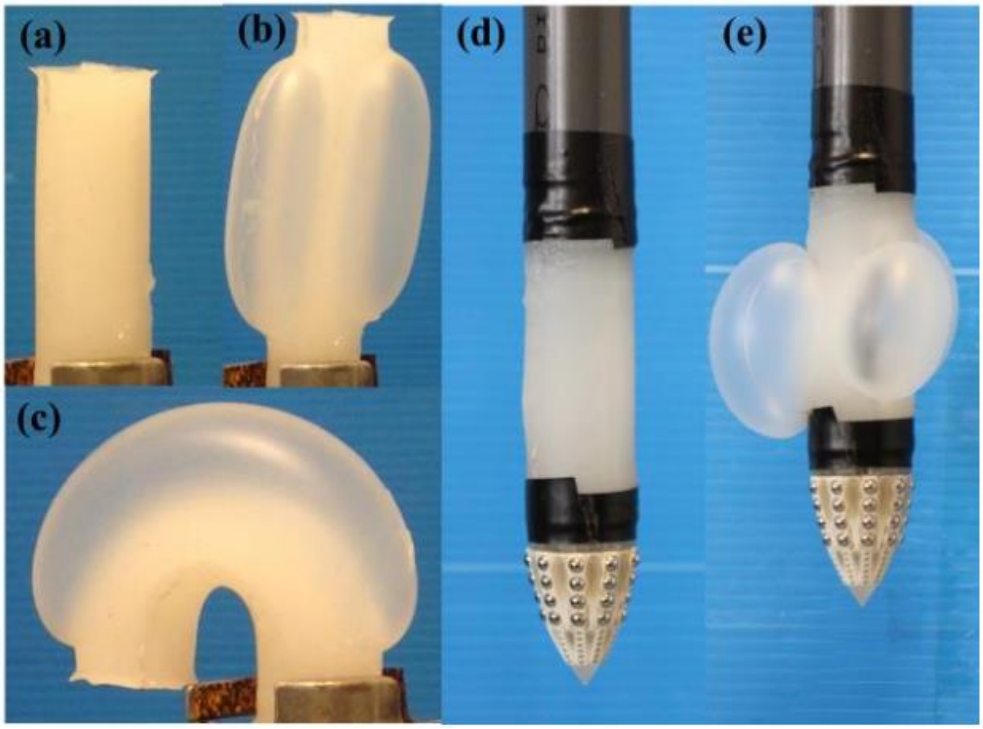

Figure 34: Plant root inspired soft robotic probe [97]

The Atlantic Razor Clam uses localized fluidization, a method to increase the water content of the substrate near itself to reduce drag forces, by pushing against the soil wall to draw in water content from the soil to dramatically increase the porosity of the surrounding substrate to reduce the energy requirements of burrowing. This enables it to burrow 70 cm deep at 1 cm/s [14]. Winter et al. have used the genetic algorithm to optimize the kinematics and timing of a pneumatic (0.4 MPa) burrowing robot called RoboClam that uses radial expansion and contraction motions to loosen soil and draw in water from the surrounding soil to emulate the burrowing locomotion of the Atlantic Razor Clam as shown in Figure 35 [14]. A blunt shaped piston is used to generate forces necessary to penetrate axially into the substrate, and other studies have

proposed similar linear penetration mechanisms useful for penetrating into soil [99].

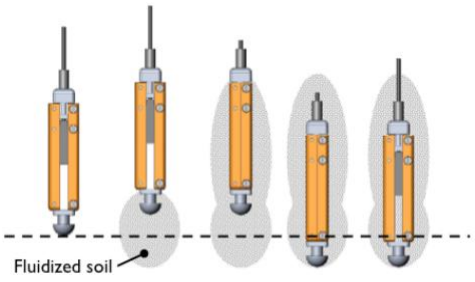

Figure 35: RoboClam utilizing localized fluidization to reduce energy requirements of burrowing [14]

By using the localized fluidization burrowing technique, the energy requirements of burrowing increases linearly with depth whereas the energy requirements of burrowing increases exponentially with depth due to significant drag forces [14, 74, 80, 100]. The fluidized zone surrounding the robot is a function of two common soil parameters: the coefficient of lateral earth pressure and the fraction angle [90]. The stresses and forces needed to deform the substrate to allow localized fluidization are well understood and the mechanics are not limited to a specific size scale [90]. A theoretical study of utilizing localized fluidization to burrow into dry soil using RoboClam was conducted, and the developed models show that contraction and expansion must occur significantly faster to prevent the dry soil from collapsing in around the device [85, 100-101]. However, further fluidizing the substrate with the device itself, rather than drawing fluid from the surrounding substrate only, may increase the soil cohesion and may be a way to increase the effectiveness of burrowing in dry soils with RoboClam like locomotion. Winter et al. presented the scaling laws of

RoboClam locomotion and postulated that a scaled device would have to operate slower [13].

Crack propagation is another technique, often used by various species of worms and plant roots, to generate penetration forces necessary to move through soil and is primarily used in wet and muddy soils that behave similar to elastic solids [83, 94, 102-104]. Linear elastic fracture mechanics are used to model this locomotion method where the burrower creates a small crack in the soil interface and generates radial forces until a critical stress is reached and the crack propagates [72, 86]. Crack growth has been shown to be stable when displacement driven and unstable when force driven [86]. A two anchor system is often utilized to provide the necessary traction forces and kinematics to penetrate into the soil and create the crack or to traverse an existing tube-like environment [72, 91, 105-109]. Worms do this in nature by generating radial forces via expansion, generating axial forces by extension, contracting the expanded segment, and then pulling the body forward in their burrow [47, 72, 110]. Another method of providing anchoring or traction forces is observed in roots that twist and turn as they grow [96]. A robotic root was designed to test various penetrator shapes and the best penetration rates for probing into soils [111]. One study, with the intent to optimize the geometry of a penetrating shell, presented the design and testing of a low pressure, hydraulically powered actuated bivalve robot that utilizes the aforementioned anchoring system that burrowed very slowly in wet soil to anchor itself at shallow depths [110]. Studies have found that the

mechanical advantage, defined by the ratio of force capabilities to body mass, of animals that generate forces (radial and axial) during burrowing locomotion scales as a function of body mass [75, 112].

Excavation methods have been observed in nature and tools have been developed that bore through the soil and remove the substrate rather than compacting the substrate into the walls of the burrow. Studies on the energetics of burrowing have shown that excavation techniques are mechanically inefficient burrowing methods [113]. Bioinspired techniques such as the shoveling motion of a mole or the backwards burrowing approach of the wolf spider have been observed [11, 92]. Gophers that use excavation techniques have been studied to show they are more efficient burrowers in soil content with high water content which further suggests that fluidized substrates are easier to penetrate as well as excavate [114]. Rodents can burrow faster in damp sands than they can in dry sands using excavation techniques that shear, scratch, and thrust the soil [115]. A study was done on the design and models for a burrowing robot for lunar exploration that utilized a screw-like auger to excavate at the burrow tip and a body geometry that causes a cylindrical section of the soil substrate to deform plastically to leave a permanent burrow. A second screw was added to the device to enable the system to move back and forth axially as well as excavate. The excavating screw was designed in a way that balanced the penetrating and anchoring forces of the penetrator [116-117], but other studies of screw excavation have been performed as well [15, 118-120]. Another lunar burrowing

robot was proposed to use a screw excavator with individually actuated mechanical anchoring segments to provide traction forces as shown in Figure 36 [16].

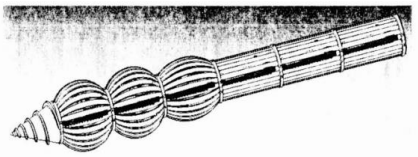

Figure 36: Proposed design of a burrowing robot for lunar applications [16]

A group of French researchers have proposed an autonomous, self-optimizing, multi-segment rigid robot that can excavate and burrow like an inchworm to navigate, detect buried objects, and map underground spaces in three dimensions. The proposed system utilizes GPS tracking, modular impact and rotary drilling mechanisms along with a soil transport system, peristaltic locomotion, and a novel mechatronic steering system. The burrow is reinforced with 3D printed structures placed by the robot as it traverses the burrow. The system can adapt to the changing burrow direction by using rigid segments connected with three degree of freedom mechanical joints. The proposed system is shown in Figure 37 [121].

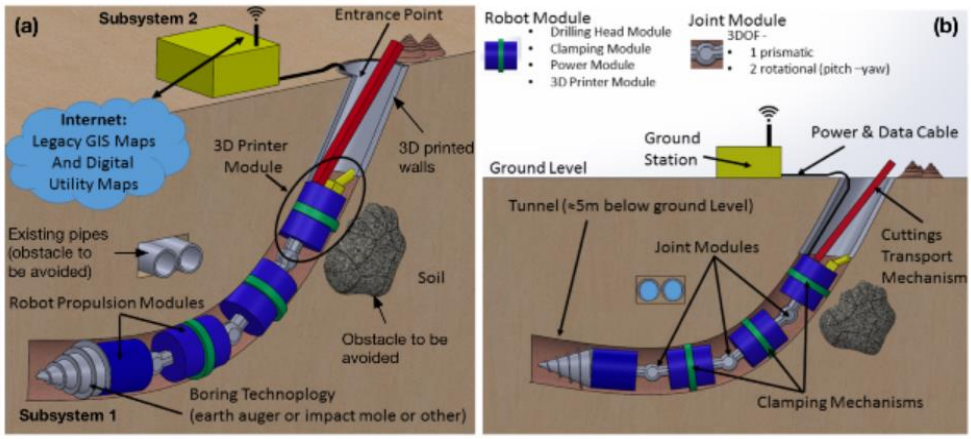

Figure 37: Proposed design of a multi-segment burrowing robot [121]

Directional boring, commonly referred to as direction drilling or horizontal directional drilling (HDD), is an excavating method that has been developed to burrow holes in a steerable manner for utility installation in dry soils [8]. Drilling fluid is supplied to a rotary cutting tool to reduce abrasion of the cutting tool, stabilize the burrow, and reduce drag experienced between objects passing through the burrow, such as pipes and cables, and the burrow wall. High viscosity fluids are used that remain in the burrow to reduce drag rather than seep into the soil like water does [8]. Steel stems are used to transmit ‘push forces’ along the boring system to the boring head. Directional boring systems can be guided by walk over locating/sensing systems that convey information back to an operator, magnetic guidance systems that read in azimuth and inclination angles to track position, and more expensive but very accurate gyro-sensing location systems. Direction boring units are very large and expensive which limits the number of specialized applications they are well suited for [6].

In recent years, many new approaches to navigating tubular environments with multi-segment soft robots have been explored. One pneumatically driven multi-segment soft robot utilized expanding segments that generated a helical shape, connected in the middle with an extending McKibben segment, to traverse through a tube [109]. The helical shape was achieved by wrapping the elastomer with differing forward and backward fiber angles along with the inclusion of a single fiber at a third wrap angle [122]. The robot experienced slipping while it moved through the tube because it was actuated serially with a single input pressure wave on the proximal end that caused a delay between the actuation of the three segments. Another reason slipping occurred was because the helical anchoring actuators changed axial length when radially expanding, which is a limitation to this multi-segment robot design. Passive valves were used between the three segments to control the fluid flow during actuation. Furthermore, the serially-actuated robot is not able to move backwards through the tube. The robot, which was developed at the University of Minnesota, is shown in Figure 38.

Figure 38: Pneumatic, serially-actuated multi-segment tube traversing robot [109]

Another example of a multi-segment soft robot is from Verma et al. who developed a pneumatically powered soft robot actuated with vacuum chambers that can move through tubes by actuating various segments of the robot sequentially. However, this robot was severely limited in its ability to generate large extensions and forces, and it was severely limited in what tube size ranges it could traverse. The robot is shown in Figure 39 [123].

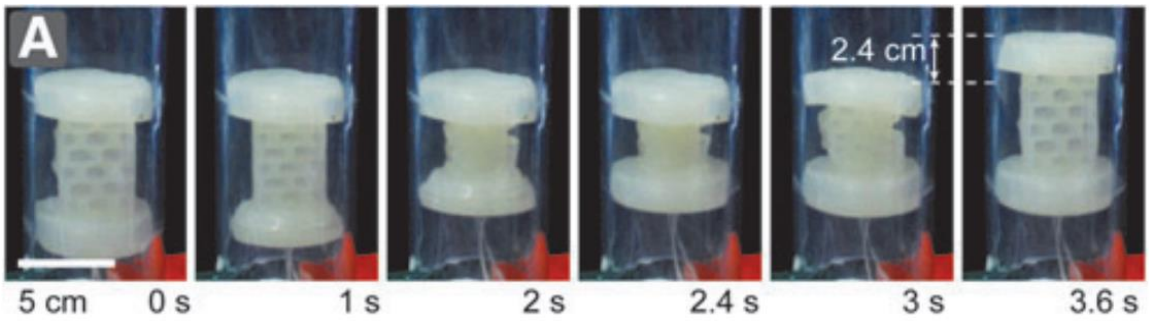

Figure 39: Vacuum chamber actuated tube traversing multi-segment robot [123]

Kamata et al. have developed a pneumatic multi-segment robot that is comprised of many axially connected soft segments to move like an earthworm through small diameter pipes for inspection applications [124]. The soft segments simultaneously displace axially and radially in a way that allows the robot to navigate through a pipe by carefully controlling the actuation timing of the segments. The extending segments utilized an extension spring, and the radially expanding segments used a straight fiber design that allowed for prescribed radial expansion and axial contraction. Because the design contained multiple extension units, it was able to account for the axial displacement of the expanding units by actuating multiple units simultaneously. The robot was able to

navigate through a tube, but the travel speed was greatly diminished as the travel distance increased due to challenges with transmitting pneumatic pressure over long distances. Figure 40 shows the design and actuation cycle of the robot, Figure 41 shows the design of the extending units, and Figure 42 shows the design of the expanding units.

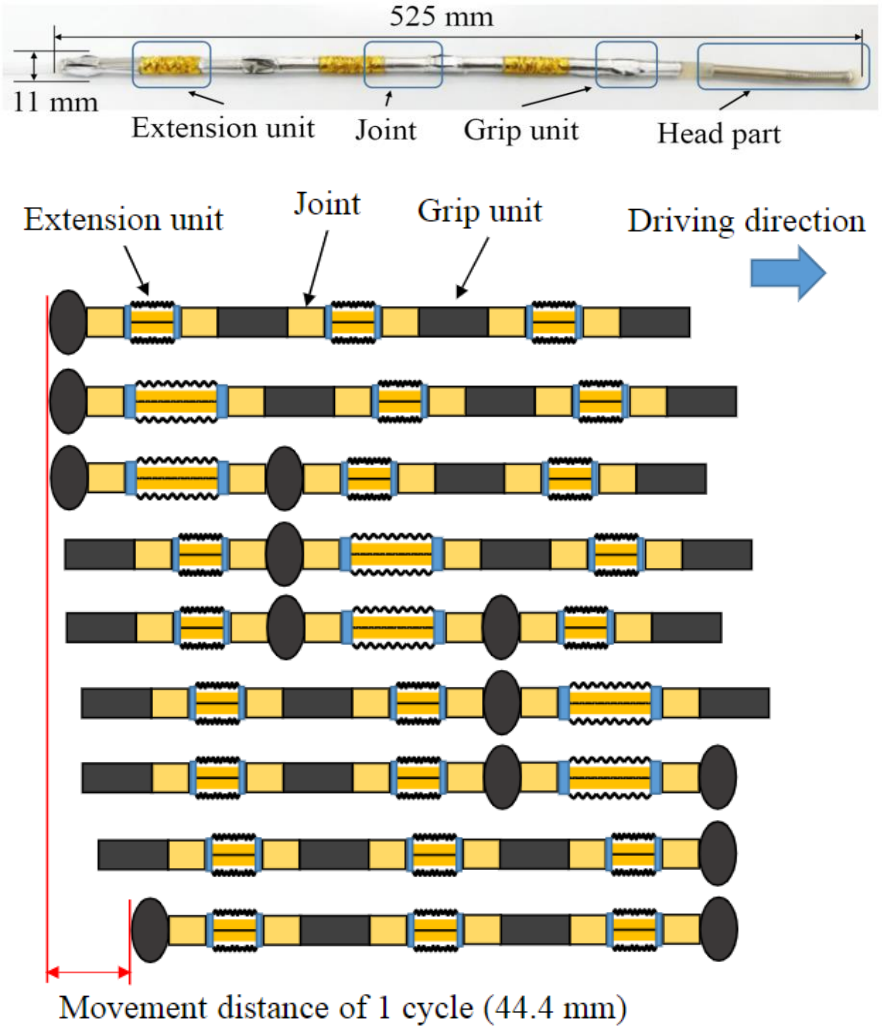

Figure 40: Multi-segment robot design and actuation cycle [124]

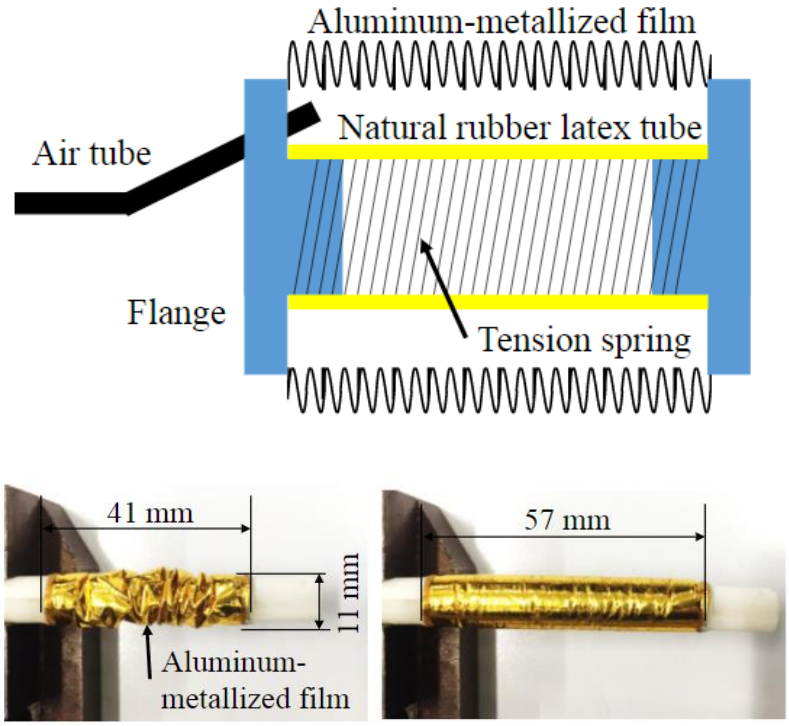

Figure 41: Extension unit design [124]

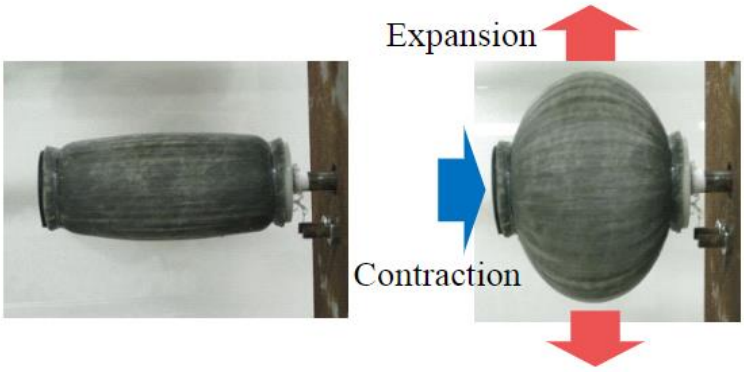

Figure 42: Expanding unit design with straight fibers causing simultaneous expansion and contraction [124]

Calderon et al. have developed a multi-material, multi-segment soft robot inspired by the locomotion of burrow worms [125]. The robot is pneumatically

driven by circular and longitudinal actuators and is able to traverse through pipes in both the horizontal and vertical directions using the peristaltic motions of an earthworm. The robot was fabricated with two spherically expanding segments and one extending segment, and it shuffled fluid between the segments to create motion in the likeness of a burrow worm. The robot was also able to move through bends in the pipe demonstrating some of the many benefits of the flexibility of soft robotics for creating complex motion. However, the robot was limited to producing small forces and displacements. The robot design and actuation cycle as it moves vertically through a pipe is shown in Figure 43.

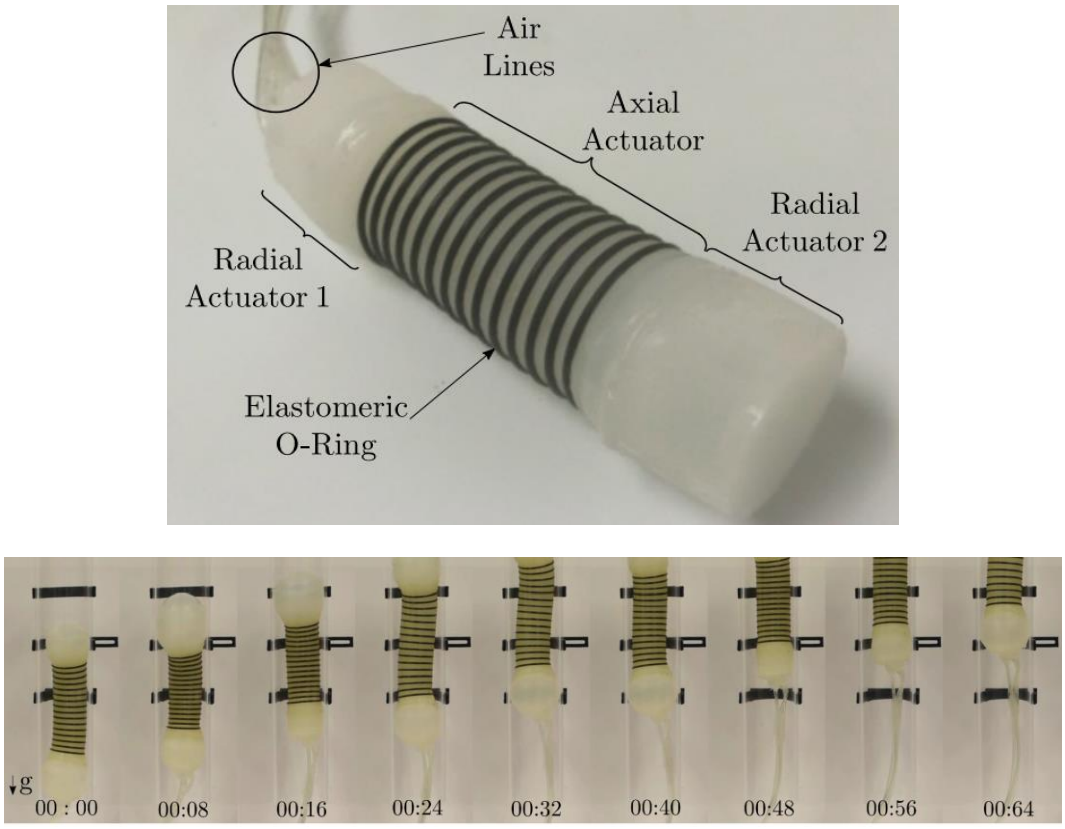

Figure 43: Burrow worm inspired multi-segment robot w/ spherically expanding radial segments [125]

Calderon et al. also developed a slightly modifed version of their pneumatic tube-traversing robot that was able to manipulate friction to crawl across flat surfaces [126]. Slight modifications were made to the radial actuators to so that the friction experienced between the surface and the bottom of the actuators could be controlled during the peristaltic motion of the actuator. Figure 44 shows the robotic system crawling across a flat surface.

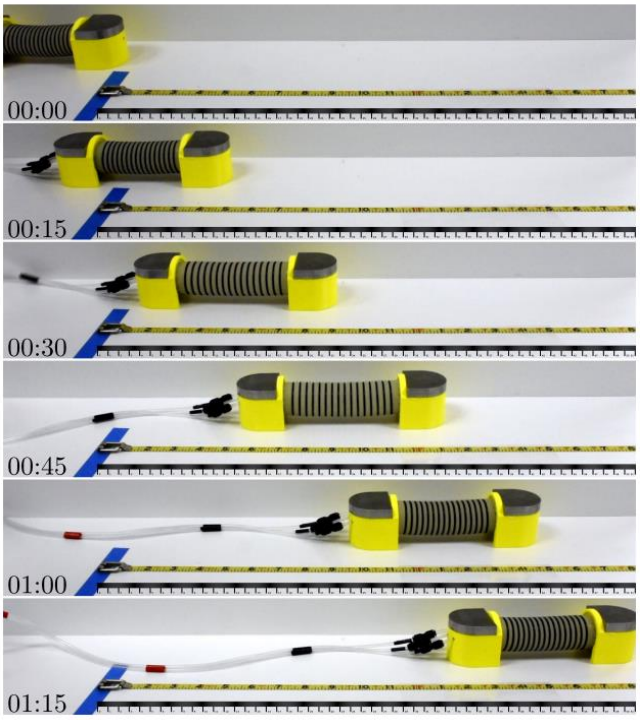

Figure 44: Multi-segment crawling robot that manipulates friction to generate traction forces [126]

Liu et al. developed a pneumatically driven, multi-segment soft robot based on biomimicry of an earth-worm by utilizing high-traction Kirigami skin to generate more friction, and therefore larger anchoring forces, in the two radially

expanding segments and a McKibben actuator to produce extension in the middle segment [127]. The silicone Kirigami skin is fabricated to act in the same manner as the bristles on an earthworm to generate larger anchoring forces when moving forward into a burrow. The robot was tested in cohesive garden soils to demonstrate the improved anchoring of the robot due to the presence of the Kirigami skin. Precise control of the distal end of the robot is limited by the fact that the contractile actuators displace axially when radially expanding. This can also lead to the actuator slipping in the burrow or tube. The overall design of the kirigami robot is shown in Figure 45, and the expanded contractile segment utilizing the kirigami skin for additional friction is shown in Figure 46.

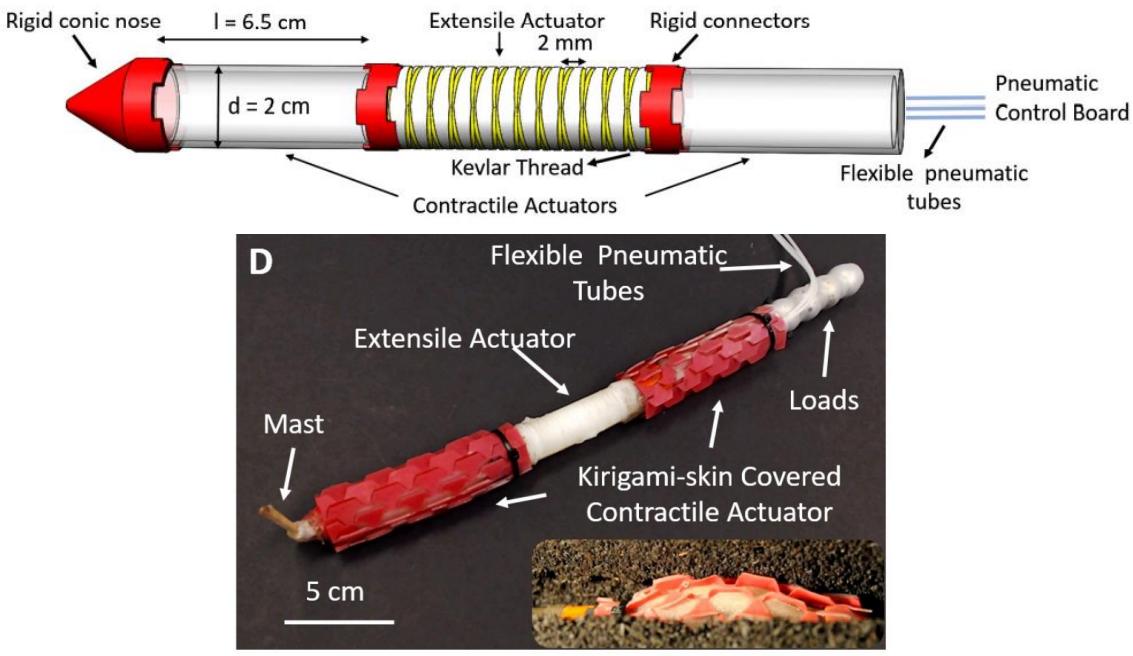

Figure 45: Kirigami-based multi-segment robot for burrowing applications [127]

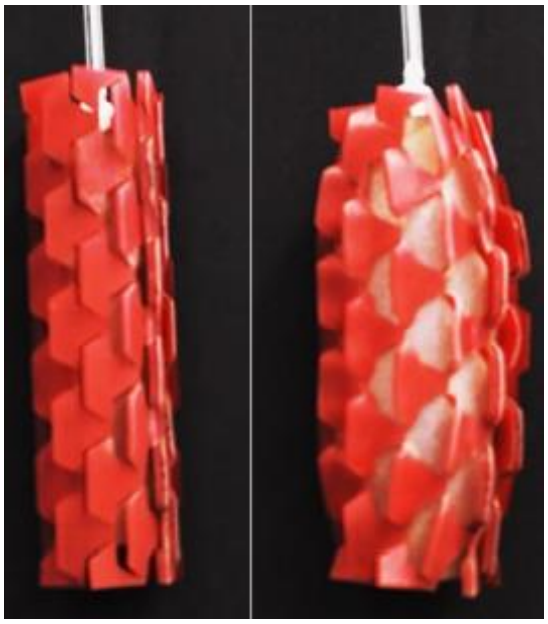

Figure 46: Radially expanding, axially contracting, Kirigami covered contractile actuators for generating traction forces [127]

Only one known hydraulically driven, multi-segment burrowing soft robot has been developed in literature to date. The multi-segment robot, privately developed by the General Electric Company (GE) in 2020 for military applications in tunneling, consists of multiple soft hydraulic artificial muscles that enable the entire robot to move like an earthworm and generate large penetration forces at the tip. The robot requires many of the segments to be actuated simultaneously such that some of the segments are generating radial anchoring forces while others are extending to generate motion and penetration forces. All the robot segments, except the tip of the robot, are similar in design and rely on actuation timing to generate the burrowing locomotion desired. The robot can adapt its gait depending on the burrow conditions but is limited in what motions the robot can

achieve due to the requirement of simultaneous actuation of the segments. Figure 47 and Figure 48 show images of the GE burrowing robot [128].

Figure 47: GE multi-segment burrowing robot (side view) [128]

Figure 48: GE multi-segment burrowing robot (top view) [128]

The GE robot is the first hydraulically driven, multi-segment burrowing robot developed from soft robotic segments, and it shows great potential for burrowing applications. However, the robot relies on its length to develop large traction forces along the burrow, requires simultaneous actuation of the segments to generate motion in the burrow, and the motions it can achieve are limited due to the wave-like actuation method. Furthermore, it appears from Figure 47 and Figure 48 that the robot utilizes externally placed electrical or hydraulic fluid lines that could be damaged by the underground burrowing environment. A video of the GE robot in action can be found at the following website link [128]. This research is ongoing at this time.

https://www.youtube.com/watch?v=VdMIFZ6ZfaE

1.2.4 Conclusion

Soil mechanics and burrowing locomotion in different substrates have been studied extensively by observing the behavior of biology. Animals and engineers have developed techniques to fluidize the substrate to reduce drag forces while moving through muddy soils, use wave-like swimming motion to navigate into sandy soils, anchor themselves in soil, and utilize crack propagation to drive into elastic soil substrates as outlined in this section. Parallels have been drawn and several burrowing robots have been developed or proposed that emulate the efficient behavior of these animals.

The pneumatically driven Kirigami robot and the hydraulically driven GE robot are the only known multi-segment soft robots that have demonstrated efficacy in burrowing applications, and the limitations of each of the robots were discussed in section 1.2.3. This thesis seeks to address some of these limitations and present a novel approach to designing a hydraulically driven, multi-segment soft robot capable of traversing a tube-like environment like a burrow. Because burrowing occurs in a confined and variable environment, soft and compliant robots that utilize the unparalleled force density of high-pressure hydraulics are a natural choice for the application. Furthermore, hydraulics offers better displacement control than pneumatics because of the compressibility of air.

An opportunity exists to use hydraulically driven, high-force soft robotic segments to develop burrowing systems that can eventually be designed to operate with energy efficient burrowing locomotion and techniques. Currently, no compact, hydraulically driven, multi-segment soft robotic systems exist that conform to the environment, allow for purely independent actuation of the robot segments for precise position control, and can produce the large forces needed in many burrowing applications.

1.3 **Thesis Overview and Specific Contributions**

The research herein presents a means to develop efficient burrowing technology by emulating nature, utilizing compliant soft robots, and exploiting the high-power density of hydraulics. The technology will reduce the need for

invasive excavation or expensive directional boring techniques and presents a more efficient approach for installation of pipes, electrical lines, and other common utilities. Additionally, this work provides methods for the design of reliable, high force soft actuators for use in many systems that require flexible actuators capable of adapting to their environments and developing large forces. Besides burrowing, potential applications enabled by the technology include pipe inspection, pipe repair, anchoring of off-shore rigs, sensor placement, mine and IED detonation, rescue operations, mining, searching for fossil fuels, exoskeleton designs, and many others.

The scope of this thesis will be limited to the development of the models, design methodologies, and manufacturing techniques for a hydraulically driven, multi-segment robot that addresses the limitations of existing burrowing robot technologies and can navigate horizontally and vertically through tubes of various diameters in a robust and energy efficient manner. The development of a soil penetrating end-effector, robot-soil interface models, and optimized gait kinematics of the robot are out of scope for this thesis and will be addressed in future work to fully realize the robot's potential for a myriad of burrowing and similar applications.

A multi-segment soft robot prototype was developed by the author as an outcome of this research. Axial and anchoring force models were developed and experimentally validated for the segments, and a multi-segment robot prototype

was developed to validate the system's ability to navigate through tubular environments. The robot was able to effectively navigate through rigid tubes of various sizes in both the forward and backward directions in both a horizontal and vertical configuration (against gravity).

The final robot prototype is shown in Figure 49. Junchi Feng, an undergraduate student in the Mechanical Energy and Power Systems laboratory, assisted the author in developing the time-lapse in Figure 50 demonstrating how the proposed robot technology could use multiple soft segments to navigate and steer through underground environments. The full-length robot animation depicted in Figure 50 can be found at the link below.

https://drive.google.com/drive/folders/1A3Jd1QleO8UoLq4XZtgizWIrq6Ro84gB?usp=sharing

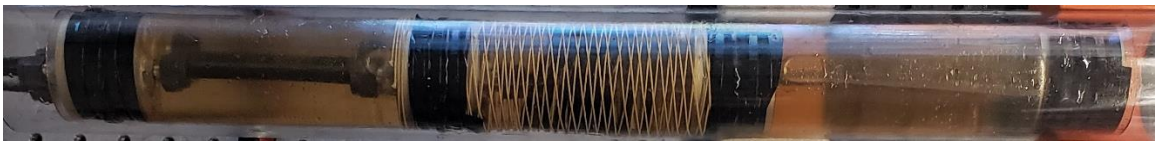

Figure 49: Finalized multi-segment soft robot

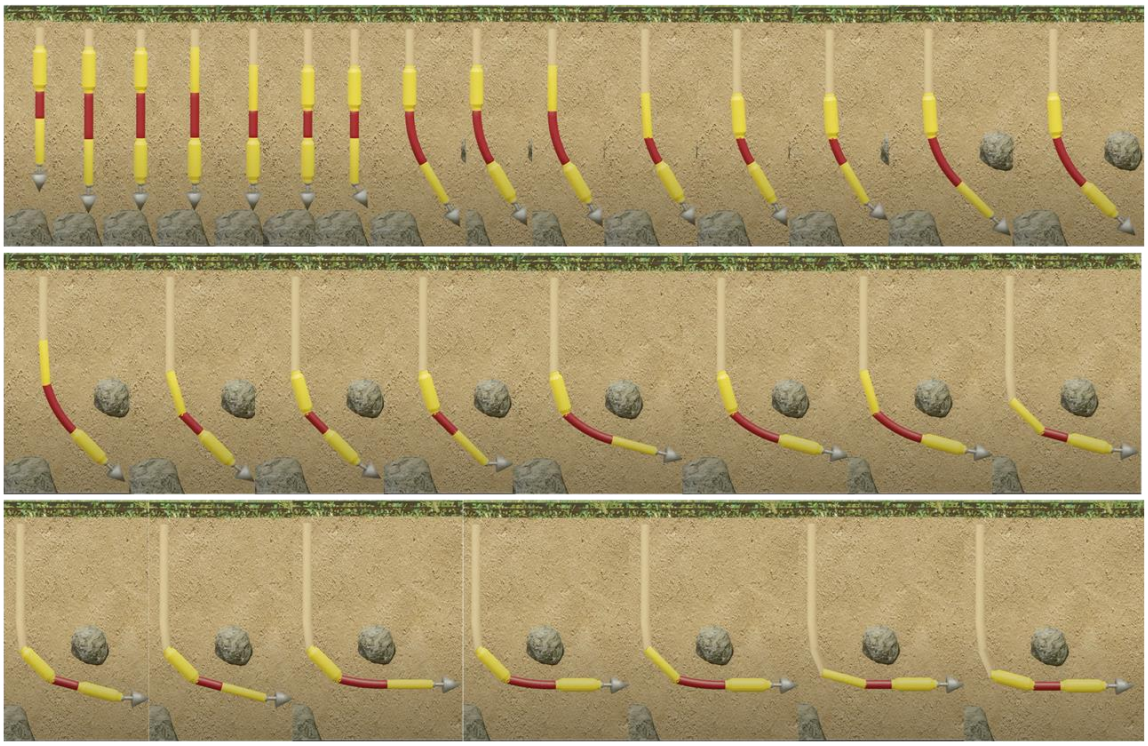

Figure 50: Time-lapse of proposed multi-segment soft robot locomotion through soil substrate – credit Junchi Feng

The following chapters investigate McKibben actuators as suitable soft robot segments for burrowing applications, explore anchoring force generating soft actuator designs, explore soft robot failure modes, validate new soft actuator force modeling techniques, and present the design approach and experimental results of the tube-traversing multi-segment soft robot. This thesis contains six chapters. The specific contributions to this thesis from each chapter are summarized as follows.

Chapter 1: Introduction

- Provides motivation for the thesis and key background information on the field of soft robotics, the McKibben actuator, burrowing mechanics, existing soft robotic burrowing technologies, and provides an overview of the structure of this thesis

Chapter 2: Hydraulic McKibben Actuator Force Studies

- Development of a new McKibben axial force model ($F(\varepsilon,t)$) that addresses variations in actuator wall thickness as an actuator is displaced and experimental validation against existing McKibben force models

- Experimental validation of the Kothera elastic force model and demonstration of the importance to include this elastic term in force modeling thicker-walled McKibben actuators

- Experimental validation of using the empirical Gent model to convert shore A durometer to elastic modulus for McKibben force modeling

- Experimental validation that layering multiple off-the-shelf fiber sleeves on a McKibben actuator to increase the resistance to a burst failure has minimal impact on the axial force generated (input pressure of ~13.9 MPa achieved)

- Confirmation that the axial force generated by contracting and extending McKibben actuators can be predicted with the same models with similar accuracy at free and displaced conditions

- Development of a novel manufacturing approach of McKibben actuators including how to manufacture custom-sized elastomers with embedded fibers at specific fiber-wrap angles

- Development and experimental validation of new elastomer bulge model to understand the relationship between input pressure, fiber spacing, and elastomer bulging/safety factor from bursting.

Chapter 3: Hydraulic McKibben Actuator Buckling Study

- Experimental confirmation that extending McKibben actuators follow traditional column buckling mechanics

- Experimental confirmation that fiber-wrapped McKibben actuators follow the same buckling behavior when buckling from compression forces developed due to internal pressure actuation as from compression forces from an external source applied to the actuator

- Experimental validation that extending McKibben actuators can develop extension forces beyond the Euler-Johnson column buckling critical load when constrained environment like a burrow

- Preliminary frame-work for treating a pressurized extending McKibben actuator in a constrained environment as two eccentrically loaded columns that axially shorten as the contact length between the actuator and the environment grows

- Experimental validation of the compressive yielding failure - which may be the most common failure mode for actuator sizes that will be used in burrowing robots

Chapter 4: Anchoring (Traction) Actuators

- Development of a novel force model for a fixed length, radially expanding soft robot actuator for determining traction force as a function of actuator geometry, actuator input pressure, and burrow (or tube) diameter

- Novel design of a fixed length, radially expanding soft robot actuator capable of generating traction forces in a wide range of burrow (or tube) diameters. The actuator consists of a constant wall thickness elastomer, a stiff threaded rod to prevent the actuator from changing length during

actuation, two aluminum segment connectors, and low-profile zip ties to secure the elastomer to the segment connectors.

- Experimental validation of the traction force model as a baseline predictive design tool

- Development of three early-stage traction actuator designs:

    - Loose sleeve modified McKibben actuator design that utilizes a strain limiting rod to prevent axial displacement and a loose fiber sleeve to limit radial expansion of the elastomer
    - Multi-layered calcium-chloride expanded actuator design that allows fibers to be embedded on a stressed elastomer and multiple elastomer compartments to be designed into a soft actuator to control deformation during actuation
    - Constant stress elastomer design to mitigate blow out failures caused from stress concentration near the segment connectors of soft actuators

Chapter 5: Multi-Segment Robot System

- Development of a novel three-segment, hydraulically driven soft robot capable of moving through both horizontally and vertically aligned tubular

environments of varying diameters. The key components of the design include the following:

  - Two radially expanding traction segments with an axial strain limiting rod to generate radial expansion and traction forces without any axial displacement
  - One axially extending McKibben segment, located between the two traction segments, to generate extension forces to move the robot through the tube or burrow
  - A single constant wall thickness elastomer containing all three robot segments and aluminum segment connectors used to partition the robot segments and connect all piping and internal components of the robot together
  - The ability to independently actuate each of the robot segments, without impacting the performance of another segment, by utilizing small diameter microbore tubing to route all fluid to and from the segments completely internally within the robot
  - Novel spiral-shaped microbore tubing design to route fluid through the extending segment to the distal traction segment regardless of the current displacement of the extending segment

- Development of a multi-segment robot design grid-search tool that sweeps a range of initial robot geometries to determine the anticipated

performance of the robot at various operating conditions for designing multi-segment robots for specific applications

- Experimental demonstration of the 457.2 mm long, 50.8 mm diameter, three-segment soft robot navigating in the forwards and backwards direction through horizontally oriented clear polycarbonate tubes with diameters of both 57.2 mm and 63.5 mm

- Experimental demonstration of the multi-segment soft robot traversing a vertically oriented 63.5 mm polycarbonate tube against gravity

Chapter 6: Conclusion

- Summarizes the thesis, ties all the research together, and discusses the future work needed to realize hydraulically powered, soft robotic burrowing systems capable of burrowing through a variety of soil substrates

Chapter 2: Hydraulic McKibben Actuator Force Studies

Existing McKibben force models have primarily focused on the low-pressure, pneumatic McKibben actuator and have limitations when being used for hydraulic McKibben design. The purpose of this chapter is to experimentally evaluate the accuracy of various McKibben actuator force models for the application of high-force actuators that may be used in burrowing or similar applications. First, an overview of existing McKibben force models is presented along with the development of a novel model developed by the author for thick-walled McKibben actuators to address existing model limitations. Twelve contracting McKibben actuators were fabricated, experimentally tested, and compared against the various force models. Five extending McKibben actuators were built to determine if there are differences in the accuracy of the force models between contracting and extending McKibben actuators. Design and manufacturing methods of the McKibben actuator are presented, and a study is presented on the efficacy of using the Gent model to predict the Young's modulus of an elastomer for design purposes. A new elastomer burst failure model is presented and compared against experimental results.

2.1 McKibben Force Modeling

The objective of this section is to analyze common McKibben force models, to construct and validate a new force model that addresses limitations of the existing models for thicker walled, hydraulically powered McKibben actuators,

and to further develop methods to quickly manufacture hydraulically powered McKibben actuators. To do this, a general overview of existing force models for McKibben actuators and the development of a novel new force model that considers the change in elastomer wall thickness during actuation and is a function of only initial actuator geometry are presented.

In a comprehensive review on McKibben actuator modeling, a need to refine the approaches for thin-walled versus thick-walled McKibben actuators was identified as well as the conclusion that there are limitations in all existing McKibben force models [53]. The thick-walled elastomer experiences considerable wall thickness change during actuation and generates significant axial elastic force when the actuator is extended; these two phenomena are often ignored when modeling pneumatic McKibben actuators [129-130]. Because pneumatic McKibben actuators typically use thin, low modulus elastomers, these modeling limitations are not as important. However, these neglected factors are significant in McKibben actuators designed for hydraulic pressures. No current model that is convenient for design and control exists that considers the varying wall thickness of the actuator as it is extended, as well as the generated elastic force from straining the actuator, and is only a function of initial actuator geometry.

The McKibben actuator was not utilized in many engineering applications until Chou and Hannaford presented their ideal actuator, virtual work-based

model to predict actuator force as a function of the input pressure and fiber wrap angle in 1996 [51]. They presented multiple variations of the model that track generated force as a function of both the fiber wrap angle and contraction ratio. While the Chou-Hannaford model was simple and accurate to within 15% for conventional thin-walled pneumatic McKibben actuators, further refinement of McKibben modeling approaches has since occurred to include fiber braid and friction effects, elastic force generation, and wall thickness effects [53, 129-131]. Multiple approaches for modeling McKibben actuators have been explored in the past including geometric approaches [35, 38, 51, 57, 132], empirical approaches [133], and approaches that consider the material properties of the elastomer [19, 129-130].

The Chou-Hannaford model is primarily investigated in this section in a few different forms [51]. When pressurized fluid is introduced into the McKibben actuator, the pressure applied on the inside walls of the actuator translates into tension in the fibers generating axial force. Three different variations of the Chou-Hannaford model, and a new variation developed by the author that addresses the limitations with existing models, are presented here as means to predict the force generated by a hydraulic McKibben actuator. Furthermore, a model for the elastic force generated by a McKibben actuator under axial deflection and a model to estimate the elastic modulus of an elastomer from durometer will be presented. The section will conclude with a model that predicts bursting failure of a fiber wrapped actuator.

All four of the following axial force models assume no elastic force is generated as the actuator is extended and that force is generated purely by converting input pressure into axial force generation in the fibers. This is addressed by adding an elastic force term to the models as presented at the end of this section. The general form of the following models enables axial force tracking as a function of only pressure and the fiber angle or only pressure and the contraction ratio, which is convenient to allow the models to be used as design tools.

2.1.1 *F(Θ),* Chou-Hannaford Model as Function of Fiber Angle

Chou and Hannaford developed the *F(Θ)* model which predicts contraction force as a function of the changing fiber wrap angle [51]. Note that contraction force is defined by convention as positive when the actuator is in tension. This model assumes no elastomer wall thickness, inextensible fibers, that the actuator remains cylindrical before and after pressure is applied, no losses, and that measurements are taken far from the system boundaries. This model does not account for elastic force generated from straining the elastomer. This model is most useful when the actuator is static and fixed on both ends because when the actuator changes length, the new fiber angle must be known to calculate the force. The fiber angle used in this model can be approximated from geometry if the actuator is extended, or the fiber angle must be physically measured which can be challenging to do accurately. The diametric constant and contraction force

are defined below where F, D_o, D, P, and θ are the contraction force, the diametric constant, the outside diameter, applied pressure, and fiber angle respectively.

$$D_o = \frac{D}{\sin(\Theta)} \tag{2.1}$$

$$F = \frac{\pi D_o^2 P}{4}(3\cos^2(\theta) - 1) \tag{2.2}$$

2.1.2 *F(ε),* Chou-Hannaford Model as Function of Contraction Ratio

Engineers from Bridgestone Corporation were the first group to begin using the *F(ε)* model, but others have followed suit [21-22, 53, 59, 134]. Most hydraulic McKibben actuator research to date uses this model. The *F(ε)* model predicts the contraction force as a function of the contraction ratio and assumes no elastomer wall thickness, inextensible fibers, that the actuator remains cylindrical before and after pressure is applied, no losses, and that measurements are taken far from the system boundaries. This model does not account for the elastic force generated from straining the elastomer. The contraction ratio is defined as:

$$\varepsilon = \frac{L_o - L}{L_o} \tag{2.3}$$

where L_o, L, and ε are the initial actuator length, the current actuator length, and the contraction ratio respectively. Note that a shortening of the actuator represents a positive contraction ratio. The force is described as:

$$F = \frac{\pi D^2 P}{4}\left(\frac{1}{\sin(\theta_o)}\right)^2 [3(1-\varepsilon)^2\cos^2(\theta_o) - 1] \quad (2.4)$$

where θ_o represents the initial fiber angle before displacement. This model is most useful when the actuator is allowed to displace because the force and displacement of the actuator can be predicted without requiring continuous knowledge of the fiber wrap angle.

2.1.3 *F(Θ,t),* Chou-Hannaford Model as Function of Fiber Angle and Accounting for Wall Thickness of Elastomer

The *F(Θ,t)* model, developed by Chou and Hannaford, predicts the contraction force as a function of the changing fiber wrap angle and accounts for the initial wall thickness of the elastomer in the derivation [51]. This is important as the fluid pressure is applied across the inner diameter, and the axial force is generated from the tension in the fibers on the outer diameter. This model does not account for the elastic force generated from straining the elastomer. This model assumes inextensible fibers, the actuator remains cylindrical before and after pressure is applied, no losses, and that measurements are taken far from the system boundaries. This model expresses the force as:

$$F = \frac{\pi D_o^2 P}{4}(3\cos^2(\theta) - 1) \quad + \pi P(D_o t_k\left(2\sin(\theta) - \frac{1}{\sin(\theta)}\right) - t_k^2) \quad (2.5)$$

where t_k is the initial wall thickness of the elastomer. This model is theoretically more accurate than the models from sections 2.1.1 and 2.1.2 and is most useful when the actuator is static and fixed on both ends because when the actuator

changes length, the new fiber angle and wall thickness must be known to calculate the generated contraction force.

2.1.4 *F(ε,t),* Contraction Wall Thickness Model as a Function of Contraction Ratio and Changing Wall Thickness

There are no existing McKibben modeling approaches that account for how the wall thickness changes non-linearly as the actuator changes length and predicts the actuator output force as a function of initial actuator geometry only. While this may not be important in pneumatic applications, much thicker walled actuators are necessary for hydraulically powered McKibben actuators to resist actuator burst failure between the fibers and prevent buckling when they are designed to generate large extension forces (Θ>54.7°). Kothera et al. have developed a model that considers variable wall thickness, but the model is a function of both current and initial wall thickness [129]. This model is particularly useful for short, thick-walled actuators that are changing length and designed to provide large elastic and extension forces – similar to what may be needed for a burrowing application.

To address these limitations, the author developed the *F(ε,t)* model that predicts the axial force as a function of the contraction ratio while accounting for the changes in elastomer wall thickness as a function of the contraction ratio when the actuator changes length. Furthermore, the new model is a function of only initial actuator geometry which is useful for design purposes. This model

assumes inextensible fibers, the actuator remains cylindrical before and after pressure is applied, no losses, and that measurements are taken far from the system boundaries. This model does not account for elastic force generated from straining the elastomer, but it does account for the change in elastomer thickness as displacement occurs. The elastic force model will be addressed separately in the next section.

Starting with the conservation of work relationship where the input work is done by the fluid pressure pushing against the internal surface of the elastomer, and the output work is done when the actuator experiences axial displacement from the change in actuator volume, the following expression is obtained.

$$-PdV = FdL. \tag{2.6}$$

The contraction force, *F* can then be solved for.

$$F = -P\frac{dV}{dL} \tag{2.7}$$

To calculate the contraction force, the following expression is developed from the geometry of the actuator [51].

$$\frac{L}{L_o} = \frac{\cos(\theta)}{\cos(\theta_o)} \tag{2.8}$$

By combining (2.3) and (2.8) and performing algebraic manipulation, the following expression is obtained.

$$\sin(\Theta) = \sqrt{1-(1-\varepsilon)^2\cos^2(\Theta_o)} \tag{2.9}$$

The initial outside diameter, D_i can be developed from geometry in a similar manner as in (2.8) [51].

$$D_i = \frac{D\sin(\Theta_o)}{\sin(\Theta)} \tag{2.10}$$

Then by combining (2.9) and (2.10), an expression for the current outside diameter, *D* is developed as a function of initial actuator geometry and contraction ratio only.

$$D = \frac{D_i\sqrt{1-(1-\varepsilon)^2\cos^2(\Theta_o)}}{\sin(\Theta_o)} \tag{2.11}$$

Rearranging (2.3) and solving for actuator length, *L* yields

$$L = (1-\varepsilon)L_o. \tag{2.12}$$

An expression for the elastomer wall thickness as a function of the actuator contraction ratio must be developed. To do this, it is assumed that the elastomeric material is incompressible (i.e., natural rubber, neoprene rubber, Buna-N rubber), and the original volume of elastomeric material before applying pressure to the actuator is the same as the volume after pressure is applied which is expressed as:

$$\left(\frac{\pi D_i^2}{4} - \frac{\pi(D_i - 2t_k)^2}{4}\right)L_o = \left(\frac{\pi D^2}{4} - \frac{\pi(D-2t)^2}{4}\right)L \tag{2.13}$$

where *t* is the current elastomer wall thickness. By combining (2.12) and (2.13), an expression for the current elastomer wall thickness, *t* is developed as a function of the contraction ratio where (2.11) is used to calculate current outside diameter, *D* as a function only of initial actuator geometry and contraction ratio.

$$t = \frac{D}{2} - \sqrt{\frac{D^2}{4} - \frac{t_k(D_i - t_k)}{1-\varepsilon}} \tag{2.14}$$

The volume, *V* of the fluid in the McKibben actuator is expressed as:

$$V = \frac{\pi(D - 2t)^2 L}{4} \tag{2.15}$$

which is completely realized by (2.11), (2.12), and (2.14) as a function of initial actuator geometry and contraction ratio only. To determine the expression for the contraction force, *F* from (2.7), the following differentiation was performed where the expressions developed in (2.12) and (2.15) were substituted into the expression.

$$F = -P\frac{dV}{dL} = -P\frac{dV/d\varepsilon}{dL/d\varepsilon} \tag{2.16}$$

The following McKibben force model as a function of contraction ratio while accounting for the changing wall thickness is expressed as:

$$F = -P\left(\pi C_1^2 + \pi C_1\left(\frac{t_k(t_k - D_i)}{C_1(\varepsilon - 1)} + D_i(1 - C_2)\left(\frac{t_k}{C_1 C_2(\varepsilon - 1)} - \frac{1}{\sin(\Theta_o)\sqrt{C_2}}\right)\right)\right) \tag{2.17}$$

For use and viewing simplicity, lumped parameter coefficients are defined as follows.

$$C_1 = \sqrt{\frac{D_i^2 C_3}{4\sin^2(\Theta_o)} - \frac{t_k(t_k - D_i)}{\varepsilon - 1}} \tag{2.18}$$

$$C_2 = 1 - \cos^2\Theta_o(\varepsilon - 1)^2 \tag{2.19}$$

2.1.5 Kothera Elastic Force Model

All the aforementioned models only consider the fiber forces of the actuator and neglect the elastic force generated due to straining the elastomer,

so the following model developed by Kothera et al. is used to predict the elastic force generated from straining the elastomer

$$F_{elastic} = E[V\left(\frac{1}{L_o} - \frac{1}{L}\right) + \frac{L}{2\pi RN^2}(tL - t_k L_o)] \tag{2.20}$$

where *E, V, R*, and *N* represent the Young's modulus of the elastomer, the total volume of the elastomer, the current outside radius of the elastomer, and the number of turns of a single braid fiber about the actuator outside diameter respectively [129]. Note that the elastic force term expressed here is needed, in addition to the force developed in the fibers from applied pressure, to predict the total actuator force if the actuator changes length. By adding $F_{elastic}$ to any of the previously mentioned force models, the total axial force can be calculated. The direction of the generated elastic force is always opposing actuator displacement relative to its relaxed state. Expressions for the total volume of the elastomer and the number of turns of a braid fiber about the actuator outside diameter are defined as:

$$V = L_o \pi (R_i^2 - (R_i - t_k)^2) \tag{2.21}$$

$$N = \frac{L_o}{2\pi R_i} \tan(\theta_o) \tag{2.22}$$

where R_i represents the initial outside radius of the elastomer. By combining (2.3), (2.11), (2.20), (2.21), and (2.22), an equivalent expression for the elastic force term is developed as a function of the contraction ratio, changing wall thickness, and initial actuator geometry that is easily combined with the aforementioned models to predict the total generated force of a McKibben actuator.

$$F_{elastic} = -\pi E[(R_i^2 - (R_i - t_k)^2)\frac{\varepsilon}{\varepsilon - 1} + \frac{2R_i^2(1-\varepsilon)^2}{R\tan^2(\Theta_o)}(t - \frac{t_k}{1-\varepsilon})] \quad (2.23)$$

By adding the $F_{elastic}$ term in (2.23) to any McKibben model that neglects the elastic force generation from straining the elastomer, total generated force is computed for a given actuator and modeling approach. Thus,

$$F_{total} = F_{fibers} + F_{elastic} \quad (2.24)$$

where F_{fibers} is the predicted fiber forces by any model that neglects elastic forces from actuator displacement, such as the four models presented in sections 2.1.1-2.1.4 and F_{total} is the total axial force generated by a McKibben actuator.

2.1.6 Converting Elastomer Durometer to Young's Modulus

Gent developed an empirical model for converting durometer to Young's modulus for elastomers [135]. Durometer is a common way to characterize elastomers, and durometer is often used as a rough correlation to the Young's modulus of a material. The Gent model is an empirically derived, commonly used first order approximation to convert a specified Type A durometer of rubber materials to the Young's modulus. The Gent model is accurate for Type A durometers ranging from 20A-80A but has been shown to have limitations for material hardness below 40A and substantial scatter in experimental data. The Gent model is presented below where *E* is the Young's modulus in MPa and *S* is the ASTM D2240 Type A durometer of the elastomer. The Gent model approximation of the Young's modulus is used throughout this study.

$$E = \frac{0.0981(56 + 7.62336S)}{0.137505(254 - 2.54S)} \tag{2.25}$$

2.1.7 New Model to Predict Elastomer Burst Failure

One common mode of McKibben actuator failure is burst failure. This occurs when the elastomer bulges through the fiber weave, and the elastomer bursts from the internal pressure as shown in Figure 51 [21]. This sub-section presents a new approach to modeling burst failure in fiber-wrapped McKibben actuators operating at high pressures.

Figure 51: Hydraulic McKibben burst failure [21]

To model the burst failure mechanics, the maximum pressure, defined here as the burst pressure, is predicted using geometry and stress analysis techniques. A simplified case of perfectly circumferentially wrapped fibers with uniform spacing is employed where the elastomer begins to bulge between fibers when pressurized. To model this interaction, the following expressions are first developed from actuator and sleeve geometry.

$$B = \frac{L_o}{\cos(\theta)} \tag{2.26}$$

$$n = \frac{B\sin(\theta)}{2\pi r} \tag{2.27}$$

B, L_o, Θ, n, and r are the total length of a single fiber, the initial length of the actuator, the fiber wrap angle, the number of turns a fiber makes along the actuator, and the outside radius of the actuator respectively. Based on the length of a single fiber and the number of turns it makes around the actuator, the number of spaces between fibers along the actuator can be calculated as

$$n_s = \frac{n(N_f - 1)}{2} \tag{2.28}$$

where n_s and N_f are the number of spaces between fibers along the actuator and the total number of fibers wrapped around the actuator respectively. Then, the spacing between the fibers along the actuator can be calculated as follows.

$$\delta = \frac{L_o}{n_s} \tag{2.29}$$

To calculate the actuator burst pressure, the actuator is treated as a thin-walled pressure vessel and a single bulge of the actuator is analyzed from a side view as the elastomer begins to bulge between fibers as shown in Figure 51. Using Hooke's Law and the thin-walled pressure vessel equation, the following expression for the stress in the elastomer is developed.

$$\sigma = E\varepsilon = \frac{Pr_{bulge}}{t} \tag{2.30}$$

σ, E, ε, P, r_{bulge}, and t represent the stress in the elastomer, the elastomer elastic modulus, the elastomer strain, internal pressure, radius of curvature of the bulge between the fibers, and the elastomer wall thickness respectively. The strain in the elastomer bulging between the fibers is calculated as

$$\varepsilon = \frac{s_{bulge} - \delta}{\delta} \tag{2.31}$$

where s_{bulge} is the bulge arc between the fiber constraints. The bulge arc is defined as

$$s_{bulge} = r_{bulge}\gamma \tag{2.32}$$

where γ is the angle between the constraining fibers as measured about the origin of the radius of curvature. By combining the three preceding equations, an expression for the angle, γ can be developed.

$$\gamma = \frac{P\delta}{tE} + \frac{\delta}{r_{bulge}} \tag{2.33}$$

Because r_{bulge} and γ are both unknown and can't be solved without knowledge of the other, an iterative solution is employed where γ is calculated using a preliminary estimation of r_{bulge} and then substituted into the expression below that is developed from geometry as shown in Figure 52.

$$r_{bulge} = \frac{\delta}{2\sin\left(\frac{\gamma}{2}\right)} \tag{2.34}$$

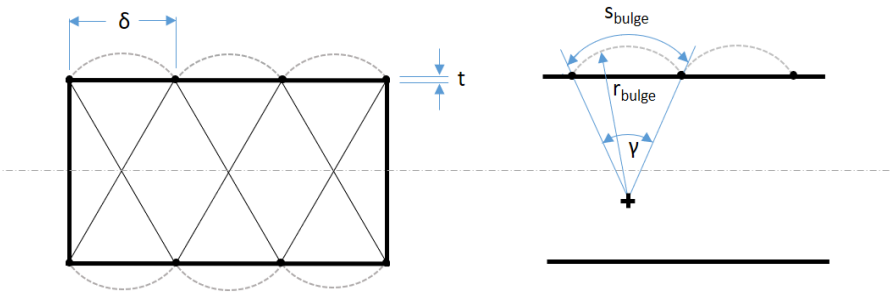

Figure 52: Relevant geometry for McKibben elastomer burst mechanics

Once the new value of r_{bulge} is calculated in (2.34), the percent error between the preliminary estimation of r_{bulge} and the new value of r_{bulge} can be calculated. The

new value of r_{bulge} is substituted into (2.33) and the iterative process is repeated until a desired convergence is reached. Once r_{bulge} has converged, it can be substituted into the following expression to calculate the pressure where the elastomer is expected to burst through the spacing between the fibers. Note that σ_{max} is the maximum tensile strength of the elastomer.

$$P_{burst} = \frac{\sigma_{max} t}{r_{bulge}} \tag{2.35}$$

2.2 Contracting McKibben Actuator Force Study

Twelve hydraulic contracting McKibben actuators of varying geometries were designed, manufactured, and tested with a custom experimental apparatus to determine agreement between the McKibben force models presented in section 2.1 and the experimental force results. Agreement between experimental Young's modulus tests of the samples is evaluated against the Gent model, and a brief examination of the impact of multiple sleeve layers is provided in this section.

2.2.1 Methods

This section introduces the actuator design, experimental apparatus, and experimental procedure used for testing the contracting McKibben actuators.

2.2.1.1 Actuator Design

The initial geometry of the designed actuators is summarized in Table 2. Note that the length of the actuator is measured at free length from crimp to crimp. Commercially available 2x2 twill pattern aramid fiber sleeves (Supplier: Rock West Composites, SKU: BR-A-100) were selected for the fiber materials because of their low cost, high strength, and resistance to abrasion. Three different pre-manufactured and commercially purchased elastomers, including 60A neoprene (Supplier: Hanna Rubber, PN: 5742821), 80A neoprene (Supplier: McMaster, PN: 5034K15), and 70A natural rubber (Supplier: McMaster, PN: 51135K631), were selected for the experiments to validate the elastic force model over a range of elastomer elastic moduli. All actuators were designed with a sufficient wall thickness to prevent bursting (safety factor against bursting greater than 3 at all operating pressures) and to be compatible with commercially available crimp fittings. The safety factor was computed by calculating the stress in the elastomer wall using equation (2.30) in section 2.1.7 and then comparing that to the maximum tensile stress the elastomer can withstand. Actuators B and C are identical besides the number of fiber sleeves and the initial length of the actuators. Actuator C was fabricated with two fiber sleeves to increase the strength of the actuator and to examine any differences in behavior between actuators fabricated with one sleeve versus two sleeves. Braided sleeves were cut to length and slid over the elastomers and off the shelf barbed hydraulic fittings (Supplier: Discount Hydraulic Hose, PN: MP-08-08) were utilized to crimp the braided sleeves to the elastomers. A layer of electric tape was adhered to the exterior of the fiber sleeves to reduce abrasion to the fibers at the fiber-fitting

interface when crimped. Figure 53 shows a fabricated hydraulic McKibben actuator used in the experiments.

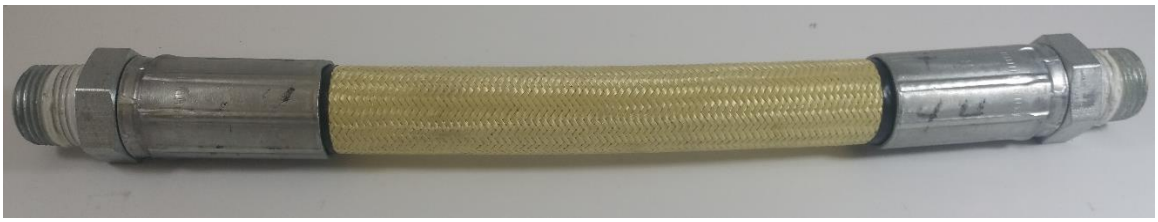

Figure 53: Fabricated McKibben actuator with crimped fitting (Actuator D)

Table 2: Fabricated McKibben actuator information

	Outside Diameter, D_i (mm)	Initial Length, $L_o\,(mm)$	Wall Thickness, t_k (mm)	Initial Fiber Wrap Angle, Θ_o (deg)	Elastomer Material	Sleeves (#)
A	12.7	202.0	1.6	48.0	60A Neoprene	1
B	19.1	238.1	3.2	45.0	80A Neoprene	1
C	19.1	231.8	3.2	45.0	80A Neoprene	**2**
D	22.2	144.5	3.2	55.6	80A Neoprene	1
E	12.7	215.5	1.6	45.0	70A NR	1
F	15.9	225.0	1.6	36.1	70A NR	1
G	17.5	199.0	2.4	40.4	70A NR	1
H	19.1	212.0	3.2	45.0	70A NR	1
I	19.1	195.0	1.6	45.0	70A NR	1
J	22.2	209.0	3.2	55.6	70A NR	1
K	22.2	209.5	1.6	55.6	70A NR	1
L	25.4	204.5	3.2	45.0	70A NR	1

**NR = Natural Rubber*

2.2.1.2 Experimental Apparatus

An experimental system was built to test the fabricated McKibben actuators. Two vises were used to secure each end of the actuators to the test bench. A stationary vise held the actuator in place on the proximal end, and the vise that was used to secure the distal end of the actuator was mounted on a lead screw to strain the actuator and to enable force measurements at different contraction ratios. A 4500 N load cell (Manufacturer: Futek, PN: LCM300) was threaded into the end cap on the distal end of the actuator and fixed to the lead screw. A 20.7 MPa pressure transducer (Manufacturer: Honeywell, PN: MLH03KPS) was used to measure the input pressure at the proximal end of the actuator. A data acquisition board (National Instruments: PCIE-6343) was used to collect axial force and pressure measurements for data processing. Hydraulic oil (Mobil DTE 25) was used to apply pressure at the proximal (left) end of the actuator, and an end cap was used to close the enclosure on the distal (right) end as shown in Figure 54.

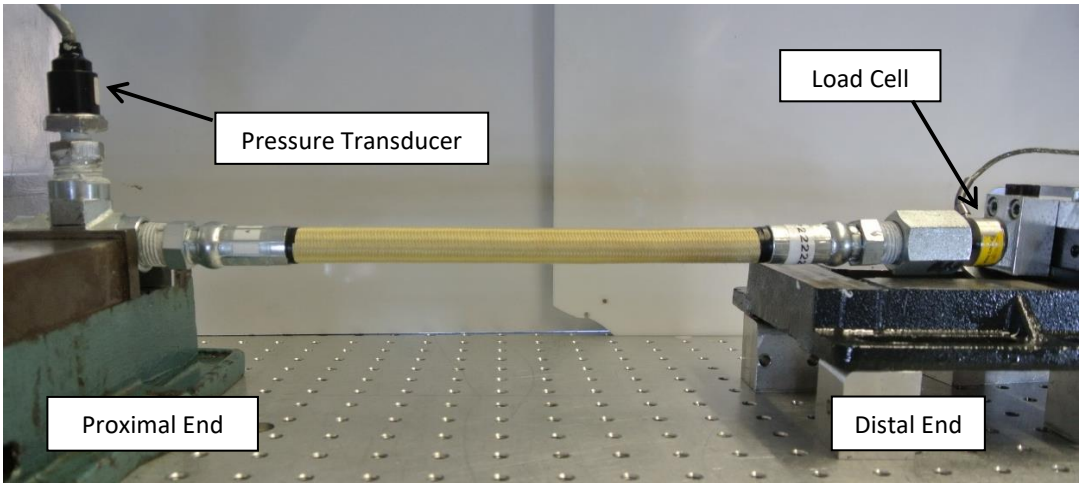

Figure 54: McKibben actuator test system

The pressure sensor was calibrated using a dead weight tester, and the load cell was calibrated using hanging weights and a cantilever beam. The data acquisition board was used to collect axial force and pressure measurements for data processing, and a low pass median filter was used to condition the signal and remove noise. An electronic reducing valve built into the hydraulic power unit (Manufacturer: Oilgear, Model: PVWH-11-LSAY-FRNN-N.O.) was used to regulate the pressure levels. The hydraulic circuit is shown in Figure 55. The entire system was enclosed in a transparent Lexan case to address safety concerns.

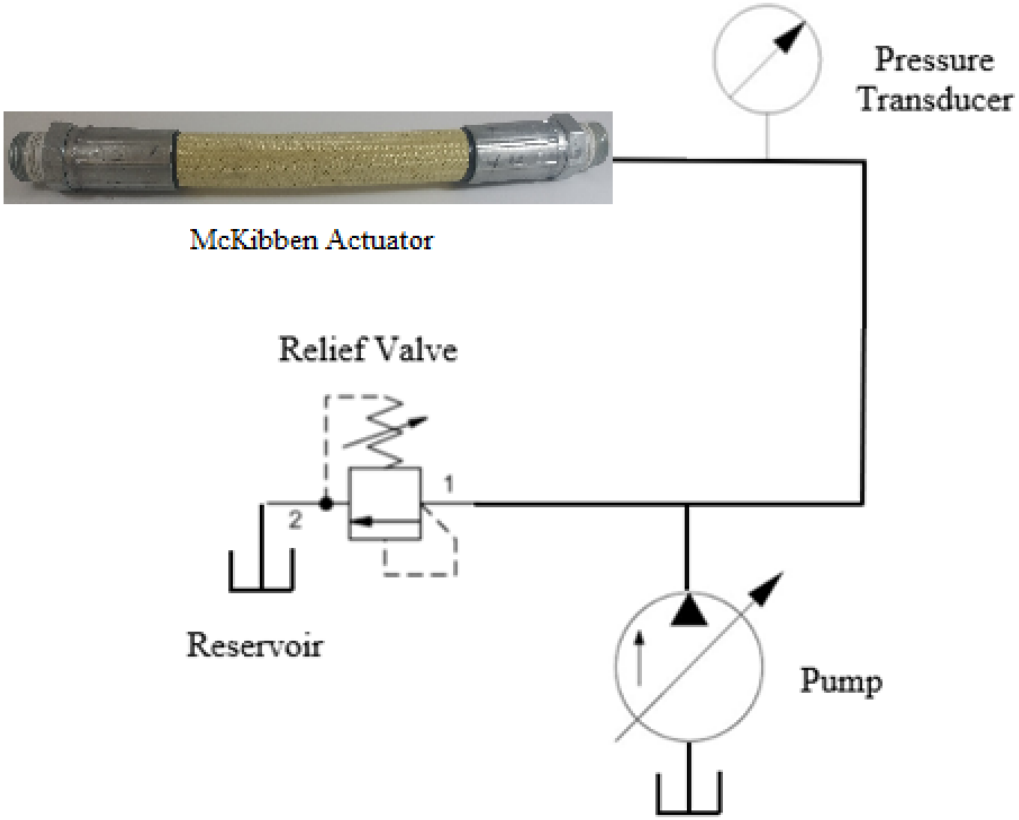

Figure 55: Hydraulic circuit

2.2.1.3 Experimental Procedure

An input pressure of 6.89 MPa was applied to Actuator A at the proximal end, and the axial force generated on the distal end was recorded. Because Actuator A failed at the end of the first set of experiments, the experimental input pressure was reduced to 2.75 MPa for Actuators B-L to ensure sufficient data collection for the analysis. The first measurement for each actuator was taken at the free length ($\varepsilon = 0$), while additional measurements were taken at an incrementally decreasing contraction ratio. After the first measurement at the free length, each actuator was lengthened using the vise lead screw to decrease the contraction ratio by 0.025 for each subsequent experiment until either the actuator reached the load cell limitations or the actuator failed[1]. Actuator pressure was turned off before each experiment as the actuator was stretched, and the elastic force generated from the elastomer extension was recorded to evaluate against the Kothera elastic force model before pressure was applied to the actuator.

The Young's Modulus was experimentally determined for the 60A neoprene, 80A neoprene, and 70A natural rubber materials. Six different elastomer tubes were tested, and two tubes of different diameters and wall thicknesses were used for testing each of the three respective materials. Each

[1] Note that lengthening the actuators decreases the fiber angle justifying how actuators D, J, and K can have an initial fiber angle greater than 54.7° but can still generate contraction forces when at a negative contraction ratio. While applications for contracting McKibben actuators at negative contraction ratios are not often found, this testing configuration was convenient for gathering force data over a range of contraction ratios, because the actuators can be stretched without the need for constant actuator pressure to be maintained.

tube, void of any fibers, was crimped on each end to hydraulic segment connectors, and the proximal end of the elastomer was threaded into the load cell on the vise lead screw to allow for force measurements at various strains while the distal end was held fixed. While the elastomer was held at free length, the elastomer midpoint was identified and a point 40 mm to either side of the midpoint was marked. The centralized 80 mm elastomer segment was used for the experiment to ensure all data was taken sufficiently away from the boundary conditions. The vise lead screw was used to extend the entire elastomer until the 80 mm segment had extended 2 mm (2.5% strain) and the generated axial force was recorded. A caliper was used to make the make the extension measurements. This procedure was done for all six tubes at all strains from 2.5% strain to 32.5% strain in 2.5% strain increments.

Experiments were conducted to measure the total generated axial force for the twelve actuators, and the experimental data were analyzed and compared to the theoretical results for each of the four McKibben force models described earlier in section 2.1. To compare the results of different experiments (i.e., different contraction ratios) for a given actuator, the same input pressure, referenced here as the nominal pressure, was used for each of the experiments for a given actuator. All experiments were run at an input pressure within 0.5% of the nominal pressure, and if pressure fluctuations were present (data points more than 0.5% from the nominal pressure), those data points were omitted from the analysis. If the elastomer was stretched in an experiment, the elastic force of the

elastomer was measured before pressure was applied to be analyzed later. A video camera was utilized to record the tests and to detect any slipping of the segment connectors, and if slipping occurred, those data points were omitted from the analysis. The mean value of the Young's modulus at all strains tested was used to obtain the experimental Young's modulus for each of the three rubber materials to compare to expected values from the Gent model in equation (2.25) found in section 2.1.

2.2.2 Results and Discussion

Using the experimental procedure and experimental apparatus, the twelve fabricated actuators were tested. Six tubes, two for each of the three rubber materials, were tested to experimentally obtain the Young's modulus of each material. The results of these investigations, as well as a discussion on the findings, are detailed below. Actuators A, F, G, H, and J failed due to slipping out of the fittings and Actuator I failed by the elastomer bursting through the fiber sleeve. Any actuator test at a specific contraction ratio where slipping or bursting occurred was omitted from the results shown below and the tests for that actuator were concluded. Actuators B, C, D, E, K, and L survived all experiments, and no data points were omitted.

2.2.2.1 Young's Modulus Test Results and Discussion

The value of the Young's modulus was determined for each of the elastomer materials to predict the generated elastic force of an actuator when extended. The results of the Young's modulus tests for the six specimens, two for

each of the three rubber materials, are presented in Figure 56. Each specimen's initial geometry and percent error from the expected Young's modulus, calculated using the Gent model in (2.25) of section 2.1 are presented in Table 3.

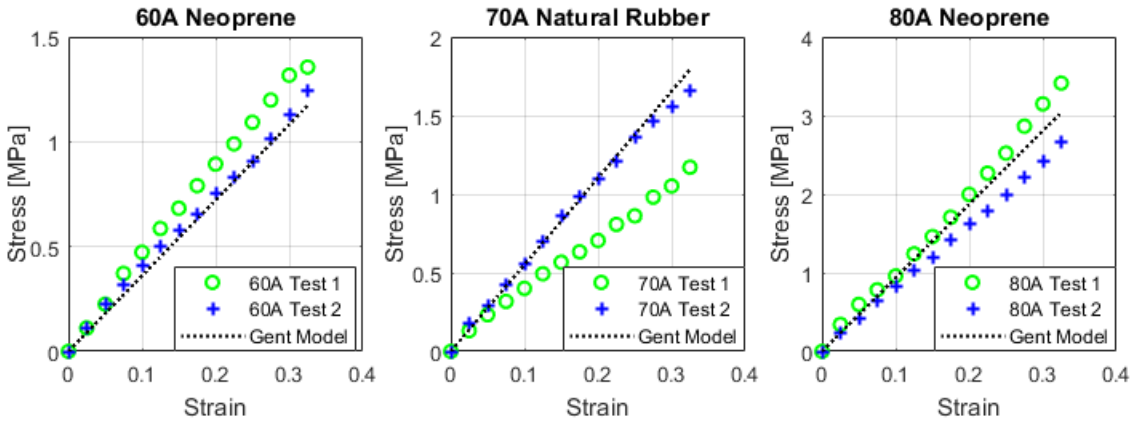

Figure 56: Results from Young's modulus experiments for 60A Neoprene, 70A Natural Rubber, and 80A Neoprene elastomers

Table 3: Results of Young's modulus experiments

Elastomer	Outside Dia., D_i (mm)	Wall Thickness, t_k (mm)	Mean Value of E for Test (MPa)	Gent Model Value of E (MPa)	Percent Error from Gent Model (%)	Mean Value of E for All Material Tests (MPa)	Mean Value Percent Error from Gent Model
60A Neo. Test 1	15.9	3.2	4.51	3.61	+25.0	4.23	+17.3 %
60A Neo. Test 2	22.2	3.2	3.95	3.61	+9.6		
70A Nat. Rub. Test 1	15.9	3.2	3.90	5.52	-29.2	4.77	-13.6 %
70A Nat. Rub. Test 2	19.1	3.2	5.63	5.52	+2.1		
80A Neo. Test 1	22.2	3.2	10.51	9.35	+12.4	9.39	-0.4 %
80A Neo. Test 2	19.1	3.2	8.27	9.35	-11.6		

The results from the Young's modulus experiments show variability in the slope of the stress-strain curves between the two specimen tests for all three materials, but they do show that the Gent model is a reasonable tool for approximating the Young's modulus of a rubber material. The total percent error, calculated as the mean of the percent error for each of the two specimen tests for the 60A neoprene, 70A natural rubber, and 80A neoprene was 17.3%, -13.6%, and -0.4% respectively. The Gent model value of the Young's modulus was used for modeling the three rubber materials in these experiments to show how the approach can be used for predictive design purposes.

2.2.2.2 Elastic Force Results and Discussion

The elastic force test was performed at all contraction ratios for each actuator before pressure was applied and compared to the predicted values of the Kothera elastic force model presented in equation (2.23) in section 2.1. The Gent model value of the Young's modulus was used for all three elastomer materials. As representative samples of the twelve tested actuators, the results for Actuator A (60A neoprene), Actuator D (80A neoprene), and Actuator I (70A natural rubber) are presented in Figure 57. The complete elastic force results for all Actuators A-L can be found in Appendix A.

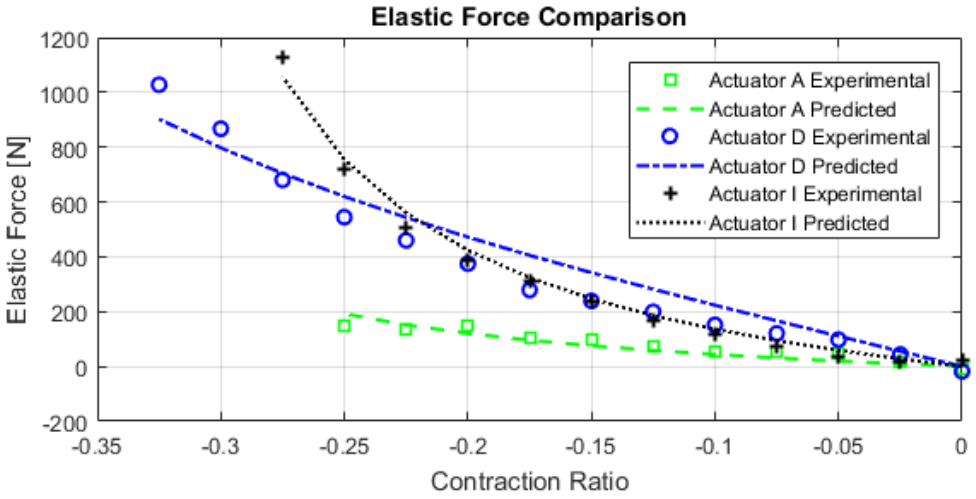

Figure 57: Elastic force comparison for Actuator A (60A Neoprene), Actuator D (80A Neoprene), and Actuator I (70A Natural Rubber)

The predicted elastic force tracked the experimental results well for all twelve of the actuators without significant error at any range of contraction ratios. These results justify the use of the Kothera elastic force model in the total force model as presented in equation (2.24) and the use of the Gent model to calculate the Young's modulus from elastomer Type A durometer. This development is particularly important for accurately modeling and designing thick-walled McKibbens driven at hydraulic pressures needed for high-force applications.

2.2.2.3 Total Axial Force Results and Discussion

The total force data was collected at each contraction ratio for each actuator and compared to the expected total force results for each of the four previously described modeling approaches. The results for Actuator A (60A neoprene), Actuator D (80A neoprene), and Actuator E (70A natural rubber) are

presented in Figure 58, Figure 59, and Figure 60 as representative samples of each material for all of the actuator results. The solid line represents the expected total force from the new thick-walled model presented in section 2.1. The complete total force results for all Actuators A-L can be found in Appendix B.

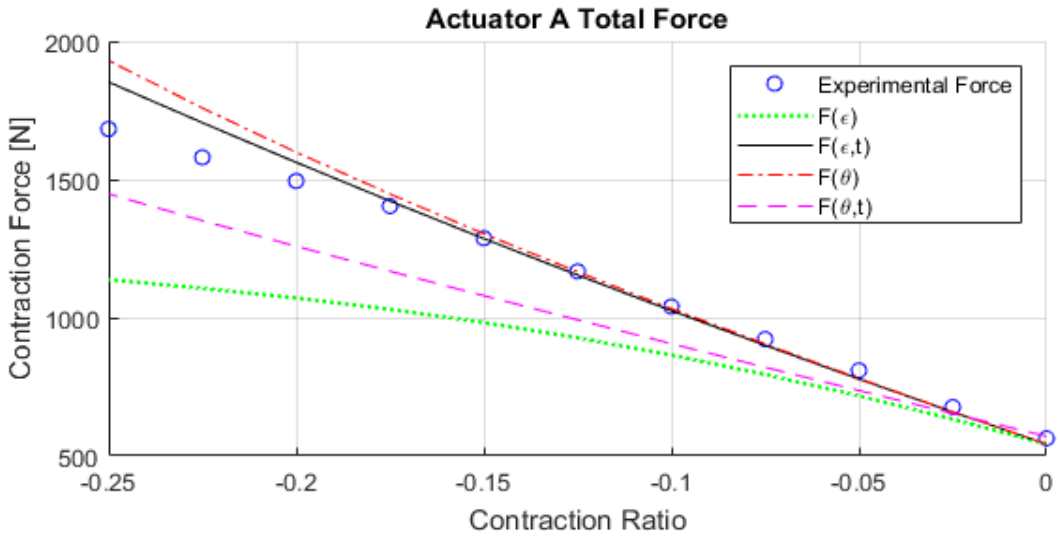

Figure 58: Total force results for Actuator A (60A Neoprene) at 6.89 MPa

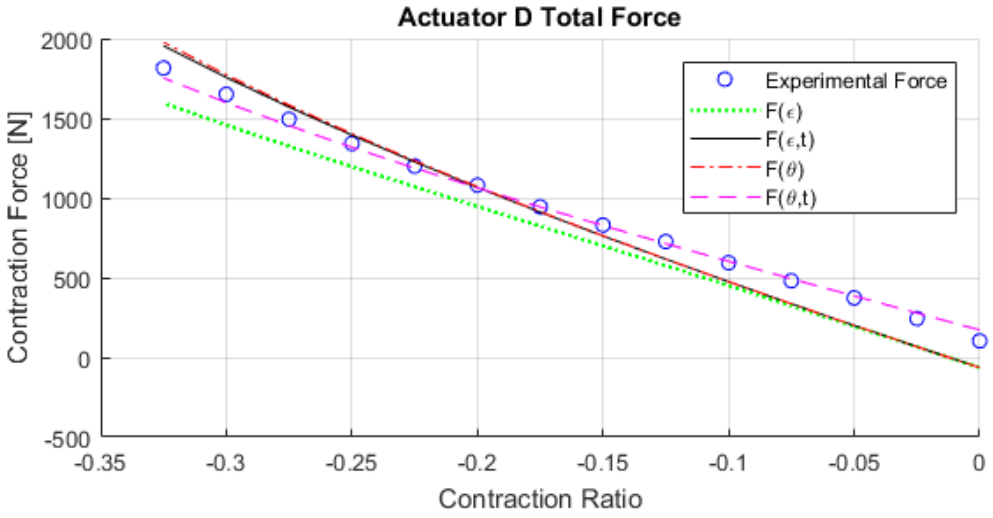

Figure 59: Total force results for Actuator D (80A Neoprene) at 2.75 MPa

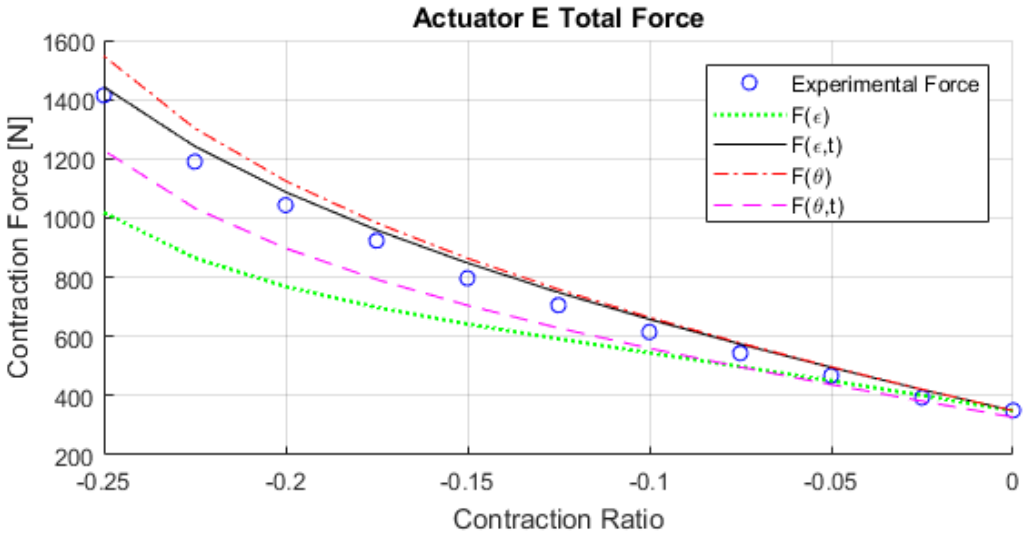

Figure 60: Total force results for Actuator E (70A Natural Rubber) at 2.75 MPa

It can be observed from the figures that the *F(ε)* model tends to drop off at more negative ratios whereas the *F(ε,t)* model better tracks the results in these ranges. The *F(Θ)* model consistently predicted more force than that *F(Θ,t)* model with varying levels of agreement with the experimental results. This trend is consistent in the total force results for all twelve of the actuators. To compare the accuracy of agreement between each of the models and the experimental data, the following equation was used to calculate the error for each model for each actuator at each contraction ratio tested.

$$\text{Error} = \left| 100 * \frac{(\text{Total measured force} - \text{Total predicted force})}{\text{Maximum measured actuator force}} \right| \tag{2.36}$$

The maximum measured actuator force was at the maximum tested contraction ratio for each actuator and using this value in the denominator of equation (2.36) instead of the total predicted force, prevented skewing the results

at data points where the expected total force was near zero. The mean value of the error values at each contraction ratio was then calculated to determine an error value of each model for each actuator. The overall average error was then calculated for each model as the mean value of the model specific errors for all actuators. The results of the model comparison are shown in Table 4.

Table 4: Overall model error for total force results

		Average of Absolute Value of Error of Each Experiment w/ Elastic Term			
	Number of Tests	F(θ)	F(ε)	F(θ,t)	F(ε,t)
Actuator A	11	3.7%	15.2%	9.0%	2.7%
Actuator B	7	7.2%	3.9%	6.8%	5.9%
Actuator C	8	5.7%	3.9%	5.7%	4.4%
Actuator D	14	5.8%	8.7%	1.4%	5.5%
Actuator E	11	4.2%	10.5%	6.1%	2.5%
Actuator F	5	8.8%	10.4%	6.2%	7.9%
Actuator G	6	9.0%	8.0%	7.3%	7.7%
Actuator H	3	9.0%	4.1%	4.8%	8.5%
Actuator I	12	10.4%	11.1%	1.4%	9.3%
Actuator J	8	30.1%	23.8%	59.6%	30.0%
Actuator K	14	11.5%	19.3%	9.0%	11.5%
Actuator L	9	14.0%	7.2%	2.5%	12.8%
	Overall Average Error	9.9%	10.5%	10.0%	9.1%

Each actuator showed varying agreement with the different models, making it difficult to draw clear conclusions about which model best predicts the force of McKibben actuators. The overall average error shows that the *F(ε,t)* model is an improvement over the *F(ε)* model for the experiments. Similarly, most of the actuators demonstrated that the *F(θ,t)* model was more accurate than the *F(θ)* model. While the overall average error of the *F(θ,t)* model is greater than the *F(θ)* model, if the results from Actuator J are not considered, the overall average error of the *F(θ,t)* and *F(θ)* model for the other eleven actuators are 5.5% and

8.1% respectively confirming that as expected, the *F(θ,t)* model is more accurate than the *F(θ)* model in general. Furthermore, the overall average error results show that the *F(ε,t)* model is generally more accurate than all other models used in the analysis. Taking a deeper look at the results, Table 5 shows the complete actuator results compared to the force models grouped in ascending order by initial wall thickness. Figure 61 shows a plot of the model error for each group of actuator wall thicknesses.

Table 5: Overall model error for total force results sorted by wall thickness

	Wall Thickness, t_k (mm)	Outside Diam., D_i (mm)	D_i/t_k	Average of Absolute Value of Error of Each Experiment w/ Elastic Term			
				F(θ)	*F(ε)*	*F(θ,t)*	*F(ε,t)*
Actuator A	1.6	12.7	7.9	3.7%	15.2%	9.0%	2.7%
Actuator E	1.6	12.7	7.9	4.2%	10.5%	6.1%	2.5%
Actuator F	1.6	15.9	9.9	8.8%	10.4%	6.2%	7.9%
Actuator I	1.6	19.1	11.9	10.4%	11.1%	1.4%	9.3%
Actuator K	1.6	22.2	13.9	11.5%	19.3%	9.0%	11.5%
Actuator G	2.4	17.5	7.3	9.0%	8.0%	7.3%	7.7%
Actuator B	3.2	19.1	6.0	7.2%	3.9%	6.8%	5.9%
Actuator C	3.2	19.1	6.0	5.7%	3.9%	5.7%	4.4%
Actuator D	3.2	22.2	6.9	5.8%	8.7%	1.4%	5.5%
Actuator H	3.2	19.1	6.0	9.0%	4.1%	4.8%	8.5%
Actuator J	3.2	22.2	6.9	30.1%	23.8%	59.6%	30.0%
Actuator L	3.2	25.4	7.9	14.0%	7.2%	2.5%	12.8%
Overall Average Error				**9.9%**	**10.5%**	**10.0%**	**9.1%**
Overall Average Error (t_k = 1.6 mm)				7.7%	13.3%	6.3%	6.8%
Overall Average Error (t_k = 2.4 mm)				9.0%	8.0%	7.3%	7.7%
Overall Average Error (t_k = 3.2 mm)				12.0%	8.6%	13.5%	11.2%

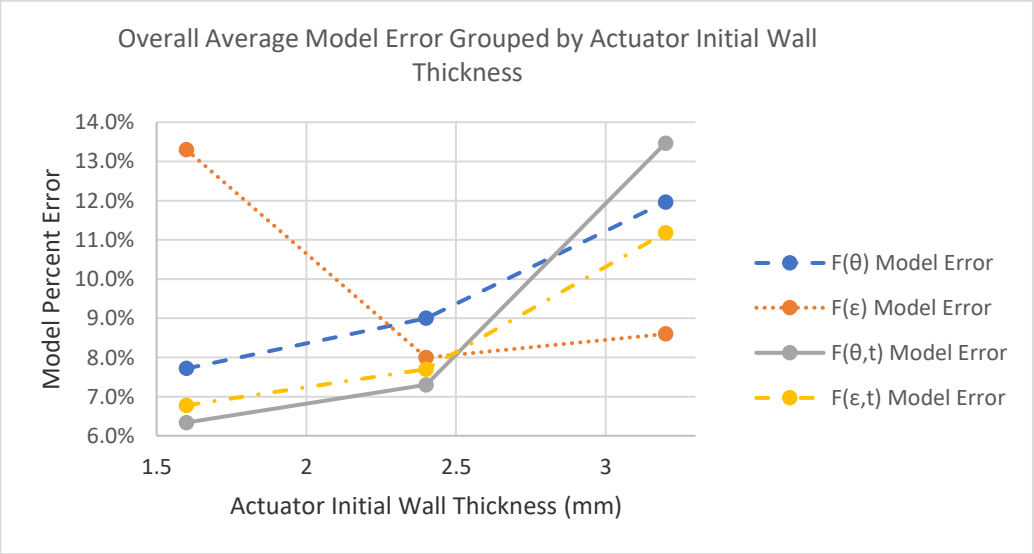

Figure 61: Overall model error based on actuator wall thickness

One important take away from these results is that the *F(ε)* and *F(ε,t)* models do the best job of predicting the force for the actuators with the thickest walls (right side of Figure 61), while the *F(θ,t)* and *F(ε,t)* models do the best job of predicting the force for the actuators with the thinnest walls (left side of Figure 61). The models were all within 1.7% overall average error for single medium thickness specimen (Actuator G). Because the *F(ε,t)* model is a function of the contraction ratio and not the fiber wrap angle, it will be particularly useful as a design tool for modeling hydraulic McKibben actuators with much thicker walls. If the wall thicknesses of the actuators in these experiments were increased or varied over a wider range, it is expected that the accuracy of the *F(ε,t)* model would continue to improve in comparison to the *F(ε)* model making the new model an important tool for future hydraulic McKibben actuator research and design.

2.2.2.4 Sleeve Comparison Results and Discussion

The total generated contraction force plotted against the contraction ratio for Actuators B and C is depicted in Figure 62. It can be observed that no significant impact is made on the axial force for actuators fabricated with one fiber sleeve (Actuator B) versus actuators fabricated with two fiber sleeves (Actuator C) given that all relevant initial actuator geometry is the same. This finding is important because layering fiber sleeves reduces the fiber spacing, which reduces the actuator's likelihood to fail from the elastomer bursting through the sleeve. Increasing the number of supporting fibers also increases the structural strength of the actuator, which reduces the likelihood of the actuator's fibers to fail in tension. Note that all figures involving a contraction ratio should be read from right to left as a negative contraction ratio refers to lengthening of an actuator.

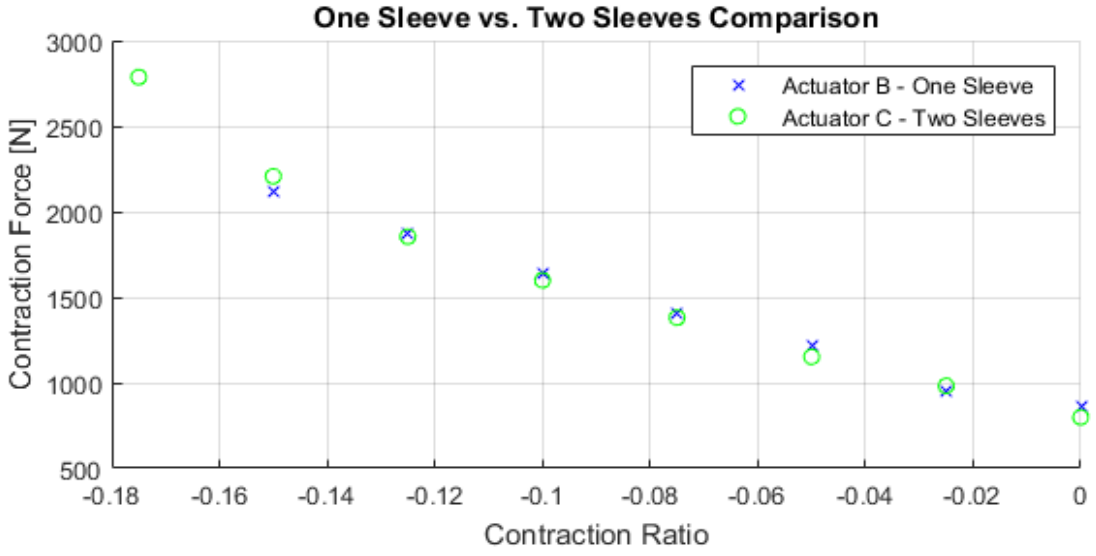

Figure 62: One sleeve versus two sleeves comparison

Once the sleeve comparison tests were completed, steadily increasing pressure was applied to Actuator C to determine how much force could be generated before the actuator or experimental apparatus failed. The actuator was able to withstand 13.79 MPa of pressure before breaking the fixturing vise with ~4600 N of contraction force. This demonstrates the high-force capabilities of McKibben actuators and provides a method to increase the robustness of hydraulic McKibben actuators.

2.3 **Extending McKibben Actuator Force Study**

McKibben actuators can be designed to produce extension forces that could be useful for burrowing applications. This section provides an overview of an extending McKibben actuator force study performed by the author. Five extending McKibben actuators were designed, manufactured, and tested in a custom experimental apparatus to further assess the new $F(\varepsilon,t)$ McKibben force model's efficacy. Experiments were conducted to determine the force generation capabilities of extending McKibben actuators in both fixed-length and displaced conditions and to understand if there are fundamental differences between extending and contracting McKibben actuator modeling approaches and failure modes. Methods for fabricating custom elastomers using 3D printed fixtures, polycarbonate tubes, injectable polyurethane, and aluminum rods are presented. Multiple methods for placing fibers at prescribed angles were also examined – as well as methods for protecting the fibers from the environment. Finally, the results of a preliminary assessment of the burst failure model presented in

section 2.1.7 is discussed. The results from the experiments are compared to various McKibben force models and are presented in this section. Note that the focus of this section is on short extending McKibben actuators that are not prone to buckling or axial compressive failure. Buckling failure of extending actuators will be studied in Chapter 3.

2.3.1 Methods

This section provides an overview of extending McKibben actuator design and manufacturing approaches, an overview of the experimental apparatus, and an overview of the experimental procedure used to test the extending McKibben actuators. Because the extending McKibben actuator design is slightly different than the design of the contracting McKibben actuators from section 2.2, an overview of relevant fiber protection and fiber placement methods is also provided in this section.

2.3.1.1 Actuator Design and Manufacturing

Five extending McKibben actuators with varying geometries were designed and manufactured for experimental testing to further validate the new *F(ε,t)* McKibben force model's efficacy throughout an extension cycle. The selected geometry of the five actuators is shown in Table 6.

Table 6: Extending actuator geometry

Actuator	Measured Length (mm)	OD (mm)	ID (mm)	Wall Thickness (mm)	Diameter at Fibers (mm)	Mean Measured Fiber Angle (deg)
1	74.6	76.2	69.9	3.2	73.0	80.8
2	76.2	76.2	66.7	4.8	73.0	79.9
3	101.6	76.2	69.9	3.2	73.0	80.0
4	104.8	76.2	66.7	4.8	73.0	79.6
5	125.4	76.2	69.9	3.2	73.0	76.2

Custom elastomers were fabricated by injecting a two-part polyurethane mixture (Polytek74-55A) into an assembly of an aluminum rod concentrically aligned in a clear polycarbonate tube constrained on each end by a 3D printed part (port block). O-rings were used to seal the contact between the 3D printed port block and the polycarbonate tube to prevent polyurethane leakage. A cross-sectional view of the mold used to fabricate the parts is shown in Figure 63, and an image of the actual injection assembly is shown in Figure 64.

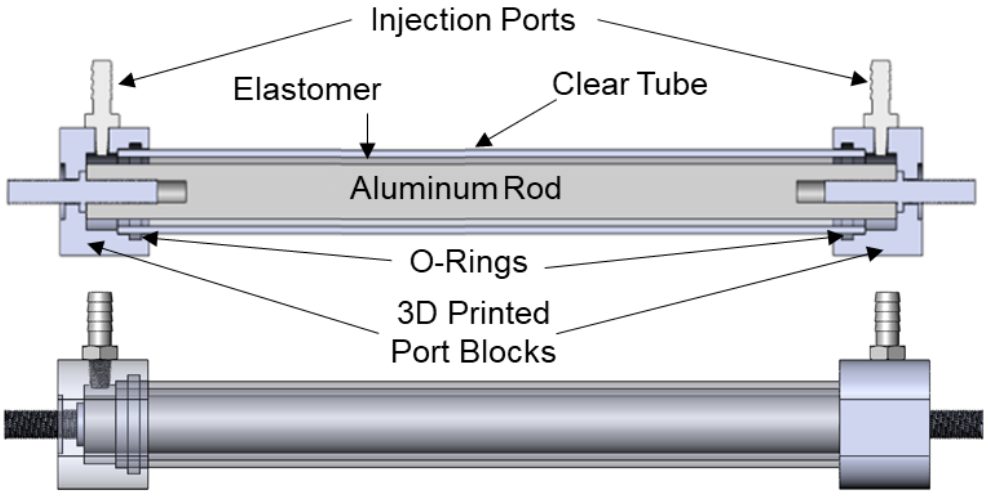

Figure 63: Polyurethane injection mold cross sectional view

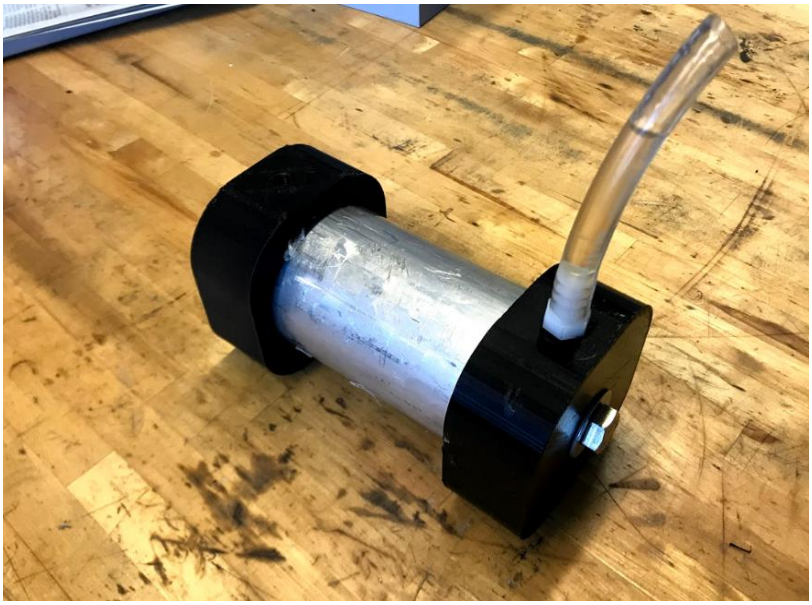

Figure 64: Elastomer fabrication assembly

First, the Polytek 74-55 polyurethane was thoroughly mixed at a 4:1 ratio to cast elastomers with a 55 Shore A durometer. The mixed (but uncured) material was then placed in a vacuum chamber for degassing to remove any air in the mixture, because bubbles can compromise the structural integrity of the elastomer. While the mixture was degassing, all the surfaces of the assembly were sprayed thoroughly with mold release including the aluminum rod, the port blocks, and the clear polycarbonate tube. Next, the aluminum rod and polycarbonate tube were placed in the port blocks and bolts were used on each end of the port blocks to tighten the entire assembly together. A washer and a small surface o-ring were used to prevent leakage near the end bolts on the port blocks. Finally, the polyurethane was carefully injected into one end of the assembly through a clear tube fitted into an injection port using a syringe, carefully avoiding bubble generation, until the mixture came out of the other end

of the assembly. Once the assembly was injected and the polyurethane had >24 hours to sufficiently cure, the port blocks and clear polycarbonate tube were removed leaving the elastomer on the outside surface of the aluminum rod as shown in Figure 65.

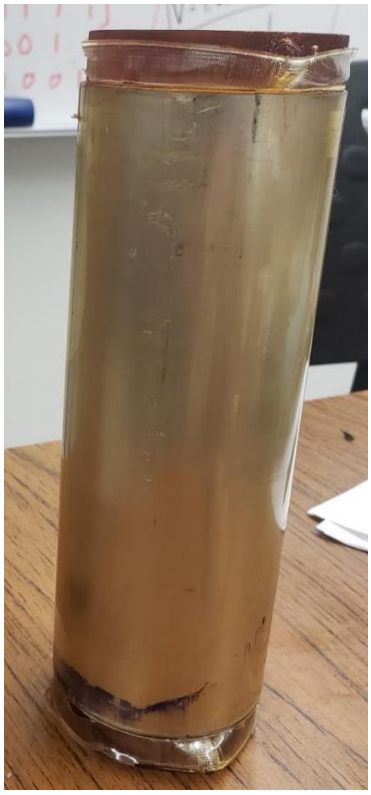

Figure 65: Elastomer on outside surface of aluminum rod

The entire aluminum rod and elastomer assembly were then loaded into a custom fiber wrapping CNC lathe, built in the Medical Robotics and Devices Laboratory at the University of Minnesota [109, 136], to apply fibers at a specific fiber angle. The lathe's belt driven gears and custom servo motors were controlled using an Arduino to dictate the chuck rotation and linear carriage speeds simultaneously. A fiber angle of 80-degrees was selected for all five

actuators because 80-degree fiber angles will produce ample extension force, the actuators can extend to large strains without reaching the kinematic lock angle of 54.7 degrees, and the lathe was able to place fibers accurately and repetitively at this angle.

Each of the fibers were tied to a 3D printed part on the proximal end of the assembly and pulled through a 3D printed part on the distal end of the assembly as shown in Figure 66 and Figure 67 to ensure the fibers were being concentrically wrapped to maintain a consistent fiber angle. The tailstock was used to verify concentricity of the rotating assembly. Four fibers were first wrapped simultaneously in the forward direction (+80 degrees), and then four fibers were placed over them in the backward direction (-80 degrees). Super glue was used to hold the fibers to the elastomer near each end after the fibers had been wrapped to keep the fibers in tension during the application process. The number of fibers was selected to prevent elastomer bursting in between the fibers as outlined in section 2.1.7. Figure 66 shows the assembly after the first four fibers were wrapped in the forward direction, and Figure 67 shows the assembly after all the fibers have been applied to the external surface of the elastomer.

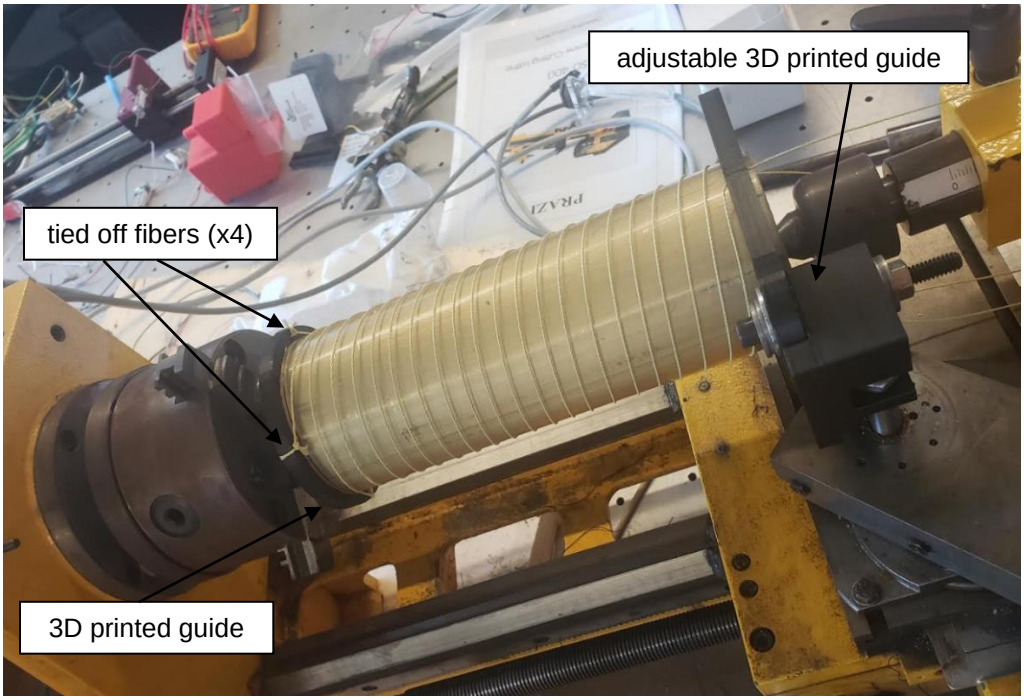

Figure 66: Four fibers wrapped in the forward direction

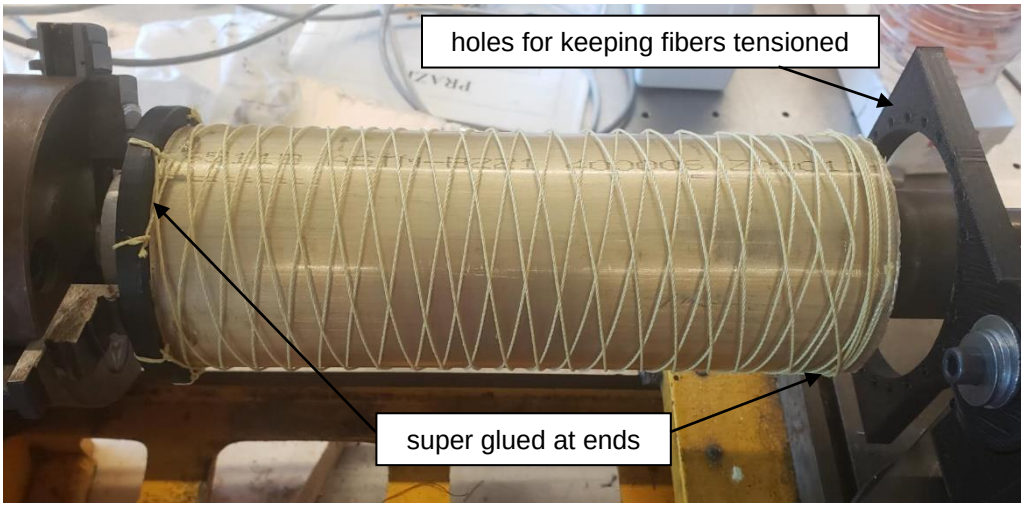

Figure 67: Completed fiber wrapping (all eight fibers)

Once the fiber wrapping was completed, the entire assembly was concentrically placed inside a larger polycarbonate tube and constrained once again on the ends with 3D printed port blocks. To protect the fibers from moving or being damaged by the environment, a second injection of polyurethane

(Polytek74-55A) was used to sandwich the fibers between two elastomer layers. The dual elastomer layers sandwiching the fibers in the injection assembly can be seen in Figure 68 and Figure 69. Other methods of fiber protection methods and fiber placement approaches were explored, and these findings can be found in Appendix C.

Figure 68: Completed elastomer with fibers sandwiched between layers

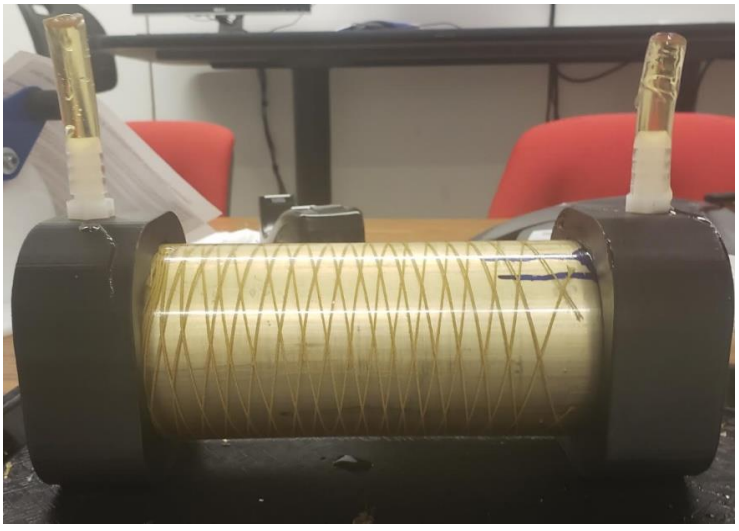

Figure 69: Completed elastomer with fibers sandwiched between layers

The completed elastomer with fibers was then removed from the assembly and slipped off the aluminum rod. Custom designed aluminum fittings with a concentric inlet hole, external slots, and zip ties were used to secure the elastomer to the fittings. Electrical tape was applied to the outside surface of the elastomer to prevent abrasion damage to the elastomer when clamping with the zip ties. A completed extending McKibben actuator is shown in Figure 70. Images of all fabricated extending actuators used in this experiment can be found in Appendix D.

Figure 70: Completed extending actuator

Note that all the fiber crossings for each actuator were measured, and the mean fiber angle was used for the analysis. An orthogonal photograph of each of the actuators was taken, the Solidworks drawing tool was used to take each fiber angle crossing measurement, and the mean value of each of the fiber angle measurements was calculated for the analysis as shown for Actuator 1 in Figure 71 and Table 7. Images of all the actuators and complete data tables of the measurements, including the standard deviation of the fiber angle measurements, can be found in Appendix E.

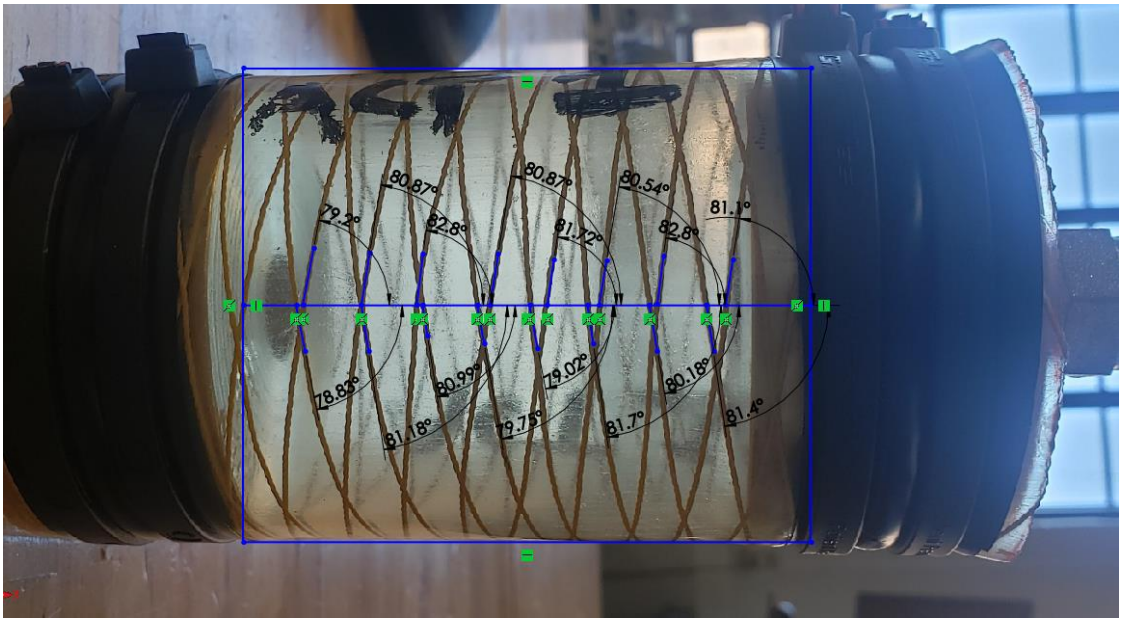

Figure 71: Extending McKibben Actuator 1 fiber angle analysis

Table 7: Extending McKibben Actuator 1 fiber angle results

Angle Measurement #	Measured Angle (degrees)
1	79.20
2	80.87
3	82.80
4	80.87
5	81.72
6	80.54
7	82.80
8	81.10
9	78.83
10	81.18
11	80.99
12	79.75
13	79.02
14	81.70
15	80.18
16	81.40
Mean Angle	**80.81**
Std. Dev	**1.158**

2.3.1.2 Experimental Apparatus

A custom frame was fabricated to allow the actuators to be mounted vertically for axial force testing to avoid side loading created by gravity in a horizontal orientation. A cross bar with a 4500 N load cell (Manufacturer: Futek,

PN: LCM300) was mounted to the frame in a way that it could be moved up and down to accommodate testing of extending actuators of any length at any displacement. This allows force testing of the actuators at free length, or at a prescribed displacement (allowing actuator distal end to extend some amount before becoming in contact with the load cell). A clear tube was mounted concentrically around the actuator and a black 3D printed cover was mounted above the actuator in case of burst failure during testing. A 20.7 MPa pressure transducer (Manufacturer: Honeywell, PN: MLH03KPS) was mounted at the actuator inlet, and the load cell on the cross brace was used to collect the experimental force data as shown in Figure 72 and Figure 73.

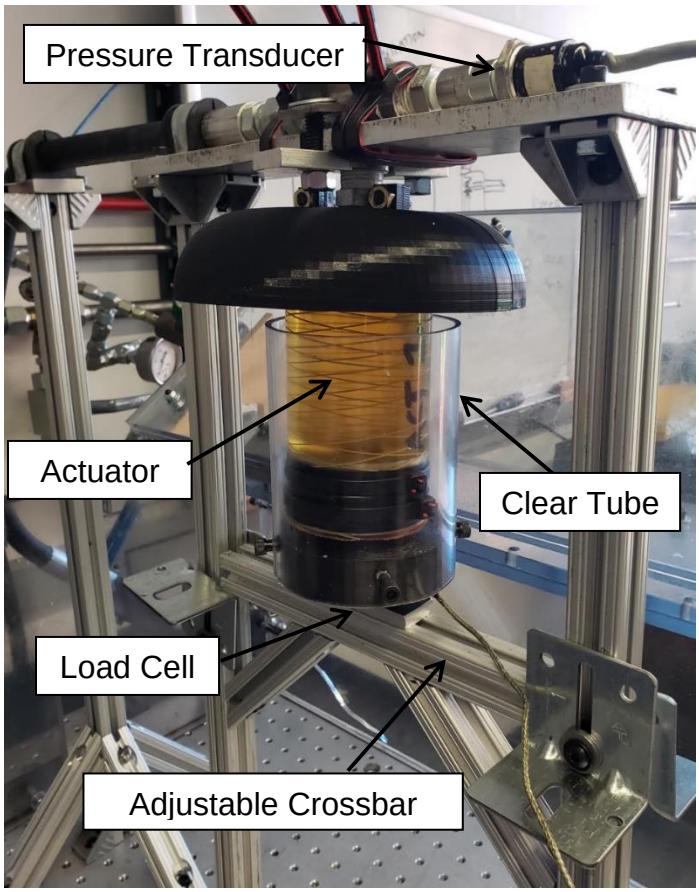

Figure 72: Custom frame with load cell on cross bar and pressure sensor at inlet

Figure 73: Side view of extending actuator, adjustable cross bar, and load cell

2.3.1.3 Experimental Procedure

The pressure sensor was calibrated using a dead weight tester, and the load cell was calibrated using hanging weights and a cantilever beam. The data acquisition board was used to collect axial force and pressure measurements for data processing. Each actuator was first tested at its free length (zero-strain, i.e., $\varepsilon = 0$) where the distal end of the actuator was in contact with the load cell. Force

data were collected with incrementally increasing input pressure until significant elastomer bulging between the fibers was observed or the actuator began leaking near the fittings. The input pressure to the actuator was supplied by a high-pressure hydraulic power unit, and the pressure was tuned down to the desired input pressure using two needle valves in a pressure-dividing circuit that was manually tuned before each experiment. A diagram of the hydraulic circuit is shown in Figure 74.

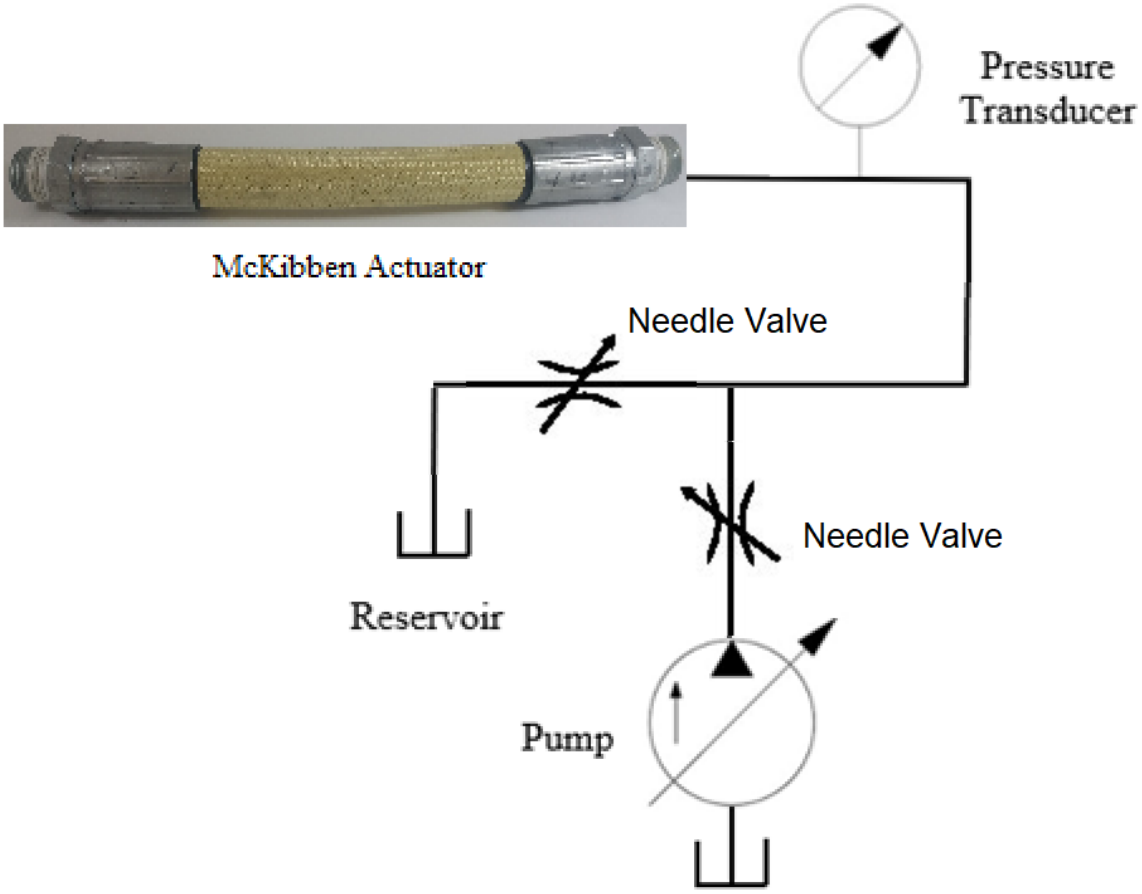

Figure 74: Hydraulic pressure reducing circuit

Once the zero-strain force tests were completed for each actuator, additional tests were conducted at different positions of the crossbar to

understand force capabilities as a function of strain. In these experiments, the crossbar with the load cell was incrementally moved further from the distal tip of the actuator so that the actuator would be allowed to extend a prescribed distance before interfacing with the load cell and beginning to collect force data (see Figure 73 above). The input pressure for all the extending actuator experiments was constant (+/- ~6%) for each actuator and selected to be the approximate pressure that caused bulging of the elastomer between the fibers in the zero-strain experiments. The results from both the zero-strain and extending experiments for all actuators were then compared to the expected results predicted by the force models described in section 2.1.

2.3.2 Results and Discussion

The experiments were conducted using the experimental apparatus, and the comparison between the McKibben force models and the experimental results are presented in this section. First, an uncertainty analysis is presented. Next, the results for the zero-strain experiments are shown followed by the extending McKibben results. An assessment of actuator failure modes, model agreement, model sensitivity to fiber angle measurements, and elastomer bulging are presented and discussed in this section. The section concludes with an analysis of elastomer bulging.

Force data for all five actuators in both sets of experiments was collected, but Actuators 1, 2, and 5 failed in their final experiment of the extending

McKibben study. These final data were omitted from the analysis. All actuator failures were due to insufficient zip tie clamping strength resulting in slipping between the aluminum segment connectors and elastomer. These failures occurred in the extended condition experiments exclusively which allowed good data to be collected first in the zero-strain experiments. These actuator failures can be observed in Figure 75, Figure 76, and Figure 77. Note that Actuator 3 and Actuator 4 did not fail at any point in the experiments.

Figure 75: Actuator 1 failure

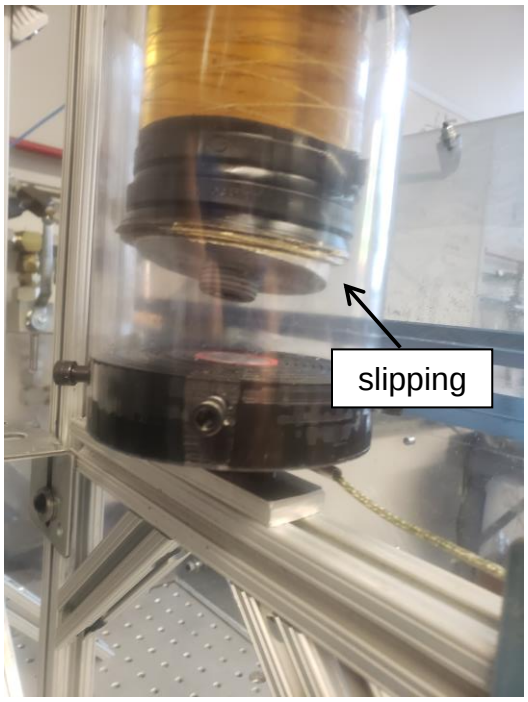

Figure 76: Actuator 2 failure

Figure 77: Actuator 5 failure

2.3.2.1 Uncertainty Analysis

An uncertainty analysis was performed to assess the error bounds of the models from measurement error in the experiments. The uncertainty values used in the analysis are shown in Table 8. These values were selected based on user measurement repeatability samples, manufacturer tolerances, and sensor precision. This uncertainty analysis was used to prepare the results shown in the following sections.

Table 8: Uncertainty table for extension force analysis

Variable	Description	Nominal Value	+/- Uncertainty
D_{fibers}	applied fiber diameter	73.03 mm	0.25 mm
L_o	initial actuator length	74.61 mm *	0.25 mm
t_k	initial wall thickness	3.18 mm	0.25 mm
$F_{extension}$	extension force	669.01 N *	7.56 N
P	pressure	0.1694 MPa *	0.0062 MPa
θ_o	fiber angle	80.8 deg *	1.1 deg *
E	Young's modulus	2.2001 MPa	0.1034 MPa
ε	contraction ratio	0.245 mm/mm *	0.02 mm/mm

* indicates the value is dependent on the individual actuator/experiment

2.3.2.2 Zero-Strain Test Results and Discussion

The zero-strain experiments were conducted for the actuators, and the experimental results were collected. Using the Laws of Propagation of Uncertainties and the values shown in Table 8, uncertainties of the $F(\varepsilon,t)$ and $F(\theta,t)$ models were calculated to be compared to the experimental results for the actuators in the zero-strain experiments. Note that when the actuators are tested at free length and do not change axial length, three of the models yield the same results: $F(\varepsilon,t) = F(\varepsilon) = F(\theta)$. The Gent model value of the Young's modulus was

used for the force analysis, and no losses are captured by any of the models. The extension force results for the free length (zero-strain) tests of the actuators are shown in Figure 78 - Figure 82. The model uncertainty at each data point was calculated, and the mean uncertainty of all the points for each model is stated in the captions for each actuator. Note that the uncertainty of all data points for a given model for a given actuator were all within 0.5% justifying presenting only the mean uncertainties in the results. The error bars on the experimental force data points were calculated using the load cell sensitivity.

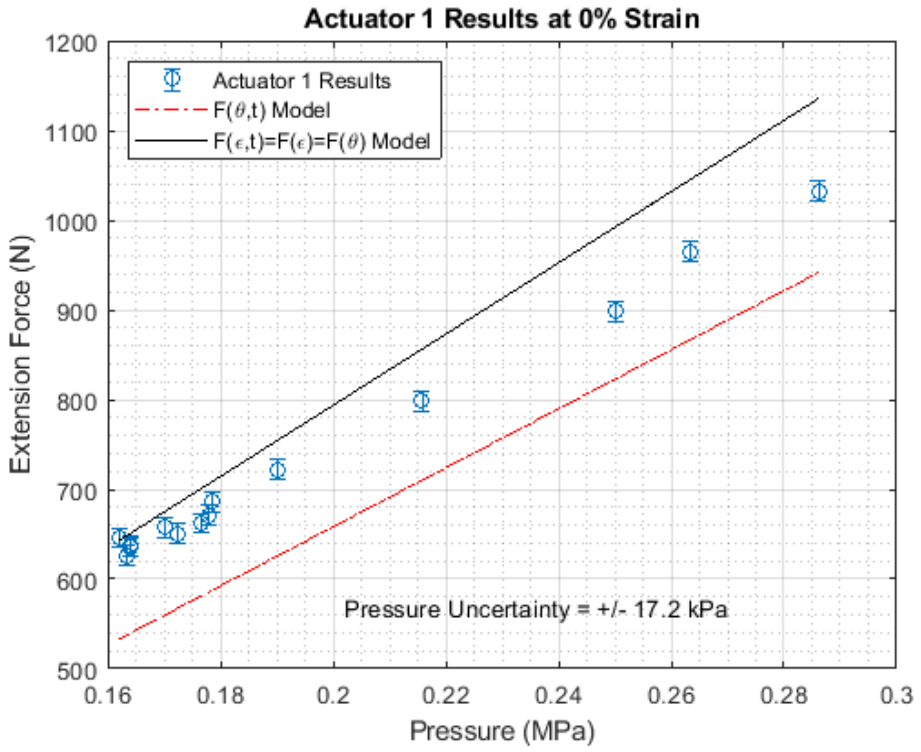

Figure 78: Actuator 1 zero-strain results (F(θ,t) uncertainty = +/- 58.8 N, F(ε,t) uncertainty = +/- 69.6 N)

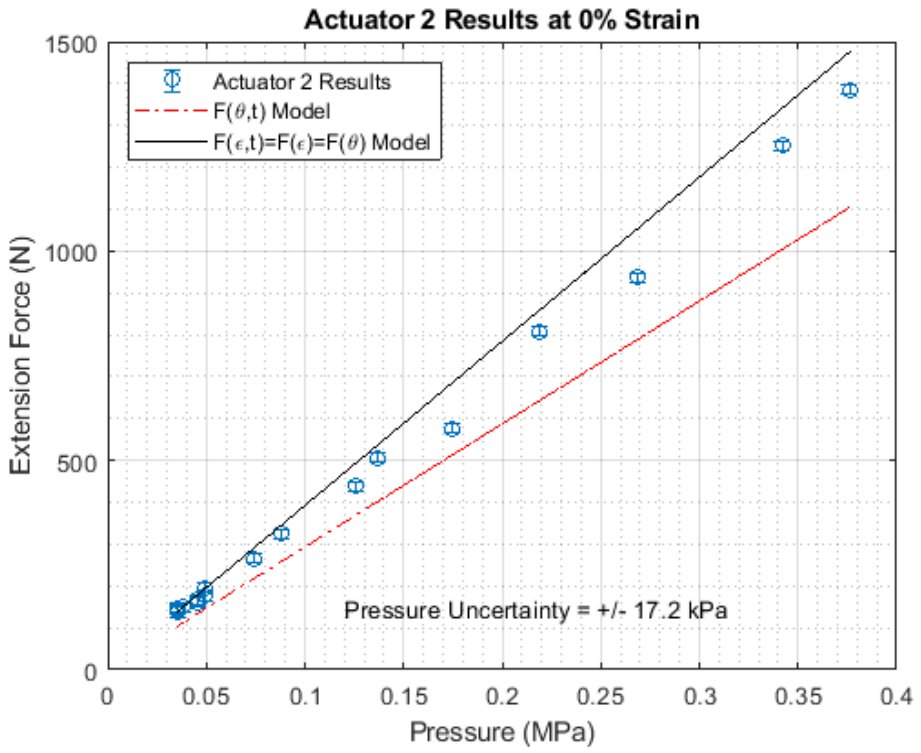

Figure 79: Actuator 2 zero-strain results (F(θ,t) uncertainty = 52.0 +/- N, F(ε,t) uncertainty = 68.4 +/- N)

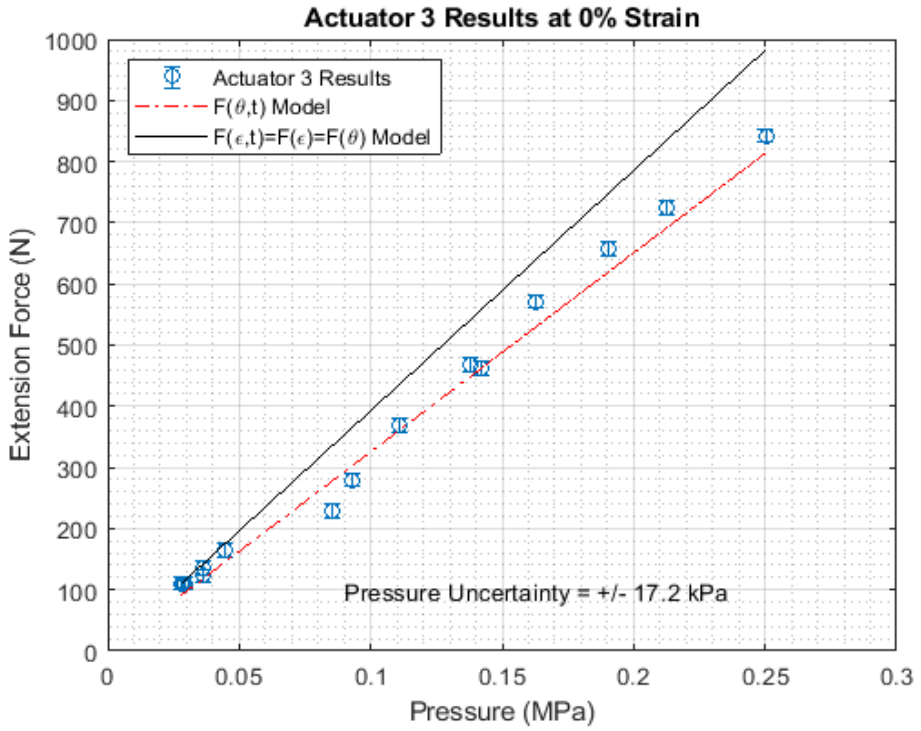

Figure 80: Actuator 3 zero-strain results (F(θ,t) uncertainty = +/- 57.0 N, F(ε,t) uncertainty = 68.2 +/- N)

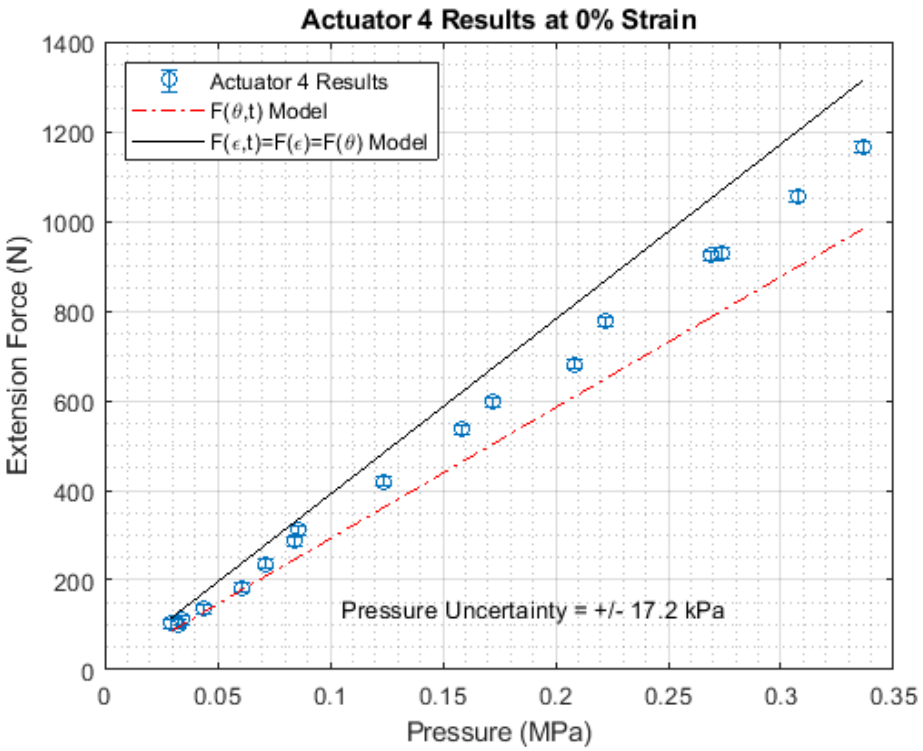

Figure 81: Actuator 4 zero-strain results (F(θ,t) uncertainty = 51.7 +/- N, F(ε,t) uncertainty = 68.0 +/- N)

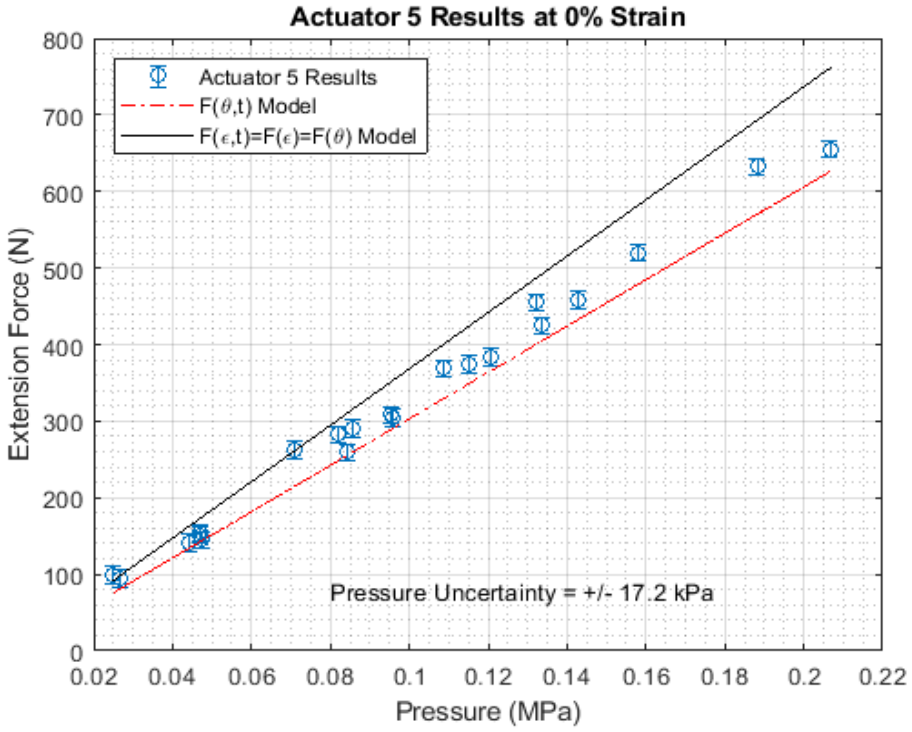

Figure 82: Actuator 5 zero-strain results (F(θ,t) uncertainty = +/- 53.8 N, F(ε,t) uncertainty = 64.8 +/- N)

As can be observed from the plots above, both models do a fairly good job of tracking the zero-strain experimental force results with the contraction-based model overestimating and the angle-based model underestimating the experimental force generation. The experimental results tend to track the lower bound of the $F(\varepsilon,t)$ very closely. Given that no losses or other factors that could impact the observed force are considered in the model, it makes sense that the $F(\varepsilon,t)$ model overpredicts the force generation of the actuators. These results suggest that all these models could be used for McKibben design purposes in zero-strain conditions.

2.3.2.3 Extension Test Results and Discussion

The extending McKibben experiments were conducted, and the experimental force results are compared to other McKibben models and discussed in this sub-section. First, the experimental results are compared to the $F(\theta,t)$ model and the $F(\theta)$ model, followed by a comparison of the experimental results to the $F(\varepsilon,t)$ and the $F(\varepsilon)$ model.

First, the $F(\theta,t)$ model is compared to the $F(\theta)$ model for the results from all actuator experiments. The model uncertainty bars were calculated using the uncertainty values in Table 8 and the Laws of Propagation of Uncertainties, and the experimental force error bars are calculated based on the load cell sensitivity. Unlike the zero-strain experiments, the predicted model results for the extending experiments are non-linear due to the changing length of the actuators.

Therefore, the model uncertainty and force measurement uncertainty error bars are all shown in the results in this sub-section to better illustrate how the results fall within the model uncertainty ranges. The comparison of the experimental results to the *F(θ,t)* and *F(θ)* models for the Actuators 1-5 is shown in Figure 83 - Figure 87. The Gent model value of the Young's modulus was used throughout extension force analysis. Since the measured pressure varied slightly in the extending experiments, the operating pressure of the data point is printed beneath for reference (MPa).

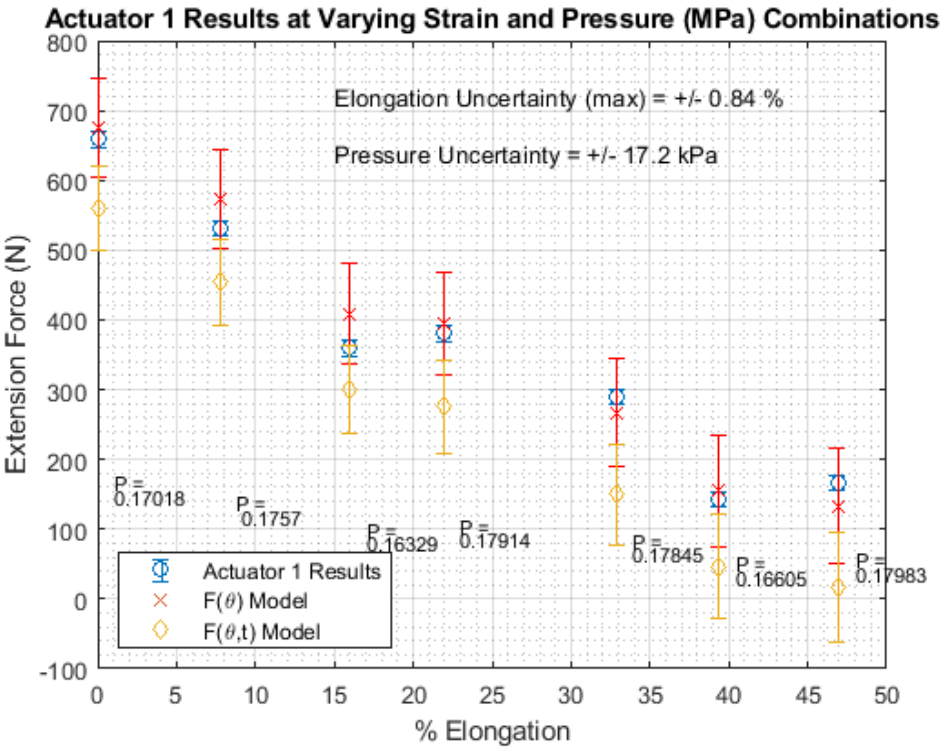

Figure 83: Actuator 1 extension results

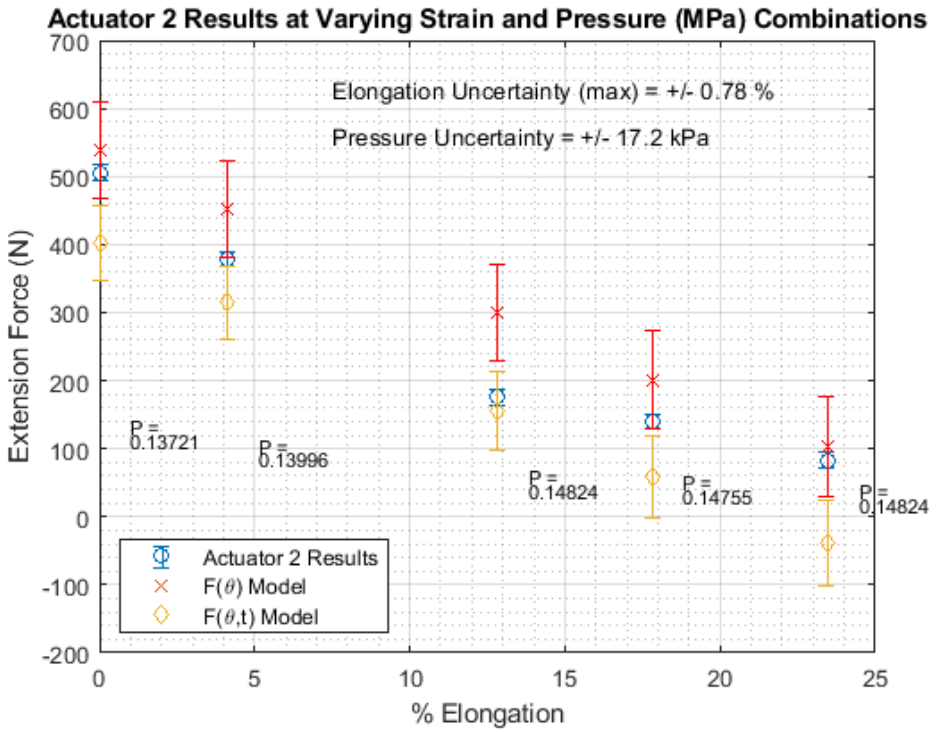

Figure 84: Actuator 2 extension results

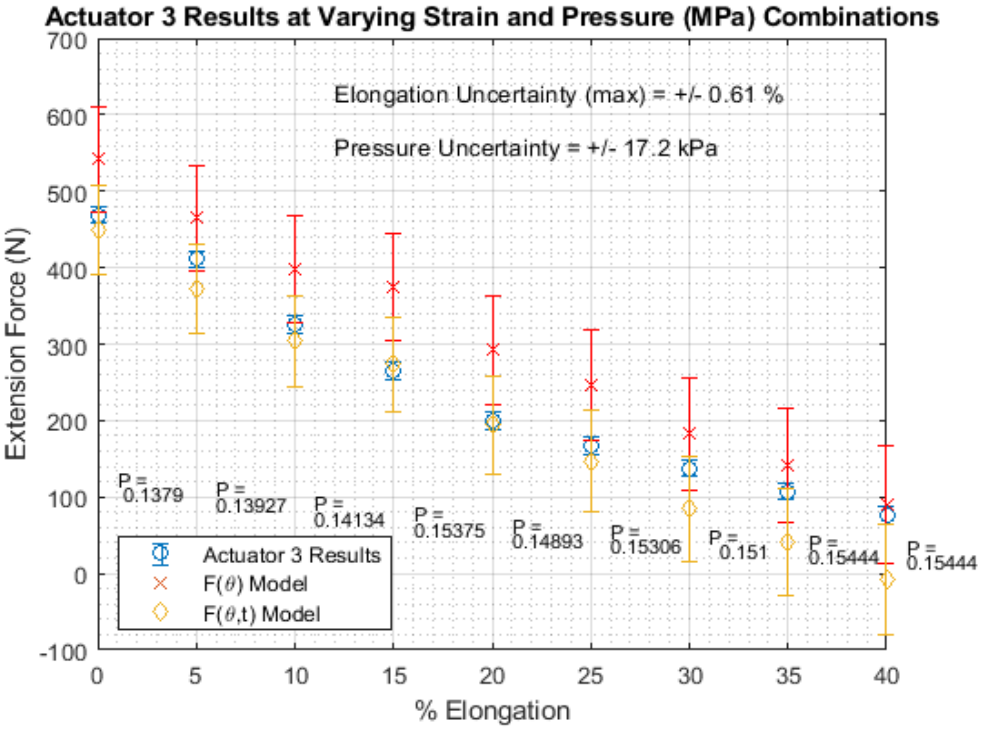

Figure 85: Actuator 3 extension results

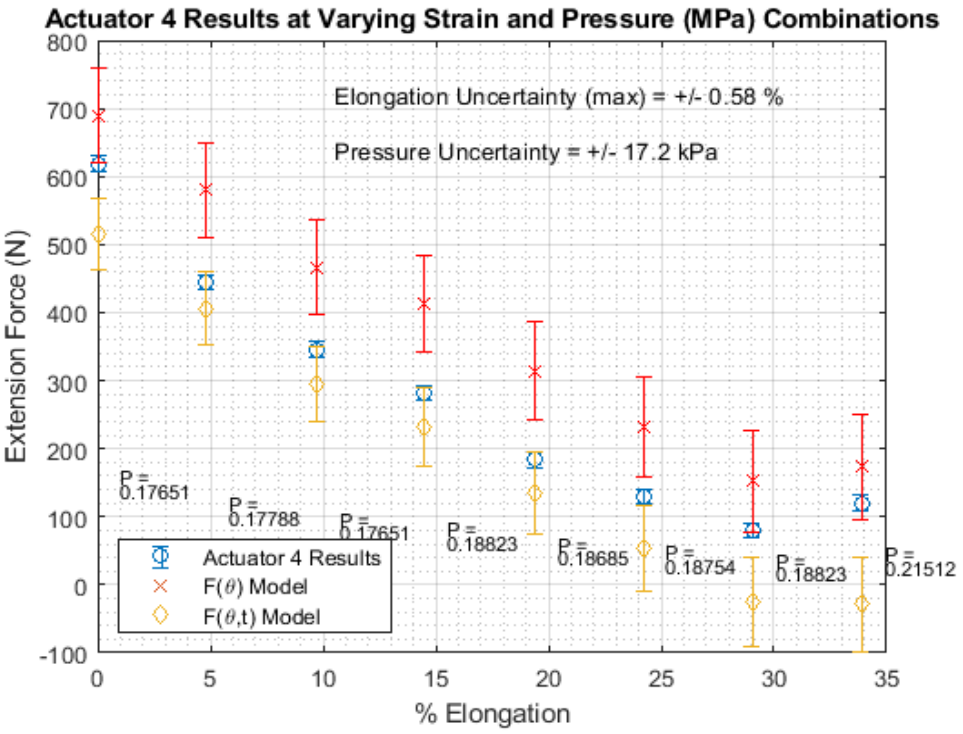

Figure 86: Actuator 4 extension results

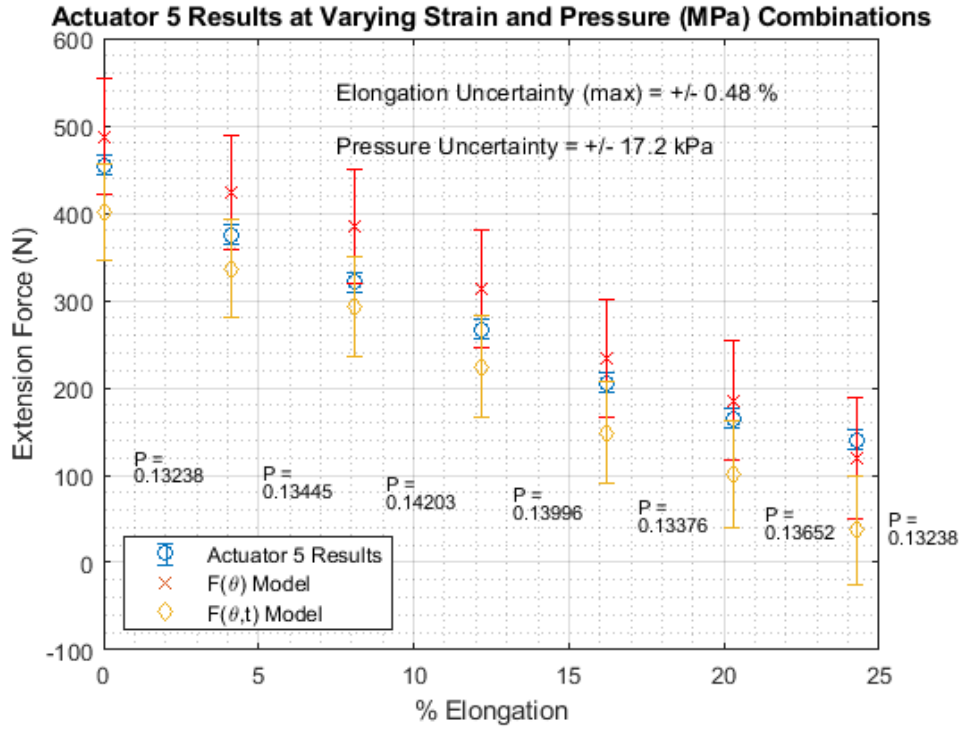

Figure 87: Actuator 5 extension results

As can be observed from the results shown above, there does not seem to be a clear trend on which of the two models better predict the extension force generation of the actuators. However, it does appear that the *F(θ)* model generally overpredicts the force, while the *F(θ,t)* model underpredicts the force. The results for all five actuators track the upper bound of the *F(θ,t)* model very well, and the experimental results fall within the error bounds of one or both models for all the extending actuator experiments.

Similar to the previous results, Figure 88 - Figure 92 show a comparison of the *F(ε,t)* and the *F(ε)* model for the extension experiments with both model and force data error bars shown. The pressure listed below each data point is in units of MPa.

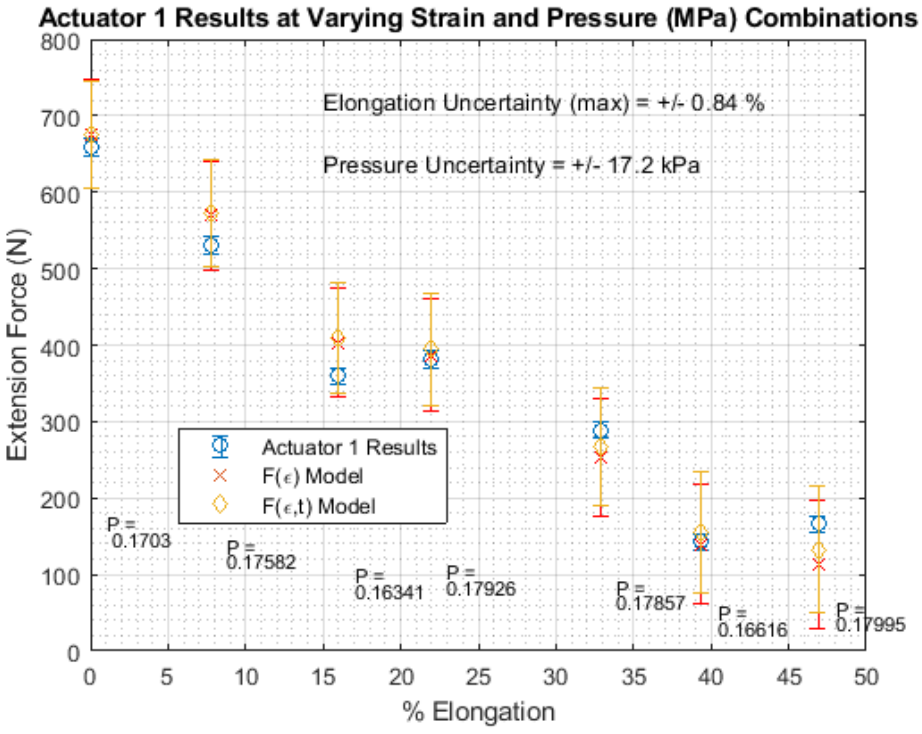

Figure 88: Actuator 1 extension results

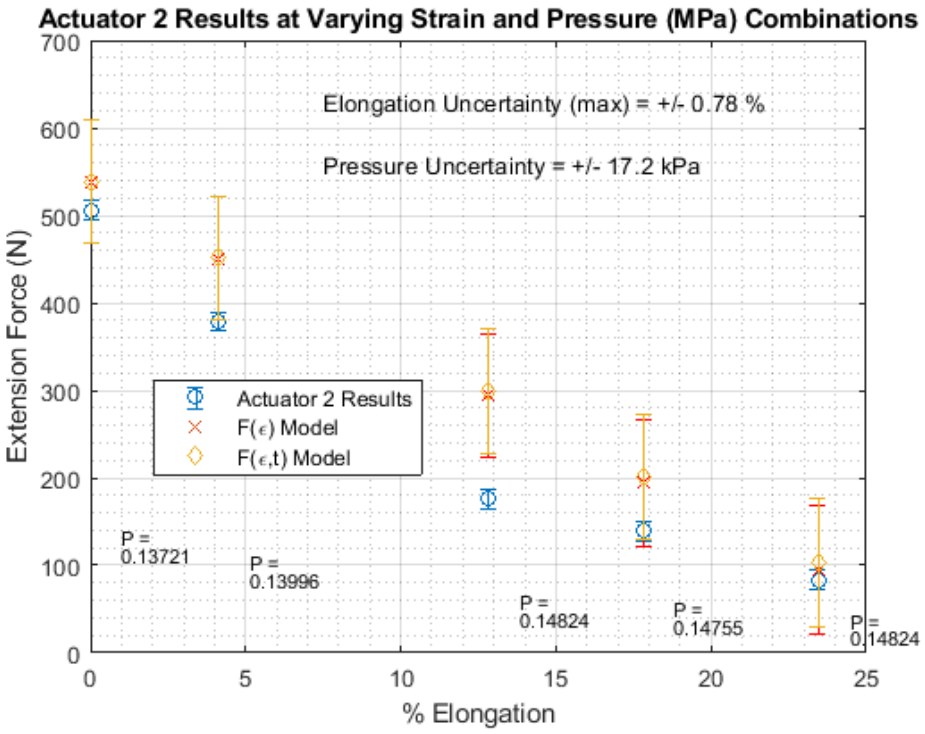

Figure 89: Actuator 2 extension results

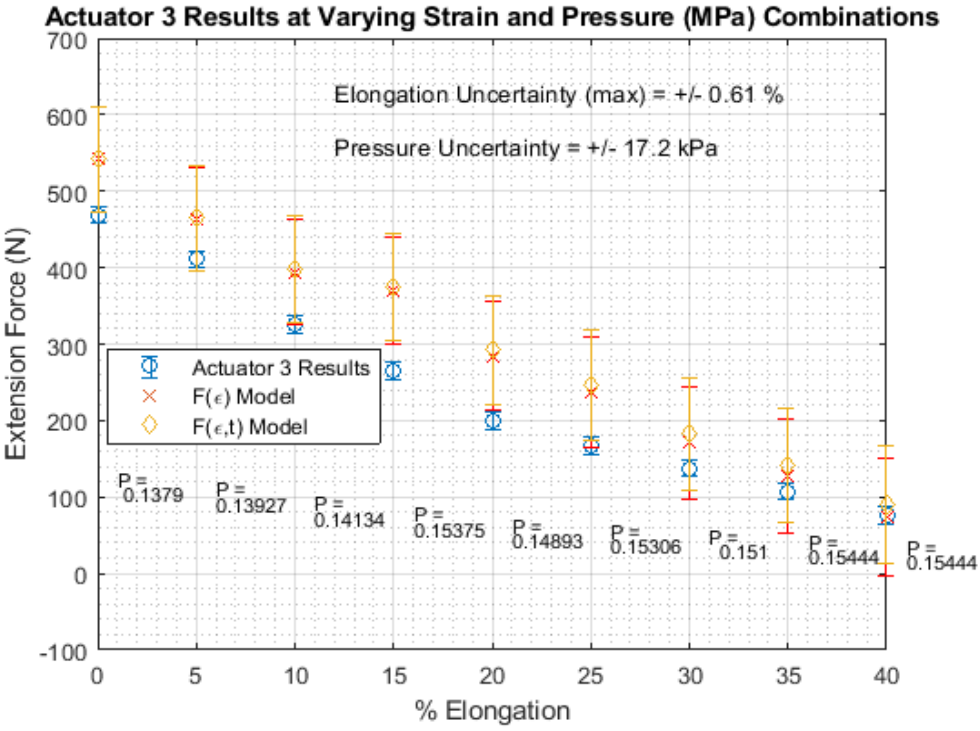

Figure 90: Actuator 3 extension results

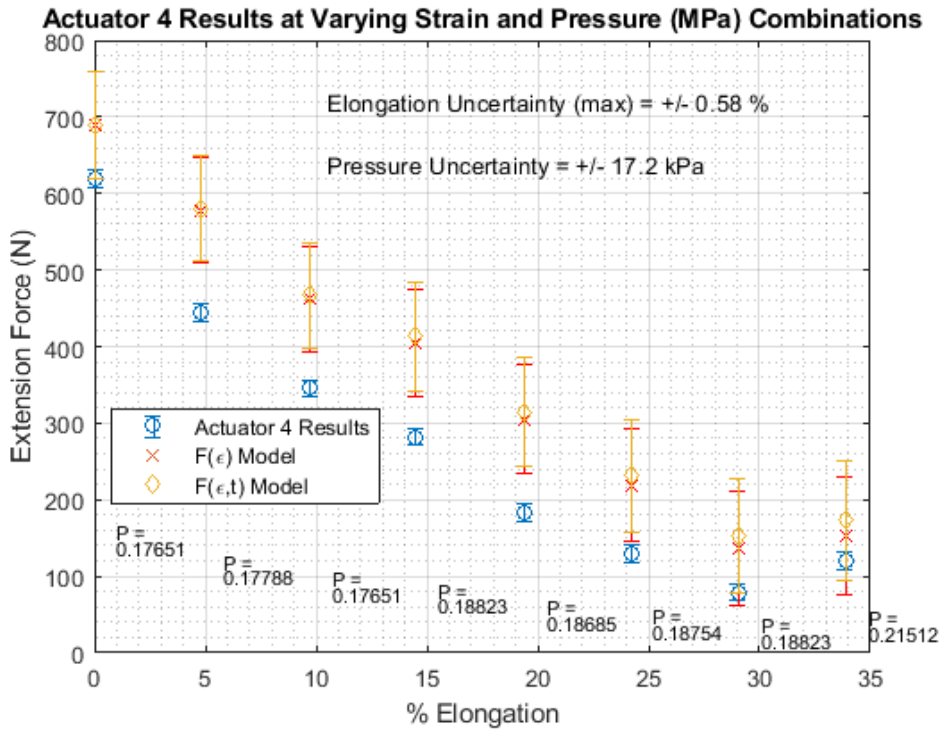

Figure 91: Actuator 4 extension results

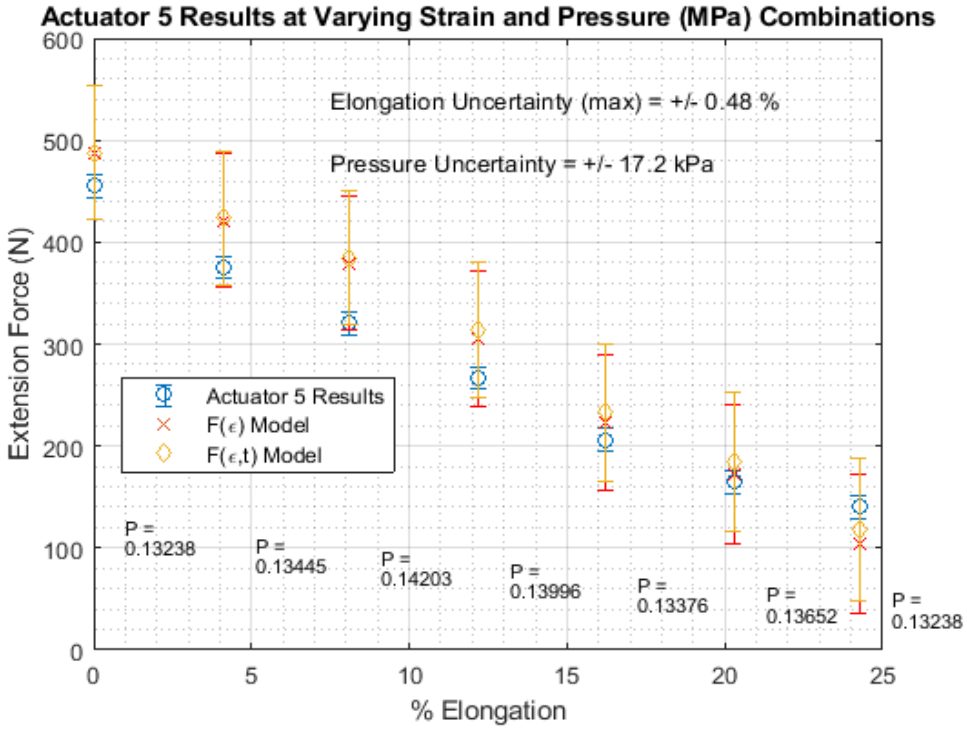

Figure 92: Actuator 5 extension results

While there appears to be some small trends to observe, it is difficult to draw conclusions about which model is best suited for modeling for this set of extending actuators. The *F(ε,t)* model predicts slightly higher forces than the *F(ε)* model with an increase in prevalence at larger strains. This phenomenon is expected because the wall thickness non-linearly varies as the actuator extends which is accounted for with the *F(ε,t)* modeling approach only. The divergence between the two contraction-ratio-based models would be expected to be more pronounced as the wall thickness to diameter ratio of the actuator increases. Nearly all the experimental data points fell within the error bounds of at least one of the two models.

All four of the McKibben force models do a reasonable job at predicting the extension force generation for predictive design purposes. To analyze the agreement between the four models and the experimental results more quantitively, each data point for each actuator was analyzed and the absolute value of the magnitude of the error for that point was calculated for each model. The mean value of the magnitude of error of all data points for all models and all actuators was then calculated to generate a quantitative error table to observe and analyze. These error results can be found in Table 9. Percent error was not used because it tends to skew the error results when the predicted force is near zero. Note that comprehensive plots, including error bands and uncertainty, of the model error for each model for each actuator as a function of percent elongation can be found in Appendix F.

Table 9: Average of absolute error magnitude (N) of each experiment w/ elastic term for extension experiments

	Average of Absolute Value of Error Magnitude (N) of Each Experiment w/ Elastic Term				
	Number of Tests	***F(θ)***	***F(ε)***	***F(θ,t)***	***F(ε,t)***
Actuator 1	7	27.18	28.13	103.30	27.18
Actuator 2	5	62.06	57.59	78.27	62.02
Actuator 3	9	64.03	56.53	35.48	64.00
Actuator 4	8	102.26	93.17	77.80	102.18
Actuator 5	7	37.19	33.91	55.44	37.17
	Overall Average Error (N)	58.54	53.87	70.06	58.51

The overall average error of the *F(θ), F(ε), F(θ,t),* and *F(ε,t)* models for all the extended actuator experiments were 58.54 N, 53.87 N, 70.06 N, and 58.51 N respectively. Losses are not accounted for in any of the modeling approaches, and there are several places where losses could have impacted these results. Both bulging and bending losses are not considered in the analysis, and these factors could impact the observed axial force. Furthermore, additional error could have been incurred from inconsistent fiber wrap angles along an actuator, imprecise fiber angle measurements, error in the elastic modulus from the Gent model, manufacturing imperfections, sensor resolution, and other geometry measurements.

Due to the uncertainty and the fact that the overall average error from of all the models is within a few Newtons, it is challenging to come to a clear conclusion about which model is best suited for modeling this set of extending McKibben actuators. However, it is clear to see that these experiments have

demonstrated that there are no obvious differences in modeling approaches for contracting and extending McKibben actuators. The *F(ε,t)* model was the second most accurate of the four models analyzed in the extending experiments, and it is expected to perform even better with thicker-walled McKibben actuators that may be well suited for high-force applications in rugged environments, such as those found in underground burrowing.

2.3.2.4 Analysis of Elastomer Bulging Between the Fibers

Bulging of the elastomer between the fibers is an observable phenomenon which may skew the expected force results for McKibben actuators. When pressurized fluid is introduced into a McKibben actuator, the pressure can cause the elastomer to bulge between the fibers causing some of the input energy to be diverted from generating axial force. It is theorized that this bulging could cause a reduction in the axial force observed, and most importantly, bulging can eventually lead to actuator burst failure if the pressure is high enough – which certainly reduces the force capabilities of an actuator. This section analyzes the burst failure model presented in section 2.1.7 for all five of the extending McKibben actuators. Figure 93 shows an example of one of the actuators exhibiting bulging behavior of the elastomer between the fibers.

Figure 93: Bulging observed in Actuator 5 of the extending McKibben experiments

The three experiments with the highest operating pressure for each actuator were analyzed. Video footage of the experiments was used to study bulging between the fibers. The time of the highest pressure was identified, and a screenshot of the actuator at that instant in time was imported into Solidworks to measure the maximum fiber spacing, δ, the bulge radius, r_{bulge} at the specific fiber span (where the most bulging is occurring), and the bulge angle, γ at the specific fiber span. These measurements are shown in Figure 94 for reference.

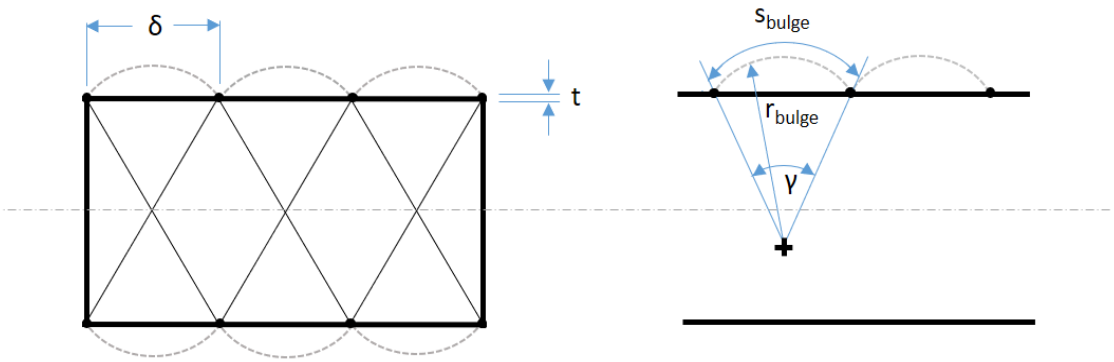

Figure 94: Relevant geometry for McKibben elastomer burst mechanics

The Gent model value for the Young's modulus was used for the analysis. Once these measurements were taken, equation (2.33) from section 2.1.7 was used to solve for the expected pressure to cause the observed bulge. This estimated pressure was then compared to the peak measured pressure to assess model agreement. The results of the assessment are presented in Table 10.

Table 10: Bulge analysis results

	Measured				Calculated		
Actuator	Peak Pressure (MPa)	Max Fiber Spacing (mm)	Bulge Radius (mm)	Bulge Angle (deg)	Expected Pressure (MPa)	Magnitude Error (MPa)	Percent Error (%)
1	0.2501	13.21	14.99	26.39	0.2225	0.0276	11.04
	0.2634	12.45	11.18	33.43	0.2975	-0.0340	-12.91
	0.2859	13.46	11.94	34.35	0.2740	0.0119	4.16
2	0.2679	14.48	23.88	17.60	0.2165	0.0515	19.21
	0.3423	14.99	19.05	23.20	0.2668	0.0754	22.04
	0.3762	16.00	30.48	15.17	0.1703	0.2058	54.72
3	0.1900	11.94	15.24	46.24	-0.0139	0.2039	107.30
	0.2120	12.95	10.92	36.11	0.2996	-0.0876	-41.32
	0.2499	12.70	10.16	39.07	0.3124	-0.0624	-24.98
4	0.2224	15.49	30.23	14.90	0.1707	0.0516	23.21
	0.2734	14.73	12.95	35.26	0.3710	-0.0977	-35.73
	0.3367	15.75	17.27	27.18	0.2909	0.0458	13.61
5	0.0823	14.99	16.00	26.56	0.2204	-0.1381	-167.71
	0.1209	13.46	14.99	26.68	0.2244	-0.1035	-85.58
	0.1580	14.99	14.22	31.85	0.2319	-0.0739	-46.75
	0.2068	12.95	11.68	33.31	0.2843	-0.0774	-37.43
					MEAN	**-0.0001**	**-12.32**

The comparison of the measured pressure and expected pressure yielded some inconsistencies throughout the analysis. However, the average magnitude error of all the data comes out to almost zero mean error, which indicates that some of the inconsistencies may be stochastic measurement error. This provides some confidence that the bulging model may be used as a baseline for designing McKibben actuators to prevent burst failure. It was challenging to get accurate measurements of the fiber spacing, bulge radius, and bulge angle using Solidworks due to the low-quality of the footage and varying camera views during the experiments. Furthermore, the fibers were sandwiched between the elastomer layers which made it even more challenging to identify where the fiber

crossings were for the analysis. This model also does not consider that variations in fiber-spacing and fiber wrap angle exist, which leads to different sized bulges to occur throughout a pressurized actuator (i.e. it is possible the bulges that were measured were not a representative sample of all the bulges on the elastomer at the point of peak pressure). Overall, the ~zero mean magnitude error and -12.32 % error indicate that this model works well to estimate the relationship between input pressure, McKibben actuator geometry, and fiber spacing for design applications. With a more robust and consistent camera set up, better agreement is expected between the model and experiments.

2.4 **Conclusion and Summary**

McKibben actuators are soft and compliant actuators that have advantages over many conventional actuators in terms of force and power density. Many modeling approaches exist to predict the force generation of McKibben actuators, but all the existing models either neglect the wall thickness of the elastomer, are inconvenient for design because knowledge of the fiber wrap angle or other changing geometry must be known, or neglect the generated elastic force from straining the actuator. While including the wall thickness is less critical in pneumatic McKibben modeling, it becomes much more important for hydraulic McKibben actuators that require thicker walls to withstand hydraulic pressures. This chapter presents an overview of the efficacy of three existing McKibben force models (*F(θ), F(ε),* and *F(θ,t)*), the Kothera elastic force model, and a new model (*F(ε,t))* developed by the author. The new model considers the

change in actuator wall thickness due to axial strain and only requires geometric values from the initial actuator geometry. These models were validated for both contracting and extending McKibben actuators. The following two sub-sections provide a summary and conclusion for the contracting and extending McKibben actuator experiments respectively.

2.4.1 Contracting McKibben Conclusion

Twelve contracting McKibben actuators were fabricated and tested. The Gent model was validated as an appropriate tool to approximate the Young's modulus of an elastomer directly from Shore A durometer. It was determined that there was limited impact to force generation from layering fiber sleeves. Four McKibben axial force models and the Kothera elastic force model were experimentally validated and discussed. Input pressure and contraction force were measured and compared to expected results for the models presented in this chapter.

Contracting Actuators B and C were fabricated with one and two fiber sleeves respectively. It was found that no significant impact is made on the total axial force generation by adding an additional fiber sleeve. This finding is important because increasing the number of supporting fibers increases the strength of the actuator and decreases the likelihood of burst failure through the fiber sleeve. One experiment conducted by the author showed that a McKibben actuator with two fiber sleeves could be pressurized to over 13.79 MPa without

failure. However, more experiments are needed to conclusively determine the impact, if any, of additional fiber sleeves on the total axial force generation and hysteresis of McKibben actuators.

Including an elastic force term in the axial force models is needed for thick-walled McKibben actuators when they are extended, because significant elastic forces are generated. It was found that using the Gent model to approximate the Young's modulus from the material's Type A durometer worked well. Experiments to predict the Young's modulus for the rubber materials were conducted, and it was found that the percent error from the Gent model value for 60A neoprene, 70A natural rubber, and 80A neoprene were 17.3%, -13.6%, and -0.4% respectively. The Gent model value of the Young's modulus was used for modeling the elastic force of the three rubber materials used in these experiments. The elastic force was collected at each contraction ratio for each actuator before input pressure was applied, and it was observed that all twelve actuators had excellent agreement with the results predicted by the Kothera elastic force model. This observation is important because it validates the Kothera elastic force model's use in the total force analysis as well as validates the approach to using the Gent model to approximate the elastomer's Young's modulus as a predictive design tool.

The total axial force was measured for the twelve actuators and the error for each of the four modeling approaches was calculated for each actuator. All

four of the modeling approaches include the Kothera elastic force term and neglect losses. It was found that the overall average error for the *F(θ), F(ε),* and *F(θ,t)* models were 9.9%, 10.5%, and 10.0% respectively, and the overall average error for the new model, *F(ε,t),* presented by the author was 9.1%. While the improvement of the new model over the other models is small, it is expected that the new model will be more accurate than existing models for hydraulic McKibben actuators with very thick walls, but more experiments are needed for clear model validation. A finding of this study is that models that track the contraction ratio instead of the fiber angle are more useful design tools because they do not require the continuous knowledge of the fiber wrap angle which is hard to measure.

2.4.2 Extending McKibben Conclusion

Five extending McKibben actuators were designed, built, and tested to determine if there are any fundamental differences between contracting and extending McKibben actuators in terms of predicting the axial force as a function of the pressure. The five actuators were all designed with 76.2 mm outside diameters to examine actuator diameters greater than those studied in the contracting McKibben experiments outlined in section 2.2. The five actuators were first tested at their free length with a ramped pressure input. Then the actuators were allowed to extend over a range of distances before force data was collected to understand how extension affects model accuracy for extending McKibben actuators. Experimental force results were compared to the four

McKibben force models presented in this chapter for the zero-strain and extending McKibben experiments. A preliminary study on the efficacy of the elastomer bulge model was also presented.

An approach to injecting custom geometry elastomers and using a custom fiber wrapping lathe was employed to fabricate the five extending McKibben actuators. Nearly all the force data points from the zero-strain extending McKibben experiments fell within the upper and lower error bounds of all four of the McKibben force models. While it was unclear which model was the best, the results show that there are no clear differences in modeling extending and contracting McKibben actuators at their free length. All the actuators survived the zero-strain experiments without issue, and three of the five actuators failed in their final extension experiments due to insufficient zip tie clamping forces between the elastomer and segment connectors. Two of the five actuators did not fail, and none of the actuators experienced buckling failure due to the low slenderness ratios of the actuators in the experiments.

The overall average error of the $F(\theta)$, $F(\varepsilon)$, $F(\theta,t)$, and $F(\varepsilon,t)$ models for all the extending actuator experiments was 58.54 N, 53.87 N, 70.06 N, and 58.51 N respectively. While non-ideal behaviors not considered by the models, such as bulging, leaking, bending, and bending, could be responsible for some of this error, user measurement related errors could have also contributed to the results. The new $F(\varepsilon,t)$ model developed by the author was the second most accurate of

the four models assessed, and it is expected that it would continue to improve its efficacy over the other models as the wall thickness of the McKibben actuator increases. The results from these experiments provide the justification to use these modeling approaches, particularly the $F(\varepsilon,t)$ model, for predictive design as well as demonstrate there are no clear differences between modeling contracting or extending McKibben actuators.

A study of the relationship between input pressure and the elastomer bulging between the fibers was presented, and an assessment of the model presented by the author was discussed. Video footage of the actuators was used to measure fiber spacing, bulge radius, and bulge angles for fifteen different experiments where bulging between the fibers was observed (three experiments for each of the five actuators), and the author's elastomer burst model was used to estimate the pressure required to cause such a bulge. This estimated pressure was compared to the experimentally measured pressure to determine if the model accurately predicts the relationship between pressure and elastomer bulging (and eventually bursting if the input pressure is sufficient). The error that was present appeared to be stochastic as almost zero mean magnitude error was found with a -12.32 percent mean error between the results and the experiments. Challenges in accurately measuring the fiber spacing, bulge radius, and bulge angle using video footage likely led to some of these inconsistencies, but the results show that this modeling approach provides a good estimate of elastomer bulging and bursting between fibers. It is expected that higher quality

images would have resulted in better agreement between the experiments and the model.

2.5 Specific Contributions of the Chapter

- Development of a new McKibben axial force model ($F(\varepsilon,t)$) that addresses variations in actuator wall thickness as an actuator is displaced and experimental validation against existing McKibben force models

- Experimental validation of the Kothera elastic force model and demonstration of the importance to include this elastic term in force modeling thicker-walled McKibben actuators

- Experimental validation of using the empirical Gent model to convert shore A durometer to elastic modulus for McKibben force modeling

- Experimental validation that layering multiple off-the-shelf fiber sleeves on a McKibben actuator to increase the resistance to a burst failure has minimal impact on the axial force generated (input pressure of ~13.9 MPa achieved)

- Confirmation that the axial force generated by contracting and extending McKibben actuators can be predicted with the same models with similar accuracy at free and displaced conditions

- Development of a novel manufacturing approach of McKibben actuators including how to manufacture custom-sized elastomers with embedded fibers at specific fiber-wrap angles

- Development and experimental validation of new elastomer bulge model to understand the relationship between input pressure, fiber spacing, and elastomer bulging/safety factor from bursting.

Chapter 3: Hydraulic McKibben Actuator Buckling Study

The purpose of this chapter is to analyze buckling behavior in extending McKibben actuators loaded in compression. McKibben actuators offer unique advantages with flexibility and customization over many conventional actuators, but McKibben actuator buckling behavior has never been extensively studied at high forces. To utilize high force extending McKibben actuators for burrowing or for similar applications, it must be determined whether McKibben actuators loaded in compression follow traditional Euler column buckling behavior – or if some other form of buckling behavior is observed due to the pressurized fluid, elastomer, and fiber wrap combination. Furthermore, buckling behavior inside of a constrained environment like a burrow will be investigated to determine if additional extension forces can be generated due to the constrained environment. Developing an understanding of how both an unconstrained and a constrained environment impacts the buckling behavior, and therefore axial force capabilities, of an extending McKibben actuator may be useful for burrowing applications. The proposed multi-segment robot in this thesis utilizes an extending McKibben actuator to move the robot along the burrow (and eventually into a substrate), and it may be possible to utilize the burrow wall to reduce buckling failure tendencies and generate larger penetration forces.

There is limited prior literature that studies the buckling behavior of McKibben actuators. Luo et al. have studied how cylindrical elastomer buckling

can be utilized to create kink valves that enables unique deformed geometry of the actuator as shown in Figure 95 [137].

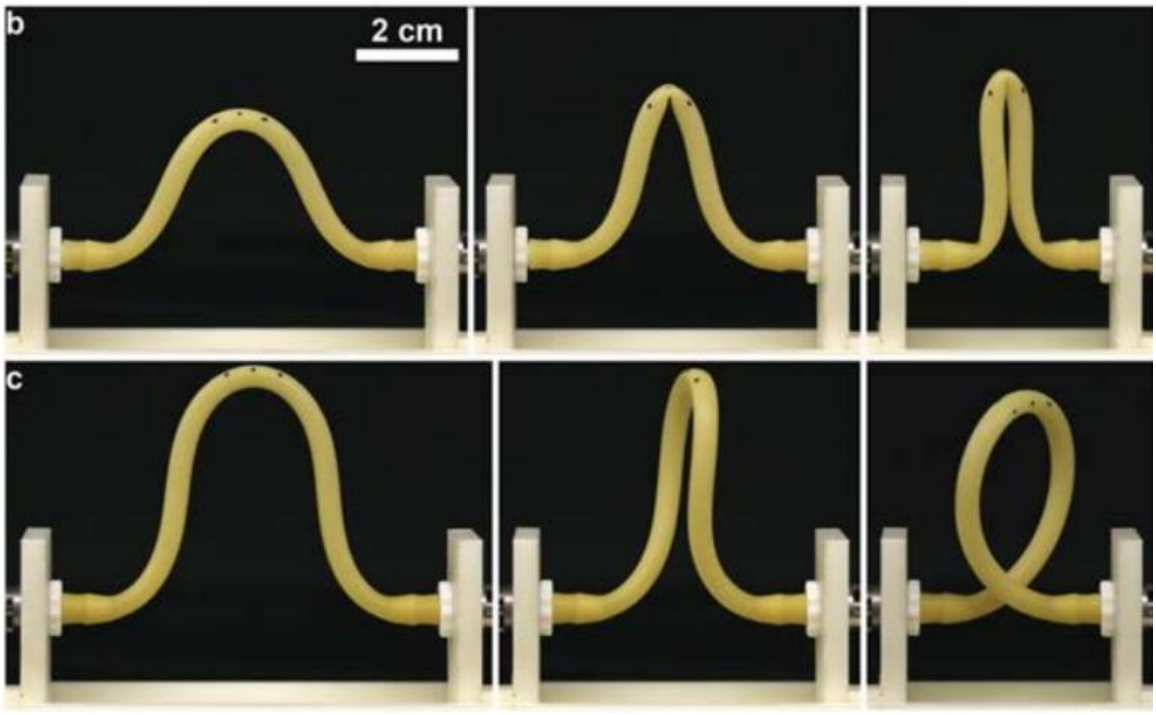

Figure 95: Buckling failure of soft actuator utilizing kink valves [137]

Jensen et al. have studied the buckling behavior of carbon nanotubes to determine if they follow traditional column buckling theory. Models to predict the compressive forces to induce buckling (bending) and kinking (a more extreme form of local buckling where wall collapse occurs) were presented and experimentally validated to show that carbon nanotubes follow traditional buckling theory and kinking forces can be predicted [138]. Figure 96 shows images of the carbon nanotubes buckling and kinking in these experiments.

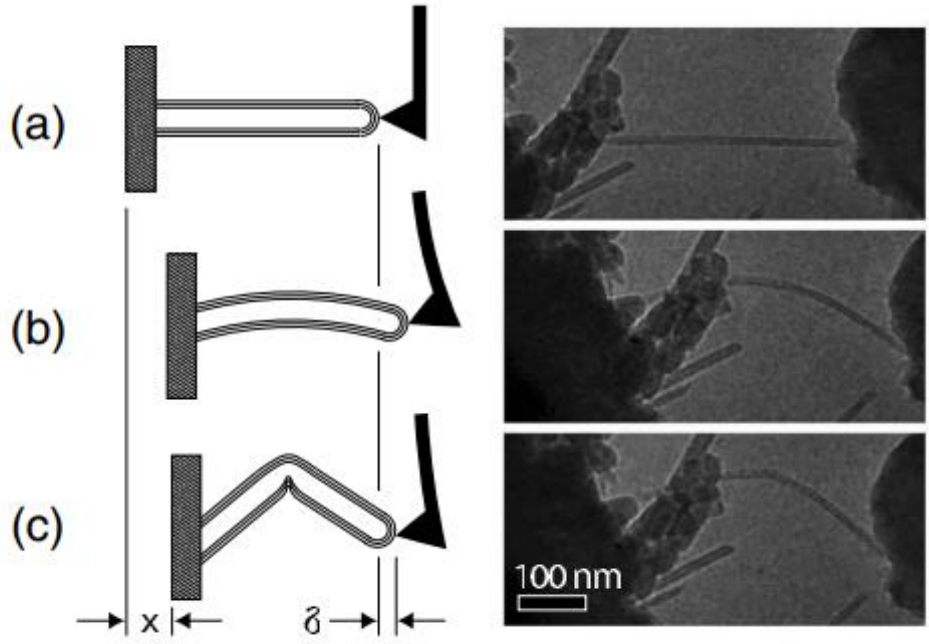

Figure 96: Carbon nanotube failure modes: a) no load, b) buckling failure, c) kinking failure [138]

Kim et al. have studied the buckling and kinking behavior of independently actuated contracting McKibben actuators connected on the ends by a connector plate by implementing a ‘resistive force’ acting laterally on the actuators and treating the entire actuator as an equivalent spring system as shown in Figure 97 [139]. However, no literature to date studies the force generation capabilities of a single extending McKibben actuator in a cylindrically constrained environment like a burrow.

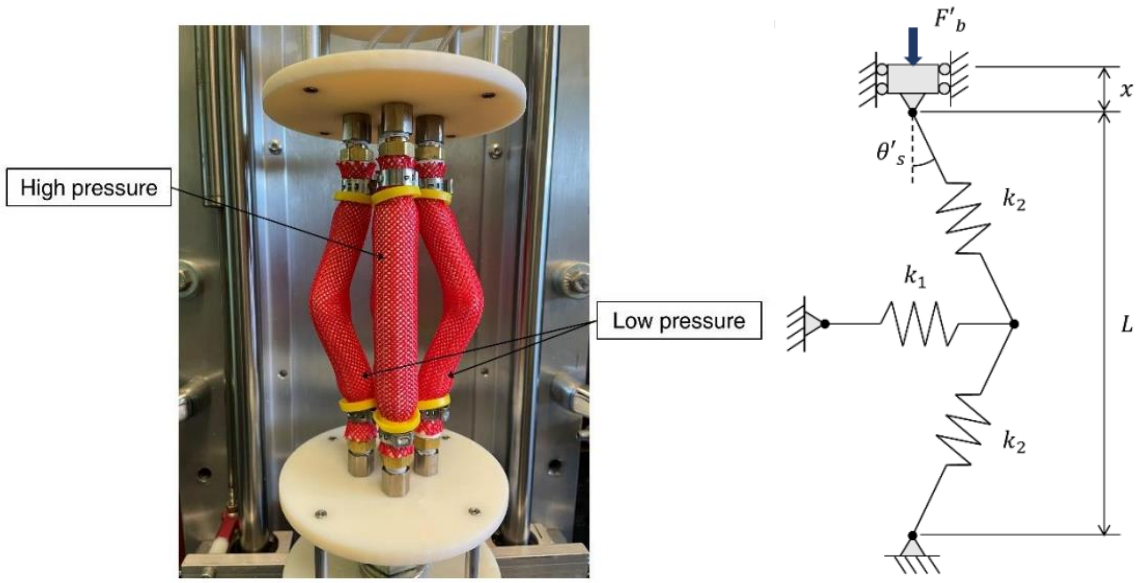

Figure 97: Resistive force modeling approach of combined contracting McKibben actuators [139]

This chapter aims to provide more clarity on the buckling behavior of extending McKibben actuators to determine if they follow Euler-Johnson buckling theory. First, a general introduction to modeling of buckling behavior is presented. Next, an overview of the actuator design, experimental apparatus, and experimental procedure for testing the actuators is provided. Finally, the results from the buckling experiments are presented followed by a discussion of the results.

Six new extending McKibben actuators were fabricated with varying lengths, inside diameters, and wall thicknesses and experiments were conducted to determine their buckling limitations. The actuators were designed to test a wide range of slenderness ratios. The extending actuators were first tested with pressurized hydraulic fluid in a static fixed-fixed loading condition to determine

the maximum force required to observe the beginning of buckling failure. Then the actuators were tested in a constrained environment with a polycarbonate tube externally mounted circumferentially around the actuators to constrain the buckling motion to determine if an environment like a burrow is beneficial for reducing buckling tendencies and propagating axial extension forces – even beyond traditional buckling failure limits. Tests were also performed on the actuators to determine if buckling failure is observed in a similar manner if an external load is applied to the actuator instead of using pressurized fluid for actuation.

3.1 **Modeling**

To assess whether extending McKibben actuators driven by pressurized fluid can be modeled using traditional column buckling theory, a review of buckling theory is presented in this section. The fiber-wrap and pressurized fluid column differentiate the McKibben actuator from a traditional column, and it is unclear they alter the buckling behavior of the McKibben actuator. Buckling is a failure mode that occurs when a beam or column is loaded in compression and buckling failure typically happens very rapidly. To design extending McKibben segments that can be used in underground burrowing, an understanding of the buckling mechanics of the actuators must be developed to design the actuators to withstand the large forces needed for such applications.

To determine the critical load that a column is predicted to buckle under, the columns slenderness ratio, S_r must be computed and is expressed as

$$S_r = \frac{l_{effective}}{k} \tag{3.1}$$

where $l_{effective}$ and k represent the effective length of the column and the radius of gyration respectively [140]. Note that the extending actuators in these experiments are in a fixed-fixed end condition and axially loaded when tested, and therefore the effective length of the actuator is half the initial length for these experiments [140]. The radius of gyration can be expressed as

$$k = \sqrt{\frac{I}{A}} \tag{3.2}$$

where I is the smallest area moment of inertia and A is the cross-sectional area at that same cross-section [140]. Columns can be defined as short, intermediate, or long based on their slenderness ratios, and depending on the classification, different buckling failure analyses must be considered. The Johnson and Euler curves are used to predict the critical buckling force depending on the slenderness ratio. Figure 98 [140] shows these various inflection points and failure zones where P_{cr} is the critical buckling load, S_{yc} is the material's compressive yield strength, and $(S_r)_D$ is defined as

$$(S_r)_D = \pi \sqrt{\frac{2E}{S_{yc}}} \tag{3.3}$$

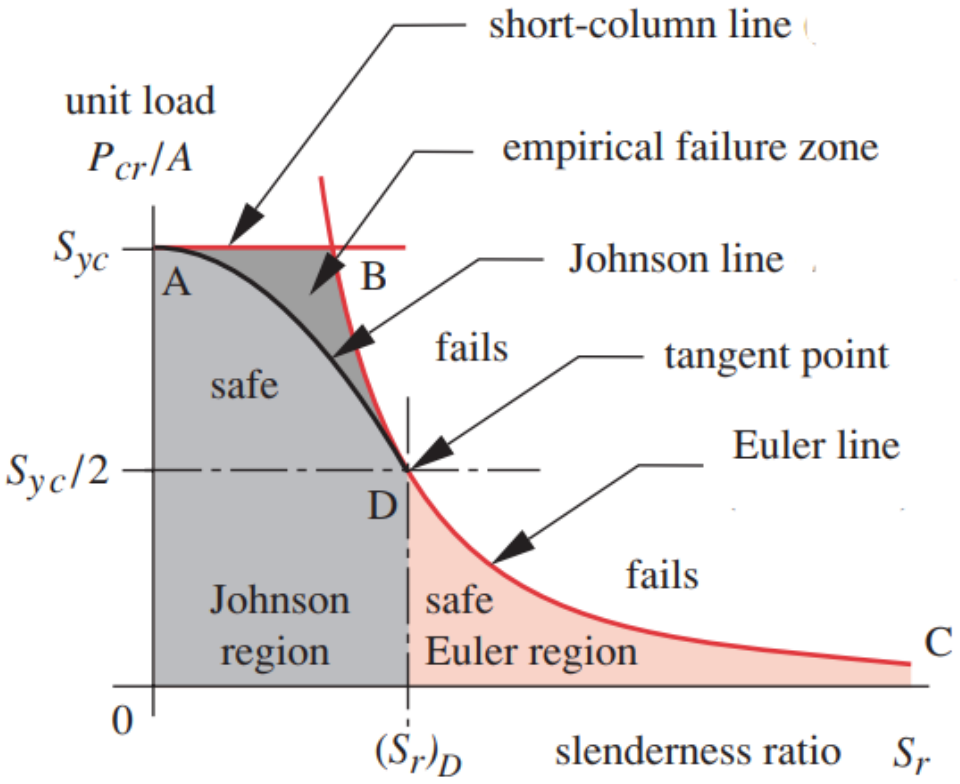

Figure 98: Euler and Johnson column buckling failure zones [140]

Once $(S_r)_D$ is calculated, if the slenderness ratio of the column being analyzed is greater than $(S_r)_D$, the column follows Euler column buckling equations. If slenderness ratio of the column is less than $(S_r)_D$, then Johnson column buckling equations are used to predict the critical buckling load for the column. For Euler columns, the critical buckling force can be expressed as shown below where *E* is the modulus of elasticity [140].

$$P_{cr} = \frac{\pi^2 AE}{4S_r^2} \tag{3.4}$$

Similarly, the critical buckling force for Johnson columns can be computed and is shown below [140].

$$P_{cr} = A(S_{yc} - \frac{1}{E}\left(\frac{S_{yc}S_r}{2\pi}\right)^2) \tag{3.5}$$

The critical buckling force is the load that is expected to cause the McKibben actuator to fail due to buckling via traditional buckling analysis techniques, but it is hypothesized that the tension developed in the fibers or the variable internal pressure distribution as deformation occurs may change the buckling mechanics of the actuator.

Note that it is possible for the compressive yield strength of the column to limit the critical compressive force an actuator can withstand before the critical buckling force predicted by the Euler or Johnson models is reached.

3.2 **Methods**

3.2.1 Actuator Design

Six custom extending McKibben actuators were designed and fabricated with varying slenderness ratios ranging from ~4-9. The actuators were fabricated by using the same elastomer injection and fiber wrapping techniques outlined in section 2.3.1. The actuators were wrapped with fibers at an 80 degree fiber angle to generate large enough forces to buckle without the need for large input pressures that may cause bursting or slipping at the segment connectors. The

geometry of the actuators can be found in Table 11, and an image of the wrapped elastomer tubes can be found in Figure 99. All actuators were wrapped with eight fibers – except for Actuator 1C which was wrapped with sixteen fibers to determine if a denser fiber wrap makes an impact on buckling behavior. Measurements of the fiber angles were taken at each crossing for each actuator, and the mean fiber angle was used for the analysis. The fiber angles were measured, and the mean angle was calculated using the same optical methods as in section 2.3.1**.** The comprehensive fiber angle measurements for all the actuators used in these buckling experiments can be found in Appendix G. Note that the actuators in this study did not have the additional outer layer of polyurethane that the actuators in section 2.3 had.

Table 11: Buckling actuator initial geometry

Actuator	Initial Length, L_o (mm)	Initial Diameter, D_i (mm)	Slenderness Ratio, S_r (mm/mm)	Wall Thickness, t_k (mm)	Initial Fiber Wrap Angle, θ_o (degrees)
1A	100.0	38.1	4.2	4.8	79.2
1B	150.8	38.1	6.3	4.8	78.0
1C	201.6	38.1	8.5	4.8	78.9
2A	100.0	38.1	4.4	6.4	79.0
2B	150.8	38.1	6.6	6.4	79.1
2C	201.6	38.1	8.8	6.4	80.2

Figure 99: Wrapped elastomers for buckling experiments

The wrapped elastomers were slipped over aluminum segment connectors machined with slots, and zip ties were used to secure the elastomer to the segment connector with a small piece of electrical tape used to avoid damaging the elastomer. The distal segment connector had a hole drilled into it that could engage with a peg (mounted to the load cell) to ensure fixed-fixed end conditions and confirm no rotation of the segment connector occurred. The proximal segment connector was connected to a hydraulic input line. Figure 100 shows the peg, mounted on the load cell, pushed into the hole on the distal segment connector of the extending actuator. Figure 101 shows renderings of the proximal and distal segment connectors. Dimensioned drawings of the segment connectors can be found in Appendix H.

Figure 100: Actuator engaged with load-cell peg

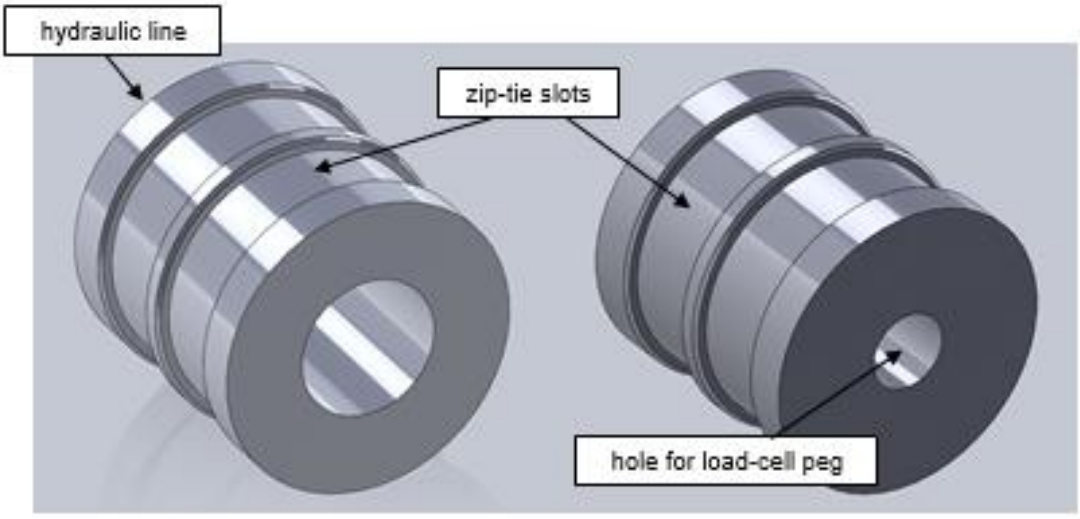

Figure 101: Proximal (left) and distal (right) segment connectors

3.2.2 Experimental Apparatus – Pressure Testing

An experimental apparatus consisting of a horizontal cross-bar that is vertically adjustable mounted with a load cell and pressure transducer (the same sensors from Chapter 2) was fabricated. The vertical orientation avoids gravitational side loading of the actuators that could create premature buckling. This is the same testing equipment and system that was discussed previously in section 2.3.1. 3D printed adapters were used to allow the adjustable height load cell to be mounted with a clear polycarbonate tube of any diameter. This was implemented to perform actuator testing in different diameter tubes while also providing a safety shield in case of actuator burst failure. Figure 102 and Figure 103 show the experimental apparatus used to conduct the unconstrained and constrained pressurized buckling experiments.

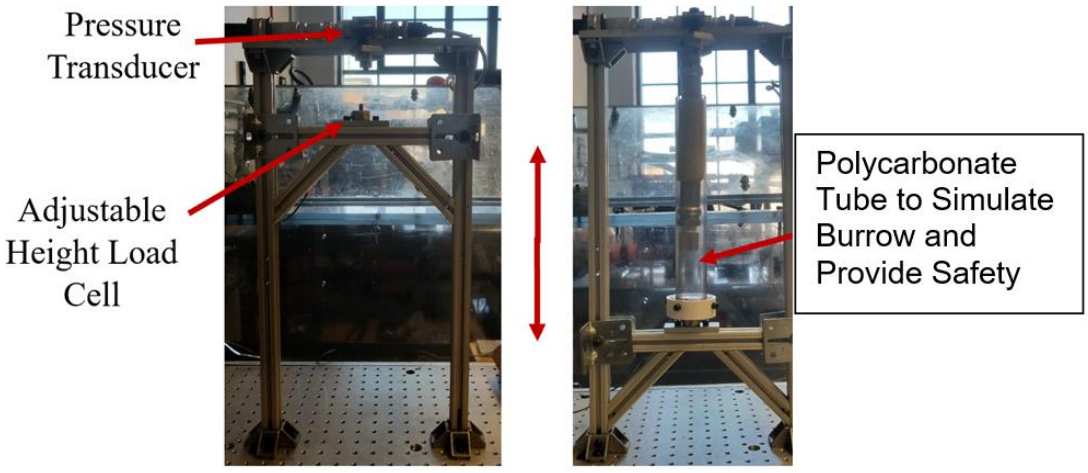

Figure 102: Buckling experimental apparatus

Figure 103: Extending McKibben actuator in experimental apparatus

3.2.3 Experimental Apparatus – External Load Testing

Another experimental apparatus was built to perform compression testing on the elastomers in a controlled manner without applying internal pressure to the actuators. The external load applying apparatus used a hydraulic press frame with custom 3D printed elastomer holders loosely set inside of a clear polycarbonate tube. The hydraulic press applied an external load to the

elastomer while the 3D printed parts ensured a consistent fixed-fixed end condition for the buckling analysis. The load cell was mounted at the bottom of the system to determine the axial force that resulted in the actuator failing. Figure 104 shows the experimental apparatus used for performing the external load experiments.

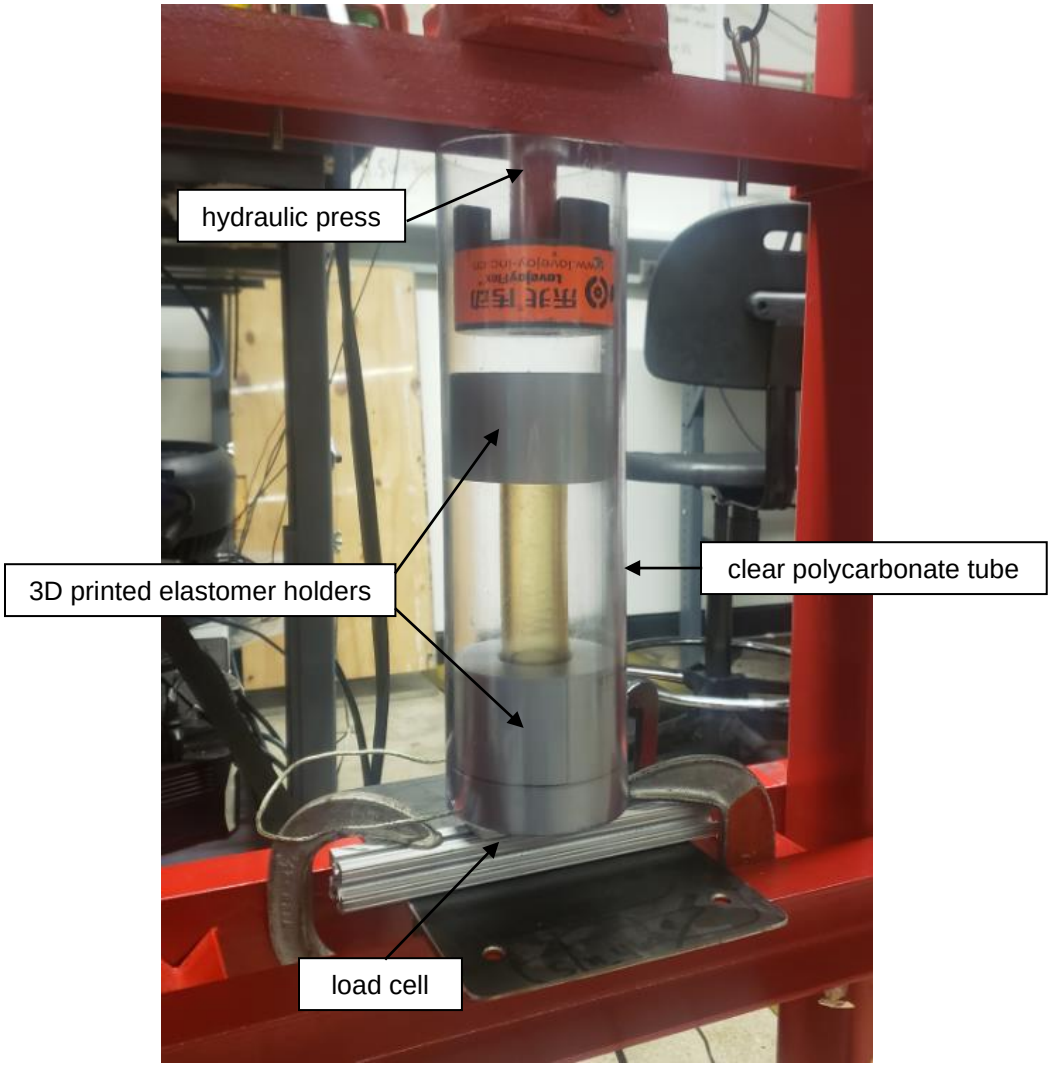

Figure 104: External load applying experimental apparatus

3.2.4 Experimental Procedure

The pressure sensor and load cell were the same used in previous experiments discussed in Chapter 2, and they were calibrated again to ensure accurate pressure and force measurements in all the experiments.

In the first set of pressurized buckling experiments, each of the six actuators were hung vertically and the horizontal cross bar was raised until the peg mounted on the load cell fit into the hole in the distal segment connector of the actuator. A slowly increasing ramped pressure was applied to each actuator and a camera was used to record the behavior of the actuator. The pressure was slowly increased until initial bending of the actuator occurred. The pressure was further incrementally increased until accelerated buckling was observed – defined by when the actuator bending rate observably increased rapidly, and the actuator experienced buckling failure. When both initial bending and accelerated buckling were observed, pressure was vented to tank to prevent catastrophic buckling failure of the actuator. Force data from the load cell and camera footage from the experiments were used to determine what force initial bending and accelerated buckling (i.e. buckling failure) was observed. For clarity, Figure 105 shows one of the actuators in the first set of pressurized buckling experiments experiencing accelerated buckling. Any actuator that failed during the experiment (leaking, slipping, etc) was omitted and rebuilt until the tests could be completed without failure.

Figure 105: Pressurized accelerated buckling failure

Once the initial and accelerated buckling force data for the six actuators was collected, two additional constrained buckling tests were performed to determine if a burrow-like environment that constrained the buckling behavior/geometry could be used to generate larger forces without experiencing buckling failure. The two most slender actuators (Actuator 1C and Actuator 2C) were placed concentrically inside a clear polycarbonate tube with an inside diameter ~20 mm larger than the outside diameter of the respective actuators. A similar ramped pressure was applied to these actuators and the buckling behavior was recorded with a camera. As the actuators buckled, the rigid clear tube walls constrained the buckling behavior and allowed the actuator to continue generating extension forces. Pressure was increased until buckling, mechanical

failure, or bursting was observed. The maximum extension force and pressure were recorded. Figure 106 shows an example of an actuator being tested in the constrained environment.

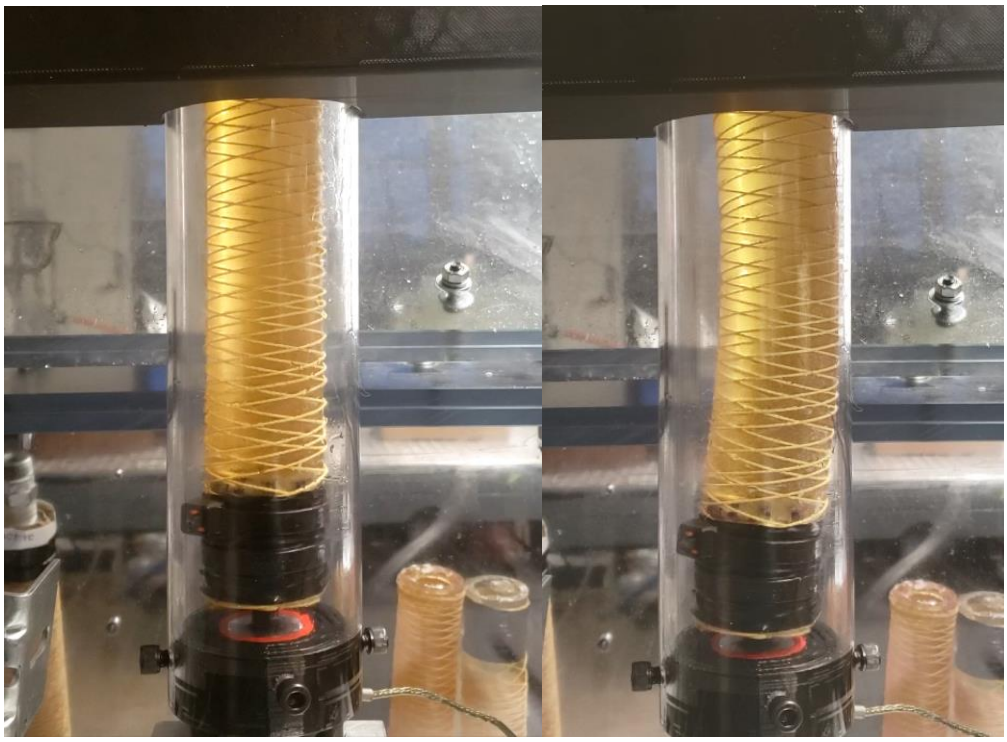

Figure 106: Constrained buckling experiment (left: no pressure, right: pressurized in tube)

Once all the pressurized buckling experiments were completed, the zip ties were cut off the actuators and the segment connectors were removed from the actuator leaving just the fiber-wrapped elastomer. The six actuators were then placed in the external load experimental apparatus to be loaded in compression with an externally applied force instead of being powered by pressurized hydraulic fluid. 3D printed fittings were used to hold each end of the

elastomer tube. The aluminum segment connectors from the pressurized experiments were 38.1 mm long, so the 3D printed elastomer holders were designed to hold a 38.1 mm length of the elastomer to replicate the end-conditions in the pressurized experiments. The hydraulic press was used to slowly generate compressive force, and a camera was used to observe the elastomer behavior. The compression test continued until buckling or compressive failure was observed. Camera footage was reviewed and the maximum force before failure was recorded from the load cell data. To verify that the six actuators were not compromised from previous experiments or fatigue, a new set of six elastomers were fabricated with the same geometry as the first six. These elastomers, without the fiber wraps, were tested in the same way as the original six elastomers.

3.3 **Results and Discussion**

The comprehensive results from the buckling study are shown in Figure 107. Each of the six actuators are listed across the horizontal axis with their slenderness ratios shown. For each actuator, the grey (1^{st}) bar represents the Euler model critical buckling force, and the yellow (2^{nd}) bar represents the compressive yielding model critical force. The orange (3^{rd}) bar represents the experimental force observed to cause buckling. The blue (4^{th}) and green (5^{th}) bars represent the external loads needed to cause compressive buckling failure for the original tubes and the new tubes respectively. The following sections will

be referring to the data shown in Figure 107. Note that the Gent model was used to select the modulus of elasticity for the buckling analysis.

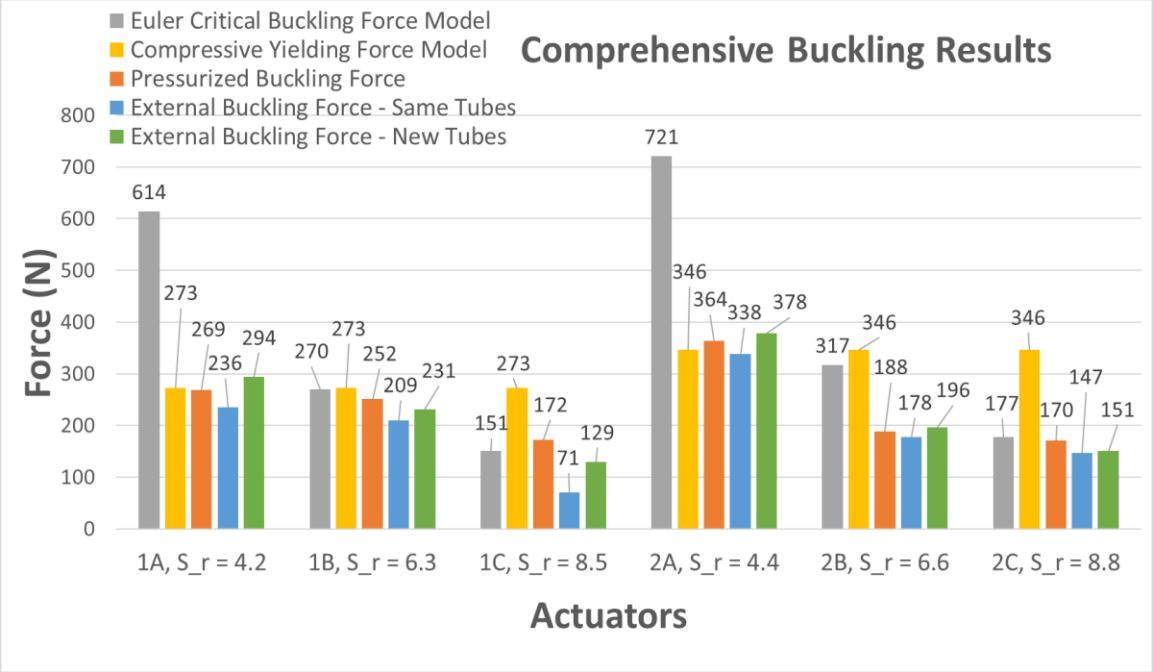

Figure 107: Comprehensive buckling results

3.3.1 Pressurized Buckling Results and Discussion

First, the six actuators were actuated under pressure at a fixed length to determine the maximum load that caused buckling failure. The orange (middle) bar on the graph shown in Figure 107 represents the extension force generated by the six actuators to cause buckling failure when actuated by pressurized hydraulic fluid. The extension force to cause buckling was always the peak force observed and was identified by using video camera footage and pressure and force versus time plots. Figure 108 shows the pressure and force versus time data for the buckling experiments for Actuator 1B as well as images of the

actuator over the time-frame. This plot demonstrates how the pressurized buckling experiments were conducted and how key data points were extracted.

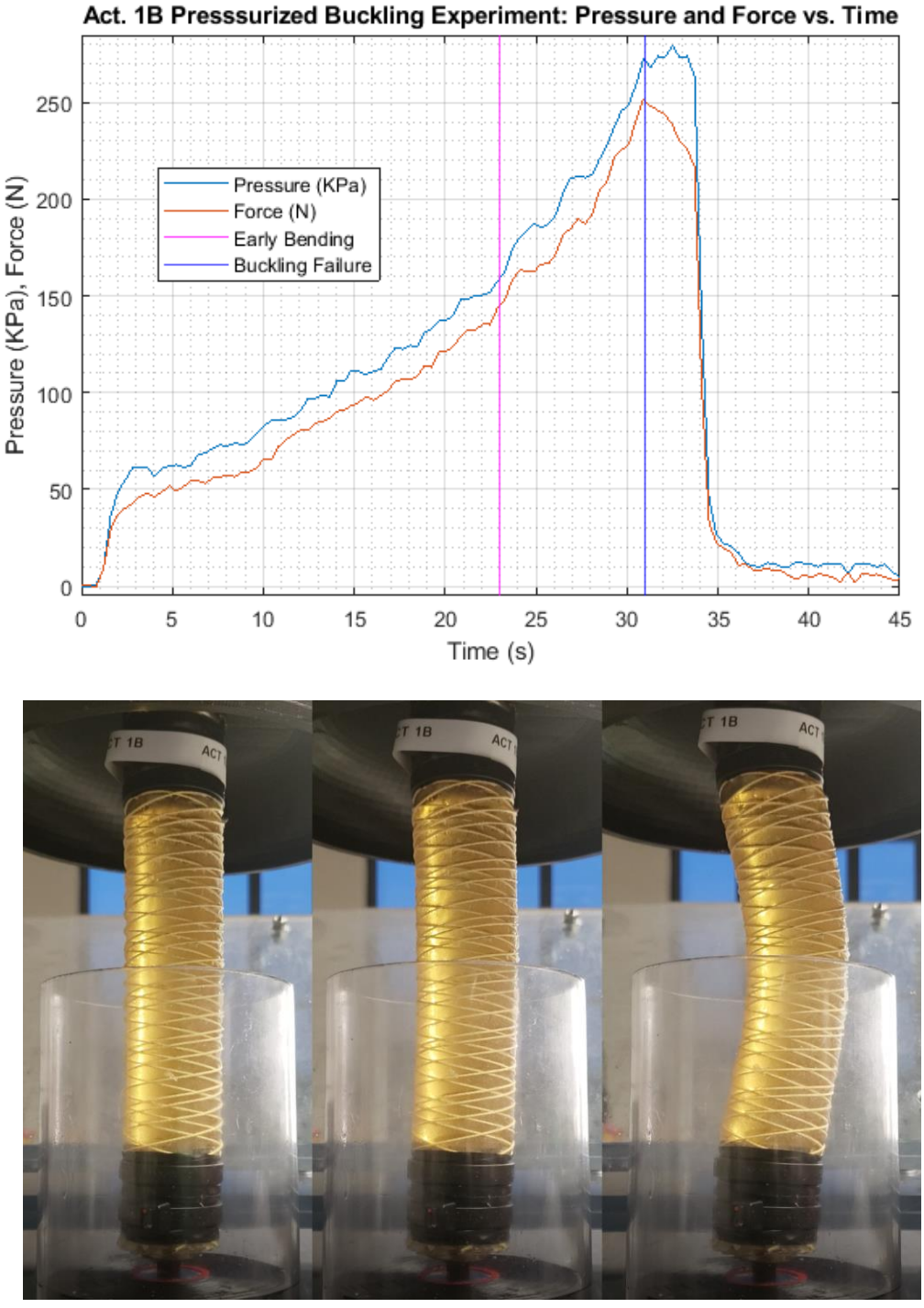

Figure 108: Pressure and force versus time with key buckling behavior shown (left: t = 0 s, middle: t = 23 s, right: t = 31 s)

The gray (furthest left) bar on the bar graph in Figure 107 represents the predicted buckling force based on Euler-Johnson column buckling models outlined earlier in this chapter. The pressurized buckling force was limited by the predicted Euler critical buckling force except for Actuator 1C which was very close. The less slender actuators were not able to get as close to the predicted Euler critical buckling force because they first experienced compressive material failure, which will be discussed in the next section.

3.3.2 Compressive Yielding Failure Results and Discussion

Compression tests were performed on short lengths of elastomer to determine the force needed to cause compressive yielding of the polyurethane cross-section to help disseminate between buckling and compressive material failure. The two least-slender actuators in the pressurized buckling experiments failed at much lower forces than Euler's column buckling theory predicted. An investigation of the compressive yield strength showed that these actuators failed due to compressive yielding before buckling. When a column is loaded in compression, it will fail from buckling once it reaches the Euler-Johnson critical buckling load or it will experience compressive material yielding once the material experiences stresses larger than its compressive strength – whichever happens first. More slender actuators are more likely to reach the Euler-Johnson critical buckling load and buckle before compressive yielding is observed, whereas less slender actuators have larger critical buckling loads causing compressive yielding failure to be more prevalent. When a column buckles, the deformed geometry is

predictable, but when a column experiences compressive yielding, the resulting deformed geometry may vary trial-to-trial.

To further investigate the difference between compressive failure and buckling failure for actuators with a low slenderness ratio, Actuator 1A's elastomer was first tested at 100.1 mm long (measured as the visible length between the 3D printed tube holders shown in Figure 104), and an increasing external load was applied until failure was observed. The actuator length was then reduced to 74.7 mm long and tested again. The actuator was cut down one more time to 49.3 mm long and an external load was again applied until failure was observed. Camera footage was used, and the compressive failure force was recorded. The type of deformation observed was not buckling deformation, but rather kinking, bowing, and bulging representative of a compressive material failure. Figure 109 shows the elastomer failing due to compressive material failure (instead of buckling).

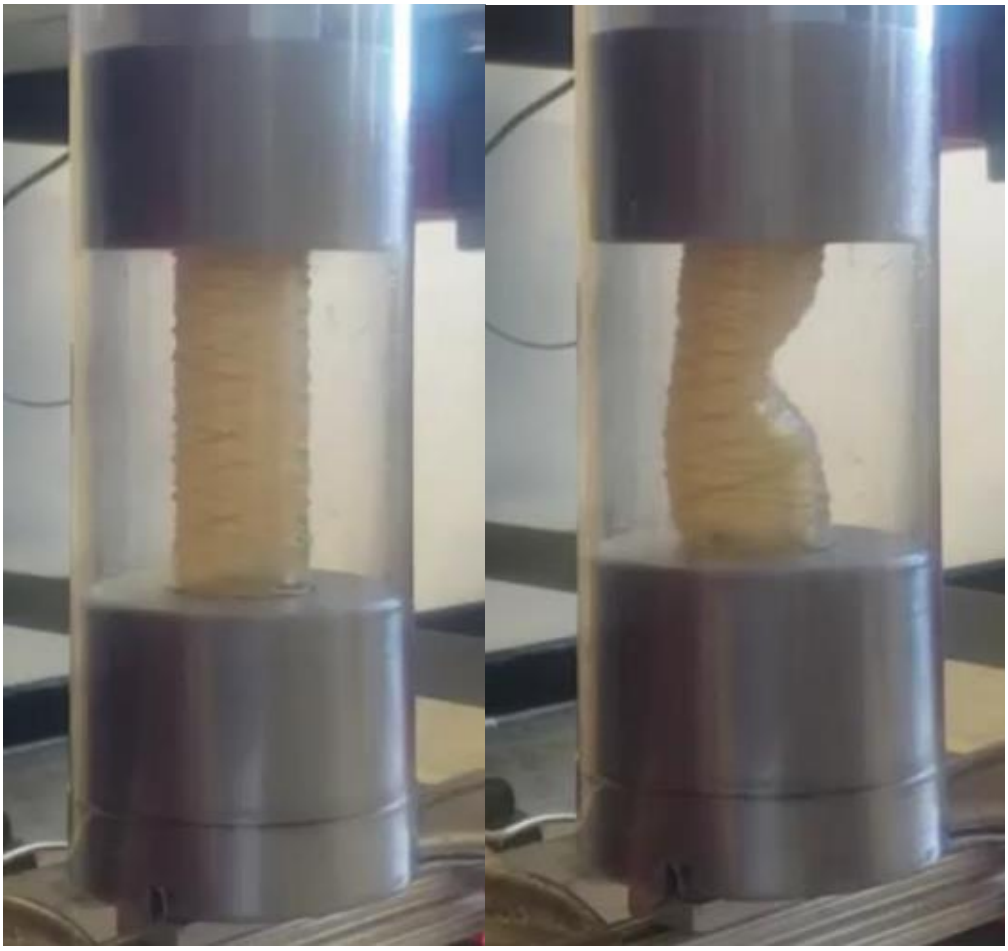

Figure 109: Compressive material failure

All three of the actuator segments failed at approximately the same force when loaded in compression which validates why the less slender actuators from the previous experiments were unable to reach the predicted Euler-Johnson buckling force in some cases for the less slender actuators. The results of the three compression tests compared to the predicted Euler-Johnson column buckling theory is shown in Figure 110.

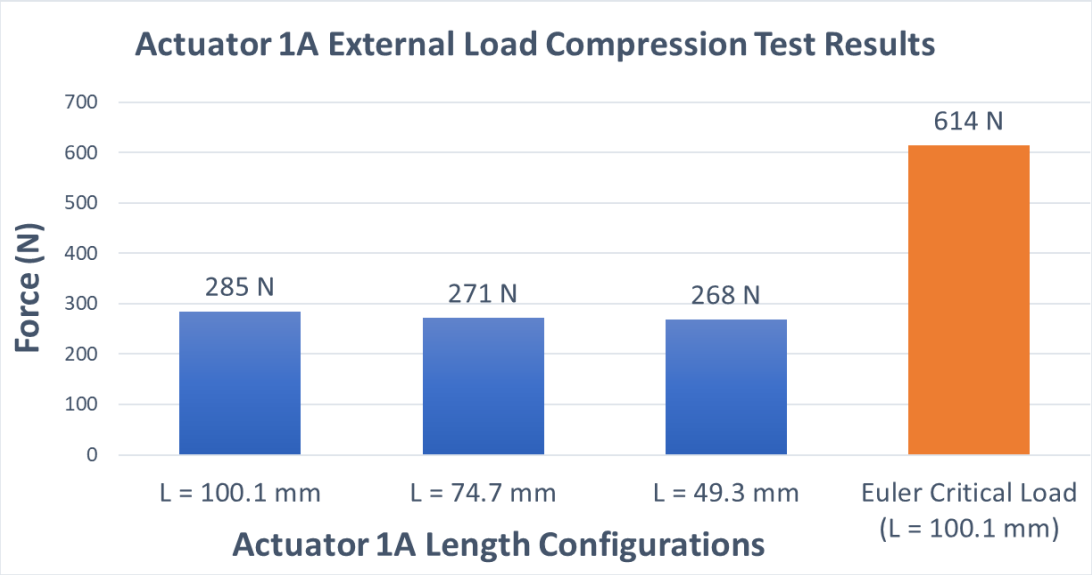

Figure 110: Actuator 1A external load compression test results

Note that Actuator 1A failed at 269 N in the pressurized experiments, and the mean value of the three failure forces just presented was 274.6 N. This indicates that Actuator 1A failed from compressive yielding in the pressurized experiments – not buckling. Dividing the mean value of the three failure forces by the cross-sectional area of the elastomer allows for the calculation of the compressive strength of the material which can then be used to calculate a predicted compressive failure force for elastomers of any geometry. The compressive strength of the Polytek74-55 polyurethane elastomer material was calculated to be 0.55 MPa. The yellow (second from the left) bar on the graph shown in Figure 107 represents the predicted force to cause the actuator to experience compressive material failure based on the compressive strength experiments just discussed and in Figure 110 above. It can be observed that the compressive yielding critical load limited the amount of compressive force some of the actuators could withstand instead of the Euler-Johnson critical buckling

force. Five of the six actuators were limited by either the compressive yielding critical load or the Euler-Johnson critical buckling load suggesting that McKibben actuators can be modeled using traditional buckling analyses. Actuator 2B was an outlier, and the source of error is thought to be in asymmetric wall thickness of the elastomer (due to the mold) or pre-existing damage to the elastomer.

3.3.3 Constrained Pressurized Buckling Results and Discussion

The two most slender actuators were actuated while constrained in a concentric tube that emulates a burrow to determine if forces beyond Euler-Johnson buckling limits can be reached in a burrow-like environment. Actuators 1C and 2C were the slenderest actuators and were selected to be tested in a constrained environment that prevented the actuators from completely buckling as input pressure was increased. The purpose of this experiment was to determine whether a burrow-like environment could be used to mitigate buckling failure and allow the actuator to generate larger extension forces. The largest forces observed in the two constrained experiments before the actuators began leaking at the segment connectors are shown in Figure 111.

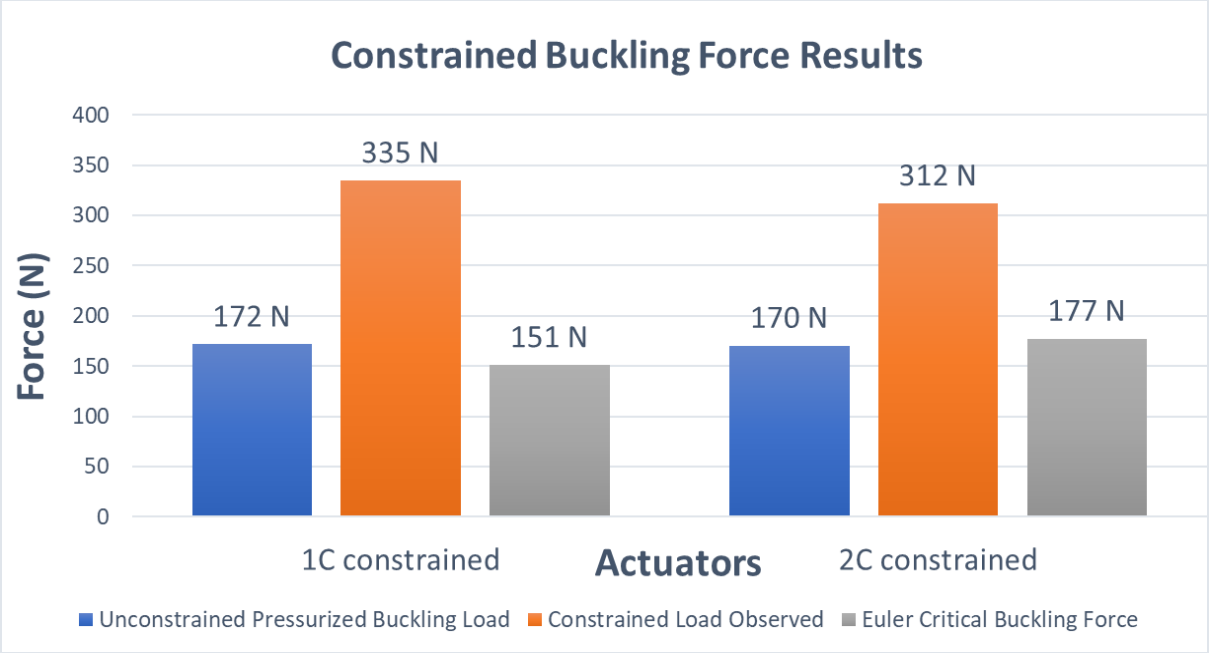

Figure 111: Constrained buckling force results

As can be observed, the actuators were able to exceed the Euler-John column buckling critical force in both experiments as well as the pressurized buckling force observed in the earlier experiments. Both actuators began to leak at the segment connectors when the maximum load was observed due to the elastomer being pulled out from under the zip-ties, but it is expected that with a more robust segment connector design, even larger extension forces could be generated. As both actuators were pressurized, they would begin bending until they came in contact with the constraining polycarbonate tube wall. As actuator pressure increased, the contact patch between the elastomer and tube wall increased – effectively splitting the actuator into two identical eccentrically loaded columns that are axially-shrinking with increasing pressure. Figure 112 depicts the lines of symmetry, the wall contact patch, the location of burst failure, and the

outline of one of the eccentrically loaded columns of a pressurized actuator in the constrained buckling experiments.

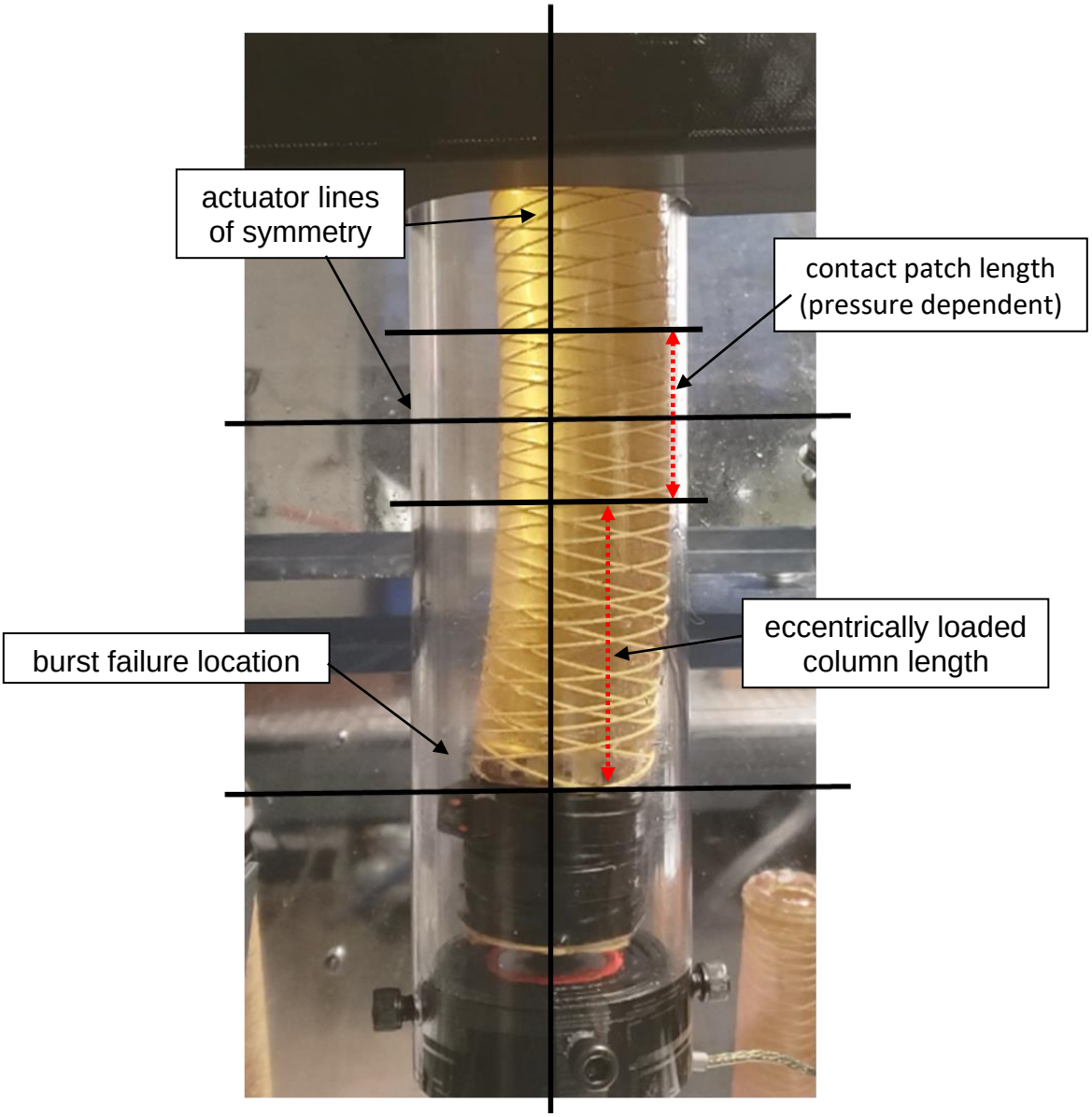

Figure 112: Pressurized actuator in constrained environment

Because the lateral deflection of the actuator is limited by the polycarbonate tube in the constrained environment, the actuator can better resist buckling failure than when operating in an unconstrained environment. The

additional force capability of the actuator due to the constrained environment could be quantified by first developing an understanding of the contact patch area between the polycarbonate tube and the elastomer as a function of the pressure and the diameter of the constraining tube. This would then allow the system to be modeled as two eccentrically loaded columns with input pressure dependent length and geometry – which empirical data shows can support larger forces than in an unconstrained environment. These experiments suggest that there may be a suitable relationship between soft extending McKibben actuators and burrow-like environments and similar applications for providing case-specific forces without buckling given that it is have shown that a constrained environment allows larger extension forces to be generated in the McKibben actuator. Additional modeling and experiments are needed to quantify the additional force capabilities of extending actuators in a constrained environment as both buckling and compressive yielding failure may impact the performance of the actuators.

3.3.4 External Load Buckling Results and Discussion

Elastomer tubes were compression tested with a hydraulic press and custom fixture to determine if buckling behavior from an external load is the same as when the actuator is pressurized. When an extending McKibben actuator is pressurized, it generates extension force and is loaded in compression. If the compressive force is large enough, buckling behavior may be observed. However, if the actuator is not pressurized, an external load could be applied to

the actuator that could induce buckling without extension forces being generated by the actuator. Experiments to validate that buckling behavior caused by an external load on an extending McKibben actuator is the same as buckling behavior caused by internal pressure were conducted.

First, the six elastomers that were used in the pressurized buckling experiments were loaded in compression using the hydraulic press experimental apparatus (with no internal pressure in the elastomers). 3D printed tube holders were used to ensure that the effective length of the experiments was the same as the original pressurized buckling experiments and that fixed-fixed end conditions were maintained. The blue (fourth from left) bar in the graph shown in Figure 107 represents the force required to cause the elastomer to fail. It can be observed in Figure 107 that the elastomers failed at slightly lower forces than in the initial pressurized buckling experiments. The assumption is that the elastomers were compromised from the previous buckling experiments.

To confirm the suspicion that the elastomers had been compromised by the previous experiments, an additional set of elastomers with the same geometry were manufactured and tested under the same conditions. The green (far right) bar in the graph shown in Figure 107 represents the force required to fail the new elastomers with the same geometry (build in the same molds). It can be observed that in all six cases, the new elastomer was able to withstand greater compressive forces before failure than the compromised tubes previously

used in experiments and subjected to many tests. The slenderer tubes were limited by the Euler-Johnson column buckling critical load and the less slender tubes were limited by the compressive yielding critical load. The results from the external load buckling tests demonstrate the importance of further investigating the impact of prior failure on buckling behavior in soft robots, but it also shows that there is no demonstrable difference in buckling mechanics of extending McKibben actuators whether driven with an internal pressure or acted upon by an external force.

3.4 **Conclusion and Summary**

A general review of traditional Euler-Johnson column buckling theory was presented, and six actuators of varying slenderness ratios were fabricated to assess whether the extending McKibben actuator follows traditional buckling theory. The six actuators were tested in an unconstrained environment to assess their buckling limit, and the two most slender actuators were tested in a constrained environment to determine if forces beyond the Euler-Johnson column buckling critical load could be achieved. The elastomer tubes were further tested by applying an external load to generate failure to determine if there were any differences in buckling behavior with or without the pressurized fluid normally used to drive the actuators. Finally, tests to determine the maximum compressive load of each actuator cross-section were conducted to determine where the actuators are expected to fail from compressive yielding instead of buckling.

The results from the pressurized buckling experiments demonstrate that the maximum compressive force that can be achieved by an extending McKibben actuator is limited by either compressive yielding or the Euler-Johnson critical buckling load – whichever is reached first. The only outlier in the data was Actuator 2B. Actuator 2B failed before reaching the compressive force or predicted buckling limits, and this is thought to be from elastomer irregularities (inconsistent wall thickness) caused by damage to the mold that was used to cast the elastomer or inconsistencies with the injection process. Note that Actuator 2B was the last actuator tested because a failure occurred in early experiments, and the actuator had to be rebuilt and retested at the end of the experiments. It was also found that the denser fiber weave of Actuator 1C (sixteen fibers vs eight fibers) did not appear to make any impact on the buckling behavior observed. The results from these experiments provide the validation that extending McKibben actuators do follow traditional buckling theory, and these models can be used for design applications like those that may be observed in a burrowing environment to move a multi-segment system along. Furthermore, it was demonstrated that by constraining the diameter of the environment (i.e. buckling in a burrow), buckling deformation can be mitigated and forces larger than the Euler-Johnson column buckling critical load can be generated by an extending McKibben actuator. A preliminary frame-work for quantifying the additional force capabilities of extending McKibben actuators in a

constrained environment was presented, but additional modeling and experimental work is needed to validate the approach.

3.5 Specific Contributions of the Chapter

- Experimental confirmation that extending McKibben actuators follow traditional column buckling mechanics

- Experimental confirmation that fiber-wrapped McKibben actuators follow the same buckling behavior when buckling from compression forces developed due to internal pressure actuation as from compression forces from an external source applied to the actuator

- Experimental validation that extending McKibben actuators can develop extension forces beyond the Euler-Johnson column buckling critical load when constrained environment like a burrow

- Preliminary frame-work for treating a pressurized extending McKibben actuator in a constrained environment as two eccentrically loaded columns that axially shorten as the contact length between the actuator and the environment grows

- Experimental validation of the compressive yielding failure - which may be the most common failure mode for actuator sizes that will be used in burrowing robots

Chapter 4: Anchoring (Traction) Actuators

Soft robots are flexible and compliant actuators that have many applications in confined environments such as tubes, pipes, or burrows. Soft expanding actuators that can generate large radial forces that anchor the segment in a tubular environment are needed for the development of the proposed multi-segment burrowing robot. These anchoring actuators, commonly referred to as traction actuators or traction segments in this thesis, may be combined in a multi-segment soft robot system to anchor the system and balance the axial forces that are being generated to move the robot along the burrow or penetrate into the soil. This type of actuator may also be useful in smaller scale applications and devices such as hand-held tools with space constraints that require large forces. A low force application of a radially expanding soft robot can be seen in the medical field with balloon angioplasty, where material in a constricted artery is compressed by the actuator as the balloon expands the blood vessel to increase blood flow [141].

This chapter aims to develop the designs, techniques, and associated models for creating anchoring segments for generating traction forces for a soft burrowing robot as it penetrates into a substrate or moves along an existing burrow. The actuators must provide enough traction force to balance the reaction forces developed when the system is moving forward through the burrow or penetrating into the soil. Furthermore, the actuator must only expand radially

(without any axial displacement) to prevent axially dislodging the robot system during actuation. Purely radial deformation is important in burrowing applications where the soil must be plastically deformed without caving in on itself. Many radially deforming soft robot actuators that exist in the literature produce simultaneous radial and axial displacement. This leads to slipping in the environment (tube) to occur. The following is a review of relevant soft actuators that produce traction forces in literature.

McDonald et al. studied how helically deforming soft segments generate traction forces in a tubular environment like the vasculature of a human being [142]. Helically deforming traction segments provide the advantage of allowing blood flow through the artery through the center of the spiral, but helical traction segments are limited in how much traction force can be developed. Furthermore, the traction force developed by the helical segments is not proportional to input pressure and depends on the axial displacement of the segment. While these types of spiral segments show merit in low-force applications like surgical robotics where maintained blood flow is critical, they provide less of a benefit to applications like burrowing where axial displacement of the traction segments is undesirable and large traction forces are paramount. Figure 113 shows the helically deforming traction segments developed in these experiments.

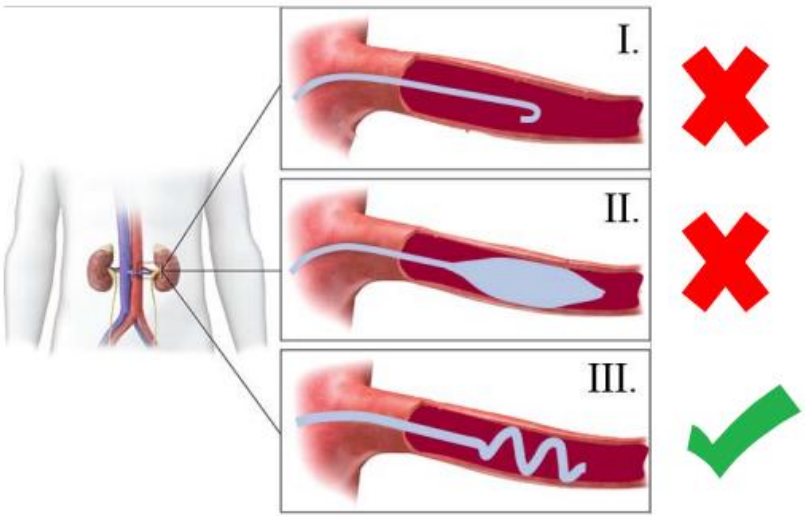

Figure 113: I) Curved end anchoring, II) balloon anchoring, III) helical anchoring [142]

Kamata et al. developed a pneumatic earthworm robot for pipe inspection and utilized a straight-fiber expanding soft segment to develop the necessary traction forces to move the robot through a pipe [124]. Straight fibers were places longitudinally along an elastomer segment, and when the segment was pressurized, it would expand radially and contract axially as shown in Figure 114. This segment design results in slipping in a tube due to the simultaneous displacement of the actuator in the axial and radial directions.

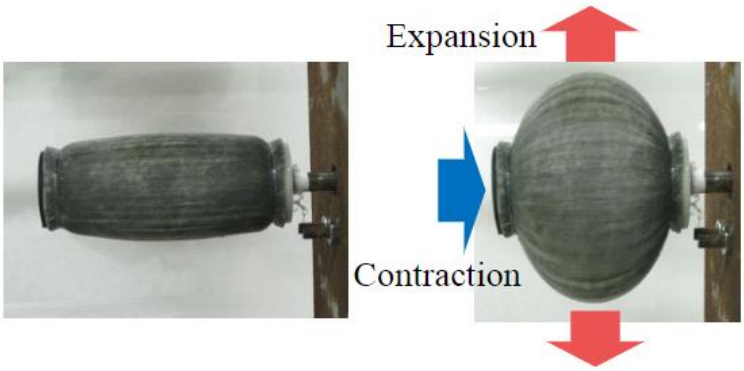

Figure 114: Expanding unit design with straight fibers causing simultaneous expansion and contraction [124]

Hammond III et al. developed a modified version of the pneumatic McKibben actuator that is equipped with radial sensors that enable position and force sensing of the actuator [70]. FEM studies were performed to model the overall deformation of the actuator as it was pressurized, because models that account for the rigid segment connectors are not readily available in literature. This modeling approach was shown effective for determining the deformation of the simultaneously axially contracting and radially expanding soft segment, which demonstrates how FEA may be used to study similar traction force generating segments. Figure 115 show the study results.

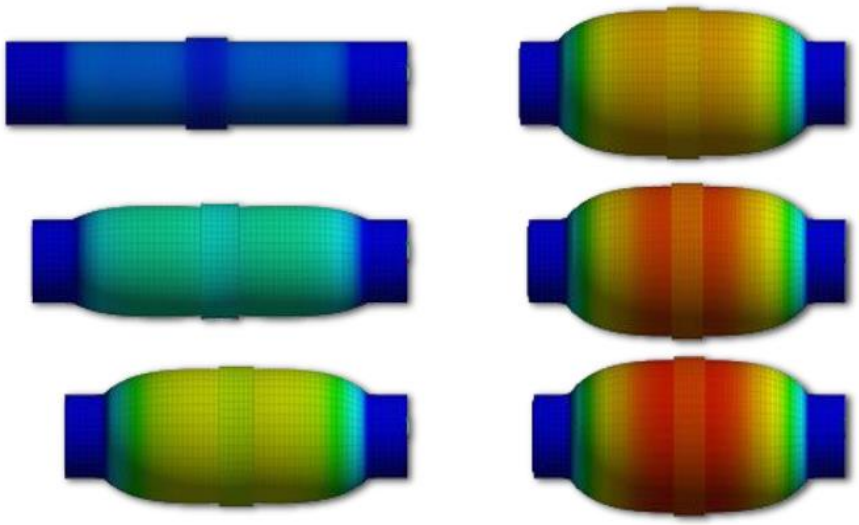

Figure 115: Pneumatic soft segment FEA deformation study (0-55.2 kPa) [70]

Liu et al. utilized high-traction Kirigami skin to generate more friction in an expanding traction actuator [127]. Silicone Kirigami skin was molded and adhered to the exterior of a contracting McKibben actuator to simulate the behavior of bristles on an earthworm as it moves through a burrow. The expanding segment was used to provide anchoring forces in garden soil, and the Kirigami skin was shown to increase generated traction forces. While the Kirigami skin method is beneficial for increasing traction forces, the segment displaces in both the axial and radial directions when actuated as shown in Figure 116.

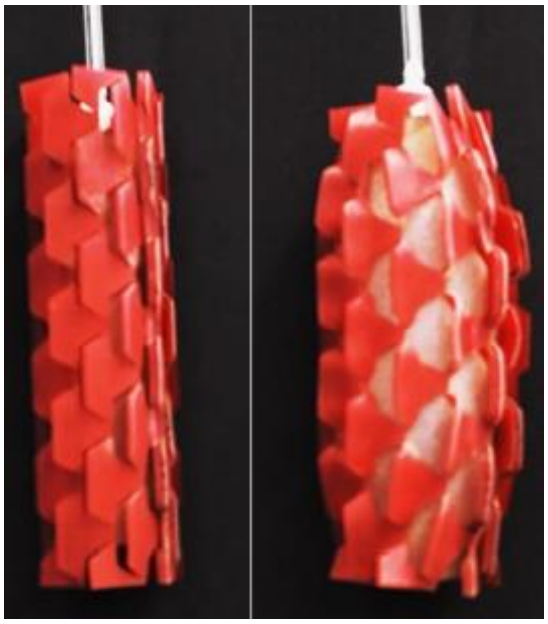

Figure 116: Kirigami skin applied to radially expanding, axially contracting McKibben actuator to improve traction force generation [127]

All these traction segment design concepts produce simultaneous displacement in the axial and radial directions which may result in some slipping in a burrowing application that utilizes alternating anchor locomotion like the multi-segment proposed system. Multiple traction force actuator designs that prevent axial slipping were investigated in this chapter, and a final actuator design was selected based on ease of manufacturing and model validation. The actuator design requirements and selection process will also be discussed in this chapter. The final actuator design consisted of a constant wall thickness elastomer clamped down to two aluminum segment connectors with zip-ties. A threaded rod was connected each segment connector to prevent axial displacement of the elastomer when pressurized (only radial expansion). However, in future designs, an inextensible cable or rope could be used to allow

the robot lateral flexibility for turning and steering while still preventing axial displacement. Because this actuator deforms in an exclusively radial manner, the actuator can generate prescribed radial forces inside a tube or burrow, and therefore prescribed traction/friction forces, without generating axial movement that might dislodge the anchoring segment.

In the absence of an explicit traction force model for a fixed length, radially expanding soft actuator in literature, a new model is developed by the author to predict the traction force capabilities of the design over a range of burrow diameters. The model is based only on initial actuator geometry, desired final actuator geometry, and operating pressure. Six actuators, consisting of three different outside diameters and two different lengths, were fabricated to experimentally assess the validity of the traction force model and overall functionality of the anchoring traction actuator. The actuators were tested at various pressures in various diameter polycarbonate tubes to determine the amount of pull-out force (‘traction force’) needed to dislodge the actuators from the polycarbonate tubes. The experimental results were compared to the predicted results from the new traction force model.

4.1 **Actuator Design**

Many soft actuator designs were examined to assess their efficacy as potential traction segments that can provide traction and anchoring forces within a burrow. The traction segments must be designed in a way that they are only

able to produce radial expansion while maintaining a constant axial length. Multiple designs were developed and assessed, and the simplest design was experimentally tested due to ease of manufacturing and model validation. Early traction segment designs will first be presented followed by an overview of the selected traction actuator design for experiments.

4.1.1 Early Designs

The first design that was explored was a loose fiber sleeve modified McKibben actuator. Because axial displacement is not needed for traction segments (and possibly detrimental with respect to burrowing locomotion), unique challenges are presented for using the McKibben actuator as a traction segment due to its inherent linear actuation mode. The actuator consisted of an elastomer and off-the-shelf aramid fiber sleeve crimped on each end of the actuator with off-the-shelf hydraulic fittings. The fiber sleeve length was much longer than the initial actuator length so that it be loose against the actuator and would allow for prescribed radial elastomer expansion when actuated. The fiber sleeve also prevents the elastomer from bursting axially when radially expanded at high pressures within a tubular environment. The actuator also utilized a concentrically located stiff threaded rod that held the two segment connectors together to maintain the constant axially length of the actuator during actuation. Literature shows that strain limiting members have been used in the soft robotics field, but they have only been used by embedding them in the elastomer or against the elastomer to generate bending of the actuator [143]. No centrally

aligned member has been used to prevent all axial displacement of the actuator to generate exclusively radial deformation of the actuator. Some other groups have developed soft robotic actuators that utilize strain limiting members, however, all those applications involve bending actuators, and the strain limiting rod is not centrally aligned [144]. Figure 117 shows the loose fiber sleeve concept, and Figure 118 shows an image of the loose sleeve modified McKibben actuator for generating anchoring forces in a tube-like environment.

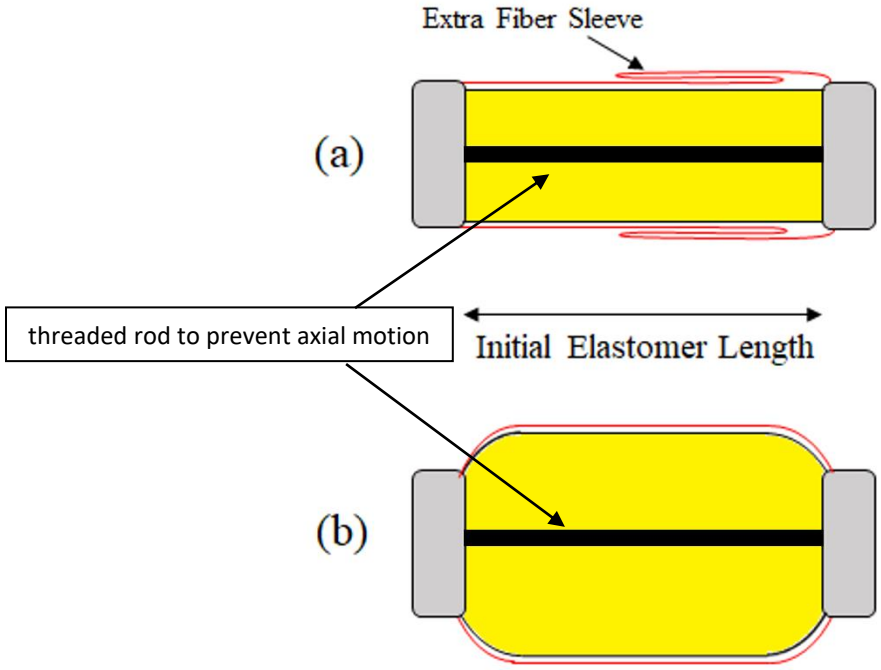

Figure 117: (a) Modified McKibben actuator with extra fiber sleeve before pressurization, (b) expanded modified McKibben actuator without axial displacement

Figure 118: Modified McKibben actuator with loose fiber sleeve and internal threaded rod

Some of the issues with the loose sleeve modified McKibben actuator design include that the fibers are not well protected from the environment, but more importantly, the loose fiber sleeve is unable to return to its original shape after an actuation cycle. Furthermore, while axial blowout failure of the elastomer is prevented, the fiber sleeve limits the actuator's maximum range of achievable expansion diameters. Because the expansion range is limited and not proportional to input pressure once the sleeve has expanded, the amount of traction force that can be generated is also limited. Early experiments were conducted, but the design was abandoned due to the actuator's inability to easily perform repetitive tests.

An alternative traction segment design utilized two elastomeric tubes separated by a fiber wrapped section. The manufacturing process utilized calcium-chloride, which when mixed with water at a specific concentration, solidifies at room temperature. The calcium chloride solution was injected to expand a cured elastomer to a desired diameter and allowed to cool and solidify. With the calcium chloride solidified, the expanded elastomer was rigid, allowing fibers to be accurately applied in forward and reverse directions at the kinematic

lock angle of 54.7 degrees. Once fibers were applied, another polyurethane layer was injected over the top to cover the original elastomer and applied fibers. Once the outer polyurethane elastomer layer cured, the calcium chloride was heated and drained out of the elastomer to release the stress in the elastomer. The idea was to replace the loose sleeve modified McKibben design with an elastomer-embedded fiber sleeve that was able to elastically return to its original position after an actuation cycle. Figure 119 shows the resulting dual elastomer layer traction segment.

Figure 119: Dual elastomer layer CaCl expanded traction segment

After many attempts, this design was abandoned due to insufficient bonding between the inner and outer elastomer layers. When the calcium chloride was removed and the elastomer was relaxed, the different stress levels between the two elastomer layers caused certain parts of the actuator elastomer layers to delaminate at the interface where the fibers were applied. This traction segment design approach shows promise for developing the ability to build multiple compartment robots with multiple user-controlled geometry elastomer

layers, but more research is needed to develop the appropriate manufacturing processes to produce robust and reliable actuators with this method.

The final abandoned traction segment design approach was first identified due to the observation that when soft robots experience blow-out failure from internal pressure, they tend to fail near the segment connectors. When blow out failure occurs, it typically occurs near the segment connectors due to a non-uniform stress profile caused by stress concentrators as shown in Figure 120.

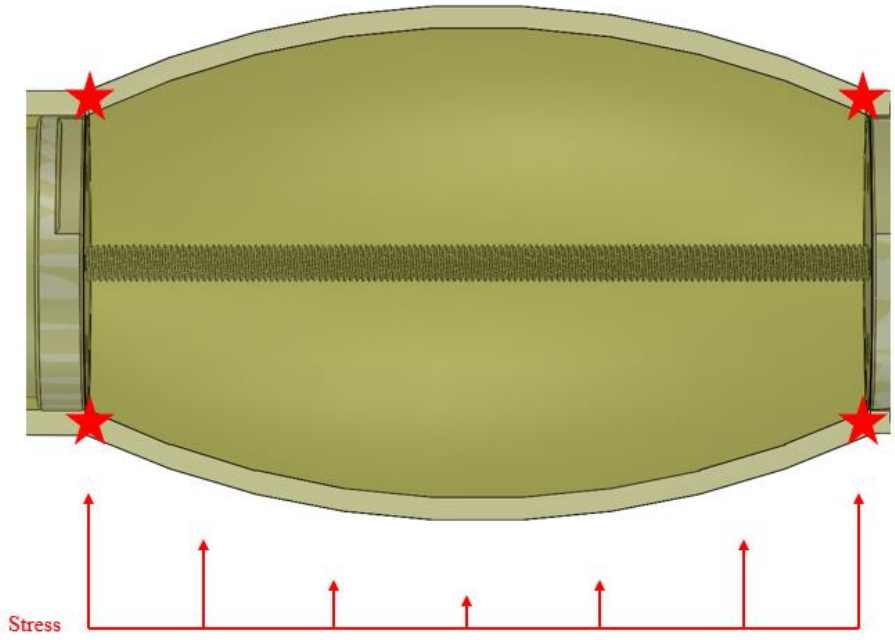

Figure 120: Common issue of blow out failure (red stars) occurring near segment connectors due to non-uniform stress profile caused by stress concentration

The proposed traction actuator would feature a design that consisted of a variable wall thickness elastomer that, when pressurized and in an expanded

state, has a near constant stress profile throughout the elastomer. By determining the initial geometry of the elastomer that is needed to provide a constant stress profile in the pressurized/expanded state, failure of the elastomer near the segment connectors can be prevented through intelligent design. The value of this design is in the ability to pre-determine the necessary geometry of the wall thickness to prevent failure near the segment connectors due to stress concentrators. Figure 121 shows the initial, undeformed state of a proposed variable wall thickness geometry traction segment design that could mitigate the deleterious effects inherently induced from the stress concentration near the segment connectors.

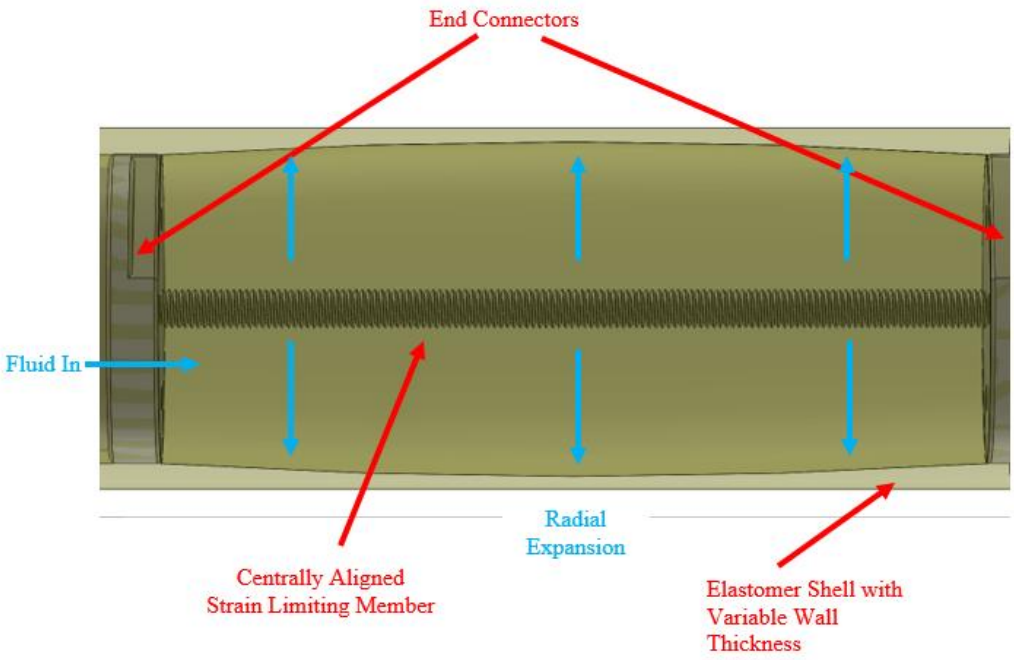

Figure 121: Relaxed, variable wall thickness traction segment initial geometry

This design method required both analytical and FEA modeling techniques to be employed to develop a model that could predict the deformed geometry of

the elastomer near the segment connectors. Early attempts to develop these modeling approaches were abandoned due to time constraints, and a constant wall thickness traction actuator design was selected for experimentation.

4.1.2 Selected Design

The final selected traction segment design consisted of a constant wall thickness elastomer, two aluminum segment connectors, hydraulic fittings, low profile zip ties, and a steel threaded rod to hold the segment connectors together. This simple design was selected because it allowed for clear experimental validation of the traction force model that will be discussed in section 4.2. Furthermore, the previously discussed traction segment design concepts require further development for practical experimental use. Low profile zip ties were utilized to allow for testing the actuators in tubes sizes only slightly larger than the actuator outside diameters (larger zip ties will contact and interfere with the tube wall). Figure 122 and Figure 123 show the segment connectors, elastomers, hydraulic fittings, electrical tape, threaded rod, and zip ties for the selected design. The specific details of the selected designs, along with the fabrication processes, will be discussed in section 4.3.1.

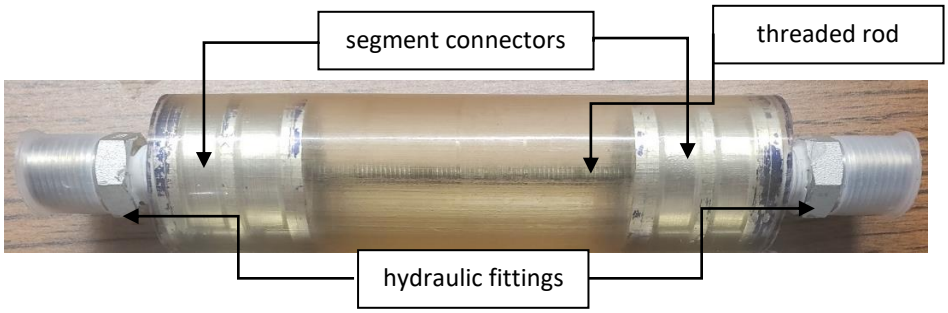

Figure 122: Traction actuator

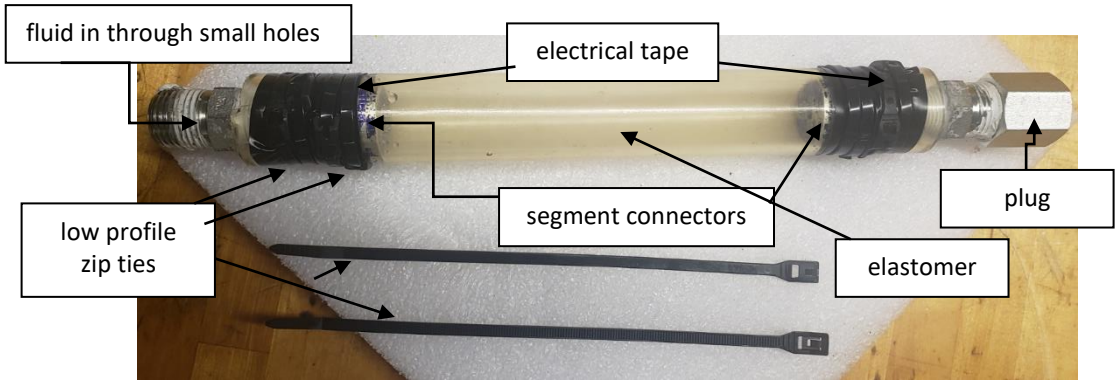

Figure 123: Traction actuator with low profile zip ties and electrical tape shown (no threaded rod shown here)

4.2 **Modeling**

There are no explicit models in current literature that predict that anchoring force capabilities of axially static length, radially expanding soft robotic actuators in an environment like a burrow. Therefore, a traction force model that predicts the amount of pull-out force needed to dislodge the pressurized traction actuator from a rigid tube was developed by the author. The model assumes an incompressible elastomer and treats the system as a thin-walled, cylindrical pressure vessel with a constant Young's modulus (no creep). The model

assumes that the actuator expands perfectly cylindrically all the way to the segment connectors, and it assumes a constant pressure distribution of the tube wall. Furthermore, the model assumes a constant coefficient of friction between the traction actuator and the environment. Losses and hysteresis are also ignored.

Because the segment connectors and internal threaded rod keep the actuator length constrained as internal pressure is applied, axial stress on the thin-walled, cylindrical pressure vessel can be ignored. So, the principal stress left on the actuator is the hoop stress, given by

$$\sigma_1 = \frac{P_{elastic}\, r_t}{t} \tag{4.1}$$

where $P_{elastic}$ is the internal pressure required to expand the actuator to a new radius r_t, and t is the expanded elastomer wall thickness. Assuming a constant-volume, isotropic elastomer material, stress on the actuator can be related to its strain through the definition of elastic modulus

$$\sigma = E\, \epsilon \tag{4.2}$$

where σ is stress, E is the elastomer's modulus of elasticity, and ε is the strain. Substituting this expression for σ into (4.1) and rearranging for $P_{elastic}$ yields the following equation:

$$P_{elastic} = \frac{E\, \epsilon\, t}{r_t}. \tag{4.3}$$

Since ε is calculated with the actuator's change in circumference divided by the original circumference,

$$\epsilon = \frac{2\pi r_t - 2\pi r_o}{2\pi r_o} = \frac{r_t - r_o}{r_o} \tag{4.4}$$

where r_o is the initial outer radius of the elastomer. Substituting this expression into (4.3) yields the following equation for $P_{elastic}$.

$$P_{elastic} = \frac{E\,(r_t - r_o)\,t}{r_t\,r_o} \tag{4.5}$$

Examining the changing thickness of the elastomer as it expands, the initial volume V_1 of the elastomer material is given by

$$V_1 = \pi\, r_o^2\, l - \pi (r_o - t_k)^2\, l \tag{4.6}$$

where l is the length of the actuator between fittings and t_k is the initial elastomer thickness. The final volume V_2 of the elastomer at its expanded radius is

$$V_2 = \pi\, r_t^2\, l - \pi (r_t - t)^2\, l \tag{4.7}$$

Since the elastomer is incompressible, the initial and final volume must be equal. Then, setting equations (4.6) and (4.7) equal and simplifying yields the following equation:

$$r_o^2 - (r_o - t_k)^2 = r_t^2 - (r_t - t)^2. \tag{4.8}$$

An expression must be obtained for t as a function of initial geometry and desired expanded radius to relate to $P_{elastic}$. So, expanding (4.8) and cancelling terms,

$$2\, r_o\, t_k - t_k^2 = 2\, r_t\, t - t^2 \tag{4.9}$$

To solve for t, the equation must be converted into quadratic form.

$$t^2 - 2\, r_t\, t + (2\, r_o\, t_k - t_k^2) = 0 \tag{4.10}$$

Solving using the quadratic formula and taking the negative root produces the final equation for the thickness of the expanded elastomer.

$$t = r_t - \sqrt{r_t^2 - t_k(2r_o - t_k)} \tag{4.11}$$

Once the actuator is expanded to its target radius against a tubular wall, the area of external wall that the actuator's pressure is being applied to is given as

$$A_{wall} = 2\,\pi\, r_t\, l_{eff} \tag{4.12}$$

where l_{eff} is the length of actuator in contact with an external wall. Since the pressure $P_{elastic}$ required to expand the elastomer to a target radius r_t is known, the net pressure applied to the area A_{wall} by the actuator is the difference between the input pressure P and $P_{elastic}$. The final model for the anchoring force radially applied by the actuator as a function of input pressure and initial and final actuator geometries can then be represented as

$$F_{anchoring} = 2\pi r_t\, l_{eff}\left(P - \frac{E\,t}{r_o\, r_t}(r_t - r_o)\right) \tag{4.13}$$

where t is defined in (4.11). For applications in which the actuator is expanded to withstand an axial load and prevent axial slipping, the traction force preventing slipping is given by multiplying (4.13) by the coefficient of static friction between the actuator and surface of contact.

$$F_{traction} = \mu_s\, F_{anchoring} \tag{4.14}$$

4.3 **Methods**

The new traction segment design presented by the author may be beneficial for providing anchoring forces in burrowing applications because it

does not generate axial displacement that can lead to slipping. The objective of the traction segment experiments is to validate the traction force model developed by the author to justify its use as a baseline tool for design and assess the experimental efficacy of the traction segment designs.

4.3.1 Actuator Design Parameters and Fabrication

A total of six actuators were fabricated for experimental testing. They consisted of three different diameters and two different lengths. The diameter ranges were selected to be similar in size (25-50 mm diameter) to what can be observed in irrigation installation and other common burrowing applications. The Polytek74-55A durometer elastomers were injected using the same port block methods described earlier in section 2.3.1. Low profile zip ties were used to secure the elastomer to the segment connectors with electrical tape acting as a barrier between the elastomer and the zip ties to prevent elastomer damage. The low-profile zip ties allowed for the actuator to be tested in smaller diameter tubes without the zip ties interfering. The geometry of the six actuators built for testing can be found in Table 12, and the six fabricated actuators can be observed in Figure 124.

Table 12: Traction actuator geometry for experiments

Actuator	Initial Length, L_o (mm)	Initial Outside Diameter, D_i (mm)	Wall Thickness, t_k (mm)
1A	84.1	31.8	3.2
1B	84.1	38.1	3.2
1C	84.1	44.5	3.2
2A	133.4	31.8	3.2
2B	133.4	38.1	3.2
2C	133.4	44.5	3.2

Figure 124: All traction actuators for experiments (top: shortest three actuators, bottom: longest three actuators – zip ties and electrical tape not applied)

The design of the slotted segment connectors in the traction segment experiments is the same as the segment connector design in the buckling actuator experiments in section 3.2.1. The only differences were that threaded holes were added to the segment connectors to allow the ¼-20 UNC threaded rod to hold the segment connectors together to prevent axial displacement, and four off-center through holes were drilled in the proximal segment connector to allow fluid flow into the actuator. The six actuators will be subjected to

pressurized pull-out tests inside a range of different diameter clear polycarbonate tubes over a range of pressures to determine the traction force capabilities of the actuators. Images of the proximal and distal segment connectors are shown in Figure 125 and Figure 126 respectively. The detailed geometry of the segment connectors can be found in Appendix I.

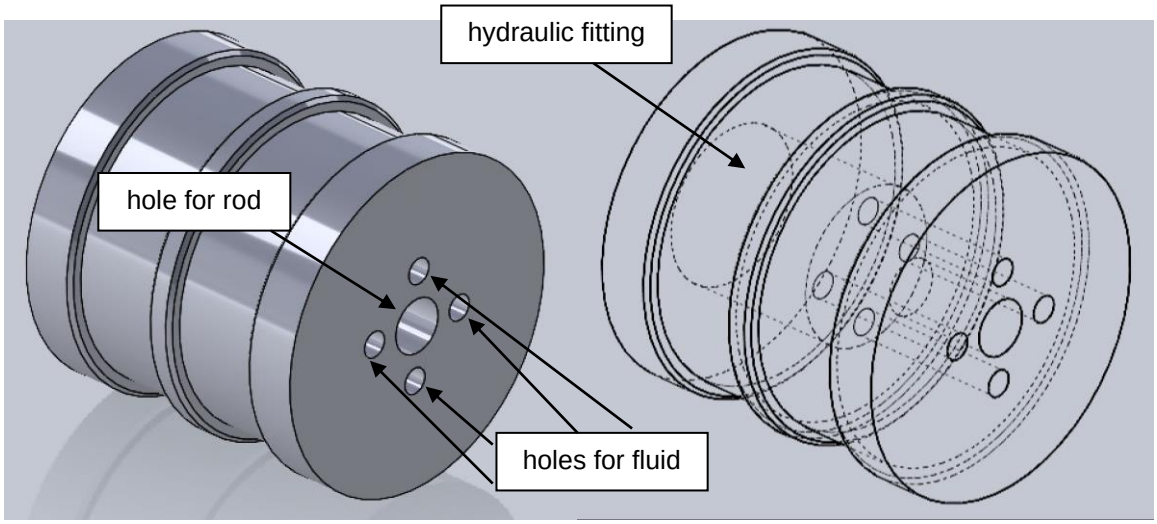

Figure 125: Traction actuator proximal segment connector

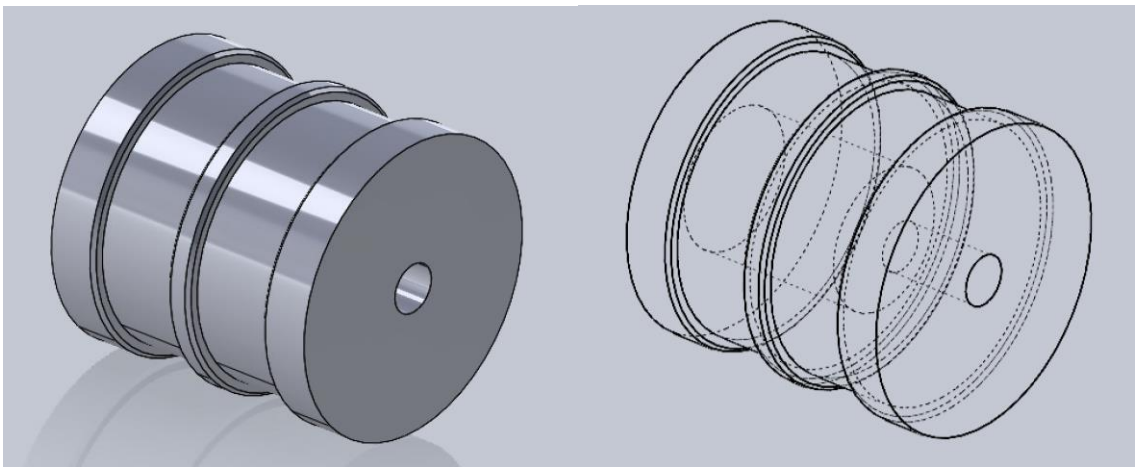

Figure 126: Traction actuator distal segment connector

4.3.2 Experimental Apparatus – Pull Out Tests

An experimental apparatus was constructed inside of a 25 mm thick Lexan case to address safety concerns related to actuator bursting. The pull-out force testing set up utilized a vise to clamp the proximal end of the traction actuator in place for testing. A 3 mm thick clear polycarbonate tube was placed concentrically over the actuator and held radially in place with two 3D printed bearings that were held in place by a 3D printed base board bolted to the table. The clear tube was able to slide back and forth axially over the actuator. A 3D printed adapter was mounted to the distal end of the clear tube, and a load cell was connected to the 3D printed adapter. The 3D printed adapter was able to mount to many different diameter clear tubes. The load cell was threaded into an eye-hook which was connected to a stiff coil tension spring. The automotive spring was connected to a manual geared winch. When the winch was cranked, the axial displacement causes the spring to generate pulling forces to pull the tube off the pressurized actuator. A pressure transducer was mounted on the proximal end to measure the input pressure to the actuator. The pressure transducer and the load cell are the same ones that were used in earlier experiments in section 2.2.1.2. Pulling the tube off the actuator, rather than pulling the actuator out of the tube, is easier to perform experimentally because managing the input hydraulic lines to the actuator during pull-out tests creates additional steps. Figure 127 displays all the components of the experimental apparatus used in the traction force experiments.

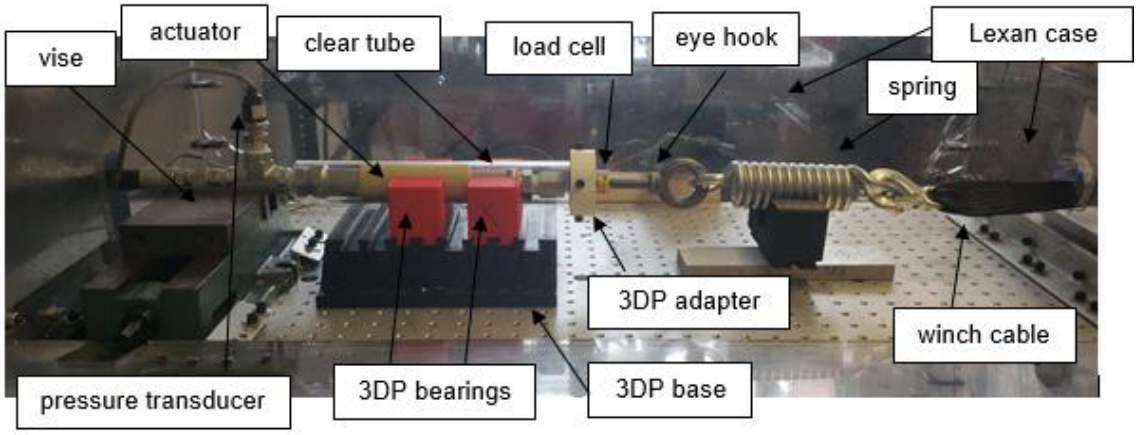

Figure 127: Traction actuator experimental apparatus

4.3.3 Experimental Apparatus – Friction Testing

An experimental apparatus was also constructed to determine the coefficient of friction between the traction actuator and the polycarbonate tube material. A rigid ramp with a polycarbonate surface was constructed that could be lifted on one end to adjust the ramp angle. The coefficient of friction was determined by the measured ramp angle at which the object begin sliding. The ramp can be observed in Figure 128.

Figure 128: Friction testing experimental apparatus

A 3D printed cart with four feet was designed that could be loaded on top with weights to determine the coefficient of friction at a specified normal force. The four feet were injected with elastomer material, but in early tests, it was determined that the coefficient of friction between Polytek74-55A polyurethane elastomer material and polycarbonate was very inconsistent. Therefore, the cart feet were covered with snug fitting fiber sleeves for testing to obtain a more consistent coefficient of friction that could be replicated in the traction force experiments. The same snug fitting fiber sleeves were placed around the actuators in the traction force experiments to validate the traction force model more easily. The sleeves were lightly coated in hydraulic oil to simulate testing conditions in the traction force experiments. Figure 129 shows the 3D printed cart with the fiber sleeves attached to the feet. The vertical peg was loaded with weights during testing.

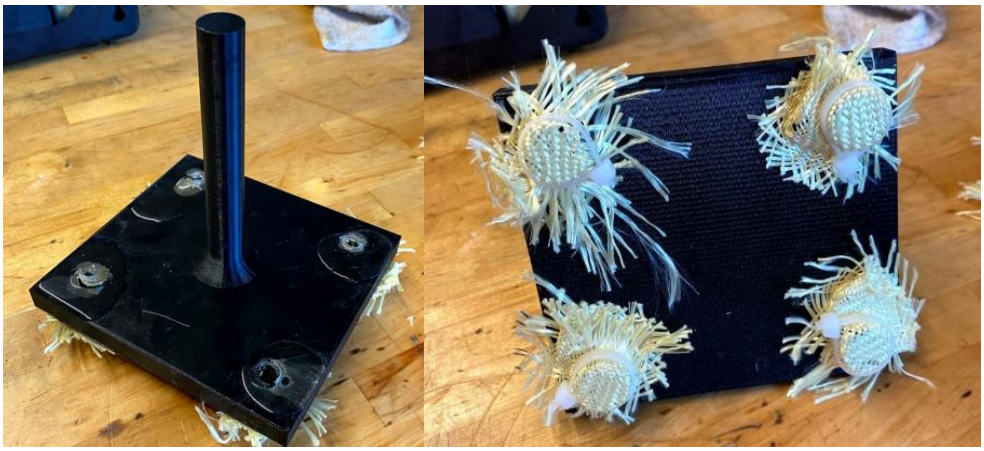

Figure 129: 3D printed cart for friction testing

4.3.4 Experimental Procedure

4.3.4.1 Friction Testing

First, the coefficient of friction between the polycarbonate and fiber sleeves were determined using the friction testing ramp and the 3D printed cart. The cart was loaded with a ~150 N load of weights and placed on the ramp in a flat position. The ~150 N load applied to the area of the four cart feet replicates similar applied pressures that will be observed in the traction force experiments. The sleeves were lightly coated in hydraulic oil. The cart was lifted slowly on one end until the cart began to slide. The height of the lifted end of the cart was measured with a meter stick, and the process was repeated a total of 26 times. The polycarbonate surface was wiped down with a lightly soaked oil rag between every test. Figure 130 shows the height measurement that was taken in the friction experiments.

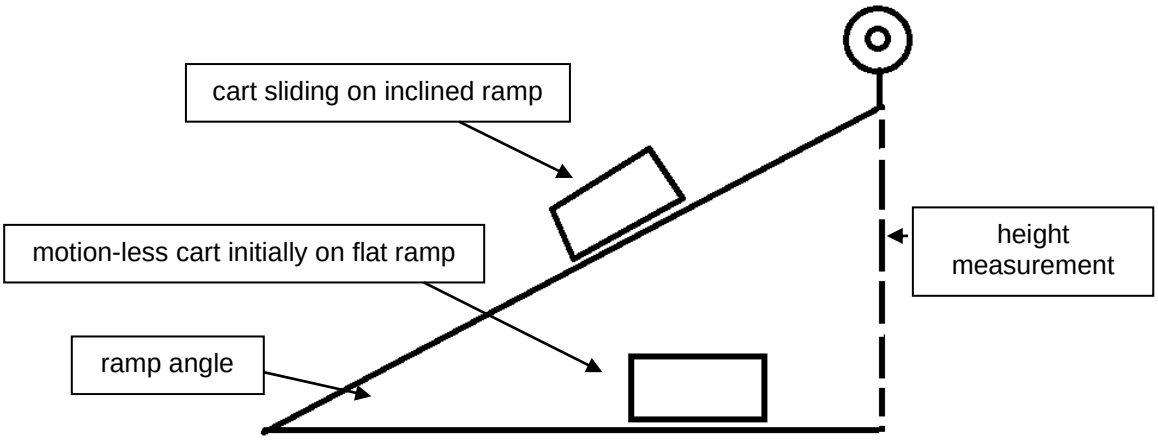

Figure 130: Flat and inclined positions of friction testing ramp

The normal force and friction force acting on the cart when it began to slip can be identified in the free-body diagram of the cart sliding on the inclined ramp shown in Figure 131.

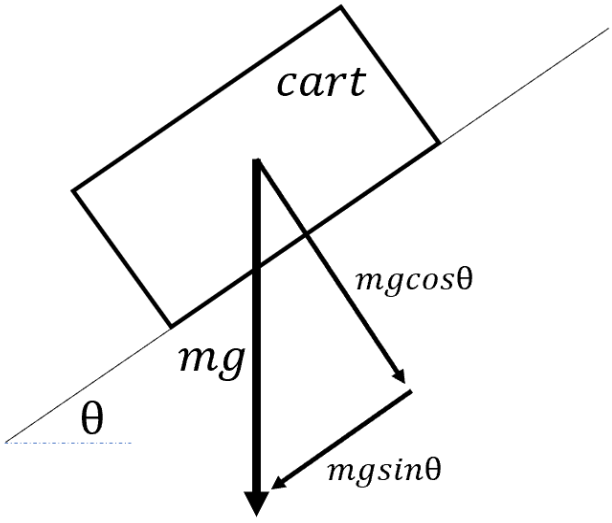

Figure 131: Free body diagram of forces on cart

The ramp angle was calculated using the ramp length and the height measurement at the point the cart slipped. The normal force and friction force are expressed below in (4.15) and (4.16).

$$F_{normal} = mgcos\theta \tag{4.15}$$

$$F_{friction} = mgsin\theta \tag{4.16}$$

The coefficient of static friction can then be calculated using the expression below.

$$\mu_s = \frac{F_{friction}}{F_{normal}} \tag{4.17}$$

4.3.4.2 Modulus Testing

The objective of these tests is to experimentally determine the Young's modulus for comparison to the empirical Gent model that was used for predicting the traction force output of the anchoring segments. Prior work has demonstrated that the Gent model is an appropriate tool for approximating the Young's modulus of a material from its Shore A durometer. Because the traction force model is sensitive to the Young's modulus, a simple experiment was conducted to measure the Young's modulus of each elastomer cross-section to verify the accuracy of the Gent model values used in the analysis. The modulus tests were only conducted on Actuators 2A, 2B, and 2C. The threaded rod was removed from the three actuators to allow it to be axially stretched. A centralized section of each elastomer was marked out, and the elastomer was incrementally stretched with the winch. The same load cell from previous experiments was used to

measure the axial force generated as the elastomer was stretched. The centralized section was measured with a ruler as it was stretched to measure the strain. Each actuator was stretched incrementally, and measurements were taken until at least 30% strain was achieved. The cross-sectional area, strain measurements, and force measurements were used to generate the stress-strain curves for the three samples to determine if they match well with the Gent model. Figure 132 shows the modulus testing set up.

Figure 132: Young's modulus testing traction actuator

4.3.4.3 Traction Force Actuator Testing

Once the friction and modulus testing were completed, the six traction actuators were subjected to pull tests to determine the amount of traction force they could produce under a series of different operating conditions. Each of the six actuators were tested in three different diameter polycarbonate tubes, and Table 13 shows the inside diameter of the polycarbonate tubes that each of the actuators were tested in.

Table 13: Polycarbonate tube diameters traction actuators are tested In

Actuator	Initial Outside Diameter, D_i (mm)	Initial Length, L_o (mm)	Tube #1 ID (mm)	Tube #2 ID (mm)	Tube #3 ID (mm)
1A	31.8	84.1	38.1	44.5	50.8
1B	38.1	84.1	44.5	50.8	57.2
1C	44.5	84.1	50.8	57.2	63.5
2A	31.8	133.4	38.1	44.5	50.8
2B	38.1	133.4	44.5	50.8	57.2
2C	44.5	133.4	50.8	57.2	63.5

The actuators were secured in the vise on the proximal end of the experimental apparatus, and they were covered with the oil coated fiber sleeve. The clear polycarbonate tubes were then slid over the fiber sleeve covered actuator for testing. Each actuator was tested in each polycarbonate tube over a range of input pressures from 0 to ~0.36 MPa. The pressure was increased until the actuator expanded to contact the clear tube, and the winch was used pull the clear tube off the actuator. Once enough force was generated to dislodge the tube from the pressurized actuator, the pressure and force data from the sensors was recorded, the actuator pressure was released, and the clear tube was replaced over the actuator. Next, the actuator pressure was increased by ~0.025 MPa, and the process was repeated for each actuator and tube combination until the actuators experienced mechanical failure or the pressure limit of 0.36 MPa was reached. The experiments were limited to pressures under 0.36 MPa to avoid burst failure before adequate traction force data could be collected. A ruler was placed next to each actuator during the experiments, and a camera was used to observe the contact length between the actuator and polycarbonate tube.

Figure 133 shows the fiber sleeve covered actuator in the experimental test set up before actuator pressurization.

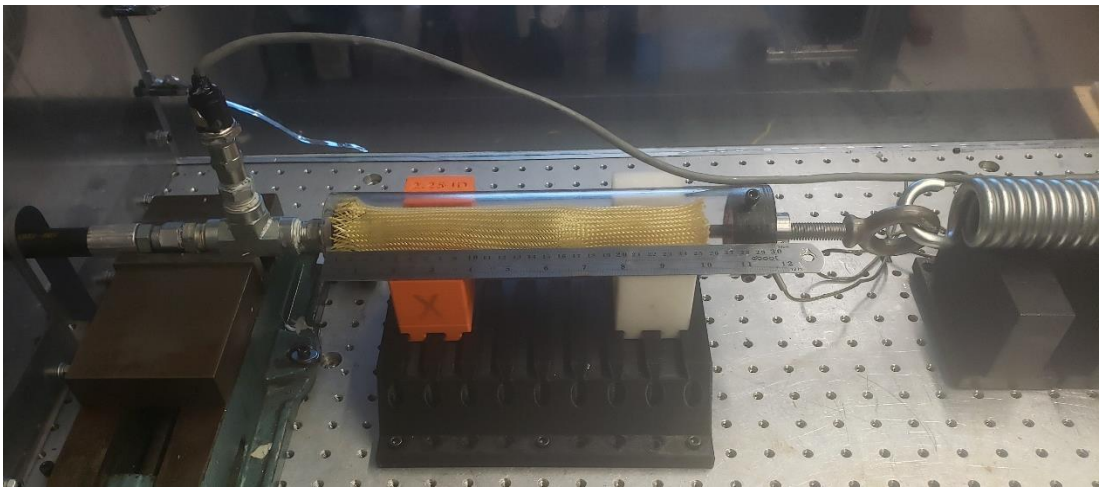

Figure 133: Traction force experiment

Because the clear polycarbonate tube slides with respect to the 3D printed bearings that are used to radially hold it in place, the friction between the tube and the bearings was characterized before any experiments were conducted. While the ~5-10 N of friction force observed between the clear tube and the 3D printed bearings was minimal, the force offset was accounted for in the final traction force results.

4.4 **Results and Discussion**

The results from the three experiments will now be presented and the anchoring force results will be compared to the model predictions.

4.4.1 Friction Testing Results and Discussion

The experiments to determine the coefficient of friction between the oil coated fiber sleeve and the polycarbonate surface were conducted. A total of 26 experiments were conducted with the ramp and weighted 3D printed cart, and the data was analyzed to calculate the measured coefficient of friction from the experiments. The results of the experiments can be observed in Figure 134.

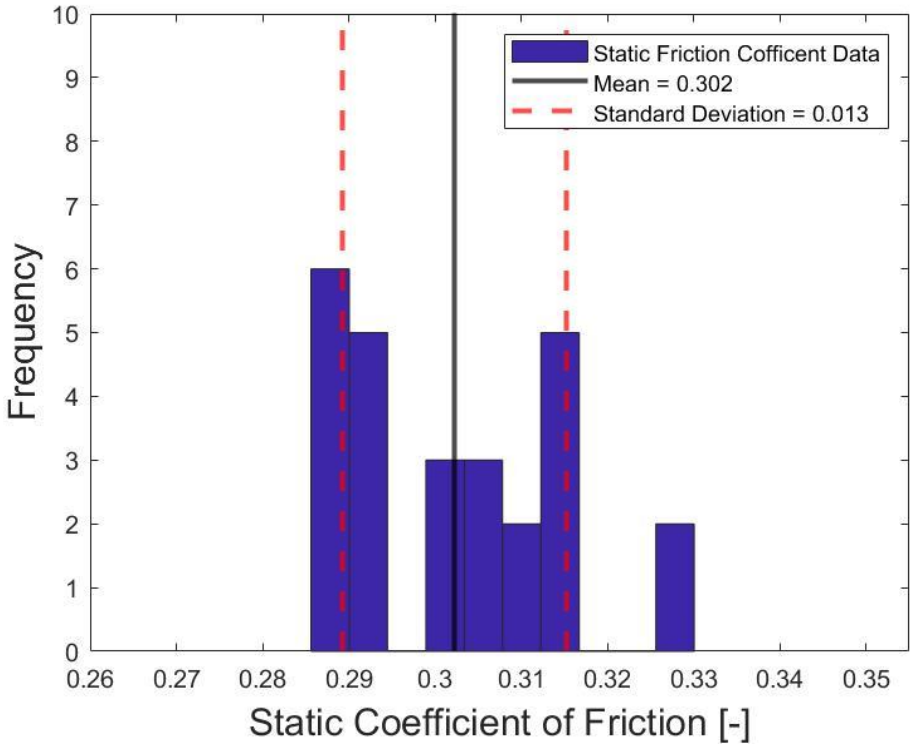

Figure 134: Friction testing results between oil coated fiber sleeve and polycarbonate

As can be observed in the results, the coefficient of friction was repeatable, and most of the data falls within one standard deviation. The mean coefficient of friction was 0.302, which was used in the traction force modeling and experimental analysis. The variability in the coefficient of friction experiments

is thought to be from the fiber pattern in the fiber sleeves. Depending on the orientation of how the cart was placed on the ramp, the fiber weave angle varied which may have caused some of the variability in friction forces, and consequently, the resulting coefficient of friction from that experiment.

4.4.2 Young's Modulus Results and Discussion

The Young's modulus testing was completed for Actuators 2A, 2B, and 2C using the experimental procedure outlined in the previous section of this chapter. The elastomer was stretched, and the strain was measured using a ruler on a centralized portion of each actuator, while the axial force was measured using a load cell. The cross-sectional area, strain, and force measurements were used to generate the stress-strain curves for the three samples. The cross-sectional area at each strain was calculated based on a constant volume assumption. Dividing the axial force by the cross-sectional area defines the axial stress. Figure 135 shows the stress-strain curves for the samples.

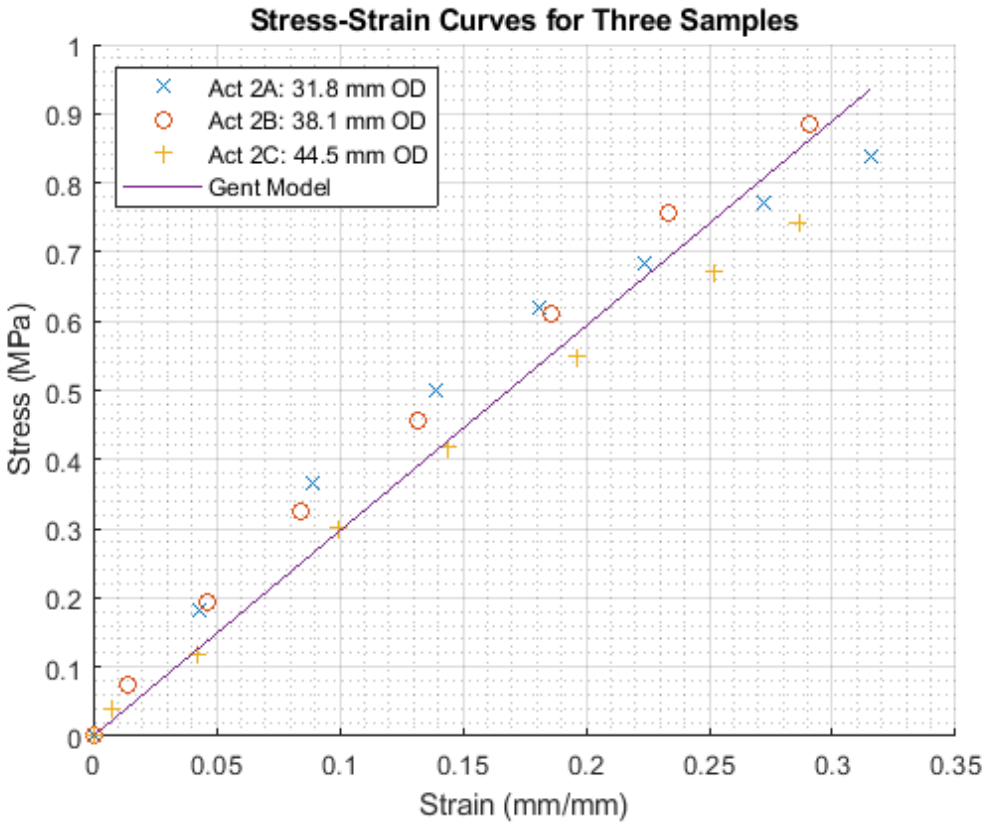

Figure 135: Stress-strain curves for actuators 2A, 2B, and 2C

As can be observed in the figure, the Gent model does a very good job approximating the Young's modulus for all three samples. Therefore, using the Gent model value of the Young's modulus is justified in the traction force modeling and analyses of these experiments. The Gent Model value of the Young's modulus that will be used in the analysis is E = 2.96 MPa.

4.4.3 Traction Force Results and Discussion

The traction force experiments were conducted, and all six actuators were tested in over a range of pressures in three different size clear polycarbonate tubes to determine the traction force generating capabilities of the actuators. For

each pull test, camera footage was reviewed to determine the contact length between the actuator and the polycarbonate tube. Figure 136 shows a screenshot of an example contact length measurement for one experiment. This contact length was then used in the traction force model to predict the traction force generated by the actuator in the experiment. Note that the relationship between actuator pressure and contact length is very non-linear and depended on the polycarbonate tube diameter. The operating pressures were selected to ensure the actuators expanded enough to contact the polycarbonate tubes. Testing an actuator in a large diameter tube at high pressure can result in the contact length being greater than the initial length of the elastomer. The comprehensive pressure, tube diameter, and contact length measurements can be found in Appendix J.

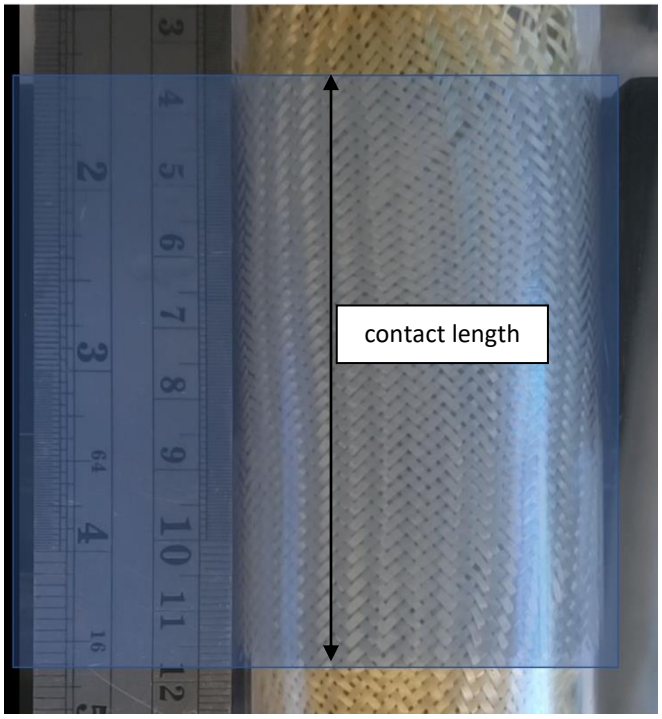

Figure 136: Contact length measurement

The traction force experiments were conducted for all six actuators in each of the three polycarbonate tubes. Many of the actuators experienced failure, and in all cases the failure was due to insufficient clamping force between the zip ties and the segment connectors that hold the elastomer in place. Data points where failure occurred were omitted or clearly noted in the results. Any time an elastomer slipped out from under the zip ties, or the zip ties broke, experiments were paused, and the actuator was rebuilt. Actuator failure occurred 7 times during the traction force experiments. In all cases of failure, stress concentration and insufficient clamping force between the zip ties and segment connectors caused the elastomer to pull out from the segment connector. Often, this led to zip tie fracture, and in one case, the elastomer material bursting. Labelled images of the failed actuators are shown in Figure 137 – Figure 143.

Figure 137: Traction Actuator 1A failure in 44.5 mm ID tube (insufficient clamping force led to elastomer slipping)

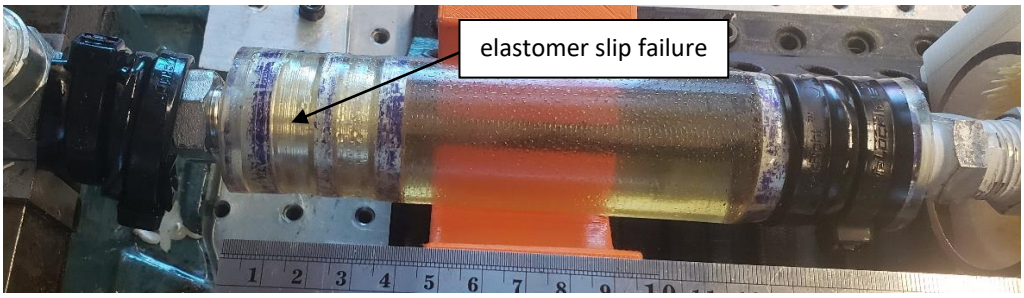

Figure 138: Traction Actuator 1B failure in 57.2 mm ID tube (insufficient clamping force led to elastomer slipping)

Figure 139: Traction Actuator 1C failure in 63.5 mm ID tube (insufficient clamping force led to elastomer slipping)

elastomer slip failure

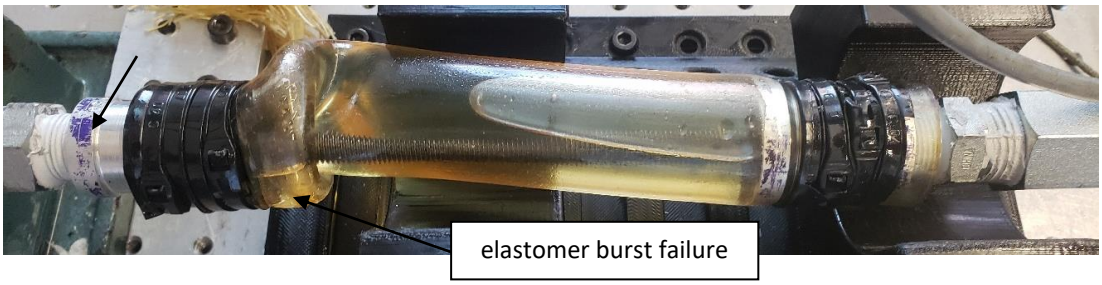

Figure 140: Traction Actuator 2A failure in 50.8 mm ID tube (insufficient clamping force led to elastomer slipping and bursting)

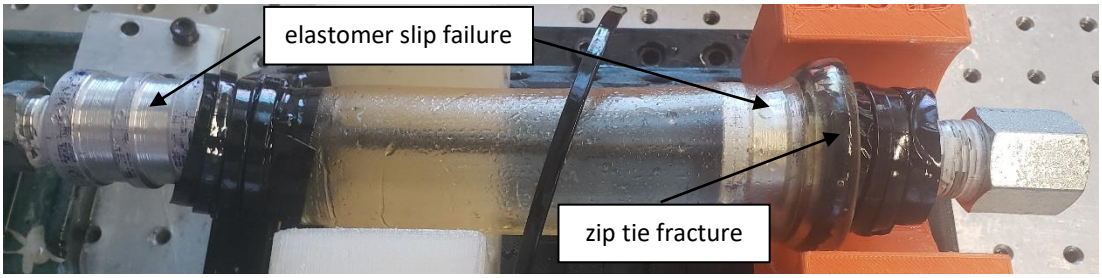

Figure 141: Traction Actuator 2B failure in 57.2 mm ID tube (insufficient clamping force led to elastomer slipping and zip tie fracture)

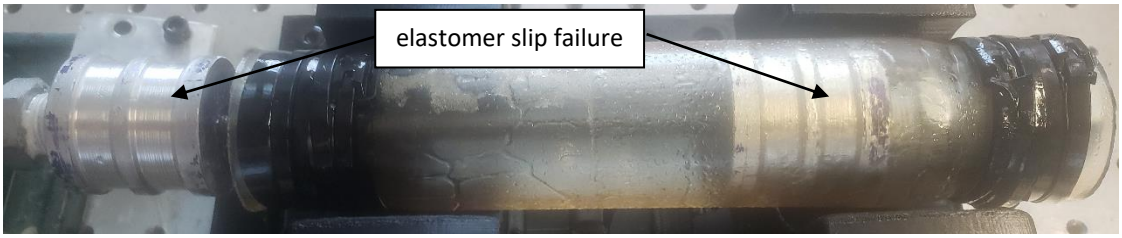

Figure 142: Traction Actuator 2C failure in 50.8 mm ID tube (insufficient clamping force led to elastomer slipping)

Figure 143:Traction Actuator 2C failure in 57.2 mm ID tube (insufficient clamping force led to elastomer slipping)

The results from the experiments for the six actuators are shown below in Figure 144 - Figure 149. Note that some data points have markers indicating failure occurred at the end of the experiment. Each figure presents the experimental and expected traction force results for one actuator in three tube sizes.

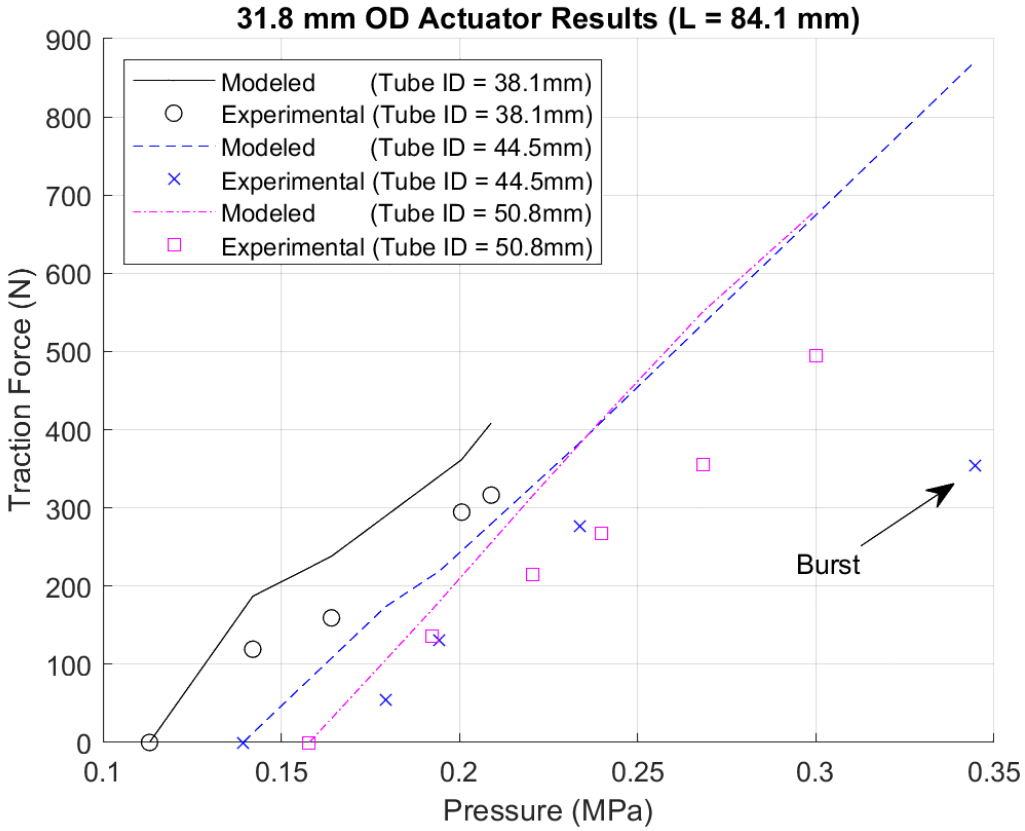

Figure 144: Actuator 1A traction force results

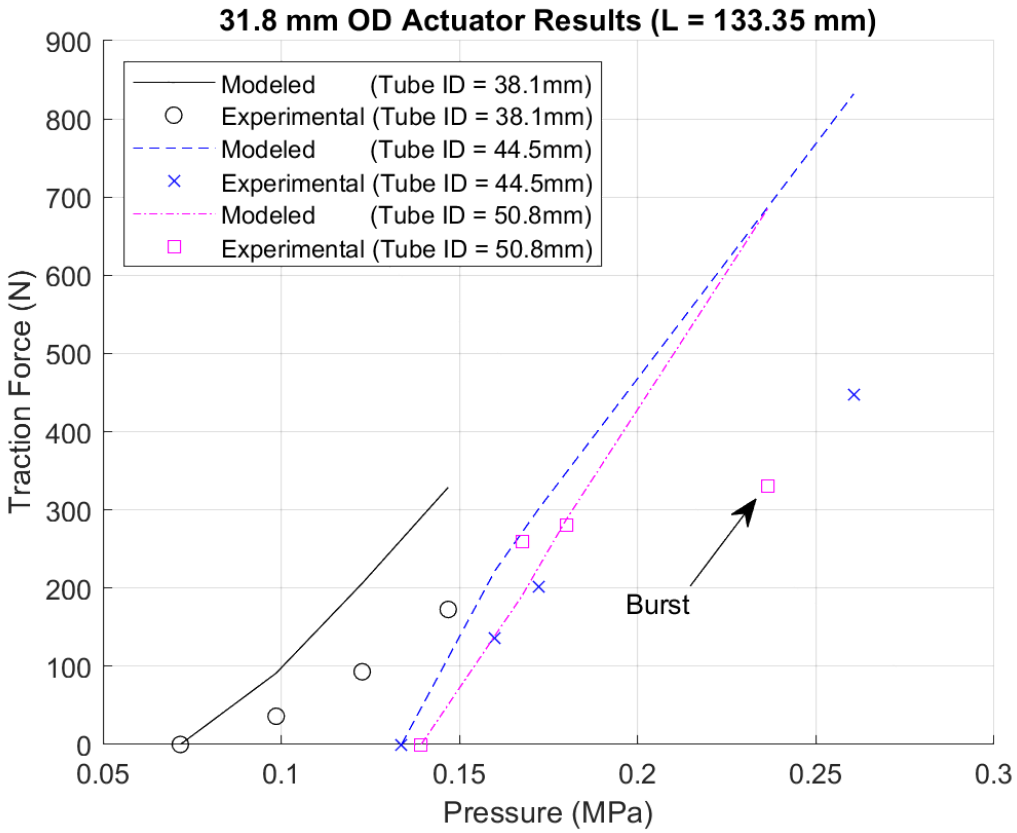

Figure 145: Actuator 2A traction force results

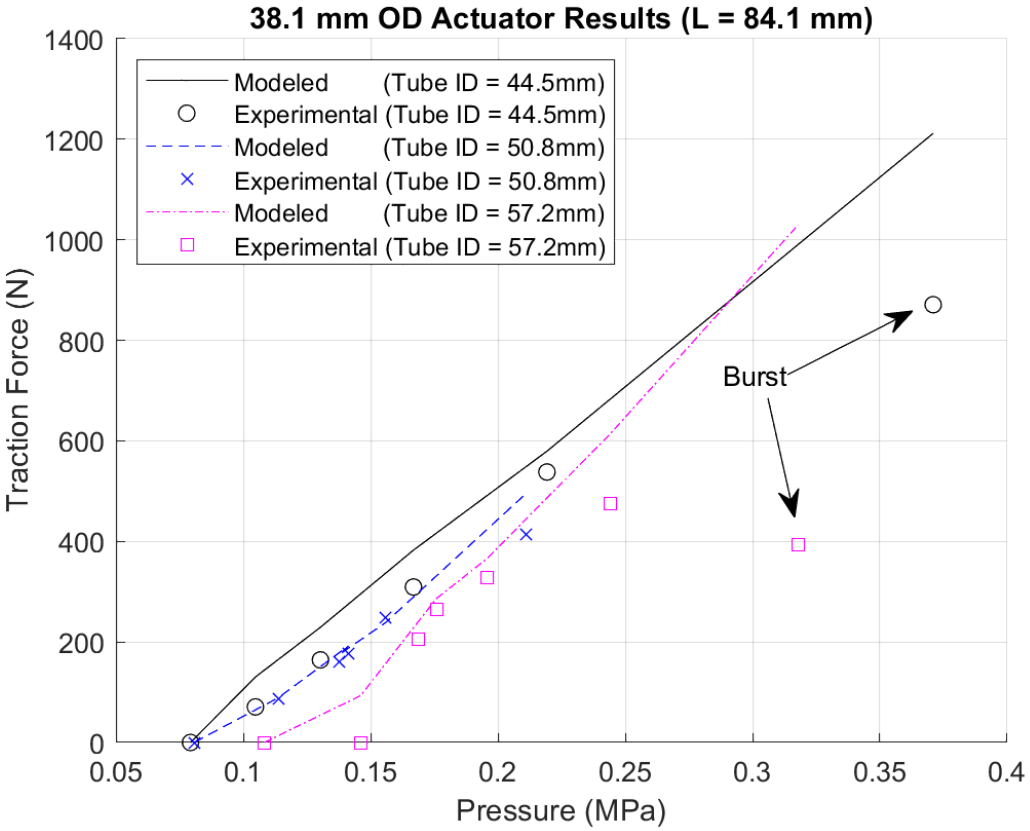

Figure 146: Actuator 1B traction force results

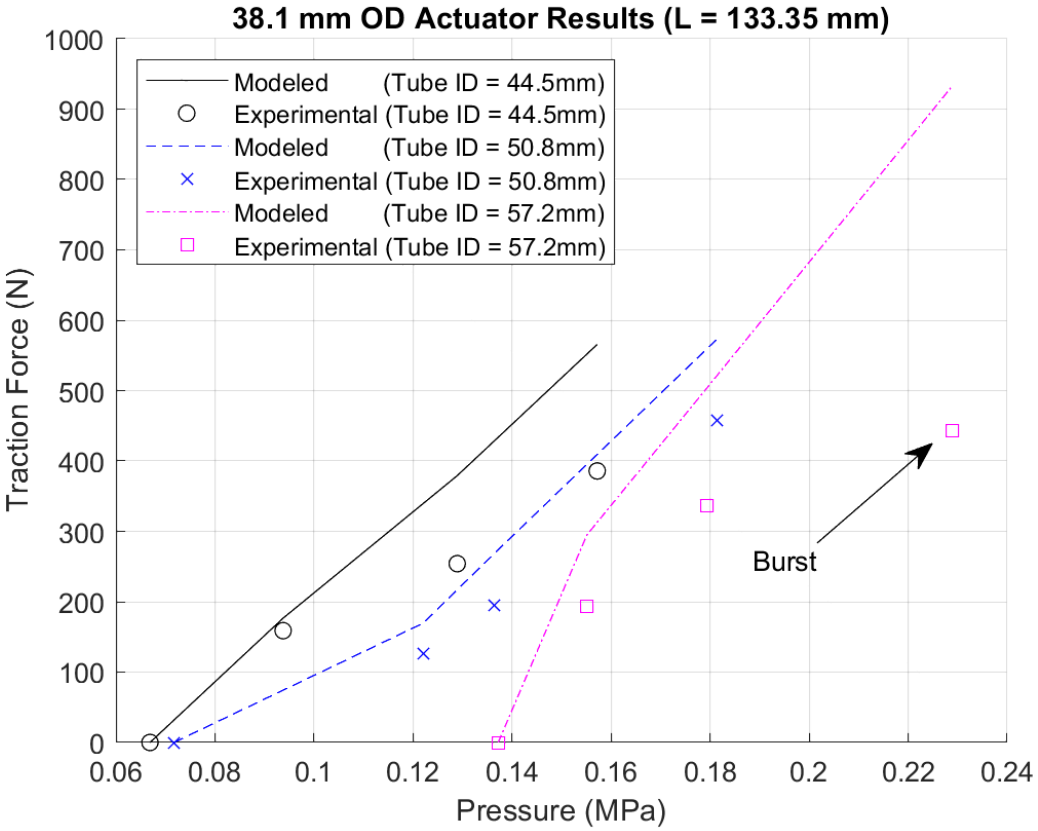

Figure 147: Actuator 2B traction force results

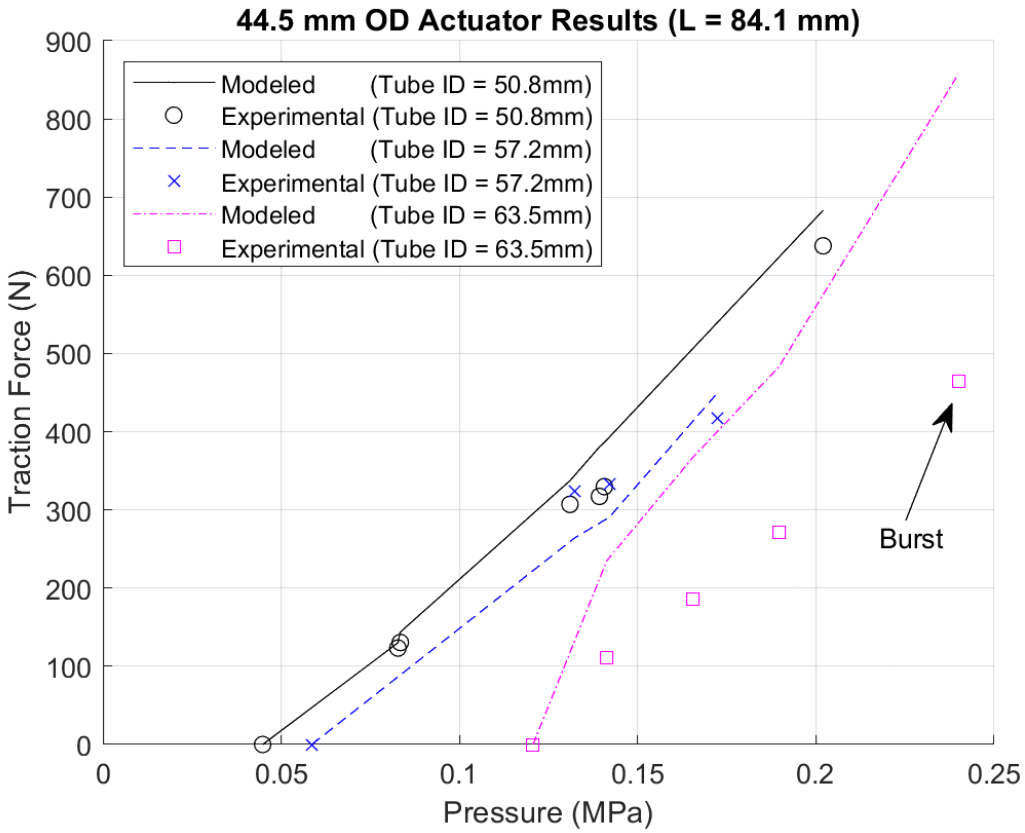

Figure 148: Actuator 1C traction force results

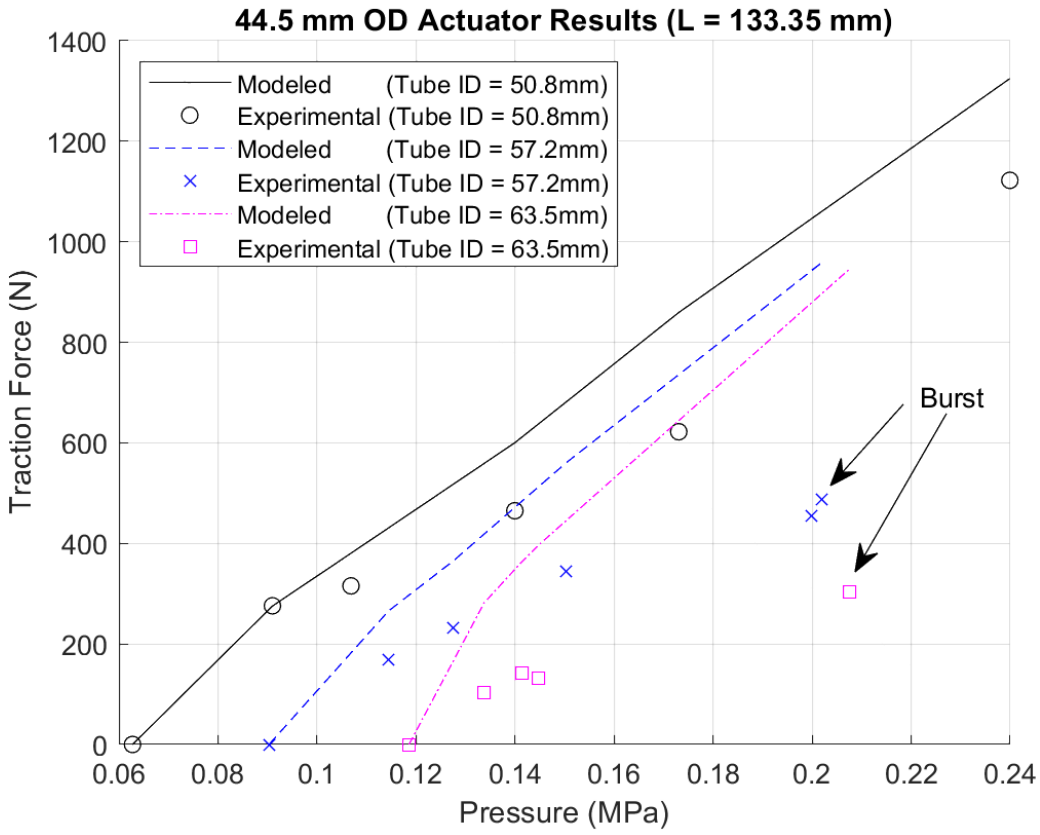

Figure 149: Actuator 2C traction force results

The results for all the experiments are very consistent. In all cases, the traction force model over predicts the traction force. As the pressure is increased, it appears that the experimental traction force tapers off while the model predicted traction force does not. Furthermore, the experimental traction force appears to generally taper off compared to the model when the actuators are expanded to larger diameters. This intuitively makes sense because the contact length varies in a more non-linear fashion when the actuator must expand significantly compared to when it is close to the same size as the tube. There did not appear to be any correlation between initial actuator geometry and model

accuracy. In the instances where failure occurred, it can be observed that the experimental traction force dropped off drastically – which makes sense since the elastomer slipped out from under the zip ties. The expected traction force was calculated using the experimentally determined coefficient of friction, the measured contact length between the actuator and the polycarbonate tube, and the Gent model value of the modulus.

While the model does a good job of providing a ball-park estimation of the traction force, there are a few sources of error that could have caused the disagreement between the experimental data and the expected traction force results. The first source of error could be from the assumption that there is a constant pressure distribution on the polycarbonate tube wall. When the traction actuator expands, it first contacts the polycarbonate tube with a small contact patch in the middle of the traction actuator. As the pressure is increased, the largest contact pressure is applied in the middle of the contact patch with the contact pressure dissipating as you move outward from the center of the contact patch. Refinement of the model to relax this assumption may yield more accurate results – especially at the higher pressures where the results dropped off and the non-constant pressure distribution on the tube wall is more prevalent.

Another source of error could have come from slight variations in the coefficient of friction between the actuator sleeve and the polycarbonate tube between experiments. The amount of oil that was present inside the

polycarbonate tubes varied between experiments. If an actuator experienced the elastomer slipping out from under the zip ties or zip tie failure, oil from inside the actuator would soak the fiber sleeve and the polycarbonate tube as it was released into the testing environment. This slight variation in lubrication may have caused some slight inconsistencies in the results due to variations in the friction coefficient.

More development work is needed to develop robust segment connectors that allow the actuator to achieve larger internal pressures without failure. However, these early experiments have allowed traction forces over 1100 N to be generated, and it is expected that with a more robust segment connector design, much larger traction forces could be achieved. Overall, these experiments have provided the necessary validation to use the traction force model as a baseline design tool for modeling traction actuators that could be used in a multi-segment burrowing robot application. Furthermore, the developed traction segments provide exclusively radial expansion, without axial slipping, that could be useful for compressing soil in a burrowing or tunneling application.

4.5 **Conclusion and Summary**

Many traction actuator designs were explored to be able to develop a soft robot capable of generating radial anchoring forces without producing any axial motion. A final design consisting of two aluminum segment connectors with a strain limiting rod connecting them, an elastomer, and low-profile zip ties was

selected for experimental testing. A new traction force model was developed for experimental validation. Six actuators, with two different lengths, three different diameters, and the same wall thickness, were fabricated for experimental testing. The six actuators were each tested in three different size polycarbonate tubes over a range of input pressures to determine the traction force generating capabilities of each actuator and to compare to the predicted force from the traction force model. The coefficient of friction between the polycarbonate surface and the oil coated fiber sleeve that was placed around the actuator was experimentally determined using an inclined ramp and a 3D printed cart. The Young's modulus used in the traction force model was selected using the empirical Gent model, which was experimentally validated for three elastomer samples.

The experimental results were very consistent for all six actuators in all the tube sizes. The traction force model tends to over-predict the traction force – especially as the input pressure of the actuators increase. While the model is accurate enough to use as a baseline traction actuator design tool, the error that is present could be from several different sources. The error could be from the assumption that the contact pressure between the actuator and the polycarbonate tube wall is constant. Error may also be caused due to variations in the coefficient of friction between the actuator sleeve and polycarbonate tube wall that arise due to varying amounts of oil being present in the system after actuator burst failure in previous experiments. Other sources of error could

include neglecting losses, the small strain assumption, and the incompressible elastomer and hydraulic fluid assumptions.

The results from this chapter show that the new traction force model can be used for practical design purposes to estimate traction force. More development work is needed to design segment connectors that can withstand larger internal pressures without slipping. Further model refinement could include accounting for the non-constant pressure distribution between the actuator and the polycarbonate tube wall. Future work will also require the model to consider a deformable environment to develop the capabilities to anchor and traverse a deformable environment such as a burrow. This will include understanding the necessary traction forces, traction force application rates, and soil stress regimes to provide sufficient anchoring of the robot and a stable, plastically deformed burrow without the need for soil excavation or risk of burrow collapse.

4.6 Specific Contributions of the Chapter

- Development of a novel force model for a fixed length, radially expanding soft robot actuator for determining traction force as a function of actuator geometry, actuator input pressure, and burrow (or tube) diameter

- Novel design of a fixed length, radially expanding soft robot actuator capable of generating traction forces in a wide range of burrow (or tube) diameters. The actuator consists of a constant wall thickness elastomer, a

stiff threaded rod to prevent the actuator from changing length during actuation, two aluminum segment connectors, and low-profile zip ties to secure the elastomer to the segment connectors.

- Experimental validation of the traction force model as a baseline predictive design tool

- Development of three early-stage traction actuator designs:

    - Loose sleeve modified McKibben actuator design that utilizes a strain limiting rod to prevent axial displacement and a loose fiber sleeve to limit radial expansion of the elastomer
    - Multi-layered calcium-chloride expanded actuator design that allows fibers to be embedded on a stressed elastomer and multiple elastomer compartments to be designed into a soft actuator to control deformation during actuation
    - Constant stress elastomer design to mitigate blow out failures caused from stress concentration near the segment connectors of soft actuators

Chapter 5: Multi-Segment Robot System

This chapter aims to combine the work from the previous chapters to design, model, fabricate, and test a multi-segment soft robot capable of traversing a tubular environment. Robots capable of traversing tubular environments would be useful in many applications such as pipe repair, search and rescue, and installation of underground cables. While many robots capable of traversing a tubular environment have been presented in prior literature, this chapter presents a multi-segment hydraulic soft robot design featuring two novel traction actuators and an extending McKibben actuator all connected axially within a single elastomer. The design features entirely internal fluid routing that enables the various segments to be actuated independently for easy control of the robot's movement. The robot's design parameters were selected based on several experimental constraints and performance objectives, and a grid-search was performed to select a final robot geometry that met the performance objectives and satisfied the experimental constraints. The robot was fabricated and experimentally tested to show it can move through tubular environments, and the results of those experiments are presented and discussed in this chapter.

In section 1.2.3, two key multi-segment, soft robots from literature with burrowing applications were introduced – the pneumatic Kirigami robot and the hydraulic GE robot. The Kirigami robot mimicked an earth-worm and utilized

alternating anchor locomotion, and the GE robot used an undulatory motion achieved by actuating many segments simultaneously to generate axial and radial forces to create motion. Both soft robot systems simultaneously generated axial displacement when radial forces were applied to anchor the system, which is not ideal for stable burrowing or similar applications where precise radial forces may need to be applied. Figure 150 and Figure 151 show the Kirigami robot and the GE robot respectively.

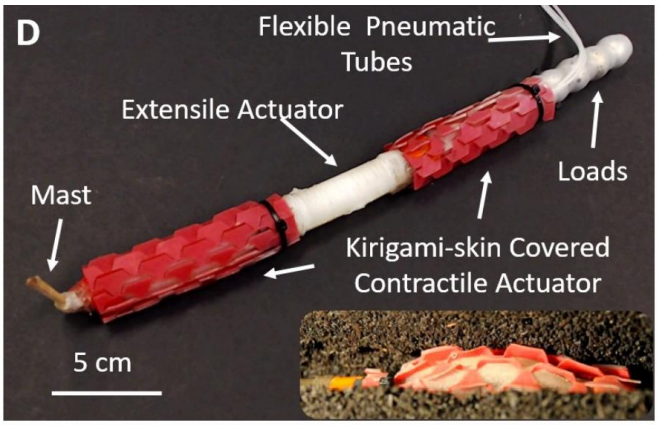

Figure 150: Kirigami multi-segment robot [127]

Figure 151: GE multi-segment robot [128]

The GE robot is limited by the fact that needs its long length to develop large traction forces resulting in a less compact design, can only achieve burrowing locomotion when segments are actuated simultaneously likely resulting in slipping along the burrow, can only achieve a limited set of motions due to its undulatory locomotion method, and appears to use external fluid and/or electronic lines that are at risk of being damaged in a burrowing environment. Similarly, the pneumatically driven, Kirigami-covered, multi-segment soft robot experiences challenges with control of the distal robot tip because the radially expanding segments simultaneously contract axially when actuated leading to slipping of the robot. Furthermore, the pneumatic Kirigami robot may experience

leakage or other issues associated with the compressibility of air due to the rugged environment observed in a burrow.

This chapter seeks to address some of these limitations and present a novel approach to designing a multi-segment burrowing soft robot capable of traversing a tube. First, the design objectives and constraints for the multi-segment robot are presented followed by an overview of the robot design details. Next, an overview of the models used to drive the selection of the final robot geometry are discussed. A grid-search is employed to understand the solution space and select the final design parameters of the robot that best meet the initial design objectives. The manufacturing and fabrication process of the robot is presented along with the experimental apparatus and experimental procedure. Finally, the results from experimentally testing the multi-segment robot's ability to traverse through tubular environments are presented and discussed.

5.1 **Constraints (Design Objectives)**

The robot geometry was selected such that it would meet several experimental constraints and robot performance objectives while traveling through the tubes. In this section, the experimental constraints and performance objectives that were used to limit the solution space for the multi-segment robot design are presented. The final objective of the robot is to demonstrate its ability to locomote through at least two different sized tubes in a horizontal configuration and at least one tube in a vertical orientation to demonstrate it can move up the

tube against gravity. The size of the tubes will be selected in the range of 50-100 mm which is what can be found in a burrowing application like installation of pipes, irrigation, or other underground utilities.

5.1.1 Experimental Constraints

There were manufacturing constraints for the multi-segment robot that were selected based on prior experience in manufacturing soft robot segments. To simplify the manufacturing process, a constant wall thickness elastomer constraint was implemented for the design. The entire robot was designed with a single continuous elastomer which resulted in the traction segments and extending segment having the same inside and outside diameters. Furthermore, the initial outside diameter of the robot was limited by what commercially available clear polycarbonate tubes were available for the elastomer casting process. The initial fiber-wrap angle for the extending segment was selected to be 80 degrees, because this is the maximum angle the fiber-wrapping lathe was able to accurately place fibers.

Since it is desired that the robot can travel in both the forward and backward directions equally effectively, axial symmetry of the robot is desirable to ensure equal traction forces can be generated by both traction segments. Therefore, the distal and proximal traction segments were selected to be the same initial length. The final experimental constraint imposed in the design of the multi-segment robot was that the entire length of the robot must be less than 610

mm to fit on the test bench. A bullet-point summary of the experimental constraints is shown below, and Figure 152 illustrates the constraints for the robot design.

- Constant wall thickness of elastomer
- Constant ID and OD of elastomer
- Elastomer must be manufacturable with readily available tubes
- Initial fiber angle = 80 degrees (best wrap angle)
- Both traction segments same length
- L_{robot} <= 610 mm ($L_{extender}$+2*$L_{traction}$+4*$L_{connection}$)

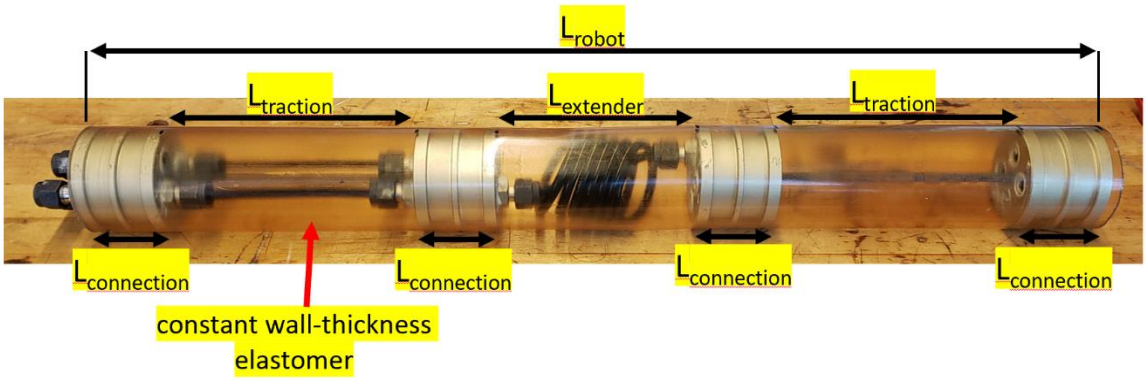

Figure 152: Robot segment lengths and experimental constraints

5.1.2 Performance Constraints and Objectives

Performance constraints were first selected to ensure that the robot was able to perform adequately in the experiments without failing. The multi-segment robot design space was limited to solutions where the safety factor against

buckling, compressive yielding, and burst failure were all greater than 3. The operating pressure of the robot was limited to 207 kPa to ensure failure of the segments did not occur before all the experiments could be conducted. In previous experiments, pressures over 207 kPa occasionally caused the elastomer to slip from the segment connectors. The solution space was also limited to extending segments that could generate at least 180 N of extension force and traction segments that could generate at least 180 N of traction force to ensure the robot was able to generate sufficient locomotion forces to anchor and move its weight up a tube against gravity. Furthermore, the traction segments must be designed to be capable of expanding to diameters up to 3 times the initial traction segment diameter. This will ensure traction forces can be generated over a wide range of tube diameters without failure.

The objective of this design methodology was to select a robot design that can produce energy efficient locomotion and forces when traveling through the tubes. Three performance objectives were selected for the multi-segment robot design, and these objectives were used to select the best designs within the solution space defined by all the experimental and performance constraints. The lone performance objective for the traction segments was to minimize the input energy per unit traction force. The first performance objective of the extending segment is to minimize the input energy per unit extension, and the final performance objective of the extending segment is to maximize the amount of

extension per robot cycle. A bullet-point summary of the performance constraints and performance objectives is shown below.

Performance Constraints

- $F_{extension} > 180$ N
- $F_{traction} > 180$ N
- $SF_{buckling}$ & $SF_{compression}$ & $SF_{burst} > 3$
- $P_{operating} < 207$ kPa
- Max Expansion Diameter > 3 times initial traction segment diameter

Performance Objectives

- Minimize energy/unit traction force
- Minimize energy/unit extension
- Maximize extension/cycle

An overview of all relevant models needed to calculate these constraint and performance values is provided in section 5.3.

5.2 **Robot Design**

The multi-segment robot design combines the traction force actuators and extending McKibben actuators from the previous chapters of this thesis. The objective of the design was to develop a multi-segment robot capable of independently actuating multiple axially connected soft robot segments with

exclusively internal hydraulic elements within the robot. This section outlines the details of the multi-segment robot design. Note that the final geometry of the robot will be presented later in section 5.4.

The design of the multi-segment robot is comprised of three segments - one axially displacing segment (extending McKibben actuator) connected on both ends to two radially expanding segments (traction actuators). The internal structure of the robot consists of four aluminum segment connectors to partition the robot segments, two threaded rods to limit the axial motion of the traction segments, and microbore tubing to allow fluid to be routed to and from the individual segments. The small diameter microbore tubing was secured with compression fittings to the segment connectors to allow for independent actuation of the robot segments without affecting the performance of any of the other segments. This also enabled the robot to run easily in the reverse direction. In the middle extending segment, the microbore tube was formed into a helical shape to allow the middle extending segment to axially displace while still allowing fluid to be routed to the most distal traction segment. The external structure of the robot is a constant wall thickness elastomer cast out of Polytek74-55A elastomer with fibers wrapped around the central extending segment of the robot. Low profile zip ties were used to secure the elastomer to the segment connectors. Figure 153 shows the side-view of a rendering of the robot, and Figure 154 depicts the cross-sectional view of the robot. Figure 155 shows an isometric view of the robot with labels of the various components of the

design. Figure 156 shows an isometric view of just the internal structure of the robot without the elastomer. The numbers on the input microbore tube lines match the number on the robot segment that they provide fluid to. Credit is given to Kevin Orpen, an undergraduate research assistant in the MEPS laboratory, for contributing to the design of this robot and for generating Figure 153 – Figure 156.

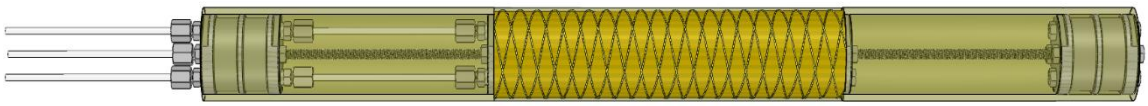

Figure 153: Multi-segment robot design rendering (side view)

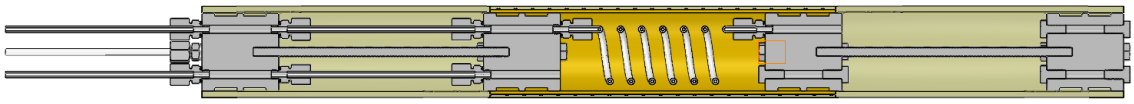

Figure 154: Multi-segment robot design rendering (cross-sectional view)

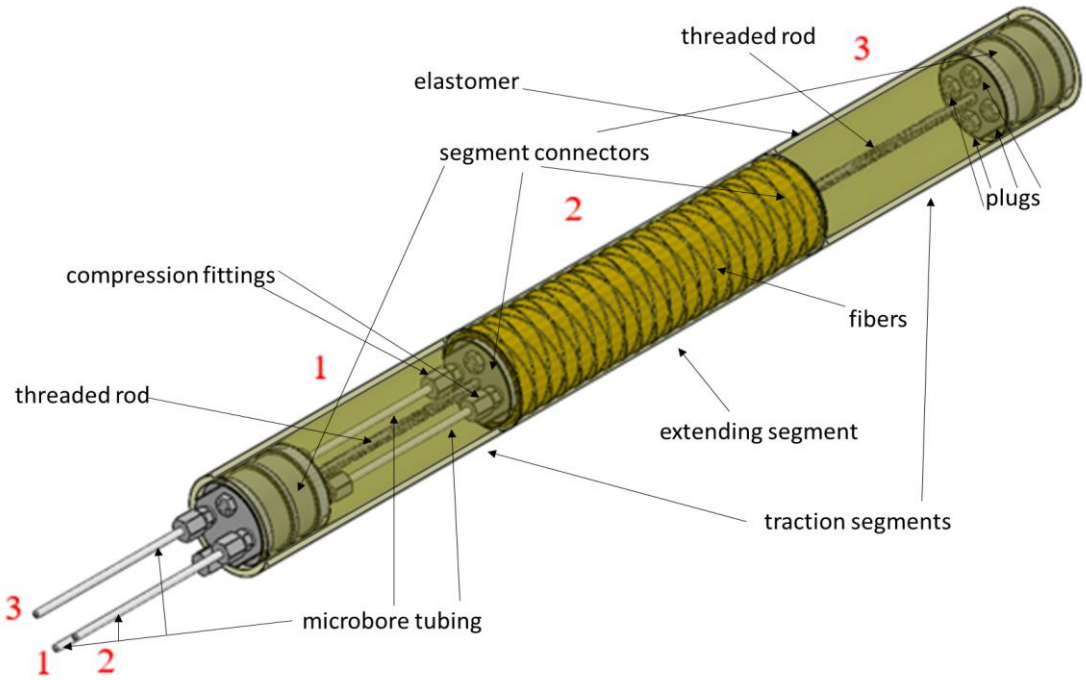

Figure 155: Multi-segment robot design (isometric view)

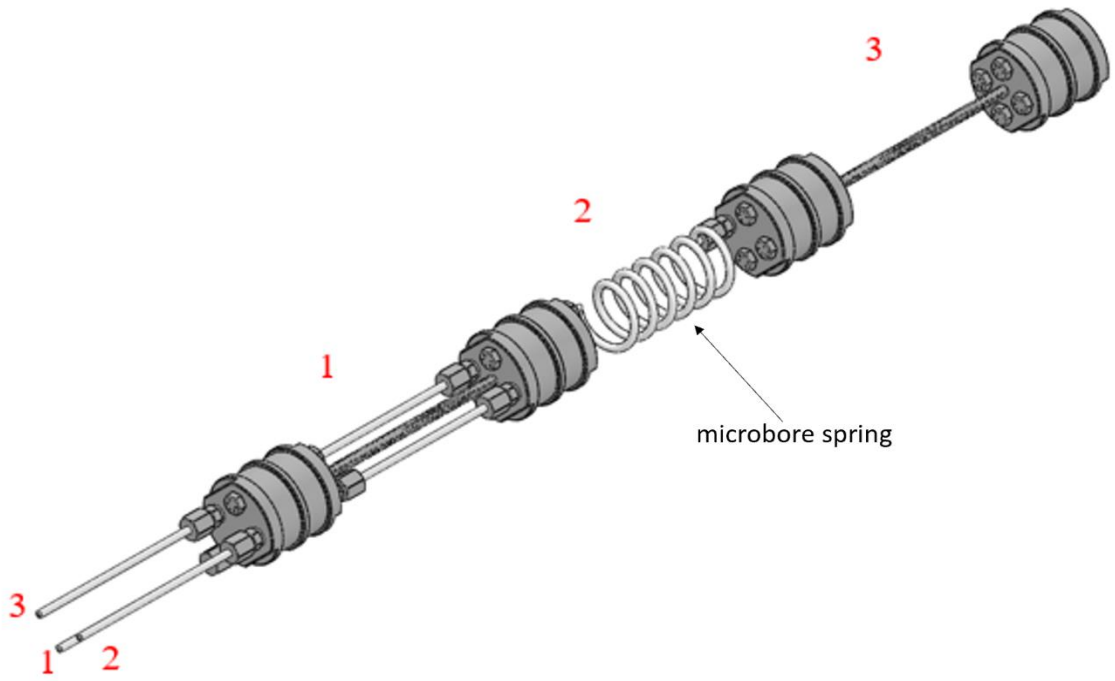

Figure 156: Multi-segment robot internal structure (isometric view)

The four segment connectors feature the same designs as those described in the previous traction actuator experiments in section 4.1.2, except that there are four through holes axially drilled around the hole for the axial strain-limiting rod to install compression fittings to mount the microbore tubing. The robot was designed to allow another fluid line to a future burrowing head to be installed, so plugs were used to block off holes that were not connected to microbore tubing. The segment connector design is shown in Figure 157.

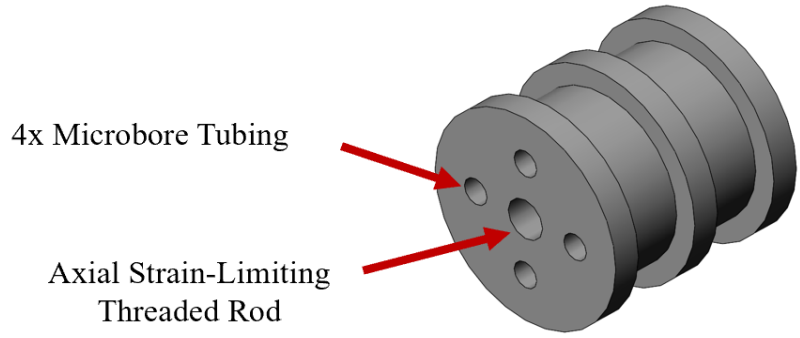

Figure 157: Multi-segment robot segment connector design

The traction segment on the proximal side of the robot was equipped with two microbore fluid lines running through it to reach the extending segment and the most distal traction segment. The most proximal traction segment of the robot did not have any microbore fluid lines running through it, but if an end effector were installed on the robot in the future, the segment could accommodate another fluid line. Figure 158 illustrates a side-view of the proximal traction segment of the robot.

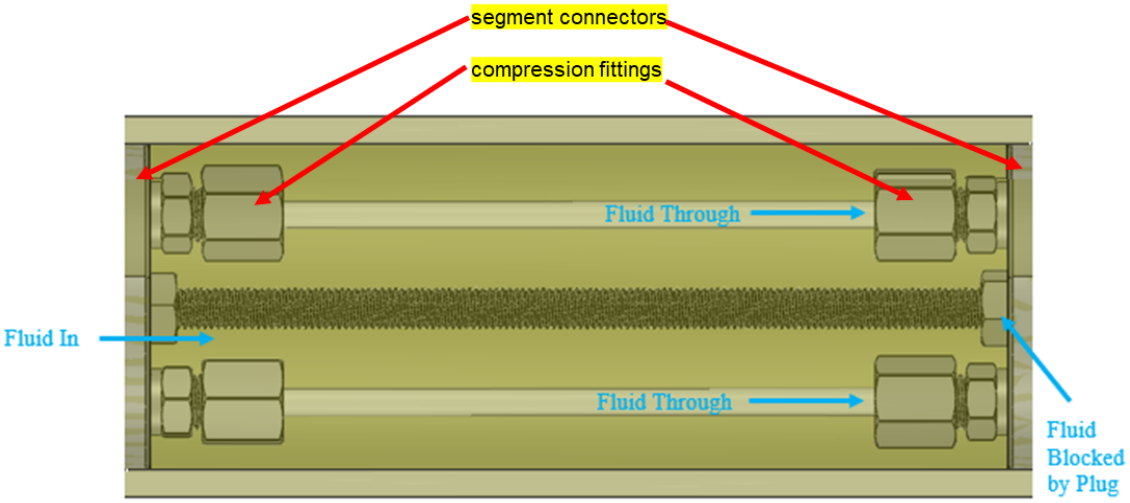

Figure 158: Proximal traction segment of the multi-segment robot (side view)

The extending segment of the robot contains a single microbore tube running through it to supply fluid to the distal traction segment. While the microbore tubing was straight and installed axially in the proximal traction segment, a new microbore tube design was developed for the extending segment to allow fluid to be routed to the distal traction segment regardless of the actuation state of the extending actuator. Nylon-12 microbore tubing with a 4.8 mm OD and a 3.0 mm ID was formed into a spiral shape with a straight section on each end that connected to a compression fitting embedded in the segment connectors on each end of the axially displacing segment. When the extending segment is actuated and changes length, the spiral tubing simply contracts or extends to allow for the fluid tubing to remain connected to the compression fittings and allow fluid to continue to be routed through the axially extending segment to further downstream segments. The spirally wound microbore fluid routing tubing system essentially acts like an elastic fluid hose (without any change in hose diameter), and it can be designed to account for the expected displacements of the axially displacing segment. Figure 159 illustrates the spiral microbore tubing design employed in the extending segment of the robot.

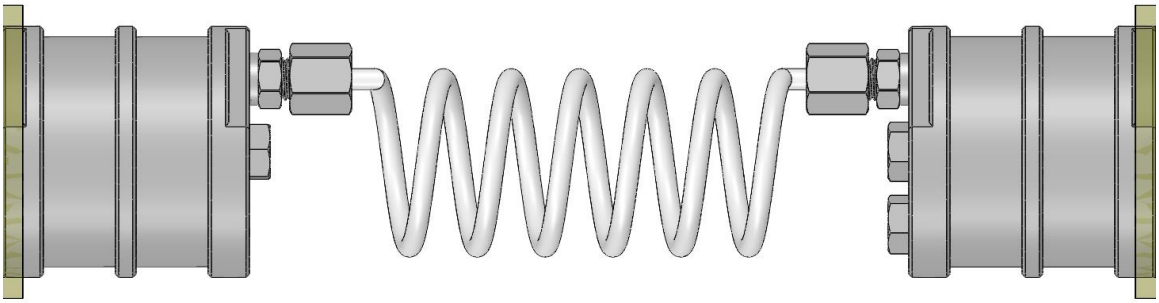

Figure 159: Extending segment illustrating internal spiral fluid routing approach without fibers and elastomer shown

This exclusively internal design to route fluid through an extending actuator is novel and useful because all known existing multi-segment systems either use some sort of serial actuation (one pressure input impacts the motion of multiple segments), use internal fluid chambers embedded within the elastomer rather than normal fluid lines (fluid lines are advantageous to achieve certain deformations as they won't collapse) to transport fluid, or use externally routed fluid lines that could be impacted by the operating environment of the robot. The ability to independently actuate the segments allows for the development of compact multi-segment soft robot systems that can be more easily controlled, and therefore useful in more applications. This approach solves the problem of being able to internally route fluid through an axially displacing soft actuator without affecting the performance of other segments within the multi-segment robot. No known prior art to date uses exclusively internal fluid routing techniques and can independently actuate fluid segments without affecting the pressure and locomotion of the other segments in the system.

5.3 Modeling

The design constraints and performance objectives described in section 5.1 will be used in a grid-search to identify the best multi-segment robot designs that satisfy all the constraints and performance objectives. To perform the grid-search, several models are needed to compute the constraint and objective values for the analysis. This section provides an overview of the models that were used to evaluate the robot performance in the grid-search to explore the design solution space. The modeling overview is divided into two sections starting with the traction segment and followed by the extending segment. Note that many of the models that are presented are a review from previous chapters, but a summary of the most relevant models is provided for context.

5.3.1 Traction Segment Modeling

The traction segment design is constrained by the total traction force and the safety factor against bursting, and the objective is to select a design that minimizes the energy per unit traction force.

First, the total traction force can be modeled as a function of initial actuator geometry by using the approach and assumptions presented in section 4.2. First, an expression for the final wall thickness, t_f of the actuator as a function of initial actuator geometry is developed based on a constant volume assumption.

$$t_f = r_f - \sqrt{r_f^2 - t_k(2r_i - t_k)} \tag{5.1}$$

The expression in (5.1) can be substituted into the following traction force model equation to generate an expression for the traction force as a function of initial actuator geometry. This model is used to calculate the traction force constraint for the grid-search.

$$F_{traction} = 2\pi r_f u_t l_o \left(P - \frac{E\, t_f}{r_i r_f}(r_f - r_i) \right) \tag{5.2}$$

Next, an expression to calculate the safety factor against burst failure is developed. By treating the traction segment as a thin-walled pressure vessel, the hoop stress, σ_h and axial stress, σ_a in the elastomer can be calculated as follows.

$$\sigma_h = \frac{pr_i}{t_k} \tag{5.3}$$

$$\sigma_a = \frac{pr_i}{2t_k} \tag{5.4}$$

The two stress components in (5.3) and (5.4) can be used to calculate the effective stress, σ_e in the elastomer as follows.

$$\sigma_e = \sqrt{\frac{\sigma_h^2 + \sigma_a^2 + (\sigma_a - \sigma_h)^2}{2}} \tag{5.5}$$

Once the effective stress in the elastomer has been calculated, a safety factor against bursting can be calculated by dividing the maximum tensile yield strength, σ_{max} by the effective stress, σ_e as shown below. This calculation is used to constrain the solution space in the grid-search.

$$SF_{burst} = \frac{\sigma_{max}}{\sigma_e} \tag{5.6}$$

Finally, an expression for the input energy per unit of traction force objective must be developed as a function of initial actuator geometry. The energy required to expand the traction segment from its initial volume to its final volume (i.e. where it contacts the wall) can be expressed as follows

$$E_{in} = \int_{V_1}^{V_2} P_{elastic}(V)dV \tag{5.7}$$

where $P_{elastic}$ is the pressure required to expand the actuator. Note that a perfectly cylindrical expansion and constant actuator length are assumed. Next, an expression for $P_{elastic}$ must be developed as a function of the volume to compute the integral and solve for the input energy in (5.7). An expression for $P_{elastic}$ from section 4.2 was presented as follows

$$P_{elastic} = \frac{Et_f(r_f - r_i)}{r_i r_f} \tag{5.8}$$

where t_f is defined in (5.1). To express $P_{elastic}$ in terms of volume, we start with an expression for the actuator fluid volume in its expanded state.

$$V = \pi r_f^2 l_o \tag{5.9}$$

Next, we rearrange the expression in (5.9) and solve for r_f. The resulting is expression is as follows.

$$r_f = \sqrt{\frac{V}{\pi l_o}} \tag{5.10}$$

The expression for t_f in (5.1) and the expression for r_f in (5.10) can be combined and substituted in (5.8) to develop an expression for $P_{elastic}$ as a function of volume. The resulting expression for $P_{elastic}(V)$ is as follows.

$$P_{elastic}(V) = \frac{E\left(\sqrt{\frac{V}{\pi l_o}} - \sqrt{\frac{V}{\pi l_o} - t_k(2r_i - t_k)}\right)}{r_i\sqrt{\frac{V}{\pi l_o}}}\left(\sqrt{\frac{V}{\pi l_o}} - r_i\right) \tag{5.11}$$

The expression for $P_{elastic}(V)$ in (5.11) can now be substituted into the input energy equation in (5.7) and integration bounds for the volume expansion can be added to the expression. The final energy equation with integration bounds is expressed as follows which can be solved numerically.

$$E_{in} = \int_{\pi r_i^2 l_o}^{\pi r_f^2 l_o} P_{elastic}(V)dV \tag{5.12}$$

The performance objective for the traction segment design is to minimize the input energy per unit traction force. Therefore, the final performance objective for the traction segment design can be expressed as follows.

$$Minimize: \frac{E_{in}}{F_{traction}} \tag{5.13}$$

5.3.2 Extending Segment Modeling

The extending segment design is constrained by the extension force and the safety factor against buckling failure. The two objectives are to minimize the energy per unit displacement and to maximize the displacement per actuation cycle. The models used to calculate these constraints and objectives are presented in this section.

First, the generated extension force of the extending segment can be modeled as a function of initial actuator geometry. The $F(\varepsilon,t)$ McKibben force

model was developed by the author in section 2.1, and it was used for modeling the extension force as a demonstration of this design approach. Because the prototype multi-segment robot in this chapter will not have overly-thick walls, other McKibben force models could have been used for this design. For short, thick-walled extenders needed in burrowing applications to generate large elastic and extension forces, the *F(ε,t)* McKibben force model is expected to perform the best for design. The Kothera elastic force term from section 2.1 was also be included in the analysis. With some simple algebraic manipulation, extension force from the fibers, F_{fibers} and the elastic force, $F_{elastic}$ can both be expressed in terms of initial actuator geometry only. The modified expressions are presented as follows.

$$F_{fibers} = P(\pi C_1^2 + \pi C_1\left(\frac{t_k(t_k - d_i)}{C_1(\varepsilon - 1)} + d_i(1 - C_2)\left(\frac{t_k}{C_1 C_2(\varepsilon - 1)} - \frac{1}{sin\Theta_o\sqrt{C_2}}\right)\right)) \tag{5.14}$$

$$F_{elastic} = -\pi E[(r_i^2 - (r_i - t_k)^2)\frac{\varepsilon}{\varepsilon - 1} + \frac{2r_i sin\Theta_o(1-\varepsilon)^2}{\sqrt{C_2}tan^2(\Theta_o)}(\frac{r_i\sqrt{C_2}}{sin\Theta_o} - \frac{t_k}{1-\varepsilon} - \sqrt{\frac{r_i^2 C_2}{sin^2\Theta_o} - \frac{t_k(2r_i\sqrt{C_2} - t_k sin\Theta_o)}{(1-\varepsilon)sin\Theta_o}})] \tag{5.15}$$

As a review from Chapter 2, the lumped parameter coefficients used in (5.14) and (5.15) are defined as follows.

$$C_1 = \sqrt{\frac{d_i^2 C_2}{4sin^2\Theta_o} - \frac{t_k(t_k - d_i)}{\varepsilon - 1}} \tag{5.16}$$

$$C_2 = 1 - cos^2\Theta_o(\varepsilon - 1)^2 \tag{5.17}$$

The total extension force, F_{total} produced by the extending McKibben segment is computed by adding the force terms in (5.14) and (5.15) together. The total

extension force constraint expression is presented as follows.

$$F_{total} = F_{fibers} + F_{elastic} \tag{5.18}$$

The second constraint for the extending segment design is the safety factor against buckling. A detailed review of relevant buckling theory is provided in section 3.1. The critical buckling load, P_{cr}, of the extending segments must first be calculated using Euler-Johnson column theory. Expressions for calculating P_{cr} for both Euler and Johnson column buckling are shown below.

$$EULER: \frac{P_{cr}}{A} = \frac{\pi^2 E}{S_r^2} \tag{5.19}$$

$$JOHNSON: \frac{P_{cr}}{A} = S_{yc} - \frac{1}{E}\left(\frac{S_{yc}S_r}{2\pi}\right)^2 \tag{5.20}$$

Once the critical buckling load is calculated using either (5.19) or (5.20), the safety factor against buckling, SF_{buckle} can be calculated as follows.

$$SF_{buckle} = \frac{P_{cr}}{F_{total}} \tag{5.21}$$

The first objective of the extending segment design is to minimize the energy per unit displacement. The energy required to extend the actuator from its initial length to its final length is defined with integration bounds as follows

$$E_{in} = \int_0^{l_f - l_i} F_{total}(x)dx \tag{5.22}$$

where x represents the displacement of the extending segment. The expression

for the total extension force, F_{total} in (5.18) can be rewritten in terms of x by defining a simple relationship between contraction ratio, ε and displacement, x as follows.

$$\varepsilon = -\frac{x}{l_o} \tag{5.23}$$

The expression in (5.23) can be substituted into (5.18) to generate an integratable expression for $F_{total}(x)$ as a function of displacement, x instead of contraction ratio, ε. Because the expression for $F_{total}(x)$ is expressed in terms of displacement, x, it can be substituted into the energy equation in (5.22). The energy equation in (5.22) can then be numerically integrated to determine the input energy required to extend the actuator. Note that the weight of the robot and the friction forces acting on the front of the robot as it locomotes are ignored in this analysis. The objective to minimize the energy per unit displacement can be expressed as follows.

$$Minimize: \frac{-E_{in}}{\varepsilon} \tag{5.24}$$

The second and final objective of the extending segment design is to maximize the displacement per actuation cycle of the robot. The most negative contraction ratio, ε_{max} (extension produces a negative contraction ratio) that an extending segment can achieve can be calculated based on the initial fiber angle, θ_o and the kinematic fiber-lock angle of θ = 54.7 degrees. As a review from Chapter 2, the relationship between initial fiber-angle, final fiber-angle, and contraction ratio can be defined with the following expression.

$$\sin(\Theta) = \sqrt{1 - (1-\varepsilon)^2 \cos^2(\Theta_o)} \tag{5.25}$$

To determine the most negative contraction ratio, $\theta = \theta_{lock} = 54.7$ degrees is substituted into (5.25) and the expression is rearranged to solve for ε_{max}. The resulting expression defines ε_{max}.

$$\varepsilon_{max} = 1 - \sqrt{\frac{1 - sin^2\,\theta_{lock}}{cos^2\,\theta_o}} \tag{5.26}$$

The maximum displacement, δ_{max} that an extending segment can achieve based on physical fiber limitations can be easily calculated by multiplying the negative contraction ratio by the initial length of the actuator as follows.

$$\delta_{max} = -\varepsilon_{max} l_o \tag{5.27}$$

5.4 **Grid-Search**

A grid-search was used to sweep through initial actuator geometry combinations to understand the solution space and determine which set of initial geometry satisfies all constraints and best meets the performance objectives for the traction segments and the extending segment. The grid-search was performed separately for extending segment and the traction segments. First, the extending segment design grid-search was performed, and extender geometry was selected. The selected extender geometry was fed into the traction segment design grid-search, and the final robot geometry was selected. An application was designed using Matlab that was able to sweep many combinations of input geometries, calculate the constraint and performance values, and visually display the solution-space for interpretation. Two undergraduate students from the

Mechanical Energy and Power Systems Lab, Junchi Feng and Jack Sonstegard, contributed significantly to the development of the application.

5.4.1 Extending Segment Grid-Search

The initial geometry variable ranges were selected for the extending segment to keep the number of solutions manageable in the grid-search. The initial fiber angle was selected to be 80 degrees. The initial geometry parameter ranges were selected based on the constraints discussed in section 5.1 and what clear tube combinations were available in the lab for fabricating the multi-segment robot elastomer. The initial length of the extending segment was allowed to vary from 76.2 mm to 152.4 mm in 25.4 mm increments. The initial outside diameter of the segment was allowed to vary from 38.1 mm to 50.8 mm in 6.35 mm increments. Finally, the wall thickness was allowed to vary between 3.2 mm and 4.8 mm.

The most negative contraction ratio (most extension) possible for each set of initial geometry was calculated using (5.26) and (5.27) from section 5.3.2, and the contraction ratio in the grid-search was allowed to vary between zero and the most negative contraction ratio in four equal increments for each set of initial actuator geometry. Once the four contraction ratio values were calculated for each set of geometries, the minimum input pressure, P_{min} required to cause the actuator to extend to each of the contraction ratios was calculated using (5.14) - (5.18) from section 5.3.2.

Because P_{min} is the minimum required pressure to extend the actuator to a specified contraction ratio, no extension force can be produced at this contraction ratio unless the pressure is increased beyond P_{min}. Two operating pressures larger than P_{min} were selected to be included in the analysis. The first value selected was the mean pressure value between P_{min} and the maximum allowable pressure, P_{max}. The second selected value was the maximum allowable pressure, P_{max}. Allowing both the extension of the actuator and the input pressure of the actuator to vary in the solution-space allows a better understanding of how the extending segment will perform in various operating situations (i.e. partially extended, max extension, various pressures, etc). A total of 24 different initial extending segment geometries were explored at four different contraction ratios at two different operating pressures, which results in a total of 192 solution points to examine. Each distinct initial geometry contains eight data points, representing the results at two different pressures at four different contraction ratios. A summary of the extending segment grid-search parameters is shown in Table 14.

Table 14: Varying parameters for extending segment grid-search

		Parameter Iterations			
Variable	**Description**	**1**	**2**	**3**	**4**
l_o	initial actuator length	76.2 mm	101.6 mm	127.0 mm	152.4 mm
d_i	initial elastomer outside diameter	38.1 mm	44.5 mm	50.8 mm	
t_k	initial elastomer wall thickness before extension	3.2 mm	4.8 mm		
ε	contraction ratio	0	0.33* ε_{max}	0.67* ε_{max}	ε_{max}
P	input fluid pressure	(P_{min}+P_{max})/2	P_{max} =		

		MPa	207 kPa		

The parameters ranges were programmed into the Matlab application, and all constraint values and performance objective values were calculated and plotted on a 3D plot. The results of the extending segment grid-search are shown in Figure 160.

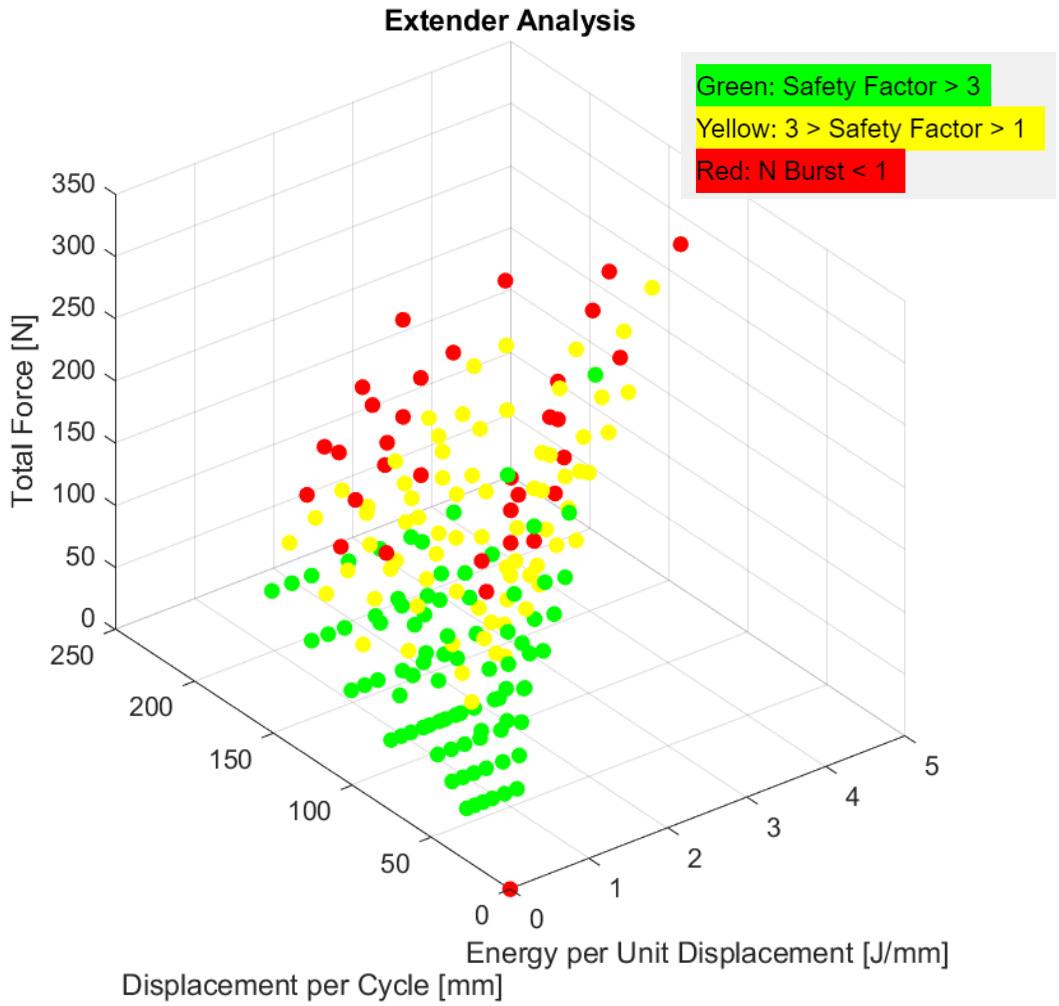

Figure 160: Extending segment grid-search results

Each dot represents one of the 24 initial geometries at one of the eight pressure-contraction ratio combinations. The color of the dot represents the safety factor against buckling failure for the geometry at the pressure-contraction ratio

combination as shown in the legend. When the Matlab application user clicks on one of the dots in the program, the eight solutions that are linked to the initial geometry are circled. Furthermore, the initial geometry of the data point and the constraint and objective values are displayed for the data point. For example, if the user clicks on the green dot in the top right of Figure 160, the depiction shown in Figure 161 is displayed.

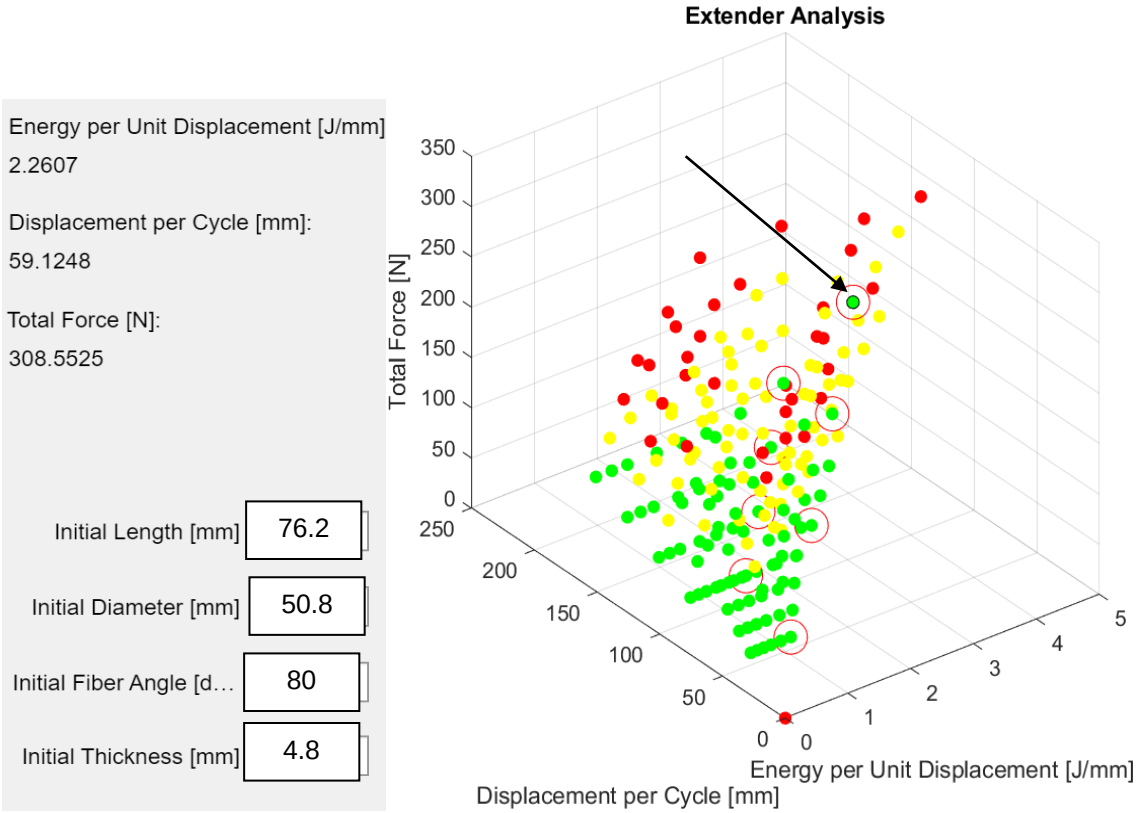

Figure 161: Extending segment grid-search results with solutions circled

The user can click through all the solution points to understand what the initial geometry of the data point was, if the data point meets the constraints, if the data point meets the performance objectives, and how other data points with the same initial geometry behave at different contraction ratios and pressures. It also allows the user to get an intuitive feel about how specific design parameters

impact the performance of the robot segment. When viewing the possible extending segment solution data points, it can be observed that there are only four possible data points with a factor of safety against buckling greater than 3 that are able to produce at least 180 N of total extension force. If we rotate the view of the 3D plot from Figure 161, the four points with a safety factor against buckling greater than 3 and total extension greater than 180 N can be easily identified as shown in Figure 162.

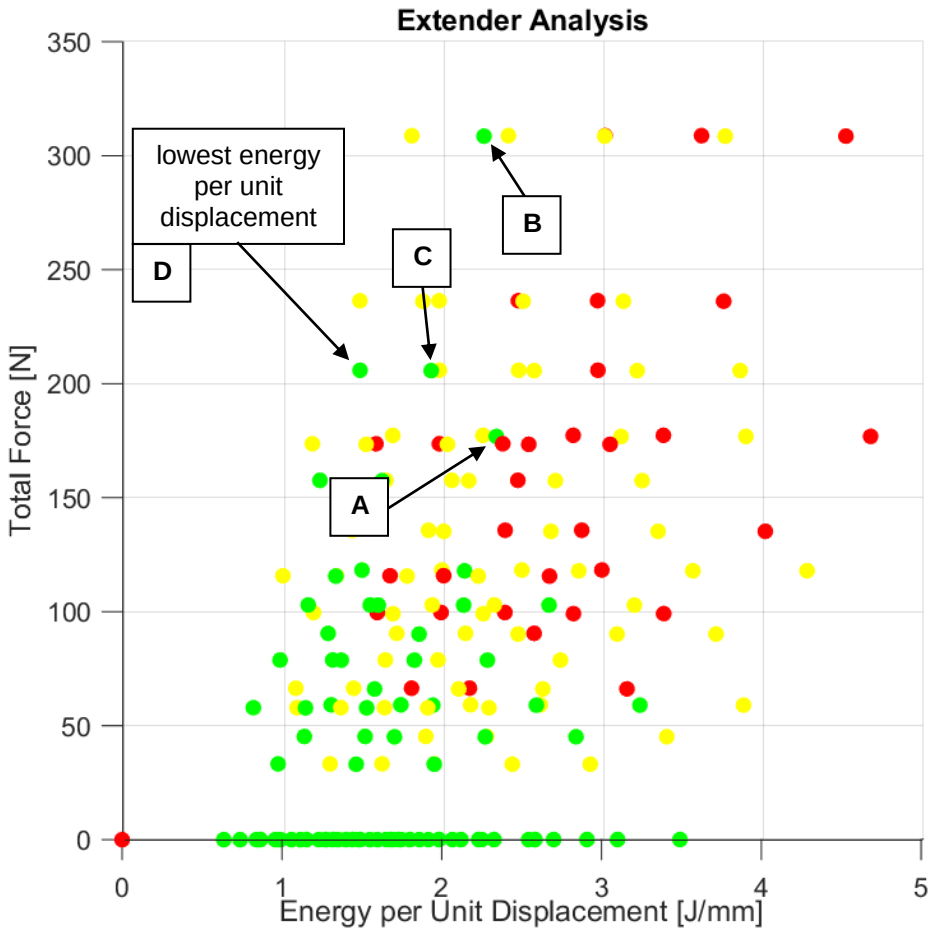

Figure 162: Extending segment grid-search with force greater than 180 N

Upon further inspection of the four potential candidates, it can be observed that data point D in Figure 162 has the lowest energy per unit

displacement. If the plot is rotated to show the total force and displacement per cycle, it can be observed that there is a trade-off between energy per unit displacement and displacement per cycle as shown in Figure 163.

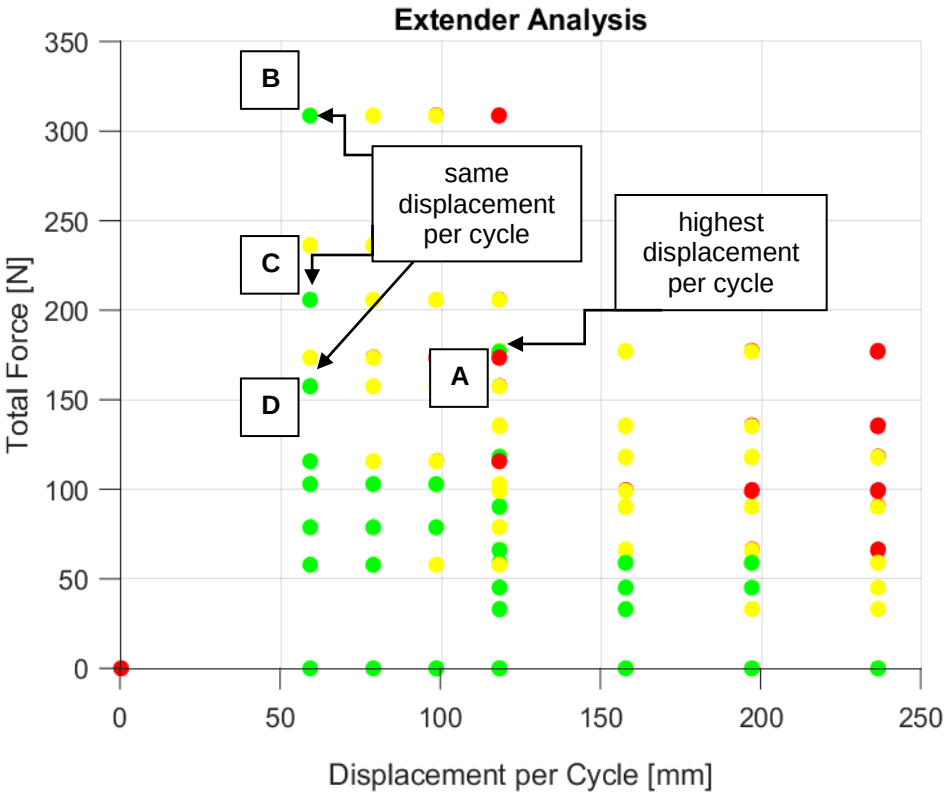

Figure 163: Extending segment grid-search results - displacement per cycle

The three solutions on the left (labelled B, C, and D in Figure 163) have the same displacement per cycle, and the solution on the right (labelled A) has a slightly larger displacement per cycle. However, solution A requires more energy per unit displacement. Upon further inspection of the potential solutions, it can be observed that data points A, B, and C are the same initial geometry actuator operating at different pressure and contraction ratio combinations. Data point D has the same initial geometry as A, B, and C with the only exception being a smaller initial wall thickness. It makes sense that the actuator geometry with the

smaller wall thickness requires less energy per unit extension. Table 15 shows the constraint and objective values, along with the initial geometry, for the four candidate data points.

Table 15: Extending segment candidate data

Variable	Data Point			
	A	**B**	**C**	**D**
Initial Length, l_o (mm)	76.2	76.2	76.2	**76.2**
Initial Diameter, d_i (mm)	50.8	50.8	50.8	**50.8**
Initial Wall Thickness, t_k (mm)	4.8	4.8	4.8	**3.2**
Initial Fiber Angle, θ_o (deg)	80	80	80	**80**
Energy per Unit Displacement (J/mm)	2.3	2.3	1.9	**1.5**
Displacement per Cycle (mm)	118.2	59.1	59.1	**59.1**
Total Extension Force (N)	176.8	308.6	205.7	**205.9**
Operating Pressure (MPa)	0.207	0.207	0.207	**0.207**

When determining which of the two actuator geometries to choose from for the final extending segment design, the geometry of data point D stands out for a number of reasons. The geometry of data point D provides the lowest energy per unit displacement of all of the candidates, and it is still able to provide displacements of nearly 60 mm per cycle within the pressure constraints. Furthermore, it has a safety factor against bursting over 3, can generate over 200 N of extension force at this displacement, and is able to operate at the 207 kPa operating pressure constraint. Therefore, solution D was selected for the multi-segment design. These extending segment design parameters will feed into the traction segment design grid-search that will be presented in the following section and eventually used to fabricate the robot for experimentation.

5.4.2 Traction Segment Grid-Search

A similar approach was employed to select the variable ranges for the traction segment design grid-search. However, the results from the extending segment design grid-search played a guiding role in selecting the traction segment geometry. Because of the constant wall thickness elastomer constraint for the entire robot, the initial outside diameter and wall thickness of the traction segments was selected to be the same as the extending segment (d_i = 50.8 mm and t_k = 3.2 mm). Keeping in mind that the two traction segments were constrained in the design to be the same length, the total robot length constraint can be used to determine the maximum allowable initial length of the traction segments. Because the entire robot length must be <= 610 mm, and it has been determined that the extending segment and four segment connectors are 76.2 mm and 38.1 mm respectively, the maximum initial length of each of the traction segments was determined to be 190.7 mm. This allows the traction segment grid-search to be set up in a simple fashion. The initial actuator length was allowed to vary between 88.9 mm and 190.7 mm in 25.4 mm increments, the initial actuator outside diameter was set to 50.8 mm, and the initial actuator wall thickness was set to 3.2 mm.

Three different traction segment expansion diameters (in this case the inside diameter of the clear polycarbonate tube the actuator will traverse) were selected for the analysis, and each expansion diameter was tested at three different operating pressures to understand how the traction segment performs in

different operating conditions. The three expansion diameters selected were 1.66, 2.33, and 3.00 times the initial traction segment diameter to ensure the traction segment could anchor across a wide range of tube diameters and meet the maximum expansion diameter constraint of 3 times the initial segment diameter outlined in section 5.1.2. It was desirable to allow the expansion diameter to vary in the analysis to understand how particular traction segment geometries performed as they radially expanded to different diameters at varying operating pressures like what would be observed in a burrowing application. Equations (5.1) and (5.8) from section 5.3.1 were used to calculate the minimum operating pressure, $P_{elastic}$, required to expand the actuator to become in contact with the tube (i.e. expand to the diameter where traction force is about to be developed). The operating pressure was allowed to vary between $P_{elastic}$ and P_{max} (207 kPa) in three increments.

Five extending segment geometries were explored at three different expansion diameters (i.e. tube diameters) at three different operating pressures, which results in a total of 45 solution points to examine (nine data points for five geometries). A summary of the traction segment grid-search parameters is shown in Table 16.

Table 16: Varying parameters for traction segment grid-search

		Parameter Iterations				
Variable	**Description**	**1**	**2**	**3**	**4**	**5**
l_o	initial actuator length	88.9 mm	114.3 mm	139.7 mm	165.1 mm	190.5 mm
d_i	initial elastomer outside diameter	50.8 mm				
t_k	initial elastomer wall thickness before extension	3.2 mm				
d_f	final expansion diameter	1.66* d_i	2.33* d_i	3.00* d_i mm		
P	input fluid pressure	$P_{elastic}$	($P_{elastic}$ + P_{max})/2	P_{max} = 207 kPa		

The parameters ranges were again programmed into the Matlab application, and all constraint values and performance objective values were calculated and plotted for interpretation. The results of the traction segment grid-search are shown in Figure 164.

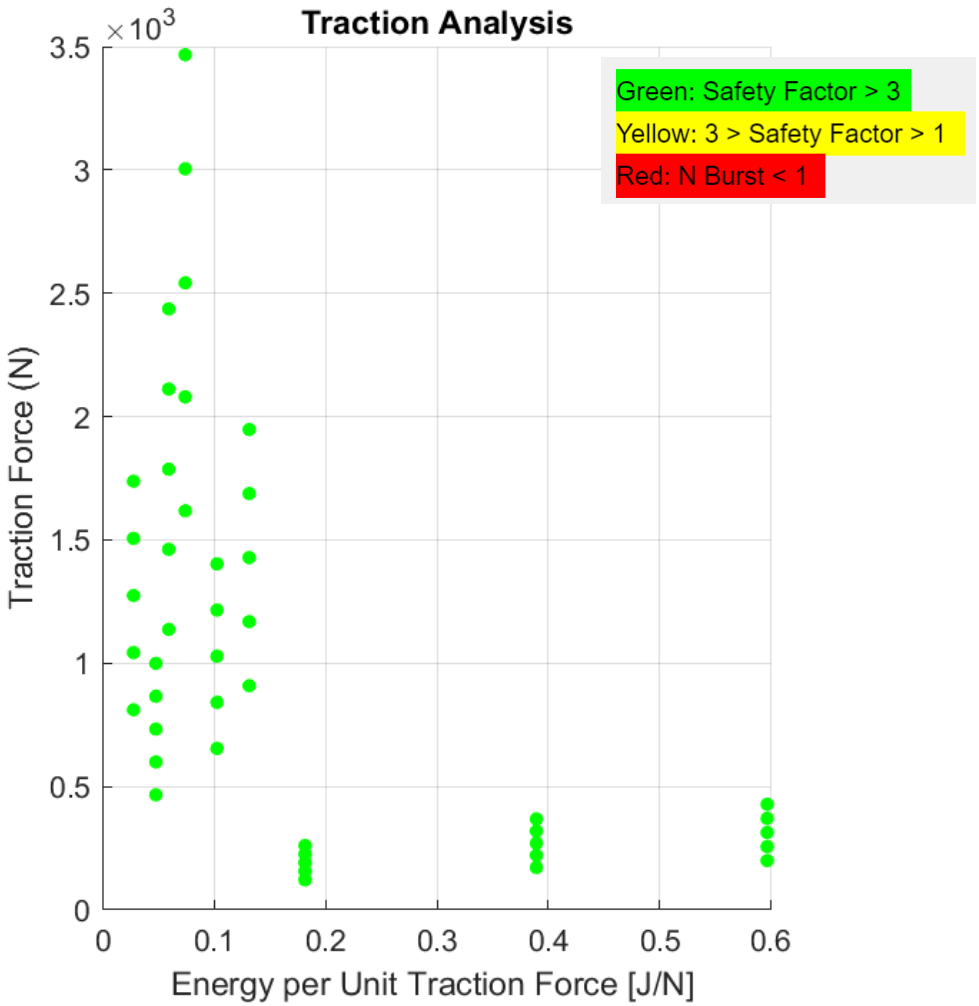

Figure 164: Traction segment grid-search results

The results from the traction segment grid-search show that all the data points meet the safety factor against bursting >= 3 constraint. When the designer selects a data point on the plot, all the other data points that have the same initial geometry are circled. This allows the designer to click through each of the data points to determine how the operating pressure and desired expansion diameter impact the energy efficiency and traction force generation capabilities of the traction segment. Figure 165 shows a data point selected and the associated geometry, constraint calculations, and performance objective calculations.

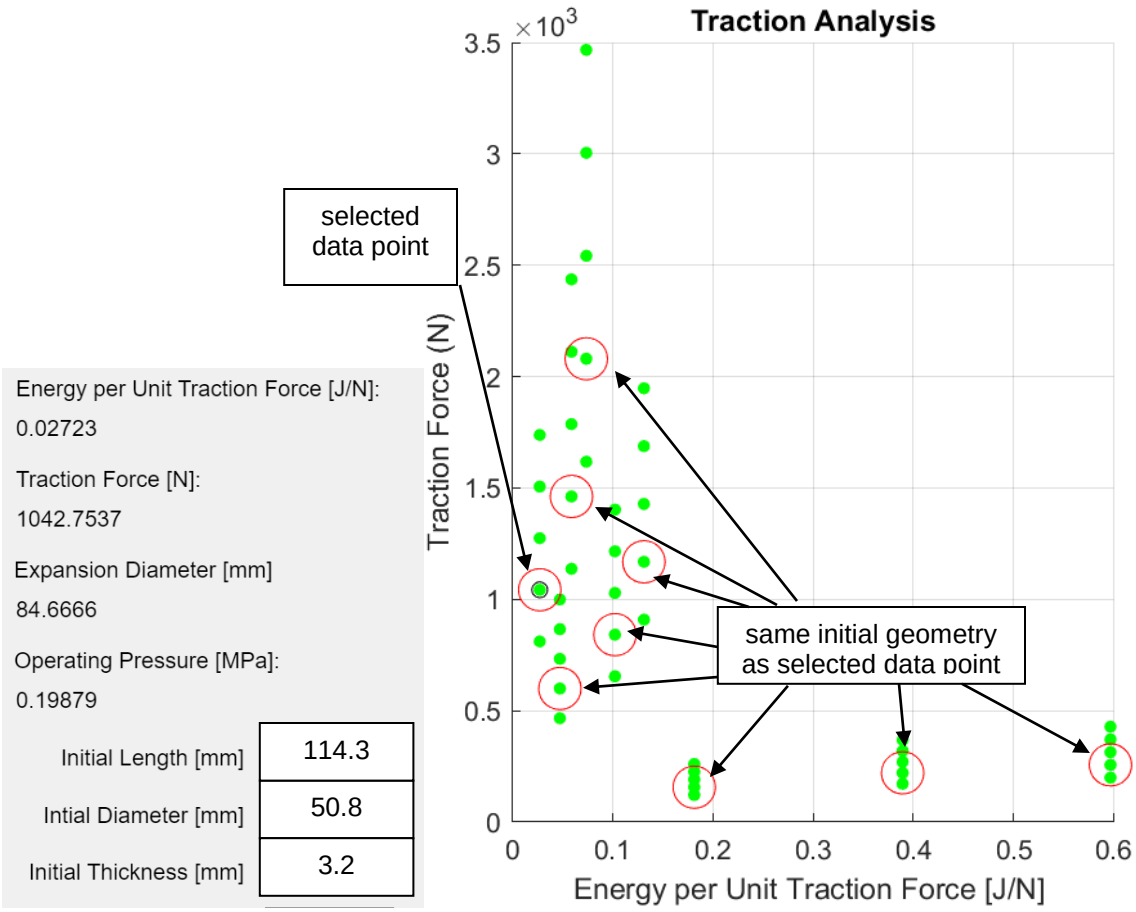

Figure 165: Traction segment grid-search results w/ data point circled

It is easy to observe from Figure 165 that nearly all the data points produce a traction force over the constraint value of 180 N. Since ample traction force can be generated with all the design options, a design that minimizes the energy per unit traction force must be selected. The five left-most, vertically-stacked data points, shown in Figure 166, have the lowest (and same) energy per unit traction force, meet the safety factor against bursting constraint, and generate sufficient traction force.

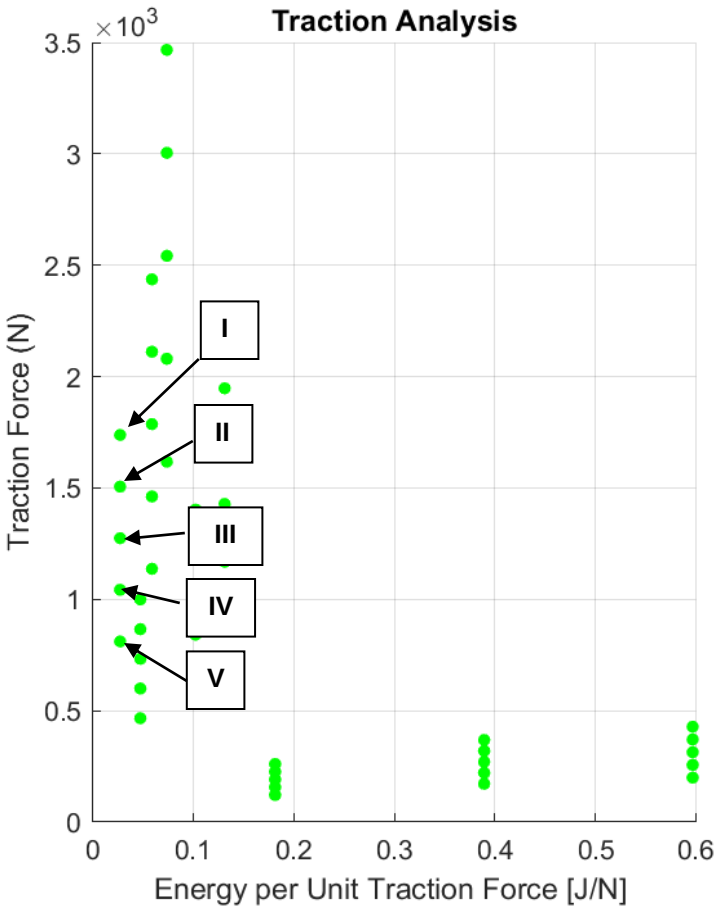

Figure 166: Traction segment grid-search results with lowest energy per unit traction force

The five labelled data points in Figure 166 are the best candidates to select for the traction segment design based on the initial constraints and performance objectives. All five of the data points have the same operating conditions (operating pressure and expansion diameter) and initial geometry, and the only difference between the five data points is the initial length of the segment. Table 17 shows the constraint, objective values, initial geometry, and operating conditions for the five candidate data points.

Table 17: Traction segment candidate data

Variable	Data Point				
	I	**II**	**III**	**IV**	**V**
Initial Length, l_o (mm)	190.5	165.1	139.7	**114.3**	88.9
Initial Diameter, d_i (mm)	50.8	50.8	50.8	**50.8**	50.8
Initial Wall Thickness, t_k (mm)	3.2	3.2	3.2	**3.2**	3.2
Energy per Unit Traction Force (J/N)	0.027	0.027	0.027	**0.027**	0.027
Traction Force (N)	1738	1506	1274	**1043**	811
Expansion Diameter (mm)	84.7	84.7	84.7	**84.7**	84.7
Operating Pressure (MPa)	0.207	0.207	0.207	**0.207**	0.207

As the models predict, the longer traction segments are expected to produce larger traction forces with the same input energy per unit traction force. However, the longer the traction segments become, the more fluid is required to actuate them, and the slower the overall actuation cycle of pumping and draining fluid in and out of the robot becomes. Furthermore, shorter traction segments allow the robot to be more compact, handle easier in testing, require less manufacturing materials, and require less extension force to move the mass of the robot along the tubular environment. Therefore, data point IV from Table 17 was selected for the traction segment design because it was the second shortest traction segment design option and is still able to produce over 1000 N of traction force at an operating pressure of 207 kPa in a burrow diameter of 84.7 mm (satisfying the expansion diameter design requirement of 3 times the initial segment diameter) with a safety factor against bursting > 3. Thus, with the segment connectors, two traction segments, and the extending segment included, the total length of the multi-segment robot is less than 610 mm. This satisfies the length requirements as well as all other constraints outlined in section 5.1. Furthermore, this design

selection simplifies the control of the robot since all three segments will run at the same operating pressure.

Because the anchoring segments interact directly with the burrow or tube-wall, it could be argued that the traction segment grid-search could have been performed first and the results could have been fed into the extending segment design. However, when analyzing the solution space of the respective segment grid-searches, it can be observed that the extra performance objective for the extending segment yielded a more complex, three-dimensional solution space with less design freedom than the traction segment solution space. This provides some justification for the sequential design process used to select the geometry of the robot segments. In future multi-segment robot designs where some of the design constraints can be relaxed (traction segment lengths can vary, non-uniform wall thickness allowed, more segments etc) for more specific robot design applications (particular soil substrate, particular expansion diameter, unique motions/forces, travel speed requirements, etc), the segment solution spaces could be solved simultaneously to develop a more detailed understanding of how the geometry of one segment can impact the performance of another segment – relative to the particular design requirements for the given application.

5.5 **Manufacturing**

The multi-segment robot was manufactured using many of the techniques discussed in earlier chapters. First, the elastomer was cast using the 3D printed

port blocks, an aluminum rod, polycarbonate tubes, and Polytek74-55A elastomer resin. The injected elastomer (still in the assembly) can be observed in Figure 167.

Figure 167: Injected elastomer in port block assembly

Once the elastomer was allowed 24 hours to cure, the port blocks were removed from the assembly. The entire aluminum rod with the elastomer covering it was loaded into the fiber-wrapping lathe, and fibers were applied over the central section of the elastomer that was designated for the extending segment of the robot. The same methods for applying fibers from previous chapters were used here. First, fibers were applied in the forward direction as shown in Figure 168 and Figure 169.

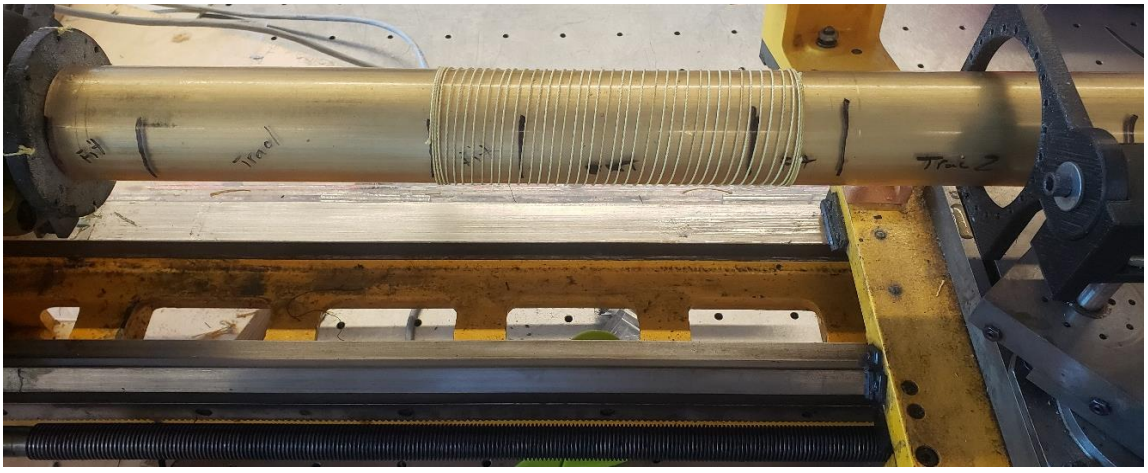

Figure 168: Forward wrapped fibers on extending section of elastomer

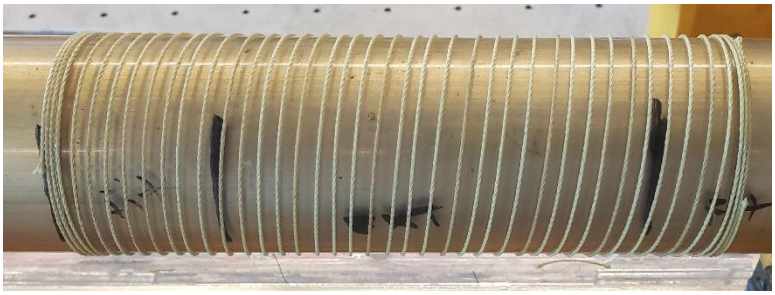

Figure 169: Close-up view of forward wrapped fibers

Once the forward fibers were applied, the next set of fibers were applied in the reverse direction. Once the second set of fibers were applied, the entire system was removed from the fiber wrapping lathe. The fiber-wrapped elastomer can be observed in Figure 170. Note that the areas designated for the segment connectors and robot segments are marked in the figure. It can be observed that fibers were applied over a longer length of elastomer to ensure that the zip ties could secure them to the elastomer and segment connectors.

Figure 170: Completed fiber-wrapped elastomer

Next, the spiral microbore spring was fabricated. First, a 3D printed mold was designed to form the spiral. Using the minimum bend radius of the Nylon-12 microbore tubing and the inside diameter of the elastomer, the mold was

designed such that the outside edge of the spiral would be in contact with the inside diameter of the elastomer in a relaxed condition. Once the 3D printed part was designed and printed with ABS filament, the microbore tubing was tightly wrapped around it and zip tied on the ends. Figure 171 demonstrates how the microbore tubing was zip tied around the 3D printed (ABS filament) mold to keep two small straight sections of microbore tubing on each end of the assembly. The straight sections will be cut to length and installed into the compression fittings in the segment connectors.

Figure 171: Microbore tube spiral zip tied to 3D printed mold

Once the microbore tube was zip tied to the 3D printed mold with a straight section on each end, a pot of water was brought to a boil. Once the water was boiling, the mold assembly was dunked under the water for 30 seconds. After 30 seconds, the mold was removed and quenched in an ice bath for 30 seconds. Next, the zip ties were cut free and the spiral microbore tube was removed from the assembly as shown in Figure 172.

Figure 172: Microbore spiral removed from 3D printed mold after ice bath (note: different clear microbore tubing shown here)

Once the microbore spiral was formed, the other straight sections of microbore tubing were cut to length for the proximal traction segment. The plugs, compression fittings, and threaded rods were installed onto the segment connectors. Finally, both straight sections and the spiral section of microbore tubing were tightened down into the compression fittings. Figure 173 shows the completed internal structure of the multi-segment robot.

Figure 173: Completed internal structure of multi-segment robot

Once the internal structure of the robot was complete, the fiber-wrapped elastomer was removed from the aluminum rod and slid over the internal structure carefully to ensure that the segment connectors and segments were all in the correct axial position. Once the internal structure was located properly within the elastomer, low profile zip ties were used to secure the elastomer to the segment connectors to form the segments of the multi-segment robot. The zip tie on the furthest distal end of the robot was left loose until the actuator was primed with hydraulic fluid to remove the air. Electrical tape was used as a barrier between the zip ties and the elastomer to prevent damage to the elastomer. Note that the spiral micro-bore tubing was slightly compressed in its final position to help prevent pull out forces between the microbore tubing and the compression fittings. Figure 174 shows the completed multi-segment robot before electrical tape and zip ties were applied.

Figure 174: Completed multi-segment robot before electrical tape and zip ties are applied (top: with fibers, bottom: without fibers)

Three input microbore lines were connected to the proximal end of the robot to supply input fluid to each of the three segments. Hydraulic fluid was forced into the segments to bleed air from the system. Once all the segments were primed with hydraulic fluid, the last zip tie was secured, and the robot was completed. Figure 175 shows the finalized and primed multi-segment robot.

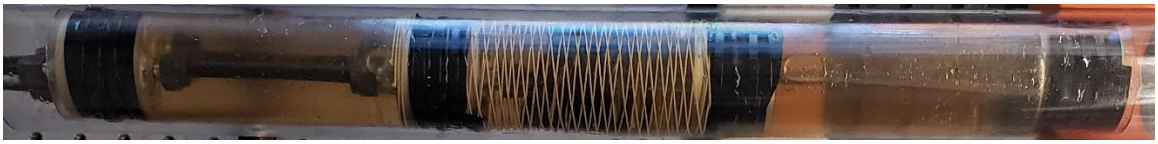

Figure 175: Finalized multi-segment robot

5.6 **Methods**

5.6.1 Experimental Apparatus

An experimental apparatus was fabricated to test the multi-segment robot as it locomotes through varying tube diameters. A 3D printed base stand was mounted to the test bench and 3D printed support blocks were mounted on the base stand. The 3D printed support blocks were able to rigidly hold polycarbonate tubes of various diameters for testing the robot over a range of tube sizes. A simple hydraulic circuit consisting of a single manual valve to actuate each robot segment was constructed and is shown in Figure 176.

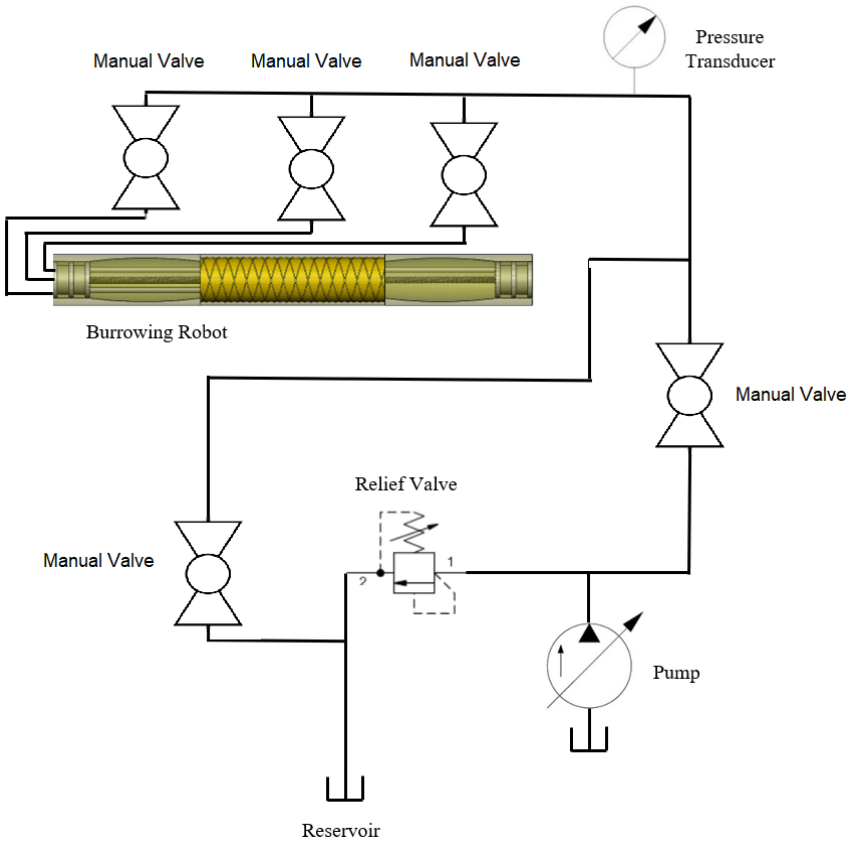

Figure 176: Hydraulic circuit for controlling the multi-segment robot

The experimental apparatus was equipped with the same pressure transducer as the previous experiments, and a labelled depiction of the test set up is shown in Figure 177.

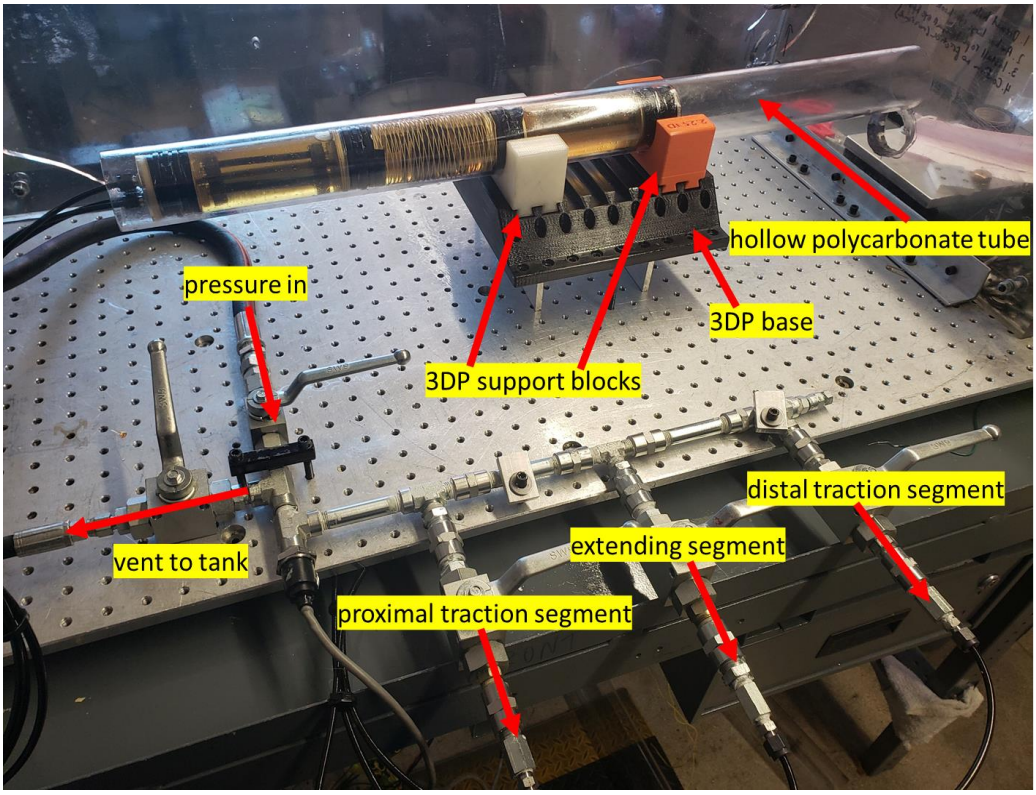

Figure 177: Experimental apparatus for multi-segment robot experiments

5.6.2 Experimental Procedure

A series of very simple experiments were conducted to validate the design and demonstrate how the multi-segment robot can navigate through tubular environments like a burrow. The 50.8 mm outside diameter multi-segment robot was tested in two different sized polycarbonate tubes with inside diameters of 57.2 mm and 63.5 mm respectively. The system pressure was set to 207 kPa for all experiments. First, the robot was tested in the 57.2 mm tube in a horizontal configuration to show that it was able to navigate in both the forward and reverse directions. Similarly, the robot was tested in a horizontal 63.5 mm tube to

demonstrate it could navigate in both directions. Finally, the robot was tested in the 63.5 mm tube in a vertical position to show it could navigate a vertically positioned tube against gravity.

First, all manual valves were closed, and the pressure relief valve was set to maintain a system pressure of 207 kPa. Next, the input pressure valve was opened to pressurize the pressure rail connecting the three actuator segments. Then the proximal traction segment valve was opened to actuate the first anchoring segment. Once the proximal traction segment expanded enough to establish a contact length between the segment and the polycarbonate tube that is the same as the initial length of the segment, the proximal traction segment valve was closed. At this point, the extending segment valve was opened, and the segment began to extend. Once the segment extended ~25 mm, the extending segment valve was closed. Next, the distal traction segment valve was opened, and the segment was allowed to expand. Once it had expanded, the proximal traction segment valve was closed, and the input pressure valve was closed to depressurize the pressure rail. The tank valve and proximal traction segment valve were opened to depressurize the proximal traction segment. Once the proximal traction segment was depressurized, the extending segment valve was opened to drain the fluid in the segment to tank. This caused the elastic force from the extending segment to pull the back end of the robot towards the anchored distal traction segment. Once the extending segment was completely relaxed, the proximal traction segment was pressurized, the distal traction

segment drained, and then the extending segment extended. This cycle was repeated to move forward and then the sequence was reversed to move the robot backward through the tubes. Figure 178 shows the motions of the three robot segments during the experiments.

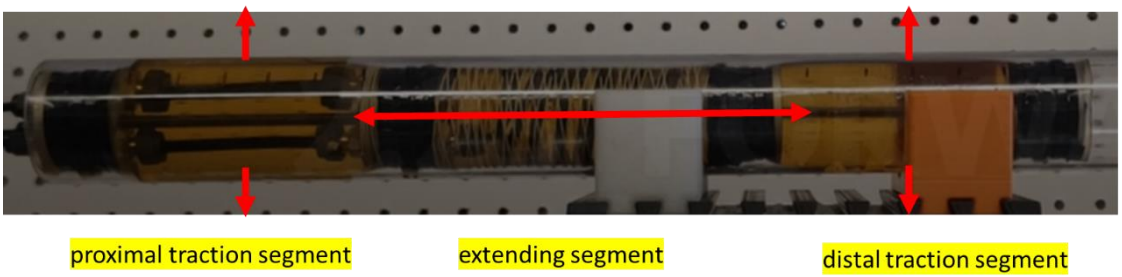

Figure 178: Multi-segment robot with motions and segments shown

5.7 Results and Discussion

The multi-segment robot was fabricated and tested in two different sized tubes following the experimental procedure to demonstrate its ability to traverse through the rigid tubes. First, the robot was placed inside the 57.2 mm inside diameter clear tube, the pressure was set to 207 kPa, and the robot actuation cycle was initiated to move the robot forward through the tube. The robot was carefully watched as the segments were actuated in case segment failure occurred, and a camera was used to record the robot as it moved forward through the tube. Figure 179 shows a screenshot of the 57.2 mm diameter tube experiment being run in the forward direction, and Figure 180 shows the sequence of segment locomotion.

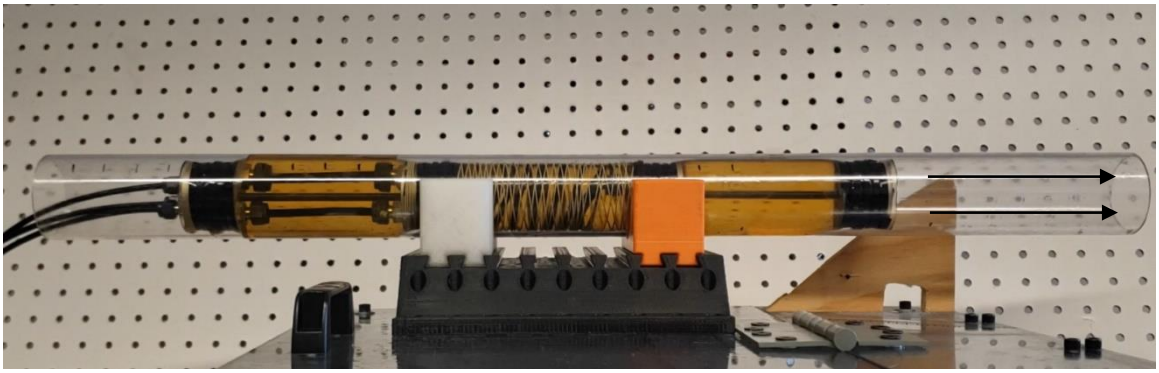

Figure 179: Multi-segment robot halfway through the 57.2 mm tube in the forward direction

Figure 180: Multi-segment robot sequence through the 57.2 mm tube in the forward direction

The flow rate of the hydraulic fluid through the small diameter microbore tubes to and from the segments was slow which caused the entire robot to move slowly throughout the tube. The robot was able to move forward through the tube in ~18 minutes using ten displacement cycles, but this time was significantly impacted by how the operator controlled the robot (care was taken not to extend the robot too far or expand the segments too much to avoid damage). Furthermore, it took an especially long time to drain the hydraulic fluid from the segments to tank when depressurizing the segments, because the elastic force of the elastomer was the only thing forcing the fluid through the microbore tubing back to tank. When the robot reached the end of the tube, the pressure was drained from all the segments, and the video recording was paused. The following link presents a sped-up speed video of the multi-segment robot traversing the 57.2 mm polycarbonate tube in the forward direction.

https://drive.google.com/file/d/13ZORqcuo8C54FzFRqbXmwd-6WkTksV9U/view?usp=sharing

The robot was easily able to extend over 25 mm in each extension cycle, and no segment failure was observed in the forward direction. Next, the exact same process was repeated except in the opposite order to cause the robot to retrace its travel and move backwards through the tube. Figure 181 shows the robot in the 57.2 mm polycarbonate tube in its first reverse actuation cycle where all three

segments are currently actuated, and Figure 182 shows the reverse sequence of locomotion through the tube.

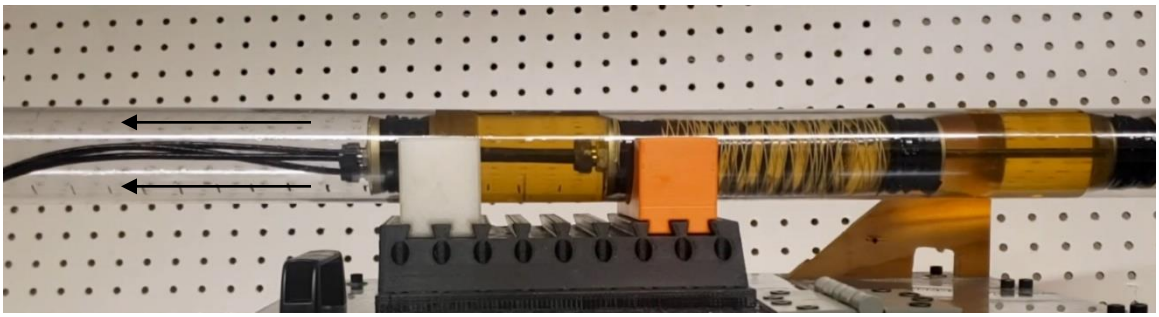

Figure 181: Multi-segment robot beginning reverse actuation cycle through the 57.2 mm tube

Figure 182: Multi-segment robot sequence through the 57.2 mm tube in the reverse direction

There was no clear operational difference between the forward and reverse cycles of the robot, and the robot was even able to perform longer extensions (some over 35 mm) in the reverse cycle than the forward cycle for the 57.2 mm polycarbonate tube. By allowing longer extensions and carefully timing the

segment actuation, the robot was able to traverse the tube in ~15 minutes with seven cycles instead of ~18 minutes with ten cycles in the forward direction. Longer extensions were avoided in early experiments to avoid damaging the robot before conducting all the experiments. The following link presents a sped-up video of the multi-segment robot traversing the 57.2 mm polycarbonate tube in the reverse direction.

https://drive.google.com/file/d/1d01_K49EHIClLMOnU3nZHhW-W0X5v8GR/view?usp=sharing

Next, the same process was employed to test the multi-segment robot in the larger 63.5 mm inside diameter polycarbonate tube. The robot was first tested in the forward direction, and the robot was carefully monitored to ensure no damage was incurred to the robot during actuation. Figure 183 shows the robot after the proximal traction segment was actuated, and the extending segment was beginning to push the front part of the robot through the tube in the forward direction, and Figure 184 shows a sequence of the robot as it traverses the tube.

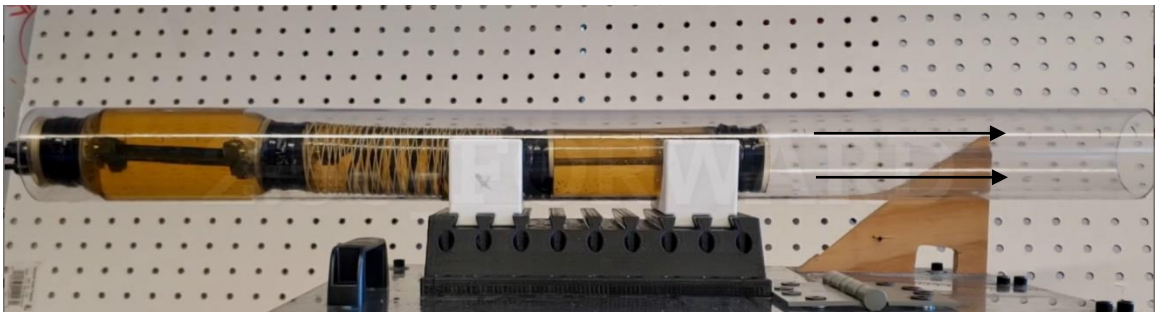

Figure 183: Multi-segment robot beginning to move through the 63.5 mm tube in the forward direction

Figure 184: Multi-segment robot sequence through the 63.5 mm tube in the forward direction

The robot performed well in the 63.5 mm tube, but the additional fluid volume required to expand the traction segments in the 63.5 mm tube slowed down how fast the robot could go through its actuation cycle and move through the tube. The robot was able to traverse the length of the tube in ~20 minutes with eight actuation cycles. The following link presents a sped-up video of the multi-

segment robot traversing the 63.5 mm polycarbonate tube in the forward direction.

https://drive.google.com/file/d/1TMSPk4p0zzEk5MNDX6DgryM-kKZ9UIu0/view?usp=sharing

The robot was also able to move in the reverse direction in the 63.5 mm polycarbonate tube without any issues. Figure 185 shows the robot with all three segments actuated halfway back through the tube in the reverse direction, and Figure 186 shows the robot locomotion sequence.

Figure 185: Multi-segment robot halfway through the 63.5 mm tube in the reverse direction

Figure 186: Multi-segment robot sequence through the 63.5 mm tube in the reverse direction

The robot was able to move in the backwards direction through the tube in ~20 minutes using eight actuation cycles, which is the same speed and number of cycles as in the forward direction. This confirmed that the robot can travel the same speed and method in both directions. The slower travel speed for the larger diameter polycarbonate tube was expected since more fluid volume is needed to be pumped into the traction segments to expand to the larger diameters. While the robot appears to sag a bit due to gravity in Figure 186, this did not appear to impact the robot's ability to move through the tube. The following link presents a sped-up video of the multi-segment robot traversing the 63.5 mm polycarbonate tube in the reverse direction without issue.

https://drive.google.com/file/d/1JoQvoIerBFqCkcrAsGtvBk0Wv4ekEpHZ/view?usp=sharing

The final experiment that was conducted was running the multi-segment robot through the 63.5 mm polycarbonate tube in the vertical direction against gravity. The robot was placed in the tube and manually held in place until the distal traction segment was actuated to anchor the robot system in the tube, so the robot could begin traversing up the tube. Figure 187 shows the robot with all three segments actuated partially up through the vertical tube (against gravity) in the forward direction, and Figure 188 shows the robot sequence.

Figure 187: Multi-segment robot halfway up through the vertical 63.5 mm tube in the forward direction

Figure 188: Multi-segment robot sequence through the 63.5 mm tube in the vertical orientation

When the robot was tested in the vertical 63.5 mm tube, two issues occurred that caused the robot to partially slip as it made its way up the tube. The first issue was caused by operator error when the input pressure was cut off to the distal traction segment before it was fully expanded. Although the operator thought the distal traction segment was fully expanded, when the proximal traction segment was vented to tank and depressurized, the entire robot began slipping down the tube because insufficient traction force was generated during that cycle in the distal traction segment. While this error could have been avoided with more attention to detail when operating the robot, it demonstrates the importance of timing segment actuation to get the best robot performance and motion. The second issue that caused the robot to slip was experienced at the

very end of the experiment where the zip ties holding the elastomer to the segment connector between the distal traction segment and the extending segment broke during the expansion of the distal traction segment. This caused fluid to shuttle between the distal traction segment and extending segment when either of them were actuated which resulted in the distal traction segment losing its ability to anchor the system. An image of the zip tie failure is shown in Figure 189.

Figure 189: Zip tie failure at segment connector between extender and distal traction segment

Overall, the robot had a few operator and robustness challenges in climbing the 63.5 mm vertical tube, but the early experimental results clearly demonstrate the functionality and promise of the multi-segment tube-traversing robot. The operator induced slipping and the zip tie failure can both be observed in the following link which presents a sped-up video of the multi-segment robot vertically climbing through the 63.5 mm polycarbonate tube in the forward direction.

https://drive.google.com/file/d/1GG2wWM2gcgu5cupZvcohVfKQj9qZTp8D/view?usp=sharing

While the design process investigated how the robot would perform in a third tube size, the robot was only tested in two tube sizes as additional development work is needed to prevent the zip ties holding the segment connectors from breaking when the robot traverses even larger tube sizes. The forward and reverse experiments in both polycarbonate tube sizes, as well as the vertical tube experiment, demonstrate that the proposed multi-segment robot design has a lot of potential for further development. The robot was able to repetitively move through tubes of varying sizes and varying orientations like what might be found in a burrowing environment. The novel microbore internal fluid routing design functioned well without any apparent fluid leakage occurring between the segments. The robot's ability to independently actuate the segments made it easy to navigate in both directions and control the segments without

impacting the performance of the other segments. Additional work is needed to refine the design of the connection between the elastomer and segment connectors to prevent zip tie failure like what was observed in the vertical tube experiments. Furthermore, the actuation of the robot segments was very slow due to the small diameter of the microbore tubing as well as the fact that the elastic force of the elastomer is the only force pushing the fluid out of the segments during depressurization. Addressing these limitations will allow the robot to be adapted to many other applications where actuation speed is critical.

5.8 **Conclusion and Summary**

The objective of this chapter was to design, model, fabricate, and experimentally test a novel multi-segment soft robot capable of producing the forces and motions to navigate through a tubular environment. First, an overview of some existing multi-segment soft robots was presented. The GE robot is the only known multi-segment burrowing soft robot developed to date. However, the GE robot has limitations. The robot requires many of the segments to be actuated simultaneously such that some of the segments are generating radial anchoring forces while others are extending to generate motion and penetration forces. The need for carefully timed, simultaneous actuation of the robot segments limits the motions that the robot can achieve. Furthermore, the GE robot relies on its long length to develop large enough traction forces to anchor the robot in the burrow which also makes the robot less compact and navigable.

A hydraulically driven three-segment soft robot capable of traversing a tube was developed by the author that combined the modeling and design work from the extending McKibben segments and the traction segments from previous chapters. The design of the robot consisted of two traction segments and one extending segment all constrained within a single elastomer. Microbore tubing routed fluid internally to the segments to enable independent actuation of the robot segments, and a novel spiral microbore tube was used to allow extension of the middle segment while still having the ability to route fluid to the distal traction segment. The ability to independently actuate the segments provides the robot with the ability to easily change gait, generate prescribed forces and motions, and operate in both the forward and reverse directions. Furthermore, the new multi-segment soft robot design was only 457.2 mm long, making it much more compact than existing soft robots such as the GE robot – yet it is still able to generate large, prescribed traction forces.

A series of experimental constraints, performance constraints, and performance objectives were introduced to evaluate what the best initial geometry of the multi-segment robot would be. The design process utilized a grid-search to determine which traction segment geometry and extending segment geometry would allow the best performance of the robot within the defined constraints. The extending segment design was limited to segments that produce at least 180 N of extension force and have a safety factor against buckling over 3 while at the same time trying to maximize the amount of

extension per cycle and minimize the required energy per unit of extension. The traction segment design was limited to segments that produce at least 180 N of traction force and have a safety factor against bursting of at least 3 while trying to minimize the required energy per unit of traction force. The constraints placed on the design were an entire robot length less than 610 mm to fit inside the experimental apparatus, a constant wall thickness elastomer to simplify robot manufacturing, and a maximum operating pressure of 207 kPa to prevent segment connector failure between the segments.

A detailed overview of the models used to calculate the constraints and performance objectives was provided in this chapter, and a detailed overview of the grid-search was presented. By sweeping through many variations of initial robot geometry in the grid-search, an understanding of how each potential robot geometry will perform against the constraints and objectives was developed. First, the extending segment grid-search results were analyzed, and the initial geometry of the extender was selected to meet all the constraints and performance objectives. Next, the traction segment grid-search was conducted, and the initial geometry that met the constraints and performance objectives was selected. Because of some of the initial design constraints for the multi-segment robot (equal length traction segments, constant wall thickness, etc), solving the geometry of the extending and traction segments in sequential order was justified. However, in future applications where very specific forces and motions are needed and some assumptions are relaxed (variable wall thickness, variable

length traction segments, different number of segments, etc), all the segment geometry of the robot should be solved simultaneously. This would allow the designer to develop an understanding of the implications of one segment's design on another segment's performance for very specific robot design. Once all the initial multi-segment robot geometry was selected, the robot was fabricated for testing, and the experimental apparatus was erected for testing the multi-segment robot's ability to forward and backwards through tubes of varying diameters.

The multi-segment robot had an outside diameter of 50.8 mm, and it was tested in two different sized polycarbonate tubes. The robot was able to easily move forwards and backwards through both the 57.2 mm and 63.5 mm inside diameter clear polycarbonate tubes. The robot took ~18 minutes to move forward and ~15 minutes to move backwards through the 57.2 mm tube, and the difference was due to the operator allowing for longer segment extensions to take place in the backward direction. Furthermore, the robot took ~20 minutes to move through the 63.5 mm tube in both directions. This confirmed the robot is able move in both directions at the same speed. It took longer for the robot traction segments to expand in the larger 63.5 mm diameter tube resulting in the slower travel speed. The robot was not able to move quickly for a couple of reasons. First, the microbore tubing used to route fluid to the segments had a very small diameter (4.8 mm OD and a 3.0 mm ID) which resulted in slow flow rates when pressurizing and depressurizing the actuator segments. Increasing

the diameter of the internal microbore tubing could exponentially increase the speed that the robot segments fill with fluid. The depressurization flow rates from the segments to tank were especially slow since only the elastic force from the segments was forcing the fluid out of the segments through the microbore tubing back to tank. In future iterations, a stiffer elastomer with a thicker wall could be used to provide more elastic force to push the fluid back to tank. Additional methods to improve the travel speed of the robot could include utilizing a lower viscosity hydraulic fluid or using a vacuum source to draw the fluid out of the segments to tank. When the extending segment was depressurized after an extension cycle, it would begin to contract and drag the proximal traction segment forward with it in the tube. The drag between the traction segment and polycarbonate tube wall was noticeable and slowed down the overall travel speed of the robot.

Finally, the robot was tested in a vertically mounted 63.5 mm inside diameter tube to assess its ability to move upwards through a tube against gravity. The robot was able to move up against gravity through the tube but slipping was experienced for a few reasons. Slipping was first noticed when the operator had released one of the traction segments before it was fully expanded, which caused the robot to slip downwards when the other traction segment was depressurized. This illustrates the importance of actuator timing and carefully monitoring the pressure of the segments as it relates to overall actuator performance. Future iterations of the design used for burrowing will require built

in sensing to determine the radial expansion and traction forces developed by the traction segments to ensure slip-free anchoring in the burrow. The second time the robot slipped was at the very end of the vertical tube experiment and occurred due to the zip ties breaking at the segment connector between the traction segment and the extending segment resulting in fluid leakage between the two segments.

One limitation of the design of the multi-segment robot for future burrowing applications is the stiffness and reliability of the current segment connector design. The current zip tie design worked well at low pressures, but the stress concentration caused failure as the pressure was increased. The prevalence to failure of the current segment connector must be addressed to reach very large pressures needed in burrowing applications. Furthermore, the traction segments experience more stress concentration as they are expanded. The current segment connector design limited the maximum pressure that the segment could withstand, which limits the robot to smaller burrow size ranges. In the future, a flexible segment connector could be utilized to address flexibility and steering concerns for burrowing applications. An inextensible microbore tube could also be used to limit the axial strain of the traction segments while concurrently providing fluid flow to the more distal segments of the robot. This would address flexibility concerns that arise from using the threaded rod for the traction segments in these experiments.

The novel multi-segment soft robot presented in this chapter was able to experimentally demonstrate the benefits of combining the force density of hydraulics with the adaptability of soft robotics. The new robot design was able to address limitations of existing multi-segment tube traversing soft robots, including both compactness and independent actuation of robot segments, as well as demonstrate the effectiveness of a novel internal fluid routing approach using microbore tubing. The robot was able to demonstrate its ability to move through horizontal and vertically oriented tubes with only minor issues observed. To further develop this multi-segment robot design into a more robust technology, additional refinement of the zip tie segment connector design is needed to ensure the robot segments can operate at large pressures without failure. Additional research is also needed to address issues with the robot's slow travel speed caused by the low elastic forces from the segments driving the fluid from the segments to tank during depressurization. In future multi-segment soft robot design applications, the constraints and objectives of the design space should be fine-tuned to address the specific needs of the application.

5.9 Specific Contributions of the Chapter

- Development of a novel three-segment, hydraulically driven soft robot capable of moving through both horizontally and vertically aligned tubular environments of varying diameters. The key components of the design include the following:

- Two radially expanding traction segments with an axial strain limiting rod to generate radial expansion and traction forces without any axial displacement
- One axially extending McKibben segment, located between the two traction segments, to generate extension forces to move the robot through the tube or burrow
- A single constant wall thickness elastomer containing all three robot segments and aluminum segment connectors used to partition the robot segments and connect all piping and internal components of the robot together
- The ability to independently actuate each of the robot segments, without impacting the performance of another segment, by utilizing small diameter microbore tubing to route all fluid to and from the segments completely internally within the robot
- Novel spiral-shaped microbore tubing design to route fluid through the extending segment to the distal traction segment regardless of the current displacement of the extending segment

- Development of a multi-segment robot design grid-search tool that sweeps a range of initial robot geometries to determine the anticipated performance of the robot at various operating conditions for designing multi-segment robots for specific applications

- Experimental demonstration of the 457.2 mm long, 50.8 mm diameter, three-segment soft robot navigating in the forwards and backwards direction through horizontally oriented clear polycarbonate tubes with diameters of both 57.2 mm and 63.5 mm

- Experimental demonstration of the multi-segment soft robot traversing a vertically oriented 63.5 mm polycarbonate tube against gravity

Chapter 6: Thesis Summary and Conclusion

Combining the adaptability of soft robotics and the power density of hydraulic power transmission provides a new perspective on soft robotic applications. The emerging field of soft robotics is expanding from traditionally pneumatic, low-force applications to include hydraulic, high-force applications such as underground burrowing and tube exploration. This thesis provided the background, modeling approaches, design techniques, and manufacturing processes for developing a multi-segment, hydraulically driven soft robot system capable of traversing rigid tubes, like a burrow, in horizontal and vertical configurations. The contributions of this thesis provide the initial framework for developing efficient burrowing systems that are needed for a myriad of applications including installation and repair of underground infrastructure, rescue operations, military applications, oil and natural gas exploration, and many other applications where excavation of the surrounding substrate or environment is undesirable. The following is a summary of the author's contributions to this thesis followed by a discussion of future work and the implications of this work.

First, a study on high-force, hydraulically driven, contracting McKibben actuators was conducted to assess limitations of existing force modeling and design approaches. A new McKibben axial force model was developed by the author that considers the impact of wall thickness, which is important for high-

force McKibben actuators that require thick walls. Contracting McKibben actuators were fabricated, and the new model was experimentally validated against three existing McKibben force models. The Kothera elastic force term was included in all the modeling approaches. It was found that the overall average error for the *F(θ), F(ε),* and *F(θ,t)* models were 9.9%, 10.5%, and 10.0% respectively, and the overall average error for the new model, *F(ε,t),* presented by the author was 9.1%. This model improvement is expected to amplify with much thicker-walled actuators needed in burrowing applications, but more experimental validation is needed for thicker-walled actuators. It was demonstrated that the empirical Gent model can be used to convert shore A durometer to elastic modulus for McKibben predictive design applications. Robust manufacturing techniques were explored, and dual-layered off-the-shelf fiber sleeves allowed the actuator to reach input pressures up to 13.9 MPa.

Next, a study was conducted on hydraulically driven, extending McKibben actuators to determine if the same modeling approaches as contracting McKibben actuators can be used for axial force modeling at free and displaced actuator conditions like those that may be observed in a burrowing or similar application. A novel manufacturing approach was developed for the extending McKibben actuators to custom-wrap and embed fibers at specific fiber-wrap angles, and a new casting process was developed to fabricate custom sized elastomers. Experimental results from testing the extending McKibben actuators confirmed that the axial force generated by contracting and extending McKibben

actuators can be predicted with the same models with similar accuracy at both free and displaced conditions. Furthermore, a preliminary elastomer bulge model was developed and experimentally validated to understand the relationship between actuator pressure, fiber spacing, and prevalence of burst failure. Further experimental testing and refinement of the preliminary burst model is needed to enable precise fiber-placement and robust extending McKibben actuator design resistant to burst failure at high pressures.

Because extending McKibben actuators are prone to buckling failure, an additional study was conducted to determine if extending McKibben actuators follow traditional column buckling behavior. The extending McKibben actuators were experimentally tested until buckling failure was observed, and it was determined that they follow traditional Euler-John column buckling models. The experiments showed that the actuators fail under compressive loads at either the critical buckling load or the compressive yielding load – whichever is reached first. Further tests were conducted to experimentally confirm that fiber-wrapped McKibben actuators buckle at the at the same critical load regardless of whether an external load was applied to the actuator or the buckling load was developed due to internal pressure actuation of the actuator. Finally, the extending actuators were tested within a constrained environment, and it was demonstrated that the constrained environment allowed the actuators to develop extension forces beyond the Euler-Johnson column buckling critical load. This is a particularly useful development for future burrowing and similar applications, and a

preliminary framework for modeling the constrained buckling behavior as two eccentrically loaded columns was presented. Further development of the eccentrically loaded column buckling modeling approach is needed to understand buckling behavior in a constrained environment like a burrow where forces beyond the critical buckling load can be achieved.

Many design and manufacturing approaches were explored to develop a soft robot segment that could produce predictable traction forces suitable for burrowing and similar applications. A novel design for a fixed length, radially expanding soft robot actuator was presented, and a new force model was developed by the author that predicts the traction force as a function of initial robot geometry, input pressure, and burrow (or tube) diameter. The traction segment robot design consisted of a constant wall thickness elastomer, an axial strain limiting rod to prevent change in axial length, two segment connectors, and low-profile zip ties clamping the elastomer to the segment connectors. Multiple traction segments were fabricated with varying geometries, and they were experimentally tested in various diameter tubes over a range of input pressures to determine the traction forces that could be developed. Experimental results validated the new traction force model as a baseline predictive design tool for the traction actuators. The traction segments demonstrated the ability to generate purely radial expansion forces that are needed to compact soil in stable burrowing applications where inefficient excavation is undesired.

The actuator designs and models developed in the McKibben actuator and traction actuator experiments were combined to develop a multi-segment soft robot capable of traversing through environments like a burrow or pipe. The three-segment, hydraulically driven soft robot design contained key features including:

- Two radially expanding traction segments to generate anchoring forces
- One axially extending McKibben segment, located between the two traction segments, to generate extension forces
- A single constant wall thickness elastomer constraining all three robot segments, aluminum segment connectors, and all piping and internal components of the robot
- The ability to independently actuate each of the robot segments, without impacting the performance of another segment, by utilizing small diameter microbore tubing to route all fluid to and from the segments completely internally within the robot
- Novel spiral-shaped microbore tubing design to route fluid through the extending segment to the distal traction segment regardless of the current displacement of the extending segment

A multi-segment robot design grid-search tool was developed that was used to determine the best initial geometry of the multi-segment robot by sweeping initial geometries and calculating the performance objectives associated with each initial geometry over a range of robot operating conditions.

A series of constraints and performance objectives were selected to filter the solution space to select a robot geometry that would be easily tested and efficient at generating motion and forces as the robot moved through a tube. Once the best geometry was selected for the robot segments, the robot was fabricated and tested in two different diameter polycarbonate tubes in both horizonal and vertical orientations. The robot was able to easily navigate through both tube sizes in both the forward and backward directions in the horizontal configuration. Furthermore, the multi-segment robot was able to move up a tube against gravity demonstrating its potential for applications such as burrowing, underground utility installation, and other applications in tight, hard-to-reach, places where specific forces and motions are required.

There are limitations that must be overcome to translate this thesis work into reliable and functioning burrowing systems that can navigate through underground soil in a feasible manner. While the contracting McKibben actuators fabricated with crimped hydraulic fittings were able to withstand up to 13.9 MPa of internal pressure, the low-profile segment connector design used in the multi-segment robot experiments failed at much lower pressures severely limiting the performance of the robot segments and their adaptability to burrowing applications. Refinement of the current segment connector design for burrowing applications could include utilizing a stronger low-profile zip tie or developing a mechanical crimp fitting to lock the elastomer and segment connector together. Future segment connectors may also be refined to be flexible which may better

aid the robot as it makes turns and navigates in tortuous burrowing environments. This could possibly be done in future work by casting the elastomer around a segment connector to further strengthen the connection and reduce stress concentration. Additional flexibility of the overall system could be achieved by integrating a cable (or similar) instead of the axial strain limiting rod in the traction segments to allow for traversing burrows or tubes with turns. The current design is limited because it requires hydraulic cables to be pulled behind the system. As the robot moves further through a tortuous burrow, the drag forces produced by the cables will become more significant. Future work might address this by adding an on-board pump and power source, an onboard accumulator, or determining a method for shuttling fluid between the segments without the need for the fluid to be pumped long distances from above ground.

The results from the multi-segment experiments demonstrated the system's ability to generate alternating anchor locomotion without slipping through tubular environments like a burrow. This traction segments were easily able to generate anchoring forces without slipping, and the traction segments could be covered in a more abrasive material (i.e. Kirigami skin) in future burrowing applications to generate additional traction forces needed for anchoring the robot in the burrow. Future work could include optimizing the traction segment elastomer profile to prevent stress concentration near the segment connectors where failure was observed to be most prevalent. Early traction experiments demonstrated that anchoring forces for burrowing

applications could be produced by the segments, and McKibben actuators were experimentally shown to be able to generate extension forces in a predictable manner. With utilization of more robust segment connectors that can withstand hydraulic pressures, the proposed segments can generate suitable forces and motions for a variety of burrowing applications. While additional experimental and development work is needed, early results suggest that this burrowing approach will allow for compressing of the soil and avoid the need for excavation in burrowing applications.

An agricultural soil strength study suggested that crops are typically planted in soils with a penetration resistance of 1500 kPa [145]. To fully penetrate such soil with a 25 mm diameter conical penetrometer (typical crop irrigation line diameter), approximately 750 N of penetration force is needed. In theory, a 25 mm diameter extending McKibben actuator with an initial fiber angle of 80 degrees could produce this force at an operating pressure of 1580 kPa. These levels of extension forces were easily obtained in the extender experiments in Chapter 2, and operating pressures much larger than 1580 kPa were obtained in early experiments. As the burrow diameter grows larger, the penetration force required grows exponentially. This is because the penetration area grows exponentially with the burrow diameter while the penetration resistance of the soil remains constant. However, the amount of penetration force that an extending McKibben actuator produces grows exponentially with the segment diameter as well. This relationship suggests that the only limitation to

scaling extending McKibben actuators to any sized burrow is the large operating pressures that can cause buckling failure and mechanical failure near the end connections. Buckling behavior of McKibben actuators has been demonstrated to be predictable. Furthermore, increasing the wall thickness and utilizing the constrained burrow environment to limit buckling failure have been shown to increase the maximum extension force obtainable before buckling is observed.

The traction segments from the multi-segment robot were designed to generate traction forces much larger than the ones that were needed to traverse the tubes in the experiments. One benefit of using this type of traction segment and alternating anchor locomotion technique is that the traction force generated scales linearly with the length and diameter of the segment (and the pressure – forgoing losses and non-linear pressure distributions). This allows the robot designer to first determine what penetration forces are needed for a particular burrow and soil substrate and then select the necessary length the traction segments to generate the prescribed traction forces. If the segments must be shorter due to some design constraint, the segments can be operated at a higher pressure to compensate for the reduction in length to generate sufficient traction forces. Some of the small diameter traction segments from the Chapter 4 studies were able to generate over 1000 N of traction force providing further evidence that this approach can be translated into real-world burrowing applications.

The multi-segment robot was not designed for optimized travel speed, and this was a severe limitation of the current design. The main factor that resulted in slow travel speeds of the robot through the tubes was low flow rates of fluid in and out of the robot segments through the small diameter internally routed microbore tubing. This issue was amplified as the desired radial expansion of the robot increased because of the increased need of fluid volume for expanding the robot to larger diameters. Potential solutions to this problem include using larger diameter microbore tubing to increase the flow rate, using a stiffer and thicker-walled elastomer to generate larger elastic forces to push the fluid out of the segments (which would also reduce burst failure from bulging), and using a vacuum to remove fluid from the segments. Another consideration for future work could be to utilize a water-based hydraulic system and vent the water to the environment when a segment must be depressurized. While this would allow the robot to rapidly empty the segment and improve the travel time of the system, it could allow the local soil substrate to become fluidized which has shown to decrease friction experienced in burrowing applications. A future multi-segment robot could also be designed to shuttle fluid to and from the segments to maintain a constant volume of fluid in the overall robot and avoid the need to shuttle fluid over long distances to and from tank.

Future multi-segment robot design optimizations must not only include the energy efficiency analysis that was included in the multi-segment robot experiments in this thesis, but they must also include prioritizing travel speed of

the robot. Increased travel speed is desirable in nearly every conceivable burrowing application, and the specific design requirements must be considered before determining the acceptable trade-offs between energy efficiency and travel speed in the application. For example, it may be OK for search and rescue robots to be very energy inefficient if fast travel can be achieved, but energy efficiency may be more critical for battery powered systems that need to travel long distances. The type and optimal locomotion of the soil being travelled through will also greatly impact the most appropriate way to optimize and constrain the design of future multi-segment robots for burrowing applications. Future robot developments could also incorporate fluidization of soil substrates and hydraulic jetting of rock/soil which are natural choices for the hydraulically powered system with fluid readily available. Future designs may include other segment types that require optimization of the overall system's gait kinematics to obtain the most efficient locomotion speed and forces. Future work will include development of robot end effectors, such as a soil penetrating head or a welding head for pipe repair, and integration of soil and/or environment models to enable design and control of the robot in a non-rigid environment like a burrow.

Bibliography

[1] C. Laschi and M. Cianchetti, “Soft Robotics: New Perspectives for Robot Bodyware and Control,” Frontiers in Bioengineering and Biotechnology, vol. 2, no. January, pp. 1–5, 2014, doi: 10.3389/fbioe.2014.00003.

[2] S. Kim, C. Laschi, and B. Trimmer, “Soft robotics: A bioinspired evolution in robotics,” Trends in Biotechnology, vol. 31, no. 5, pp. 287–294, 2013, doi: 10.1016/j.tibtech.2013.03.002.

[3] CDC, “Trenching and Excavation,” National Institute for Occupational Safety and Health Education, 2013. https://www.cdc.gov/niosh/topics/trenching/default.html

[4] “Open Trench Excavation,” City of Portland, Oregon. https://www.portlandoregon.gov/bes/article/490269

[5] “Trencher,” 2017. https://en.wikipedia.org/wiki/Trencher_(machine)

[6] D. Willoughby, Horizontal Directional Drilling. New York: Mcgraw-Hill, 2005.

[7] “Horizontal Directional Drilling Overview - Benefits and Limitations,” Directional Technologies, Inc., 2017. https://www.directionaltech.com/directional-drilling/

[8] “Horizontal Directional Drilling,” Netwas Group Oil, 2017. https://www.netwasgroup.us/horizontal-directional/soil-conditions-1.html

[9] R. D. Maladen, Y. Ding, C. Li, and D. I. Goldman, “Undulatory swimming in sand: subsurface locomotion of the sandfish lizard.,” Science (New York, N.Y.), vol. 325, no. 5938, pp. 314–318, 2009, doi: 10.1126/science.1172490.

[10] M. J. Kuhlman, B. D. Sanders, L. Zabowski, and J. A. Gaskin, “Robotic Tunneling Worm for Operation in Harsh Environments,” no. July, 2011.

[11] T. Kobayashi, H. Tshukagoshi, S. Honda, and A. Kitagawa, “Burrowing Rescue Robot Referring to a Mole’s Shoveling Motion,” Symposium on Fluid Power, pp. 4–9, 2011.

[12] S. Smallwood and M. Morrison, “Estimating burrow volume and excavation rate of pocket gophers (Geomyidae),” The Southwestern Naturalist, vol. 44, no. 2, pp. 173–183, 1999.

[13] D. S. Dorsch and A. G. Winter, “Design of a Low Energy, Self Contained Subsea Burrowing Robot Based on Localized Fluidization Exhibited by Atlantic Razor Clams,” 2016.

[14] A. G. Winter V, R. L. H. Deits, D. S. Dorsch, A. E. Hosoi, and A. H. Slocum, “Teaching RoboClam to dig: The design, testing, and genetic algorithm optimization of a biomimetic robot,” IEEE/RSJ 2010 International Conference on Intelligent Robots and Systems, IROS 2010 - Conference Proceedings, no. 617, pp. 4231–4235, 2010, doi: 10.1109/IROS.2010.5654364.

[15] M. Hayashi and Y. Kawamura, “Development of DigBot for Surveying the Underground after the Disaster,” no. 2, pp. 2–3, 2012.

[16] B. Gasser, J. Johnson, J. Ben, N. Toy, and C. Boyles, “Lunar Wormbot,” 2011.
[17] K. Nagaoka, T. Kubota, I. Nakatani, and S. Tanaka, “Drilling Mechanism of Autonomous Burrowing Robot for Lunar Subsurface Exploration,” no. June, 2008.
[18] K. N. Nordstrom, D. S. Dorsch, W. Losert, and A. G. Winter, “Microstructural view of burrowing with a bioinspired digging robot,” Physical Review E - Statistical, Nonlinear, and Soft Matter Physics, vol. 92, no. 4, 2015, doi: 10.1103/PhysRevE.92.042204.
[19] K. Iwata, K. Suzumori, and S. Wakimoto, “A method of designing and fabricating Mckibben muscles driven by 7 MPa hydraulics,” International Journal of Automation Technology, vol. 6, no. 4, pp. 482–487, 2012.
[20] W. Kobayashi, K. Ito, and S. Yamamoto, “Displacement Control of Water Hydraulic McKibben Muscles with Load,” JFPS International Journal of Fluid Power System, vol. 8, no. 2, pp. 107–112, 2015.
[21] M. Mori, K. Suzumori, S. Seita, M. Takahashi, T. Hosoya, and K. Kusumoto, “Development of very high force hydraulic McKibben artificial muscle and its application to shape-adaptable power hand,” 2009 IEEE International Conference on Robotics and Biomimetics, ROBIO 2009, pp. 1457–1462, 2009, doi: 10.1109/ROBIO.2009.5420382.
[22] M. Mori et al., “Development of power robot hand with shape adaptability using hydraulic McKibben muscles,” Proceedings - IEEE International Conference on Robotics and Automation, pp. 1162–1168, 2010, doi: 10.1109/ROBOT.2010.5509489.
[23] D. Du, Y. Ma, X. Guo, and H. Lu, “Research on a forestation hole digging robot,” 2010 International Conference on Intelligent Computation Technology and Automation, ICICTA 2010, vol. 2, pp. 1073–1076, 2010, doi: 10.1109/ICICTA.2010.793.
[24] T. D. Levine, H. B. Hansen, and G. W. Gerald, “Effects of shell shape, size, and sculpture in burrowing and anchoring abilities in the freshwater mussel Potamilus alatus (Unionidae),” Biological Journal of the Linnean Society, vol. 111, no. 1, pp. 136–144, 2014, doi: 10.1111/bij.12178.
[25] A. G. Winter and A. E. Hosoi, “Identification and evaluation of the atlantic razor clam (Ensis directus) for biologically inspired subsea burrowing systems,” Integrative and Comparative Biology, vol. 51, no. 1, pp. 151–157, 2011, doi: 10.1093/icb/icr038.
[26] D. Trivedi, C. D. Rahn, W. M. Kier, and I. D. Walker, “Soft robotics: Biological inspiration, state of the art, and future research,” Applied Bionics and Biomechanics, vol. 5, no. 3, pp. 99–117, 2008, doi: 10.1080/11762320802557865.
[27] A. D. Marchese, R. K. Katzschmann, and D. Rus, “A Recipe for Soft Fluidic Elastomer Robots,” Soft Robotics, vol. 2, no. 1, pp. 7–25, 2015, doi: 10.1089/soro.2014.0022.
[28] B. a Trimmer, A. E. Takesian, B. M. Sweet, C. B. Rogers, D. C. Hake, and D. J. Rogers, “Caterpillar locomotion : A new model for soft- bodied climbing and burrowing robots,” 7th International Symposium on

Technology and the Mine Problem, Monterey, CA May 2-5, 2006, pp. 1–10, 2006.
[29] H. T. Lin, G. G. Leisk, and B. Trimmer, “GoQBot: A caterpillar-inspired soft-bodied rolling robot,” Bioinspiration and Biomimetics, vol. 6, no. 2, 2011, doi: 10.1088/1748-3182/6/2/026007.
[30] M. Calisti et al., “An octopus-bioinspired solution to movement and manipulation for soft robots,” Bioinspiration & Biomimetics, vol. 6, no. 3, 2011, doi: 10.1088/1748-3182/6/3/036002.
[31] R. Pelrine, R. Kornbluh, Q. Pei, and J. Joseph, “High-Speed Electrically Actuated Elastomers with Strain Greater than 100%,” Science, vol. 287, no. 5454, pp. 836–839, 2000.
[32] B. R. Wang, Y. L. Jin, and D. Wei, “Modeling of Pneumatic Muscle with Shape Memory Alloy and Braided Sleeve,” International Journal of Automation and Computing, vol. 7, no. 3, pp. 283–288, 2010, doi: 10.1007/s11633-010-0504-x.
[33] K. Suzumori, “Elastic materials producing compliant robots,” Robotics and Autonomous Systems, vol. 18, no. 1–2, pp. 135–140, 1996, doi: 10.1016/0921-8890(95)00078-X.
[34] J. Bishop-Moser and S. Kota, “Design and Modeling of Generalized Fiber-Reinforced Pneumatic Soft Actuators,” IEEE Transactions on Robotics, vol. 31, no. 3, pp. 536–545, 2015, doi: 10.1109/TRO.2015.2409452.
[35] G. Krishnan, J. Bishop-Moser, C. Kim, and S. Kota, “Kinematics of a Generalized Class of Pneumatic Artificial Muscles,” Journal of Mechanisms and Robotics, vol. 7, no. November, pp. 1–9, 2015, doi: 10.1115/1.4029705.
[36] P. Polygerinos et al., “Modeling of Soft Fiber-Reinforced Bending Actuators,” IEEE Transactions on Robotics, vol. 31, no. 3, pp. 778–789, 2015, doi: 10.1109/TRO.2015.2428504.
[37] G. Singh and G. Krishnan, “An isoperimetric formulation to predict deformation behavior of pneumatic fiber reinforced elastomeric actuators,” IEEE International Conference on Intelligent Robots and Systems, vol. 2015-Decem, pp. 1738–1743, 2015, doi: 10.1109/IROS.2015.7353602.
[38] W. Liu and C. R. Rahn, “Fiber-Reinforced Membrane Models of McKibben Actuators,” Journal of Applied Mechanics, vol. 70, no. November 2003, p. 853, 2003, doi: 10.1115/1.1630812.
[39] A. A. M. Faudzi, M. R. M. Razif, I. N. A. M. Nordin, K. Suzumori, S. Wakimoto, and D. Hirooka, “Development of bending soft actuator with different braided angles,” IEEE/ASME International Conference on Advanced Intelligent Mechatronics, AIM, pp. 1093–1098, 2012, doi: 10.1109/AIM.2012.6266037.
[40] F. Connolly, C. J. Walsh, and K. Bertoldi, “Automatic design of fiber-reinforced soft actuators for trajectory matching,” Proceedings of the National Academy of Sciences, vol. 114, no. 1, p. 201615140, 2016, doi: 10.1073/pnas.1615140114.
[41] J. Wirekoh et al., “Design of flat pneumatic artificial muscles A constrained maximization formulation to analyze deformation of fi ber reinforced

elastomeric actuators," Smart Materials and Structures, vol. 26, no. 6, p. 65024, 2017, doi: 10.1088/1361-665X/aa6dc6.
[42] P. Polygerinos, Z. Wang, K. C. Galloway, R. J. Wood, and C. J. Walsh, "Soft robotic glove for combined assistance and at-home rehabilitation," Robotics and Autonomous Systems, vol. 73, pp. 135–143, 2015, doi: 10.1016/j.robot.2014.08.014.
[43] Z. Chen, A. Zou, Z. Qin, X. Han, T. Li, and S. Liu, "Modeling and fabrication of soft actuators based on fiber-reinforced elastomeric enclosures," Actuators, vol. 10, no. 6, Jun. 2021, doi: 10.3390/act10060127.
[44] T. Kanno, S. Ohkura, O. Azami, T. Miyazaki, T. Kawase, and K. Kawashima, "Model of a coil-reinforced cylindrical soft actuator," Applied Sciences (Switzerland), vol. 9, no. 10, May 2019, doi: 10.3390/app9102109.
[45] A. Sedal, M. Fisher, J. Bishop-Moser, A. Wineman, and S. Kota, "Auxetic Sleeves for Soft Actuators with Kinematically Varied Surfaces," in IEEE International Conference on Intelligent Robots and Systems, 2018, pp. 464–471. doi: 10.0/Linux-x86_64.
[46] J. Nagase, S. Wakimoto, T. Satoh, N. Saga, and K. Suzumori, "Design of a variable-stiffness robotic hand using pneumatic soft rubber actuators," Smart Materials and Structures, vol. 20, no. 10, p. 105015, 2011, doi: 10.1088/0964-1726/20/10/105015.
[47] K. A. Daltorio, A. S. Boxerbaum, A. D. Horchler, K. M. Shaw, H. J. Chiel, and R. D. Quinn, "Efficient worm-like locomotion: slip and control of soft-bodied peristaltic robots," Bioinspiration & Biomimetics, vol. 8, no. 3, p. 035003, 2013, doi: 10.1088/1748-3182/8/3/035003.
[48] A. Calderón, J. Zagal, and A. Pérez-Arancibia, "A Pneumatically-Driven Soft Robot Biologically Inspired by Earthworms," no. April, 2016.
[49] C. Ferraresi, W. Franco, and A. M. Bertetto, "Straight Fiber Pneumatic Muscle: An Actuator with High Traction Force," The Sixth Internation Conference on Fluid Power, pp. 787–798, 1999, [Online]. Available: https://www.directionaltech.com/directional-drilling/
[50] J. Bishop-Moser, G. Krishnan, and S. Kota, "Force and moment generation of fiber-reinforced pneumatic soft actuators," IEEE International Conference on Intelligent Robots and Systems, pp. 4460–4465, 2013, doi: 10.1109/IROS.2013.6696997.
[51] C. P. Chou and B. Hannaford, "Measurement and modeling of McKibben pneumatic artificial muscles," IEEE Transactions on Robotics and Automation, vol. 12, no. 1, pp. 90–102, 1996, doi: 10.1109/70.481753.
[52] M. Mori, K. Suzumori, M. Takahashi, and T. Hosoya, "Very High Force hydraulic McKibben Artificial Muscle with a p-Phenylene-2,6-benzobisoxazole Cord Sleeve," Advanced Robotics, vol. 24, no. 1–2, pp. 233–254, 2010.
[53] B. Tondu, "Modelling of the McKibben artificial muscle: A review," Journal of Intelligent Material Systems and Structures, vol. 23, no. 3, pp. 225–253, 2012, doi: 10.1177/1045389X11435435.

[54] D. G. Caldwell, G. A. Medrano-Cerda, and M. Goodwin, “Control of pneumatic muscle actuators,” IEEE Control Systems Magazine, vol. 15, no. 1, pp. 40–48, 1995, doi: 10.1109/37.341863.
[55] T. Kametani and O. Umezawa, “Flexible Hydraulic Actuator for Space manipulators,” JSME International Journal, vol. 14, pp. 369–375, 1966, doi: 10.1248/cpb.37.3229.
[56] Z. Zhang, J. Hou, D. Ning, Y. Gong, and X. Gong, “Modeling and Experiments on the Drive Characteristics of High-Strength Water Hydraulic Artificial Muscles,” Smart Materials and Structures, vol. 26, no. 5, 2017.
[57] D. Sangian, S. Naficy, G. M. Spinks, and B. Tondu, “The effect of geometry and material properties on the performance of a small hydraulic McKibben muscle system,” Sensors and Actuators A: Physical, vol. 234, pp. 150–157, Oct. 2015, doi: 10.1016/j.sna.2015.08.025.
[58] M. A. Meller, M. Bryant, and E. Garcia, “Reconsidering the McKibben muscle: Energetics, operating fluid, and bladder material,” Journal of Intelligent Material Systems and Structures, vol. 25, no. 18, pp. 2276–2293, 2014.
[59] Z. Zhang, Y. Gong, and J. Hou, “Research on High-Strength Water Hydraulic Artificial Muscle for Underwater Manipulator”.
[60] K. Iwata, K. Suzumori, and S. Wakimoto, “Development of contraction and extension artificial muscles with different braid angles and their application to stiffness changeable bending rubber mechanism by their combination,” Journal of Robotics and Mechatronics, vol. 23, no. 4, pp. 582–588, 2011.
[61] Z. Zhang, Y. Jia, J. Che, P. Liu, and Y. Gong, “The effects of manufacturing parameters on static characteristics of water hydraulic artificial muscles,” IEEE Access, vol. 8, pp. 200669–200679, 2020, doi: 10.1109/ACCESS.2020.3034187.
[62] J. E. Slightam and M. L. Nagurka, “Theoretical modeling, analysis, and experimental results of a hydraulic artificial muscle prototype,” FPMC, vol. 1654, pp. 1–10, 2019.
[63] B. K. S. Woods, C. S. Kothera, and N. M. Wereley, “Fluidic Artificial Muscle Actuator and Swaging Process Therefor,” US 8,307,753 B2, 2009 doi: 10.1126/science.Liquids.
[64] Z. Zhang, J. Che, D. Ning, P. Liu, and Y. Gong, “Effects of the geometry and material properties on the mechanical strength and failure modes of water hydraulic artificial muscles,” Smart Materials and Structures, vol. 30, no. 8, Aug. 2021, doi: 10.1088/1361-665X/ac0671.
[65] A. Faudzi, N. Azmi, M. Sayahkarajy, W. Xuan, and K. Suzumori, “Soft manipulator using thin McKibben actuator,” in IEEE/ASME International Conference on Advanced Intelligent Mechatronics, 2018, pp. 334–339.
[66] S. Koizumi, S. Kurumaya, H. Nabae, G. Endo, and K. Suzumori, “Braiding thin McKibben muscles to enhance their contracting abilities,” IEEE Robotics and Automation Letters, vol. 3, no. 4, pp. 3240–3246, Oct. 2018, doi: 10.1109/LRA.2018.2851025.

[67] A. A. M. Faudzi, J. Ooga, T. Goto, M. Takeichi, and K. Suzumori, “Index Finger of a Human-Like Robotic Hand Using Thin Soft Muscles,” IEEE Robotics and Automation Letters, vol. 3, no. 1, pp. 92–99, Jan. 2018, doi: 10.1109/LRA.2017.2732059.
[68] T. Abe et al., “Fabrication of ‘18 weave’ muscles and their application to soft power support suit for upper limbs using Thin McKibben Muscle,” IEEE Robotics and Automation Letters, vol. 4, no. 3, pp. 2532–2538, Jul. 2019, doi: 10.1109/LRA.2019.2907433.
[69] S. Kurumaya, K. Suzumori, H. Nabae, and S. Wakimoto, “Musculoskeletal lower-limb robot driven by multifilament muscles,” ROBOMECH Journal, vol. 3, no. 1, Dec. 2016, doi: 10.1186/s40648-016-0061-3.
[70] L. Tiziani, T. Cahoon, and F. Hammond, “Sensorized Pneumatic Muscle for Force and Stiffness Control,” in ICRA2017: IEEE International Conference on Robotics and Automation, 2017, pp. 5545–5552.
[71] S. Kittisares, H. Nabae, G. Endo, K. Suzumori, and R. Sakurai, “Design of knee support device based on four-bar linkage and hydraulic artificial muscle,” ROBOMECH Journal, vol. 7, no. 1, Dec. 2020, doi: 10.1186/s40648-020-00165-2.
[72] R. D. Hunter and H. Y. Elder, “Burrowing dynamics and energy cost of transport in the soft-bodied marine invertebrates Polyphysia crassa and Priapulus caudatus,” Journal of Zoology, no. 218, pp. 209–222, 1989.
[73] R. D. Maladen, Y. Ding, P. B. Umbanhowar, A. Kamor, and D. I. Goldman, “Mechanical models of sandfish locomotion reveal principles of high performance subsurface sand-swimming.,” Journal of the Royal Society, Interface / the Royal Society, vol. 8, no. 62, pp. 1332–45, 2011, doi: 10.1098/rsif.2010.0678.
[74] A. G. Winter, R. L. H. Deits, and A. E. Hosoi, “Localized fluidization burrowing mechanics of Ensis directus,” The Journal of Experimental Biology, vol. 215, pp. 2072–2080, 2012, doi: 10.1242/jeb.058172.
[75] K. J. Quillin, “Ontogenetic scaling of burrowing forces in the earthworm Lumbricus terrestris.,” The Journal of experimental biology, vol. 203, no. Pt 18, pp. 2757–2770, 2000.
[76] B. Vanhooydonck, R. Boistel, V. Fernandez, and A. Herrel, “Push and bite: Trade-Offs between burrowing and biting in a burrowing skink (Acontias percivali),” Biological Journal of the Linnean Society, vol. 102, no. 1, pp. 91–99, 2011, doi: 10.1111/j.1095-8312.2010.01563.x.
[77] K. Dorgan, P. Jumars, B. Johnson, and B. Boudreau, “Macrofaunal Burrowing : the Medium Is the Message,” Oceanography and Marine Biology: An annual review, vol. 44, no. January, pp. 85–121, 2006.
[78] K. M. Dorgan, “The biomechanics of burrowing and boring,” Journal of Experimental Biology, vol. 218, no. 2, pp. 176–183, 2015, doi: 10.1242/jeb.086983.
[79] R. Alexander, “Principles of Animal Locomotion,” 2002, doi: 10.1017/CBO9781107415324.004.

[80] S. Jung, A. G. Winter, and A. E. Hosoi, “Dynamics of digging in wet soil,” International Journal of Non-Linear Mechanics, vol. 46, no. 4, pp. 602–606, 2011, doi: 10.1016/j.ijnonlinmec.2010.11.007.
[81] D. I. Goldman, “Colloquium: Biophysical principles of undulatory self-propulsion in granular media,” Reviews of Modern Physics, vol. 86, no. 3, pp. 943–958, 2014, doi: 10.1103/RevModPhys.86.943.
[82] C. Li et al., “Towards a terramechanics for bio-inspired locomotion in granular environments,” ASCE Earth and Space Conference, no. Nedderman 1992, pp. 264–273, 2012.
[83] J. Che and K. M. Dorgan, “It’s tough to be small: dependence of burrowing kinematics on body size.,” The Journal of Experimental Biology, vol. 213, no. Pt 8, pp. 1241–50, 2010, doi: 10.1242/jeb.038661.
[84] W. Mairaing, “Penetration resistance of soils in relation to penetrometer shape,” 1978.
[85] M. Isava and A. G. Winter V, “Razor clam-inspired burrowing in dry soil,” International Journal of Non-Linear Mechanics, vol. 81, pp. 30–39, 2016, doi: 10.1016/j.ijnonlinmec.2015.12.005.
[86] K. M. Dorgan, S. R. Arwade, and P. a Jumars, “Burrowing in marine muds by crack propagation: kinematics and forces.,” The Journal of experimental biology, vol. 210, no. Pt 23, pp. 4198–4212, 2007, doi: 10.1242/jeb.010371.
[87] K. M. Dorgan, C. J. Law, and G. W. Rouse, “Meandering worms : mechanics of undulatory burrowing in muds,” Proceedings of the Royal Society B: Biological Sciences, vol. 280, no. February, pp. 1–9, 2013, doi: http://dx.doi.org/10.1098/rspb.2012.2948.
[88] A. E. Hosoi and D. I. Goldman, “Beneath Our Feet: Strategies for Locomotion in Granular Media,” Annual Review of Fluid Mechanics, vol. 47, no. 1, pp. 431–453, 2015, doi: 10.1146/annurev-fluid-010313-141324.
[89] C. Senatore and M. Wulfmeier, “Investigation of stress and failure in granular soils for lightweight robotic vehicle applications,” Proceedings of the 2012 Ground Vehicle Systems Engineering and Technology Symposium (GVSETS), no. Figure 1, pp. 1–12, 2012, [Online]. Available: http://www.diva-portal.org/smash/record.jsf?pid=diva2:586861
[90] a G. Winter, V, R. L. H. Deits, D. S. Dorsch, a H. Slocum, and a E. Hosoi, “Razor clam to RoboClam: burrowing drag reduction mechanisms and their robotic adaptation.,” Bioinspiration & biomimetics, vol. 9, no. 3, p. 036009, 2014, doi: 10.1088/1748-3182/9/3/036009.
[91] K. M. Dorgan, P. a Jumars, B. Johnson, B. P. Boudreau, and E. Landis, “Burrowing mechanics: burrow extension by crack propagation.,” Nature, vol. 433, no. 7025, p. 475, 2005, doi: 10.1038/433475a.
[92] R. B. Suter, G. E. Stratton, and P. R. Miller, “Mechanics and energetics of excavation by burrowing wolf spiders, Geolycosa spp.,” Journal of insect science (Online), vol. 11, no. 22, p. 22, 2011, doi: 10.1673/031.011.0122.
[93] S. B. Emerson, “Burrowing in frogs,” Journal of Morphology, vol. 149, no. 4, pp. 437–458, 1976, doi: 10.1002/jmor.1051490402.

[94] M. Keudel and S. Schrader, “Axial and radial pressure exerted by earthworms of different ecological groups,” Biology and Fertility of Soils, vol. 29, no. 3, pp. 262–269, 1999, doi: 10.1007/s003740050551.
[95] A. M. Abdalla, D. R. P. Hettiaratchi, and A. R. Reece, “The mechanics of root growth in Granular media,” Journal of Agricultural Engineering Research, vol. 14, no. 3, pp. 236–248, 1969, doi: 10.1016/0021-8634(69)90126-7.
[96] A. G. Bengough, B. M. McKenzie, P. D. Hallett, and T. A. Valentine, “Root elongation, water stress, and mechanical impedance: A review of limiting stresses and beneficial root tip traits,” Journal of Experimental Botany, vol. 62, no. 1, pp. 59–68, 2011, doi: 10.1093/jxb/erq350.
[97] A. K. Mishra, F. Tramacere, R. Guarino, N. M. Pugno, and B. Mazzolai, “A study on plant root apex morphology as a model for soft robots moving in soil,” PLoS ONE, vol. 13, no. 6, Jun. 2018, doi: 10.1371/journal.pone.0197411.
[98] A. Mishra, F. Tramacere, and B. Mazzolai, “From plant root’s sloughing and radial expansion mechanisms to a soft probe for soil exploration,” in RoboSoft 2018: IEEE Conference on Soft Robotics, 2018, pp. 24–28.
[99] J. Grygorczuk et al., “Advanced Penetrators and hammering Sampling Devices for Planetary Body Exploration,” Esa/Estec, no. April, pp. 1–22, 2011.
[100] M. Isava and A. G. Winter V, “An Experimental Investigation of Digging Via Localized Fluidization, Tested With RoboClam: A Robot Inspired by Atlantic Razor Clams,” Journal of Mechanical Design, vol. 138, no. 12, p. 125001, 2016, doi: 10.1115/1.4034218.
[101] A. G. Winter, D. S. Dorsch, A. H. Slocum, A. E. Hosoi, and R. L. H. Deits, “Multi-Substrate Burrowing Performance and Constituitive Modeling of RoboClam: A Biomimetic Robot Based on Razor Clams,” International Design Engineering Technical Conferences & Computers and Information in Engineering Conference, pp. 1–7, 2010.
[102] K. M. Dorgan, S. R. Arwade, and P. A. Jumars, “Worms as wedges: Effects of sediment mechanics on burrowing behavior,” Journal of Marine Research, vol. 66, no. 2, pp. 219–254, 2008, doi: 10.1357/002224008785837130.
[103] S. Grill and K. M. Dorgan, “Burrowing by small polychaetes – mechanics, behavior and muscle structure of Capitella sp.,” The Journal of Experimental Biology, vol. 218, no. 10, pp. 1527–1537, 2015, doi: 10.1242/jeb.113183.
[104] S. Ruiz, D. Or, and S. J. Schymanski, “Soil Penetration by Earthworms and Plant Roots-Mechanical Energetics of Bioturbation of Compacted Soils.,” PloS one, vol. 10, no. 6, p. e0128914, 2015, doi: 10.1371/journal.pone.0128914.
[105] E. Trueman, “Bivalve Mollusks: Fluid Dynamics of Burrowing,” vol. 152, no. 3721, pp. 523–525, 1966.

[106] S. Stanley, “Why Clams have the Shape they Have: An Experimental Analysis of Burrowing,” Paleontological Society, vol. 1, no. 1, pp. 48–58, 2016.
[107] a. Menciassi, S. Gorini, G. Pernorio, L. Weiting, F. Valvo, and P. Dario, “Design, Fabrication and Performances of a Biomimetic Robotic Earthworm,” 2004 IEEE International Conference on Robotics and Biomimetics, pp. 274–278, 2004, doi: 10.1109/ROBIO.2004.1521789.
[108] H. Fang, C. Wang, S. Li, J. Xu, and K. W. Wang, “Design and experimental gait analysis of a multi-segment in-pipe robot inspired by earthworm’s peristaltic locomotion,” Proceedings of the SPIE Conference on Smart Structures/NDE 2014, vol. 9055, no. 734, p. 90550H, 2014, doi: 10.1117/12.2044262.
[109] M. D. Gilbertson, G. McDonald, G. Korinek, J. D. van de Ven, and T. M. Kowalewski, “Serially Actuated Locomotion for Soft Robots in Tube-Like Environments,” IEEE Robotics and Automation Letters, vol. 2, no. 2, pp. 1140–1147, 2017, doi: 10.1109/LRA.2017.2662060.
[110] A. Koller-Hodac et al., “Actuated bivalve robot study of the burrowing locomotion in sediment,” Proceedings - IEEE International Conference on Robotics and Automation, no. May, pp. 1209–1214, 2010, doi: 10.1109/ROBOT.2010.5509329.
[111] A. Tonazzini, L. Popova, F. Mattioli, and B. Mazzolai, “Analysis and characterization of a robotic probe inspired by the plant root apex,” Proceedings of the IEEE RAS and EMBS International Conference on Biomedical Robotics and Biomechatronics, pp. 1134–1139, 2012, doi: 10.1109/BioRob.2012.6290772.
[112] J. a Kurth and W. M. Kier, “Scaling of the hydrostatic skeleton in the earthworm Lumbricus terrestris.,” The Journal of experimental biology, vol. 217, no. Pt 11, pp. 1860–7, 2014, doi: 10.1242/jeb.098137.
[113] F. Luna and C. D. Antinuchi, “Cost of foraging in the subterranean rodent Ctenomys talarum: effect of soil hardness,” Canadian Journal Of Zoology-Revue Canadienne De Zoologie, vol. 84, no. 5, pp. 661–667, 2006, doi: 10.1139/Z06-040.
[114] D. Vleck, “The Energy Cost of Burrowing by the Pocket Gopher Thomomys bottae,” Physiological Zoology, vol. 52, no. 2, pp. 122–136, 1979.
[115] B. Lovegrove, “The Cost of Burrowing by the Social Mole Rats (Bathyergidae) Cryptomys damarensis and Heterocephalus glaber: The Role of Soil Moisture,” 2016.
[116] K. Nagaoka and T. Kubota, “Analytic study on screw drilling mechanism,” 2009 IEEE International Conference on Robotics and Biomimetics, ROBIO 2009, pp. 1579–1584, 2009, doi: 10.1109/ROBIO.2009.5420396.
[117] K. Nagaoka, T. Kubota, M. Otsuki, and S. Tanaka, “Robotic screw explorer for lunar subsurface investigation: Dynamics modelling and experimental validation,” 2009 International Conference on Advanced Robotics, 2009.

[118] H. Omori, T. Nakamura, T. Yada, T. Murakami, H. Nagai, and C. Uni-, “Excavation Mechanism for a Planetary Underground Explorer Robot,” pp. 1273–1279, 2010.
[119] F. Becker, S. Börner, R. Lichtenheldt, and K. Zimmermann, “Enabling Autonomous Locomotion into Sand – A Mobile and Modu- lar Drilling Robot,” pp. 307–312, 2016.
[120] C. Darukhanavala, A. Lycas, A. Mittal, and A. Suresh, “Design of a bimodal self-burying robot,” Proceedings - IEEE International Conference on Robotics and Automation, pp. 5600–5605, 2013, doi: 10.1109/ICRA.2013.6631381.
[121] “Badger Project,” 2017. http://www.badger-robotics.eu/badger/content/concept-and-approach
[122] J. Bishop-Moser, G. Krishnan, C. Kim, and S. Kota, “Design of soft robotic actuators using fluid-filled fiber-reinforced elastomeric enclosures in parallel combinations,” IEEE International Conference on Intelligent Robots and Systems, pp. 4264–4269, 2012, doi: 10.1109/IROS.2012.6385966.
[123] M. S. Verma, A. Ainla, D. Yang, D. Harburg, and G. M. Whitesides, “A Soft Tube-Climbing Robot,” Soft Robotics, vol. 5, no. 2, pp. 133–137, Apr. 2018, doi: 10.1089/soro.2016.0078.
[124] M. Kamata, S. Yamazaki, Y. Tanise, Y. Yamada, and T. Nakamura, “Development of Pneumatically Driven Peristaltic-Type Robot for Long Distance Inspection in Half-inch Pipes,” in IEEE International Conference on Advanced Intelligent Mechatronics (AIM), 2017, pp. 309–314.
[125] A. A. Calderon, J. C. Ugalde, J. C. Zagal, and N. O. Perez-Arancibia, “Design, fabrication and control of a multi-material-multi-actuator soft robot inspired by burrowing worms,” in 2016 IEEE International Conference on Robotics and Biomimetics, ROBIO 2016, 2016, pp. 31–38. doi: 10.1109/ROBIO.2016.7866293.
[126] J. Z. Ge, A. A. Calderón, and N. O. Pérez-Arancibia, “An Earthworm-Inspired Soft Crawling Robot Controlled by Friction,” cs.RO, vol. 1707, no. 0408, Jul. 2017, [Online]. Available: http://arxiv.org/abs/1707.04084
[127] B. Liu, Y. Ozkan-Aydin, D. Goldman, and F. Hammond, “Kirigami skin improves soft earthworm robot anchoring and locomotion under cohesive soil,” in RoboSoft 2019: IEEE Conference on Soft Robotics, 2019, pp. 828–833.
[128] General Electric, “Earthworm-Like Robot for Superfast, Ultra-efficient Tunnel Digging,” May 20, 2020.
[129] C. S. Kothera, M. Jangid, J. Sirohi, and N. M. Wereley, “Experimental Characterization and Static Modeling of McKibben Actuators,” Journal of Mechanical Design, vol. 131, no. 9, pp. 1–10, 2009, doi: 10.1115/1.3158982.
[130] G. K. Klute and B. Hannaford, “Accounting for Elastic Energy Storage in McKibben Artificial Muscle Actuators,” Journal of Dynamic Systems, Measurement, and Control, vol. 122, no. 2, p. 386, 2000, doi: 10.1115/1.482478.

[131] S. Davis and D. G. Caldwell, “Braid Effects on Contractile Range and Friction Modeling in Pneumatic Muscle Actuators,” The International Journal of Robotics Research, vol. 25, no. 4, pp. 359–369, 2006, doi: 10.1177/0278364906063227.
[132] H. F. Schulte, “The characteristic of the McKibben artificial muscle,” The application of external power in prosthetics and orthotics, pp. 94–115, 1962.
[133] K. C. Wickramatunge and T. Leephakpreeda, “Empirical Modeling of Pneumatic Artificial Muscle,” Proceedings of the International MultiConference of Engineers and Computer Scientists, vol. II, no. 0, pp. 3–7, 2009, [Online]. Available: http://www.iaeng.org/publication/IMECS2009/IMECS2009_pp1726-1730.pdf
[134] G. Andrikopoulos, G. Nikolakopoulos, and S. Manesis, “A Survey on applications of Pneumatic Artificial Muscles,” 2011 19th Mediterranean Conference on Control and Automation, MED 2011, pp. 1439–1446, 2011, doi: 10.1109/MED.2011.5982983.
[135] A. N. Gent, “On the relation between indentation hardness and Young’s modulus,” Institution of Rubber Industry -- Transactions, no. 34, pp. 46–57, 1958.
[136] B. Hamlen, G. Mcdonald, M. Gilbertson, D. Ng, and T. Kowalewski, “Automated Manufacturing of Fiber-Reinforced Elastomeric Enclosures for Patient Specific Catheter Robots,” in Design of Medical Devices Conference, 2019, pp. 1–4. [Online]. Available: http://asmedigitalcollection.asme.org/BIOMED/proceedings-pdf/DMD2019/41037/V001T10A016/5171395/v001t10a016-dmd2019-3300.pdf
[137] K. Luo, P. Rothemund, G. M. Whitesides, and Z. Suo, “Soft kink valves,” Journal of the Mechanics and Physics of Solids, vol. 131, pp. 230–239, Oct. 2019, doi: 10.1016/j.jmps.2019.07.008.
[138] K. Jensen, W. Mickelson, A. Kis, and A. Zettl, “Buckling and kinking force measurements on individual multiwalled carbon nanotubes,” Physical Review B - Condensed Matter and Materials Physics, vol. 76, no. 19, Nov. 2007, doi: 10.1103/PhysRevB.76.195436.
[139] J. Y. Kim, N. Mazzoleni, and M. Bryant, “Modeling of resistive forces and buckling behavior in variable recruitment fluidic artificial muscle bundles,” Actuators, vol. 10, no. 3, pp. 1–24, Mar. 2021, doi: 10.3390/act10030042.
[140] R. Norton, Machine Design, 5th ed. Pearson, 2014.
[141] W. Castaneda-Zuniga et al., “The mechanism of balloon angioplasty,” Diagnostic Radiology, vol. 135, pp. 565–571, 1980.
[142] G. Mcdonald, A. Safdari, and T. M. Kowalewski, “Traction of Helical Soft Continuum Actuators for Endoluminal Robots Motivation Methods Results and Conclusion,” 2017.
[143] A. Mazzeo, S. Morin, R. Shepherd, G. Whitesides, and W. Kalb, “Flexible Robotic Actuators,” US 9,506,455 B2, Nov. 29, 2016

[144] F. Ilievski et al., “Soft Robotic Actuators,” US 2017/0097021 A1, Apr. 06, 2017
[145] Garderen, K, “Forecasting growth and levels in loglinear unit root models” University of Amsterdam, pp. 1-52, 2005.

Appendix A: Elastic Force Results for All Contracting McKibben Actuators

Appendix A shows the elastic force results for all the contracting McKibben Actuators A-L from section 2.2.2.2 before pressure was applied to the actuators.

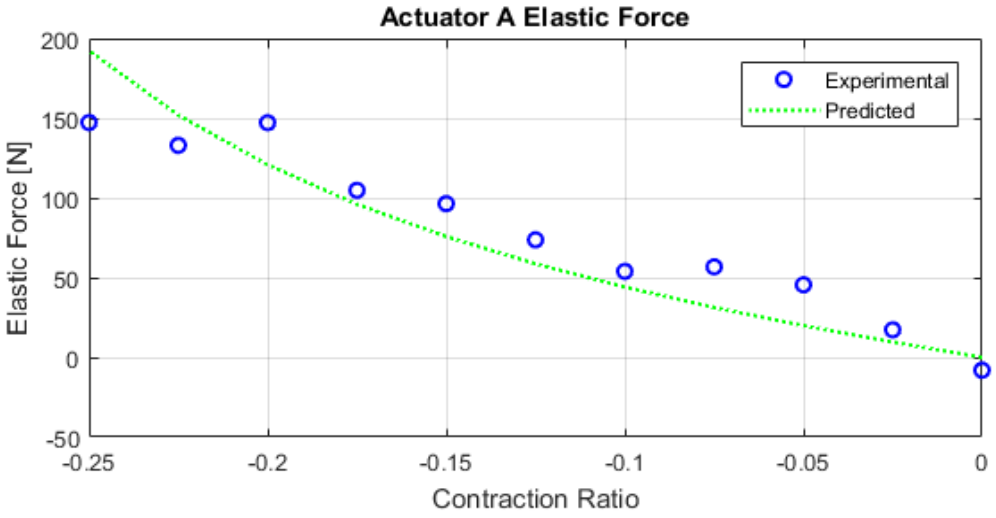

Figure 190: Elastic force of contracting McKibben Actuator A

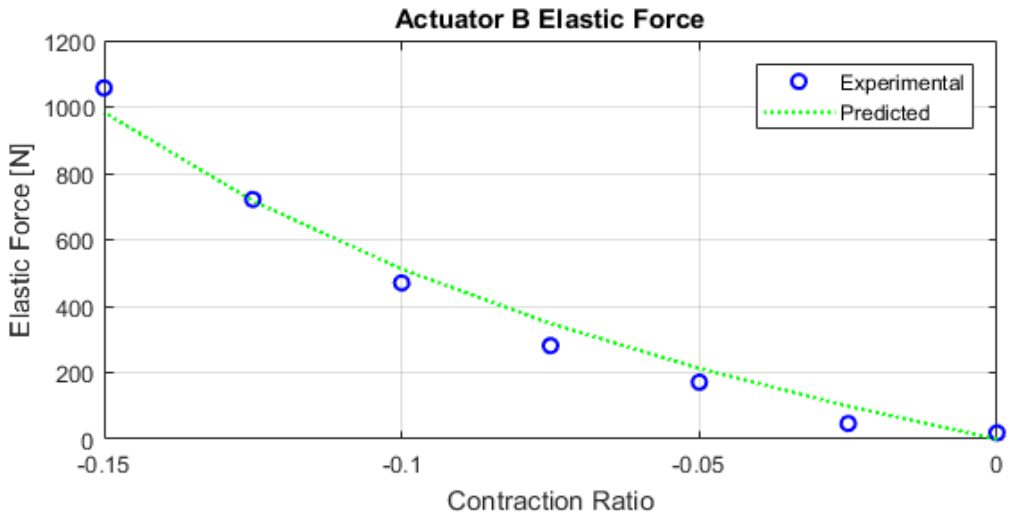

Figure 191: Elastic force of contracting McKibben Actuator B

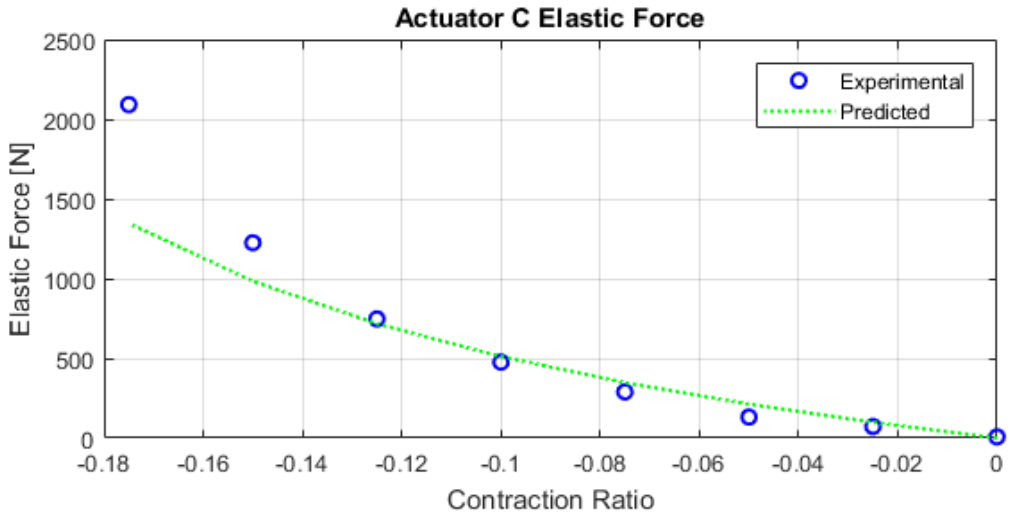

Figure 192: Elastic force of contracting McKibben Actuator C

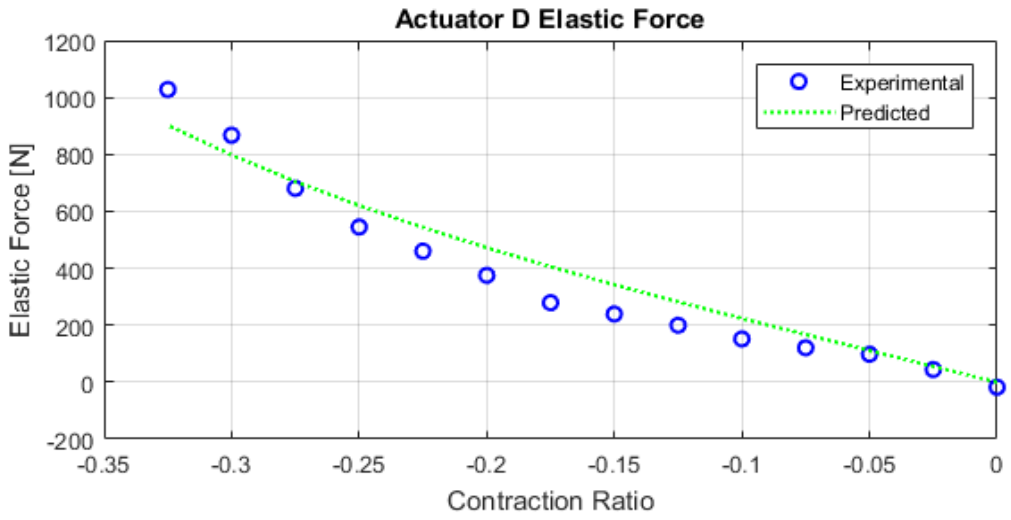

Figure 193: Elastic force of contracting McKibben Actuator D

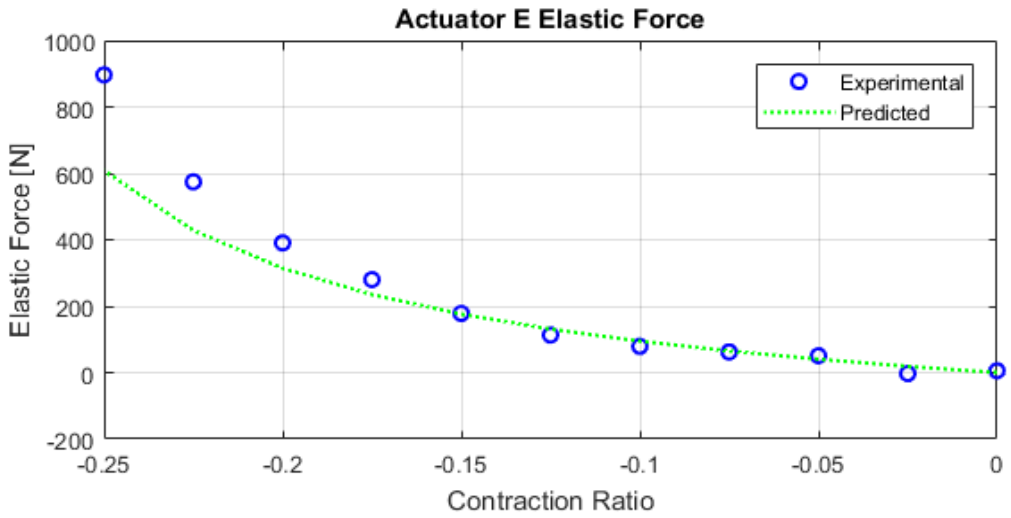

Figure 194: Elastic force of contracting McKibben Actuator E

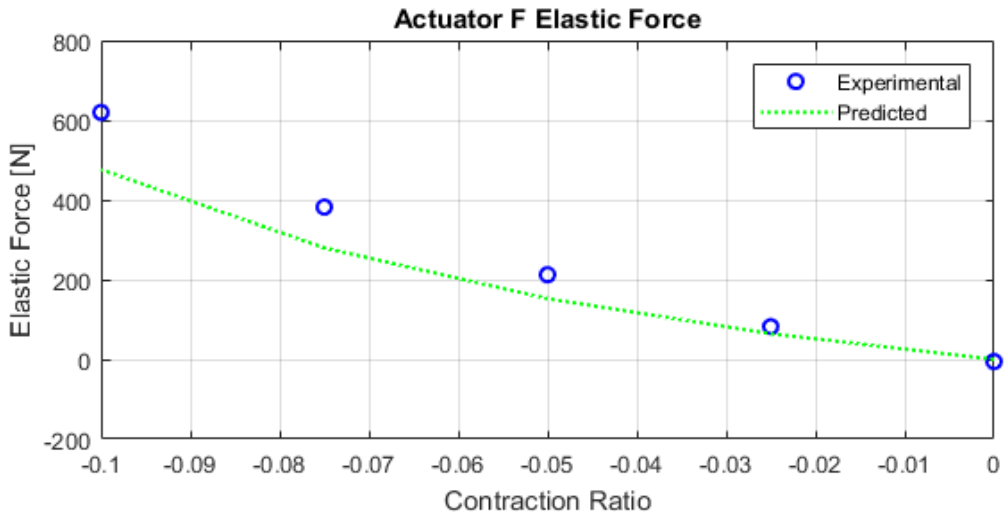

Figure 195: Elastic force of contracting McKibben Actuator F

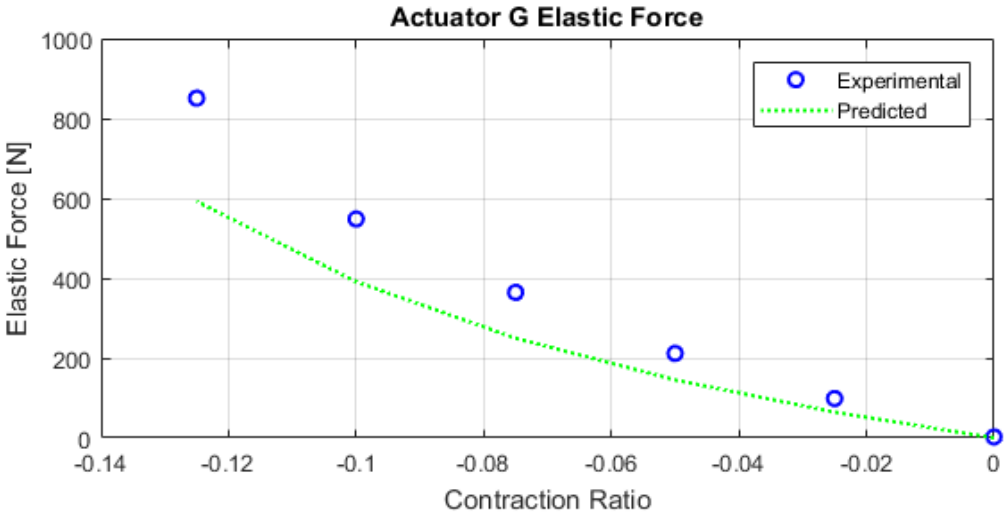

Figure 196: Elastic force of contracting McKibben Actuator G

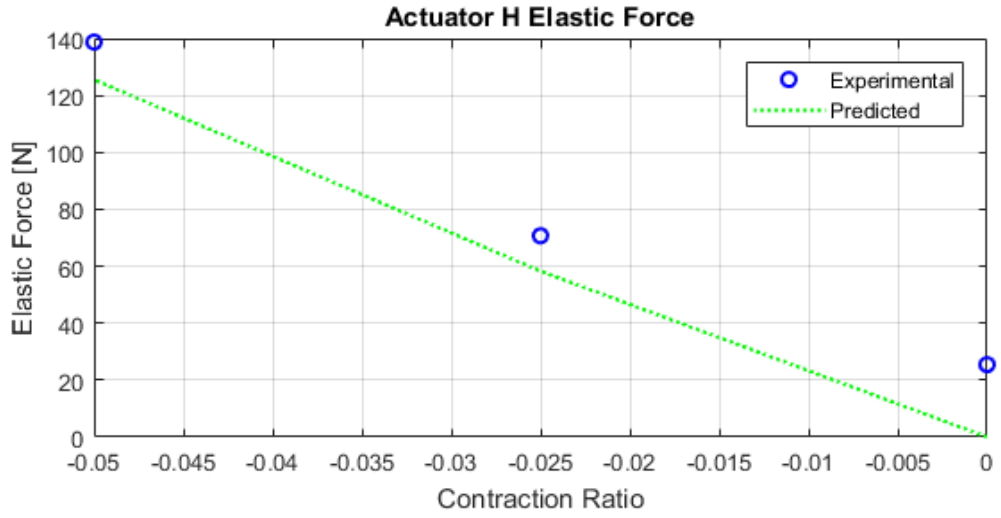

Figure 197: Elastic force of contracting McKibben Actuator H

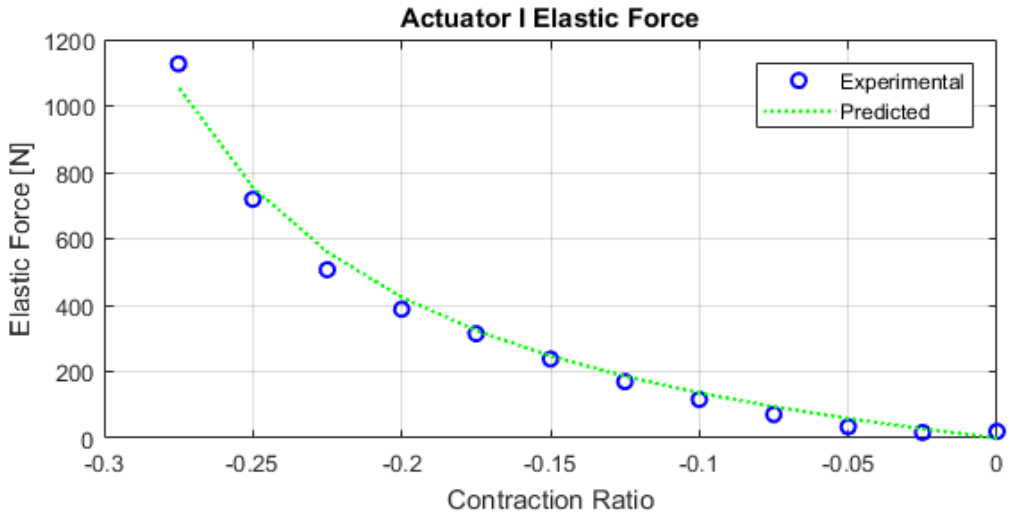

Figure 198: Elastic force of contracting McKibben Actuator I

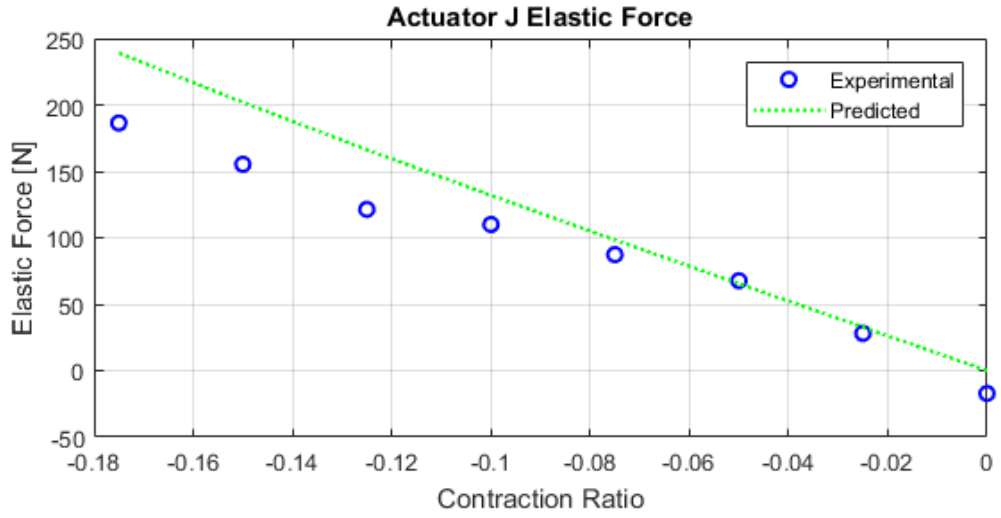

Figure 199: Elastic force of contracting McKibben Actuator J

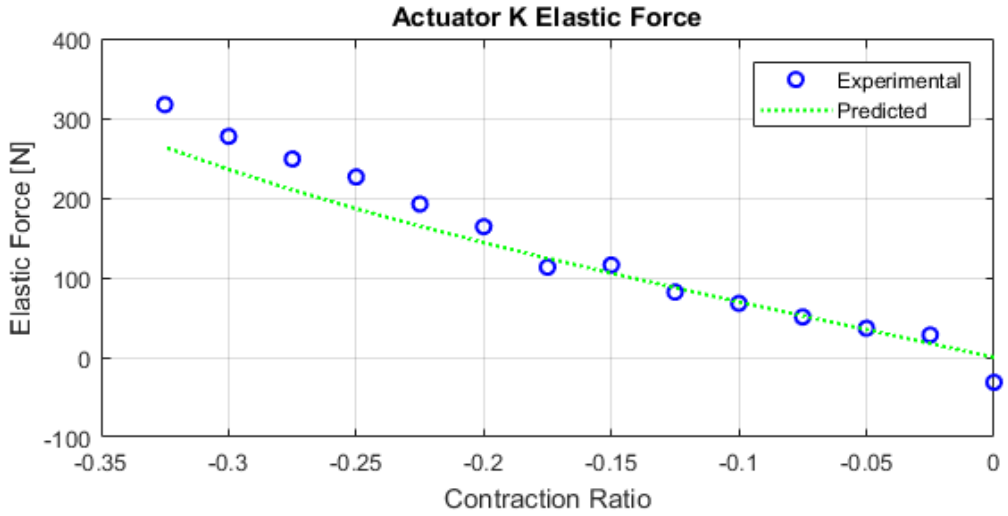

Figure 200: Elastic force of contracting McKibben Actuator K

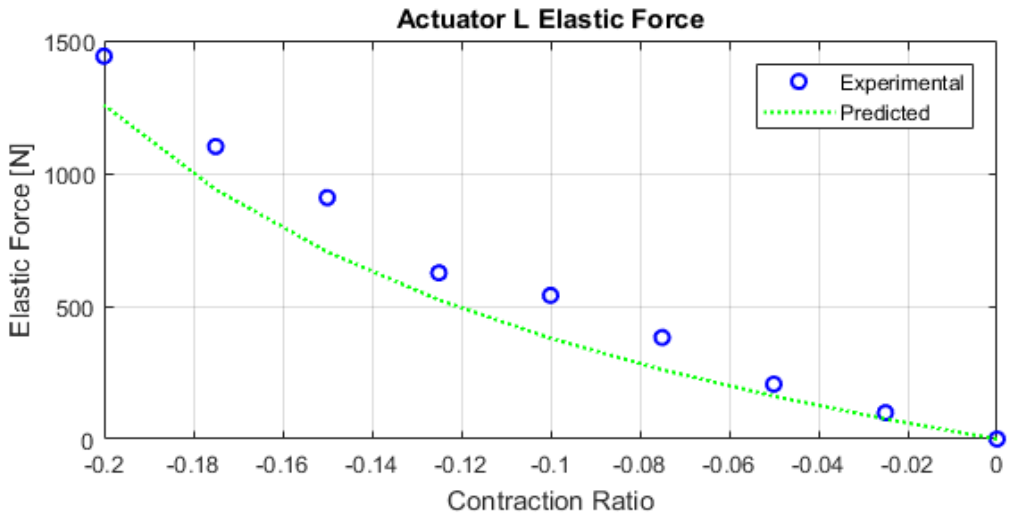

Figure 201: Elastic force of contracting McKibben Actuator L

Appendix B: Total Force Results for All Contracting McKibben Actuators

Appendix B shows the total axial force results for all the contracting McKibben Actuators A-L from section 2.2.2.3 after pressure was applied to the actuators.

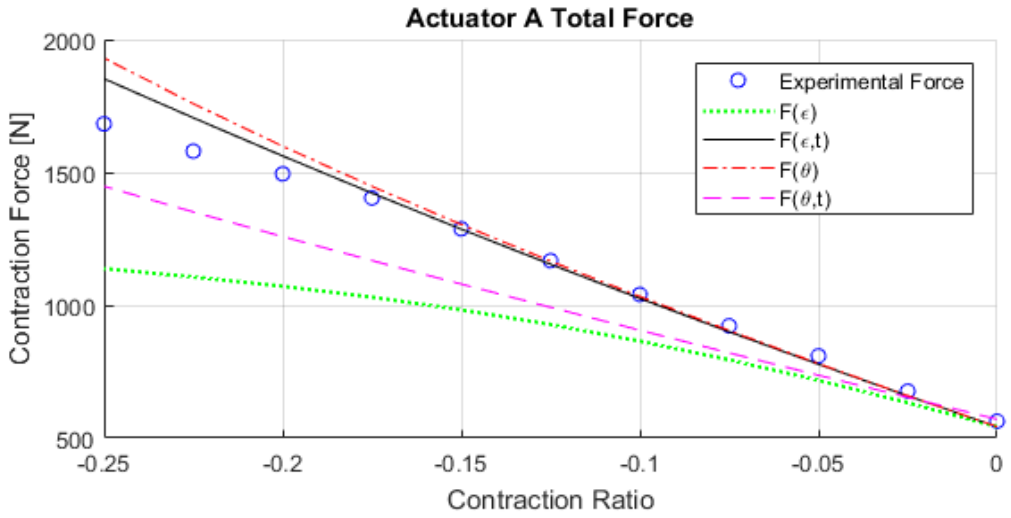

Figure 202: Total force results for Actuator A (60A Neoprene) at 6.89 MPa

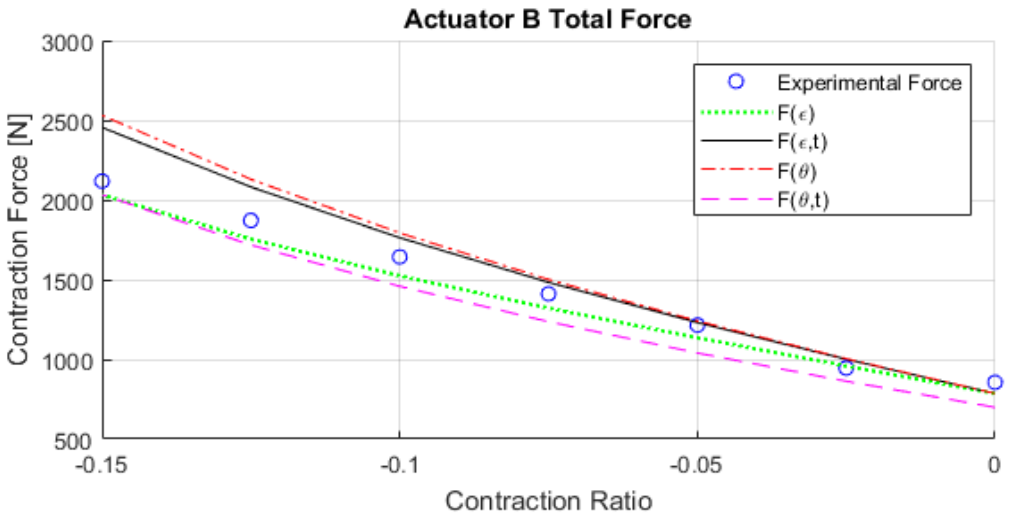

Figure 203: Total force results for Actuator B (80A Neoprene) at 2.75 MPa

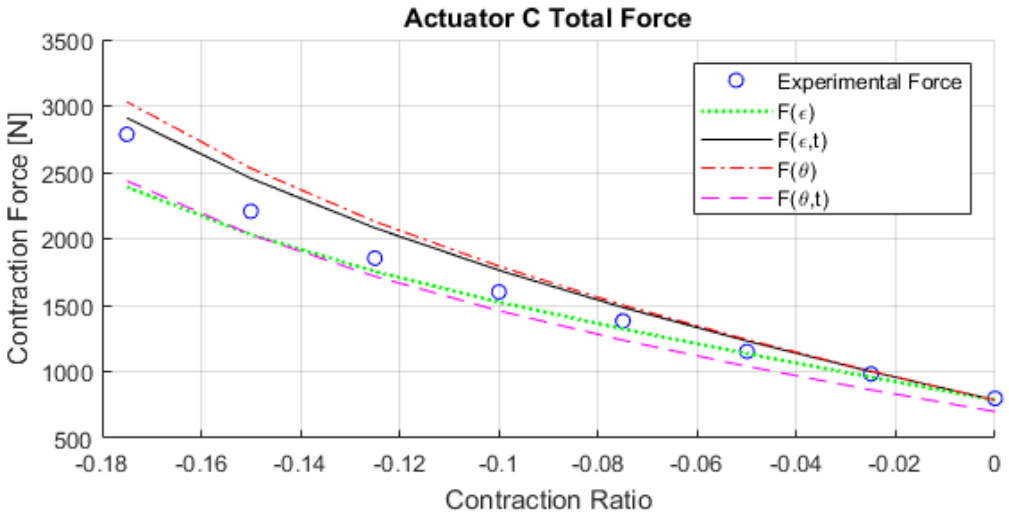

Figure 204: Total force results for Actuator C (80A Neoprene) at 2.75 MPa

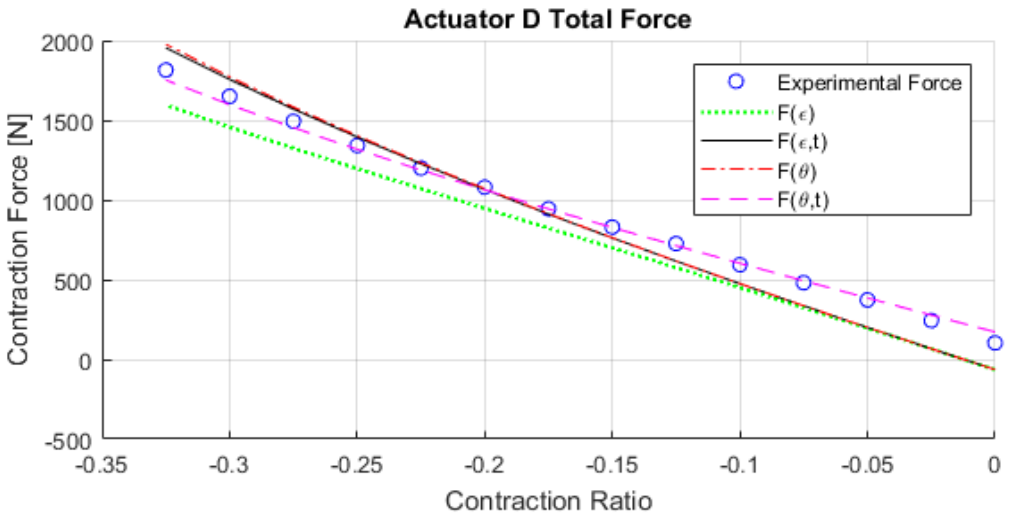

Figure 205: Total force results for Actuator D (80A Neoprene) at 2.75 MPa

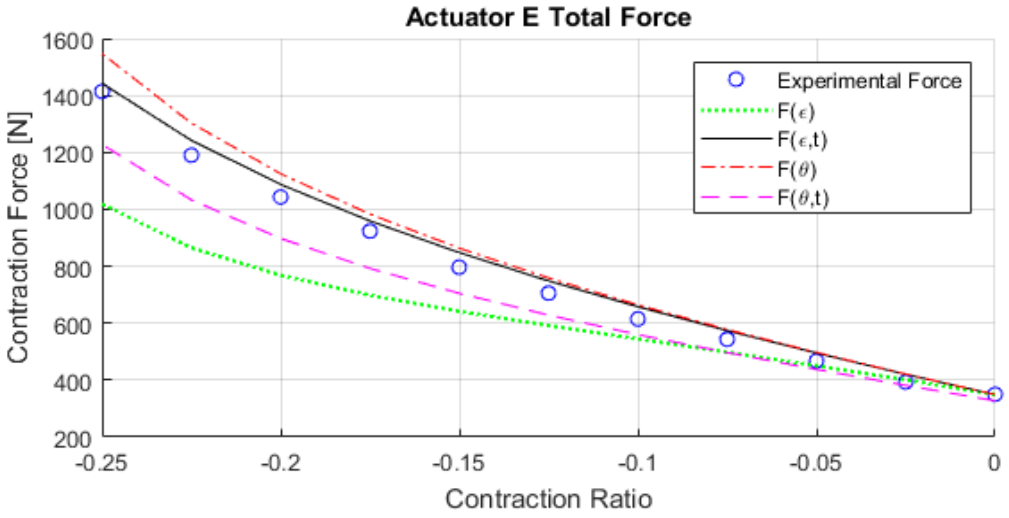

Figure 206: Total force results for Actuator E (70A Natural Rubber) at 2.75 MPa

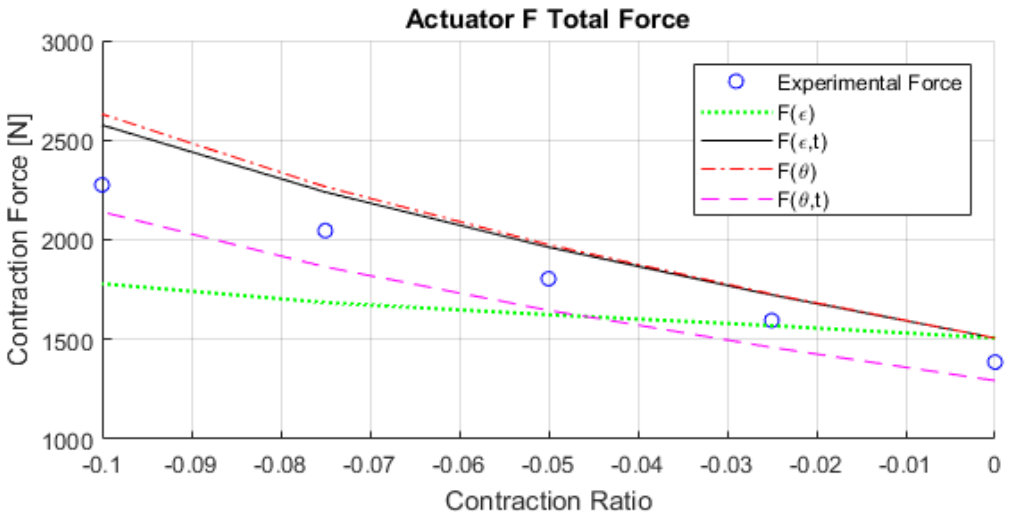

Figure 207: Total force results for Actuator F (70A Natural Rubber) at 2.75 MPa

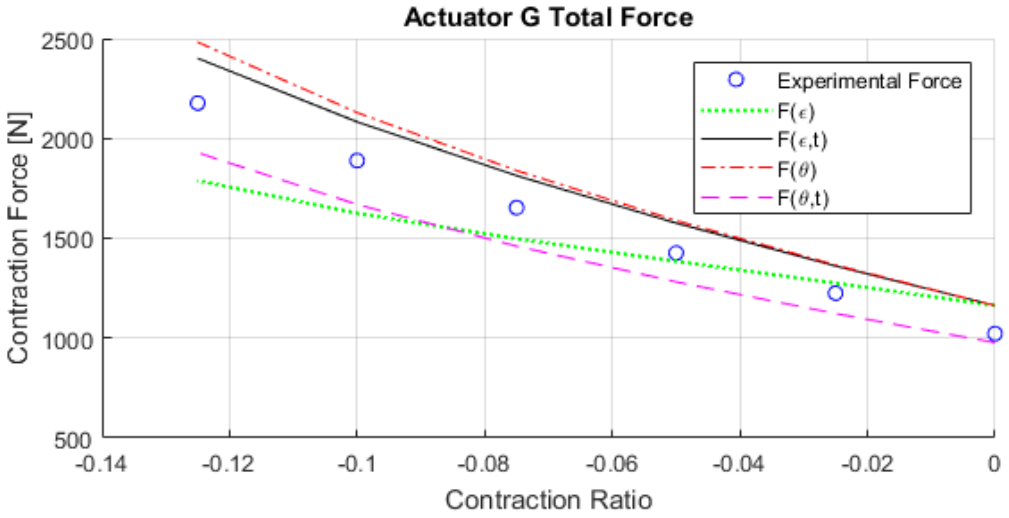

Figure 208: Total force results for Actuator G (70A Natural Rubber) at 2.75 MPa

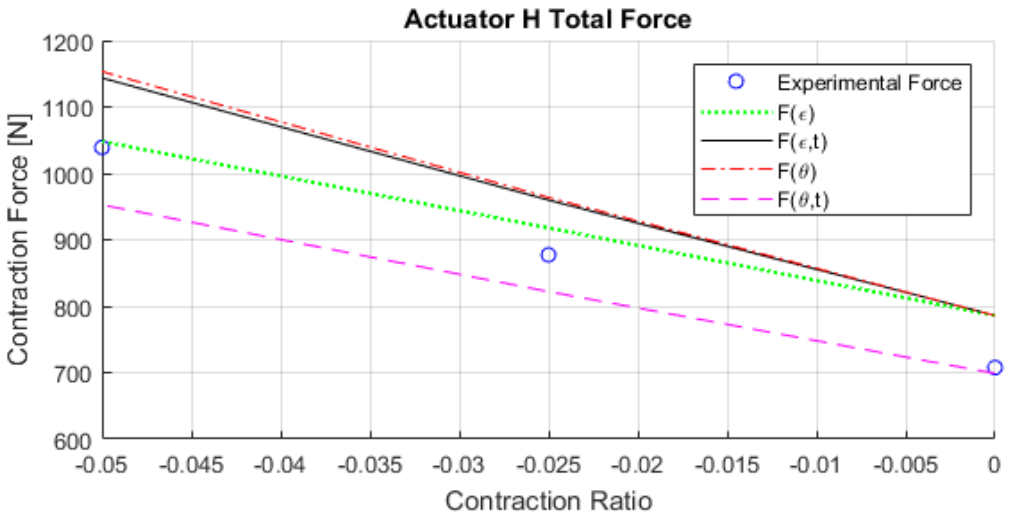

Figure 209: Total force results for Actuator H (70A Natural Rubber) at 2.75 MPa

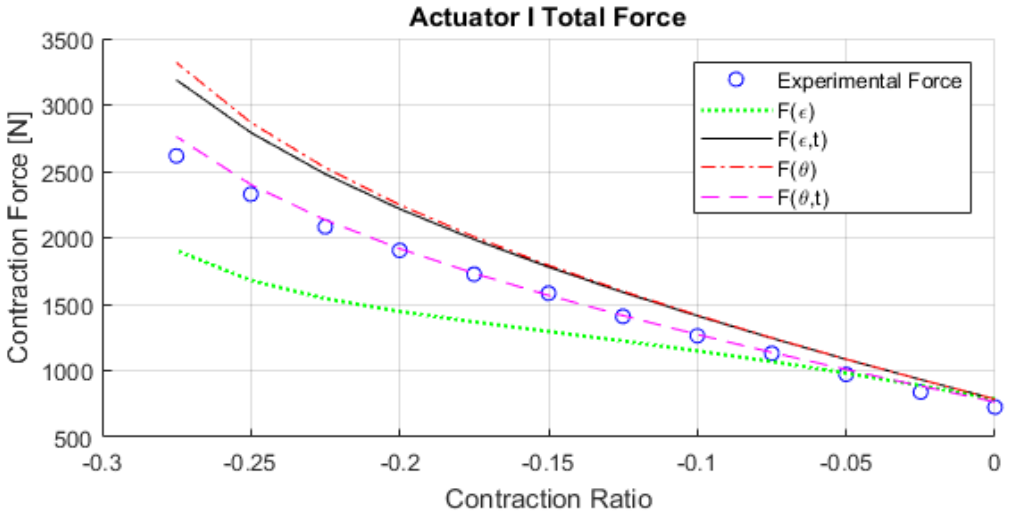

Figure 210: Total force results for Actuator I (70A Natural Rubber) at 2.75 MPa

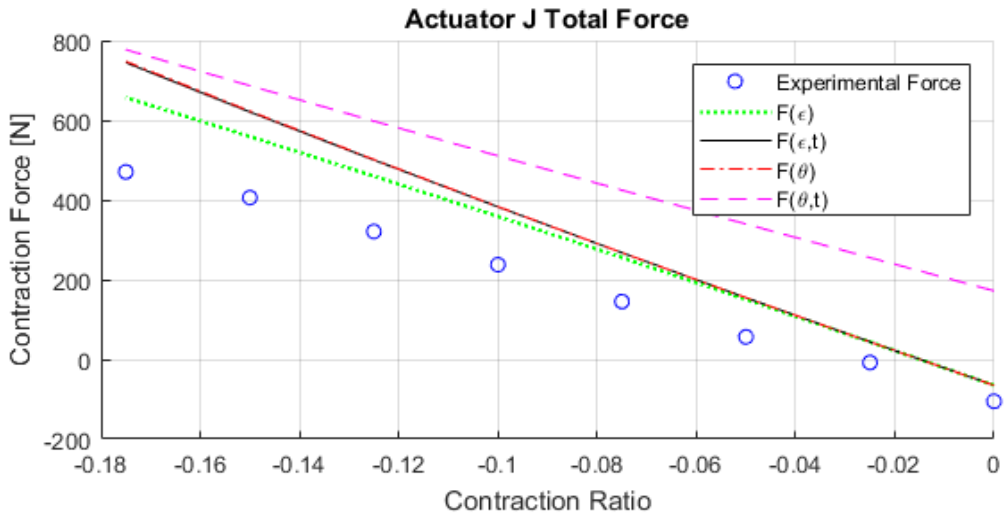

Figure 211: Total force results for Actuator J (70A Natural Rubber) at 2.75 MPa

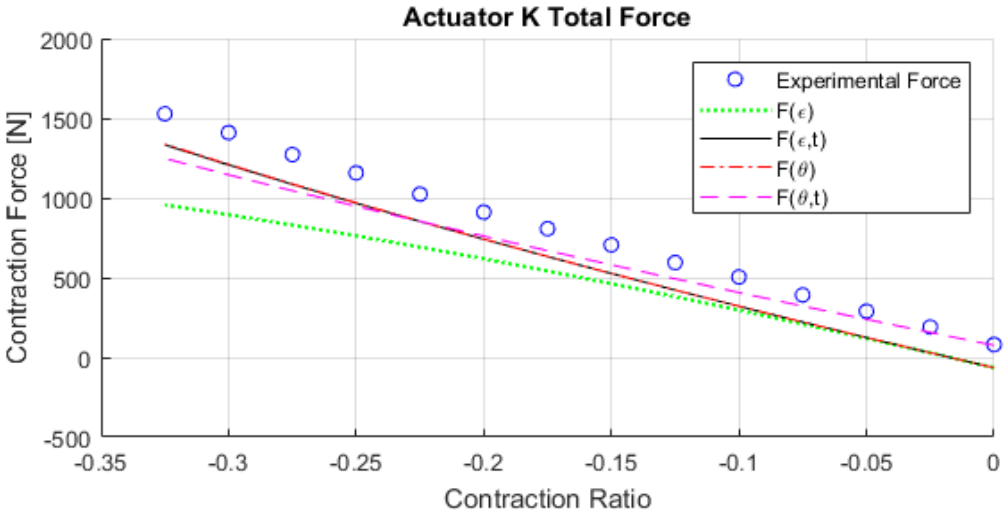

Figure 212: Total force results for Actuator K (70A Natural Rubber) at 2.75 MPa

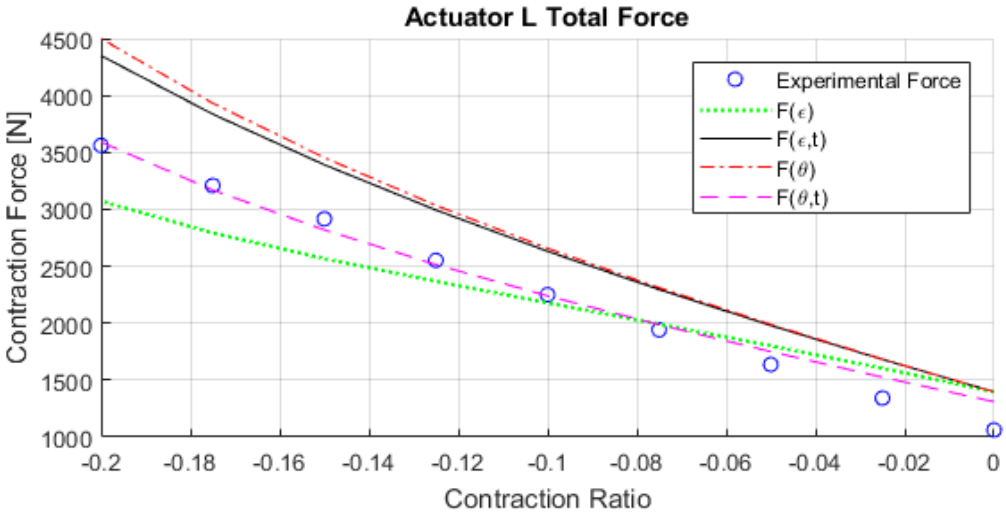

Figure 213: Total force results for Actuator L (70A Natural Rubber) at 2.75 MPa

Appendix C: Other Fiber Protection and Fiber Placement Methods

Appendix C is a summary of fiber protection and fiber placement methods that were explored in the process of designing the extending McKibben actuators that were tested in section 2.3.

The commercially available 2x2 twill aramid fiber sleeves used in the contracting McKibben experiments are limited to more shallow fiber angles not useful for producing extension forces due to the inherent physics of the continuous fiber weave. Thus, methods for protecting and applying fibers at a custom fiber angle were explored. While these methods were not used to produce the extending actuators used in the experiments, they may be value for future research.

The fiber wrapping lathe provides a customizable fiber wrapping capability (and was used to wrap the actuators used in these experiments), but other methods were examined as well. A method identified for placing fibers in a prescribed and repeatable manner was utilizing 3D printed fiber wrap guides for the forward and backward wrap angles and using thin double-sided tape to ensure the fibers remained in place. First, the forward wrapping 3D printed guide is slid concentrically over the elastomer to guide hand wrapping of the fibers around the elastomer wrapped in double-sided tape. Once the forward wrapping was completed and the fibers were adhered to the elastomer, the forward guide

is cut off and the backward guide placed over the elastomer. The second fiber is then wrapped using the backward guide to complete the fiber wrapping process. A demonstration of this method is shown in Figure 214. A downfall of this method is that it is very time intensive, although it allows for highly customized fiber placement.

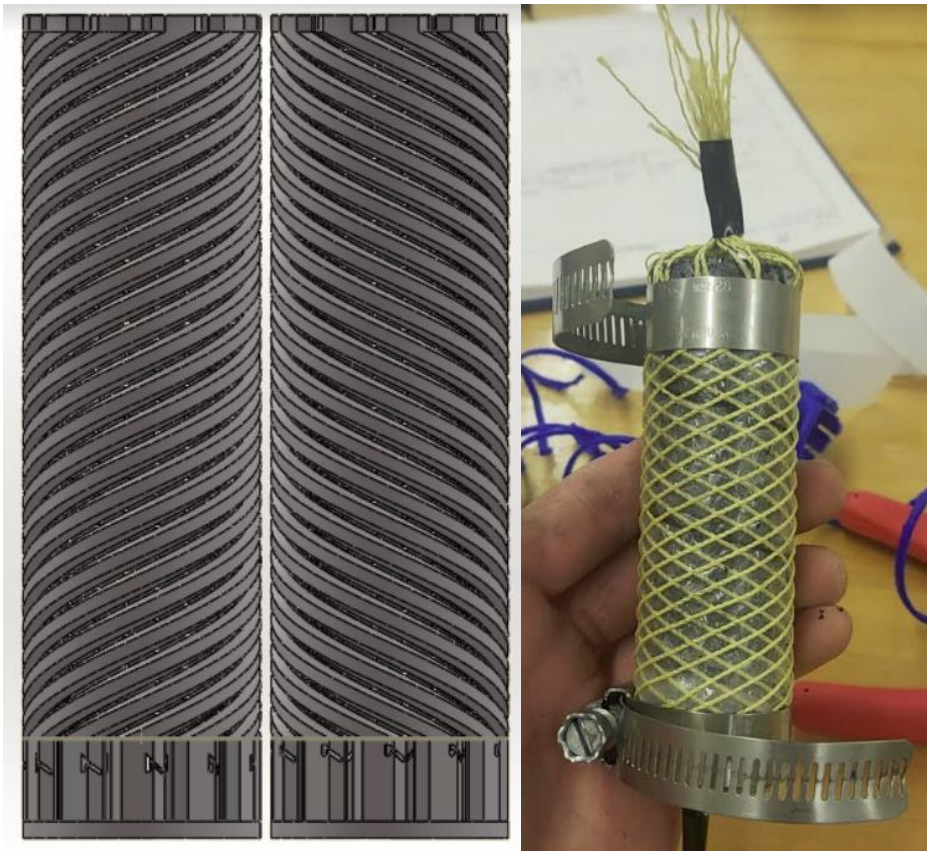

Figure 214: Forward and backward fiber wrapping guides (left), wrapped elastomer (right)

Before utilizing the dual elastomer fiber sandwiching methods to manufacture the actuators used in the experiments, various fiber protection

methods were examined ranging from dipping the elastomer in a coating chemical, spraying sealing chemicals on the outside of the elastomer, and wrapping the elastomer in a protective coating. The only method that showed merit was using polyvinylchloride heat shrink tubing which provides a 300% elongation to break once heat is used to concentrically shrink the tubing onto a fiber wrapped elastomer. A demonstration of this technique is shown in Figure 215.

Figure 215: Fiber wrapped elastomer coated with polyvinylchloride heat shrink tubing

Appendix D: Fabricated Extending McKibben Actuator Photos

Appendix D shows the fabricated extending McKibbens for Chapter 2.

Figure 216: All extending McKibben actuators (Actuators 1-5)

Appendix E: Extending Actuator Fiber Angle Measurements

Appendix E shows all the fiber angle measurements that were taken for determining the mean fiber angle for the extending McKibben actuators in section 2.3.

ACT 1:

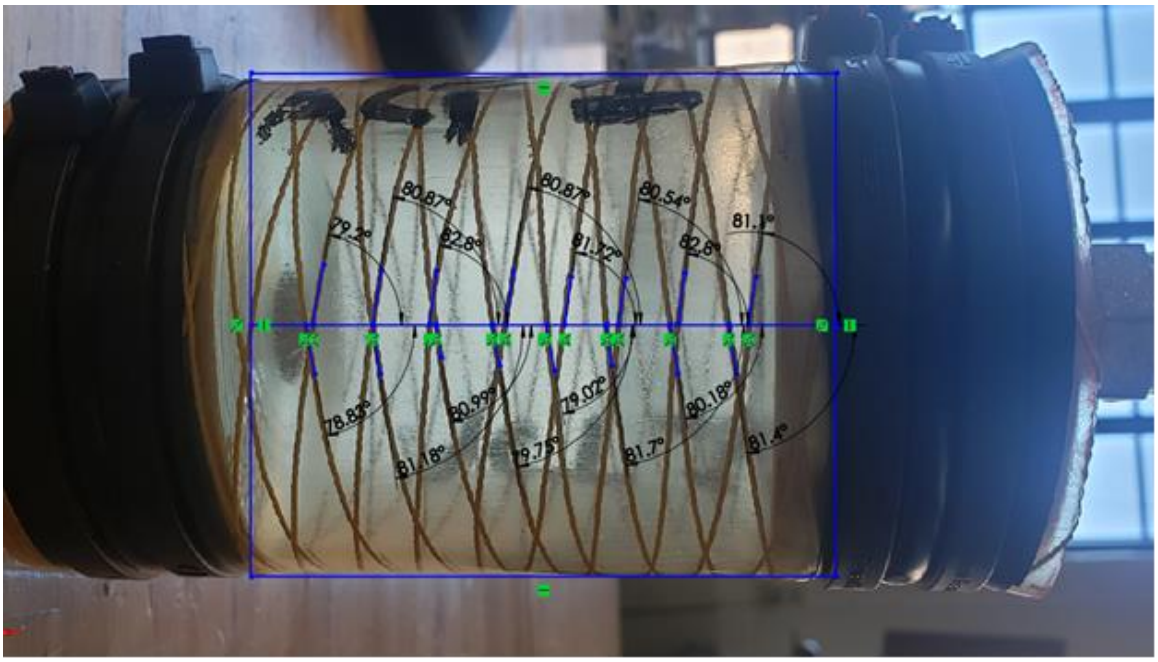

Figure 217: Extending McKibben Actuator 1 fiber angle analysis

Table 18: Extending McKibben Actuator 1 fiber angle results

Angle Measurement #	Measured Angle (degrees)
1	79.20
2	80.87
3	82.80
4	80.87
5	81.72
6	80.54
7	82.80
8	81.10
9	78.83
10	81.18
11	80.99
12	79.75
13	79.02
14	81.70
15	80.18
16	81.40
Mean Angle	**80.81**
Std. Dev	**1.158**

ACT 2:

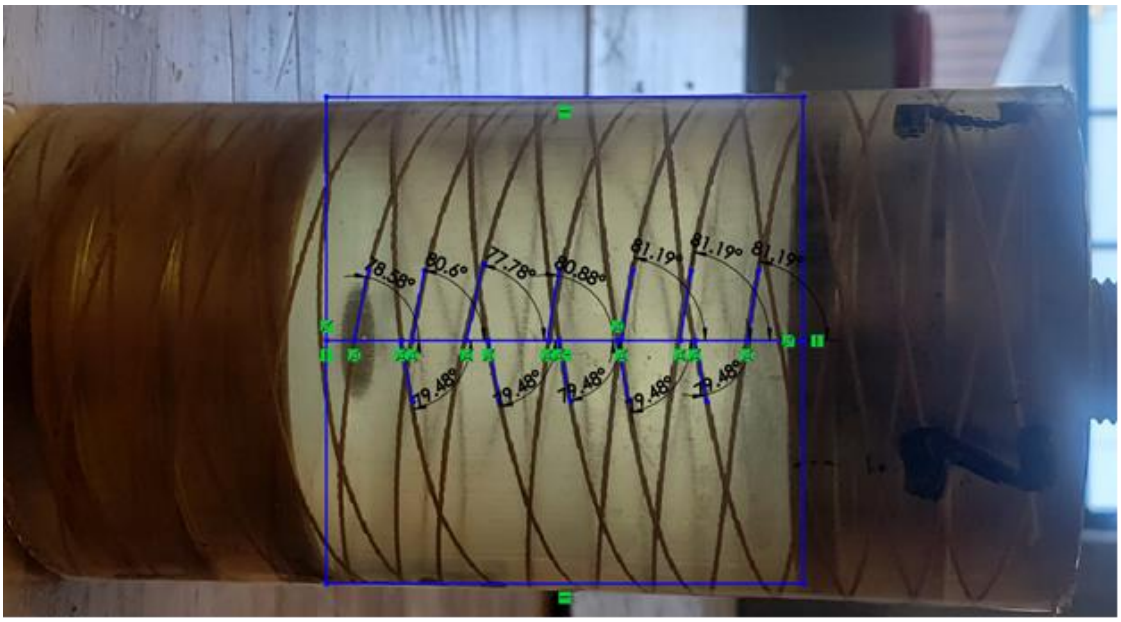

Figure 218: Extending McKibben Actuator 2 fiber angle analysis

Table 19: Extending McKibben Actuator 2 fiber angle results

Angle Measurement #	Measured Angle (degrees)
1	78.68
2	80.60
3	77.78
4	80.88
5	81.19
6	81.19
7	81.19
8	79.48
9	79.48
10	79.48
11	79.48
12	79.48
Mean Angle	**79.91**
Std. Dev	**1.053**

ACT 3:

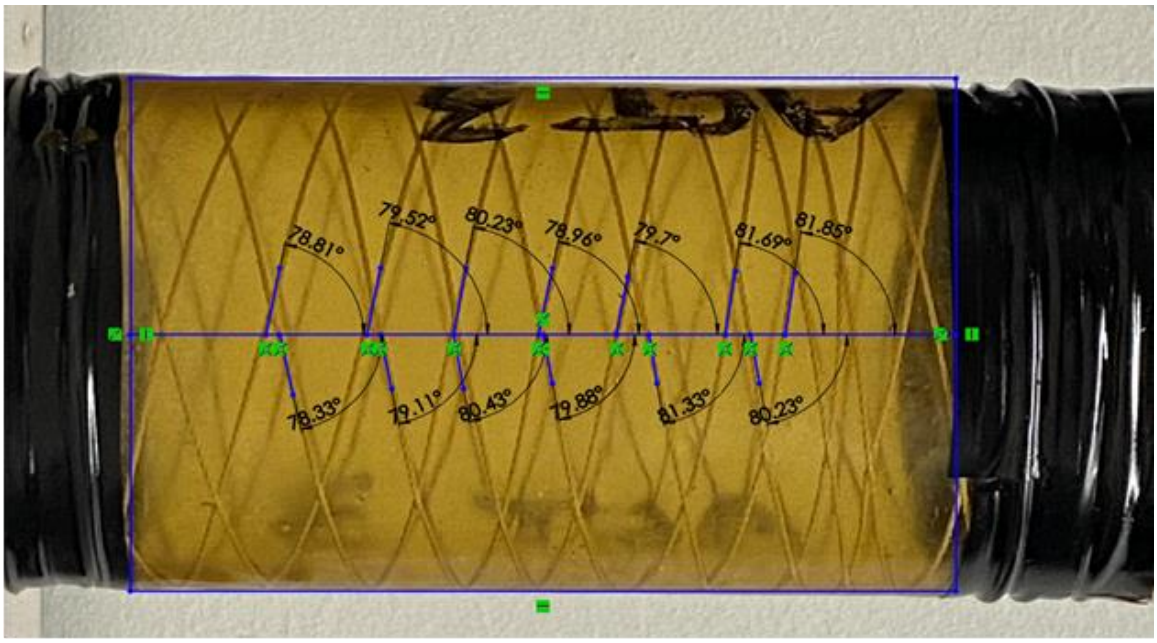

Figure 219: Extending McKibben Actuator 3 fiber angle analysis

Table 20: Extending McKibben Actuator 3 fiber angle results

Angle Measurement #	Measured Angle (degrees)
1	78.81
2	79.52
3	80.23
4	78.96
5	79.70
6	81.69
7	81.85
8	78.33
9	79.11
10	80.43
11	79.88
12	81.33
13	80.23
Mean Angle	**80.01**
Std. Dev	**1.065**

ACT 4:

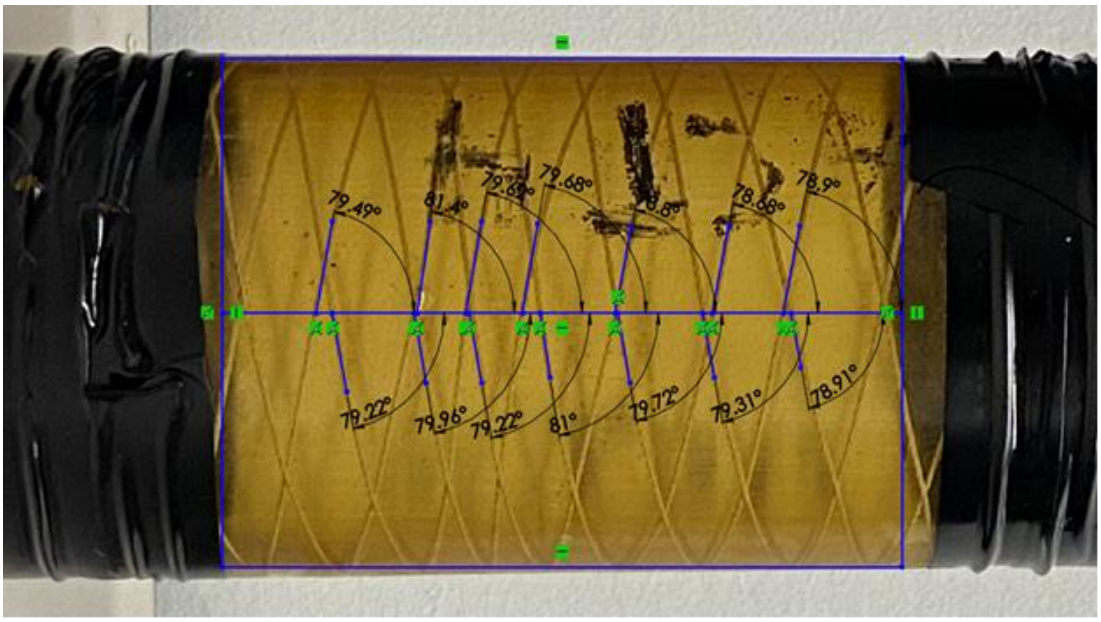

Figure 220: Extending McKibben Actuator 4 fiber angle analysis

Table 21: Extending McKibben Actuator 4 fiber angle results

Angle Measurement #	Measured Angle (degrees)
1	79.49
2	81.40
3	79.62
4	79.68
5	78.80
6	78.68
7	78.90
8	79.22
9	79.96
10	79.22
11	81.00
12	79.72
13	79.31
14	78.91
15	79.56
16	76.40
Mean Angle	**79.56**
Std. Dev	**1.08**

ACT 5:

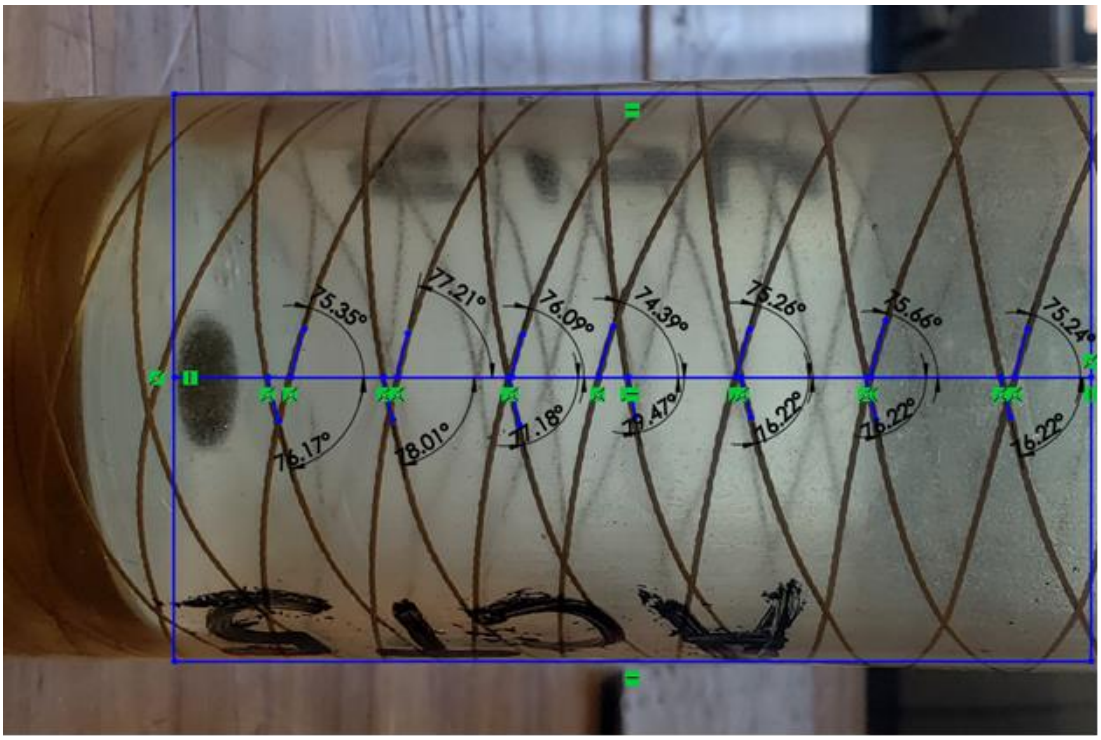

Figure 221: Extending McKibben Actuator 5 fiber angle analysis

Table 22: Extending McKibben Actuator 5 fiber angle results

Angle Measurement #	Measured Angle (degrees)
1	73.35
2	77.21
3	76.09
4	74.39
5	75.26
6	75.66
7	75.24
8	76.17
9	78.01
10	77.18
11	79.47
12	76.22
13	76.22
14	76.22
Mean Angle	**76.19**
Std. Dev	**1.45**

Appendix F: Extending Actuator Extension Error Plots

Appendix F shows the extending McKibben actuator error tables and error plots for the extension experiments in section 2.3

Table 23: Average of absolute value of percent error of each experiment w/ elastic term

	Average of Absolute Value of Percent Error (%) of Each Experiment w/ Elastic Term				
	Number of Tests	**F(θ)**	**F(ε)**	**F(θ,t)**	**F(ε,t)**
Actuator 1	7	9.51	12.07	181.11	9.52
Actuator 2	5	22.70	20.39	102.64	22.68
Actuator 3	9	22.40	18.60	141.56	22.38
Actuator 4	8	31.98	29.17	146.12	31.96
Actuator 5	7	12.96	13.28	62.43	12.96
	Overall Average Error (%)	19.91	18.70	126.77	19.90

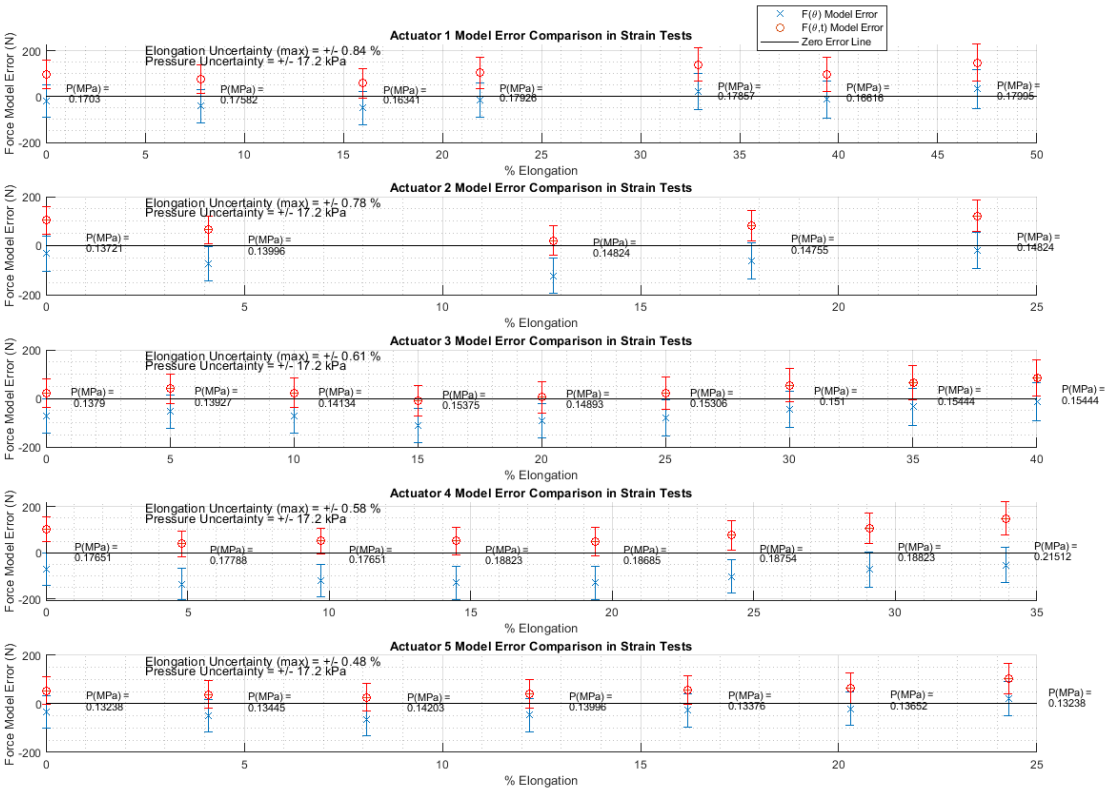

Figure 222: Actuator 1-5 extension experiments magnitude of error - angle based models

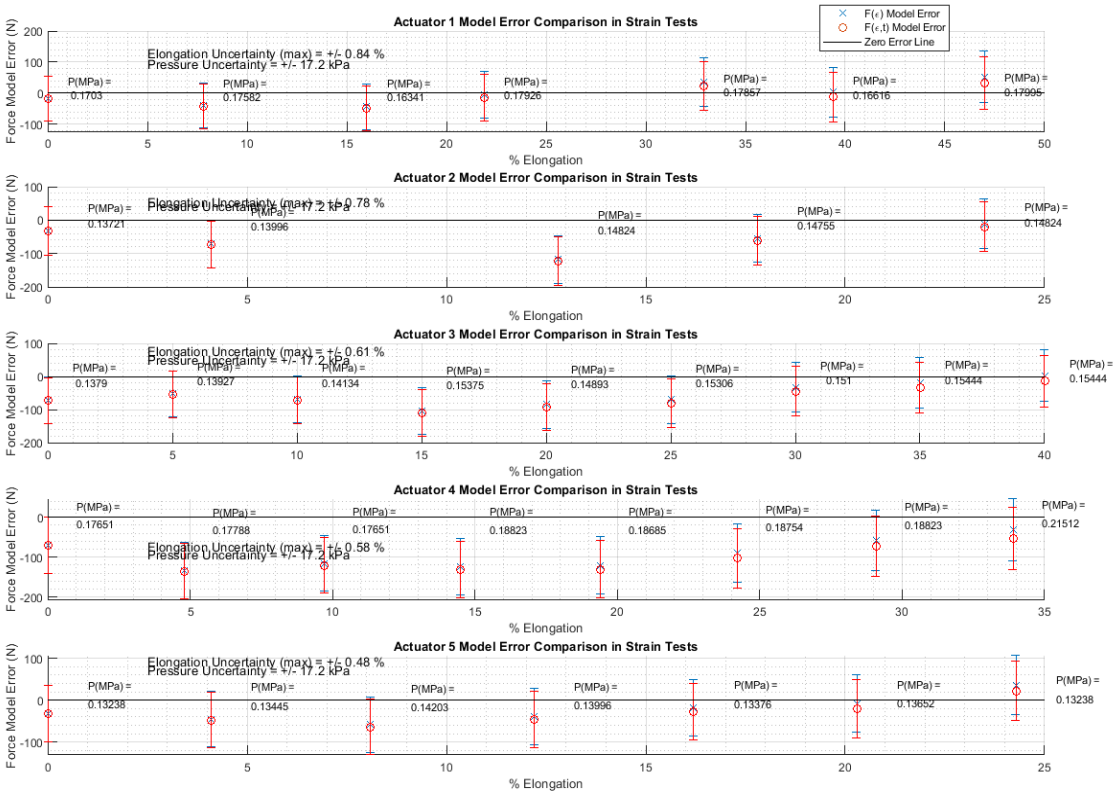

Figure 223: Actuator 1-5 extension experiments magnitude of error - strain based models

Appendix G: Buckling Actuator Fiber Angle Measurements

Appendix G shows all the fiber angle measurements that were taken to determine the mean fiber angle of the buckling actuators used for experimentation in Chapter 3.

ACT 1A:

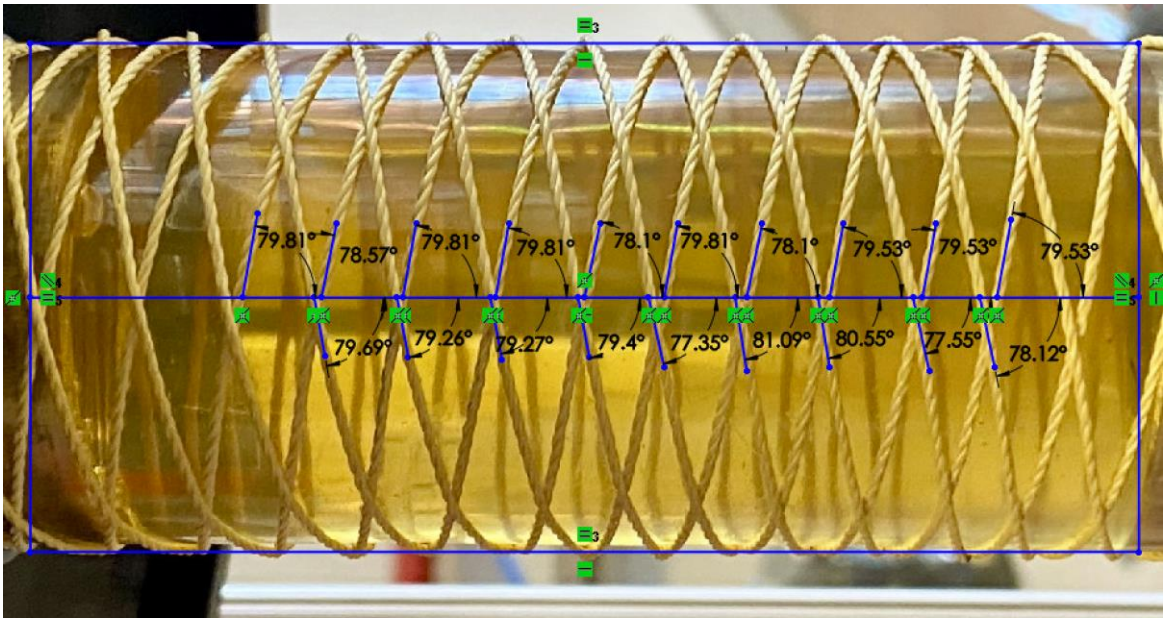

Figure 224: Actuator 1A fiber angle crossings

Table 24: Actuator 1A angle measurements

Angle Measurement #	Measured Angle
1	79.81
2	78.57
3	79.81
4	79.81
5	78.10
6	79.81
7	78.10
8	79.53
9	79.53
10	79.69
11	79.26
12	79.27
13	79.40
14	77.35
15	81.09
16	80.55
17	77.55
18	78.12
Mean Angle	**79.19**
Std. Dev	**0.9864**

ACT 1B:

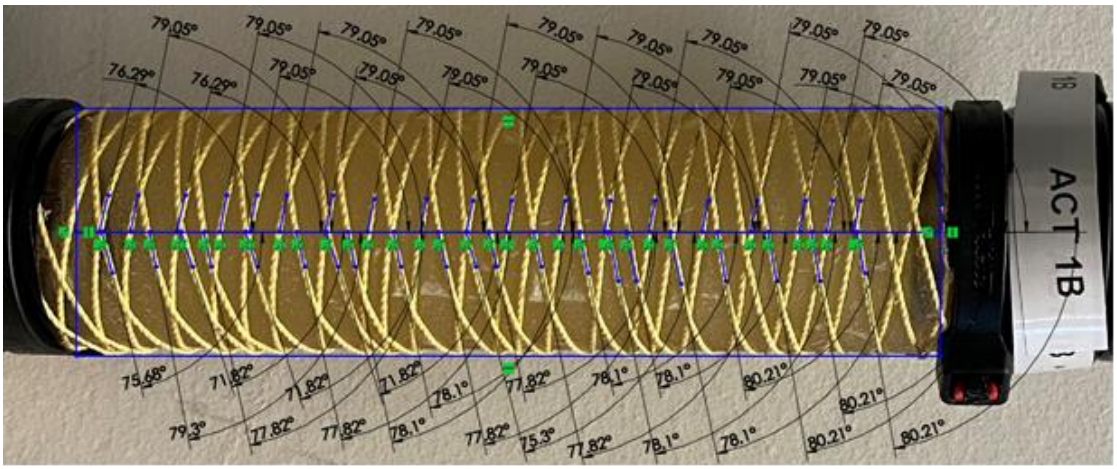

Figure 225: Actuator 1B fiber angle crossings

Table 25: Actuator 1B angle measurements

Angle Measurement #	Measured Angle
1	76.29
2	79.05
3	76.29
4	79.05
5	79.05
6	79.05
7	79.05
8	79.05
9	79.05
10	79.05
11	79.05
12	79.05
13	79.05
14	79.05
15	79.05
16	79.05
17	79.05
18	79.05
19	79.05
20	75.68
21	79.30
22	71.82
23	77.82
24	71.82
25	77.82
26	71.82

27	78.10
28	77.82
29	75.30
30	77.82
31	77.82
32	78.10
33	78.10
34	78.10
35	78.10
36	80.21
37	80.21
38	80.21
39	80.21
Mean Angle	**78.02**
Std. Dev	**2.1078**

ACT 1C:

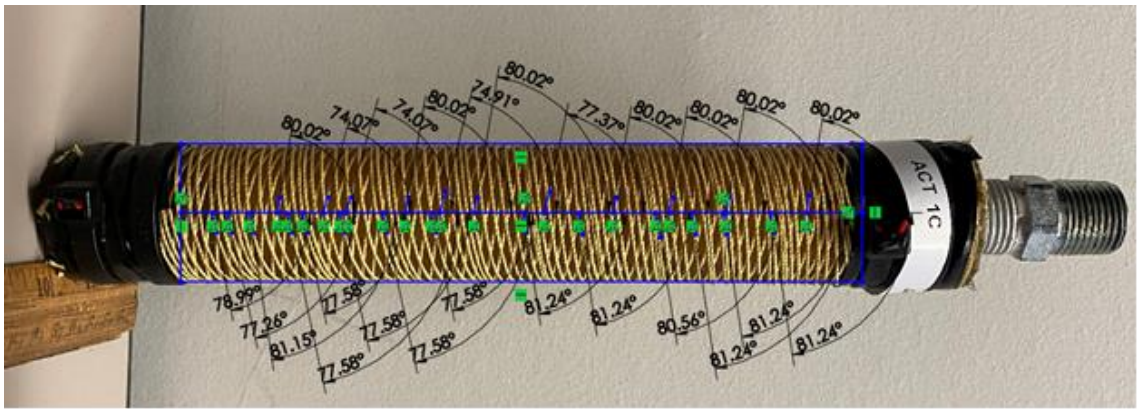

Figure 226: Actuator 1C fiber angle crossings

Table 26: Actuator 1C angle measurements

Angle Measurement #	Measured Angle
1	80.02
2	74.07
3	74.07
4	80.02
5	74.91
6	80.02
7	77.37
8	80.02
9	80.02
10	80.02
11	78.99
12	77.26
13	81.15
14	77.58
15	77.58
16	77.58
17	77.58
18	77.58
19	81.24
20	81.24
21	80.56
22	81.24
23	81.24
24	81.24
Mean Angle	**78.85**
Std. Dev	**2.2268**

ACT 2A:

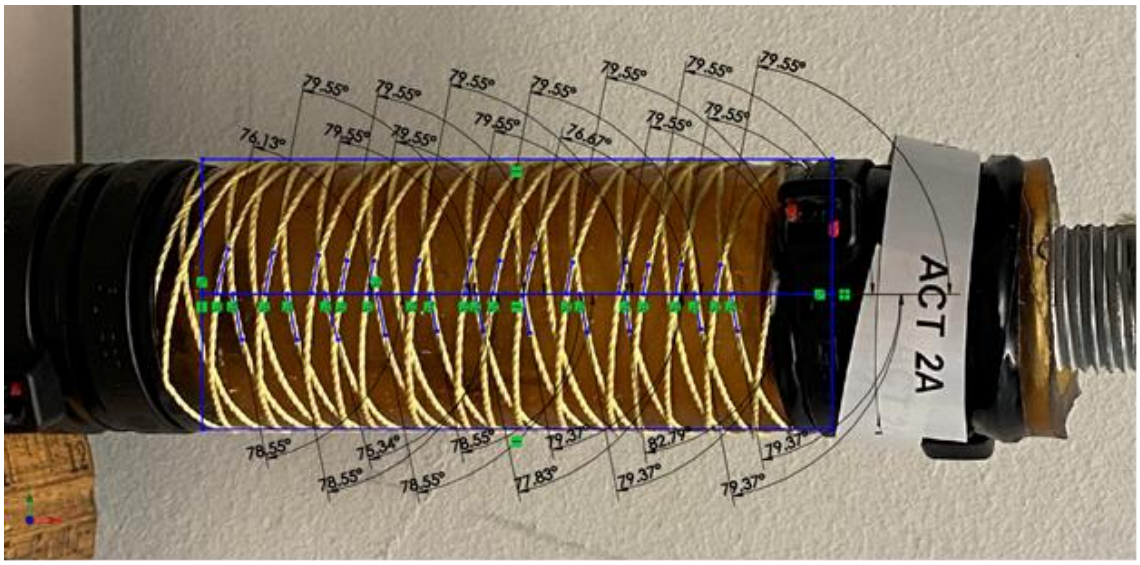

Figure 227: Actuator 2A fiber crossings

Table 27: Actuator 2A angle measurements

Angle Measurement #	Measured Angle
1	76.13
2	79.55
3	79.55
4	79.55
5	79.55
6	79.55
7	79.55
8	79.55
9	76.67
10	79.55
11	79.55
12	79.55
13	79.55
14	79.55
15	78.55
16	78.55
17	75.34
18	78.55
19	78.55
20	77.83
21	79.37
22	79.37
23	82.79
24	79.37
25	79.37
Mean Angle	**79.0016**

Std. Dev	1.3825

ACT 2B:

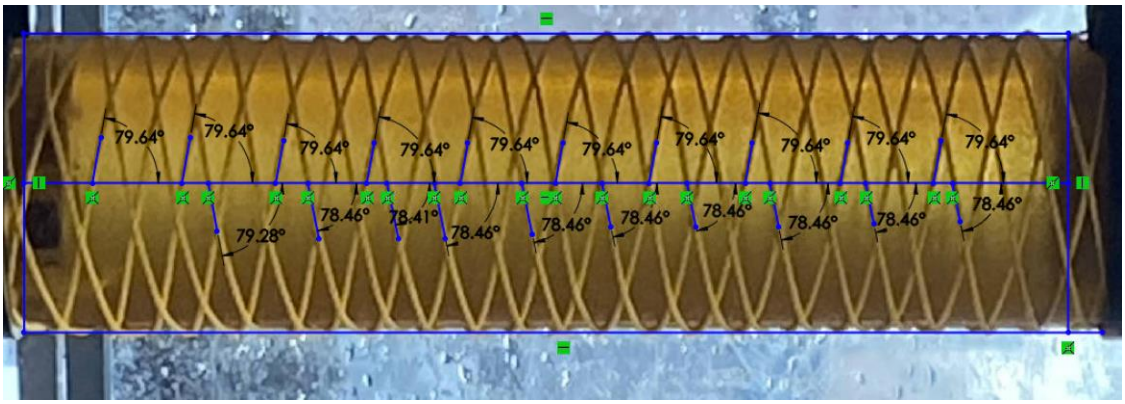

Figure 228: Actuator 2B fiber crossings

Table 28: Actuator 2B angle measurements

Angle Measurement #	Measured Angle
1	79.64
2	79.64
3	79.64
4	79.64
5	79.64
6	79.64
7	79.64
8	79.64
9	79.64
10	79.64
11	79.28
12	78.46
13	78.41
14	78.46
15	78.46
16	78.46
17	78.46
18	78.46
19	78.46
20	78.46
Mean Angle	**79.0885**
Std. Dev	**0.57873**

ACT 2C:

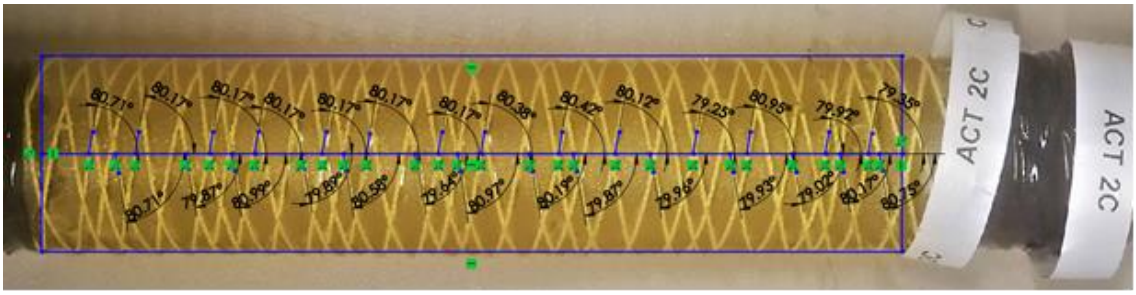

Figure 229: Actuator 2C fiber crossings

Table 29: Actuator 2C angle measurements

Angle Measurement #	Measured Angle
1	80.17
2	80.17
3	80.17
4	80.17
5	80.17
6	80.17
7	80.17
8	80.38
9	80.42
10	80.12
11	79.25
12	80.95
13	79.92
14	79.35
15	80.75
16	80.17
17	79.02
18	79.93
19	79.96
20	79.87
21	80.19
22	80.97
23	79.64
24	80.58
25	79.89
26	80.99

27	79.87
28	80.71
Mean Angle	**80.147**
Std. Dev	**0.4765**

Appendix H: Buckling Segment Connector Drawings

Appendix H shows the geometry of the aluminum segment connectors for the buckling segments used to fabricate the traction actuators in Chapter 4.

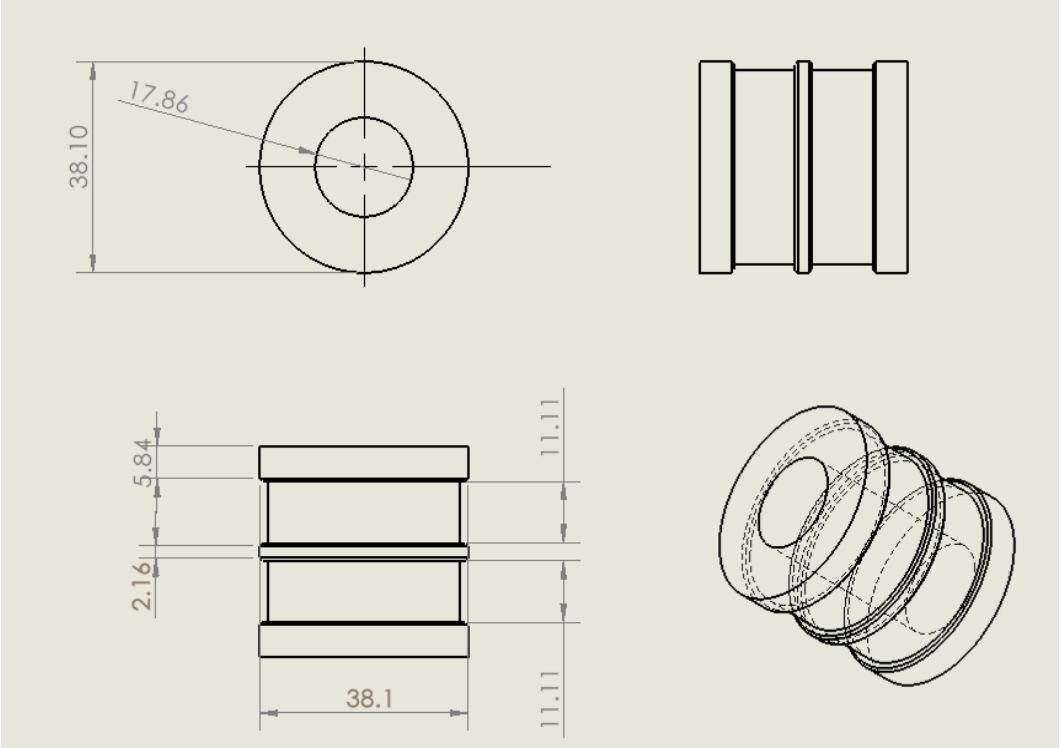

Figure 230: Proximal segment connector for buckling experiments. Dimensions are in mm.

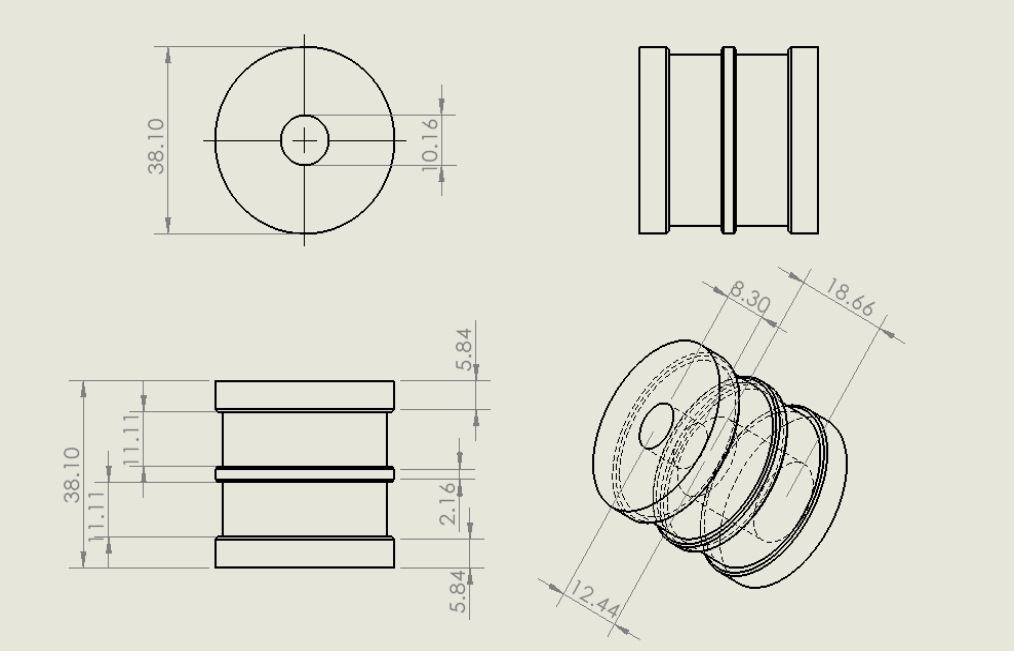

Figure 231: Distal segment connector for buckling experiments. Dimensions are in mm.

Appendix I: Segment Connector Drawings for Traction Segment

Appendix I provides geometry of the segment connectors used to fabricate the traction segments used in experiments in Chapter 4.

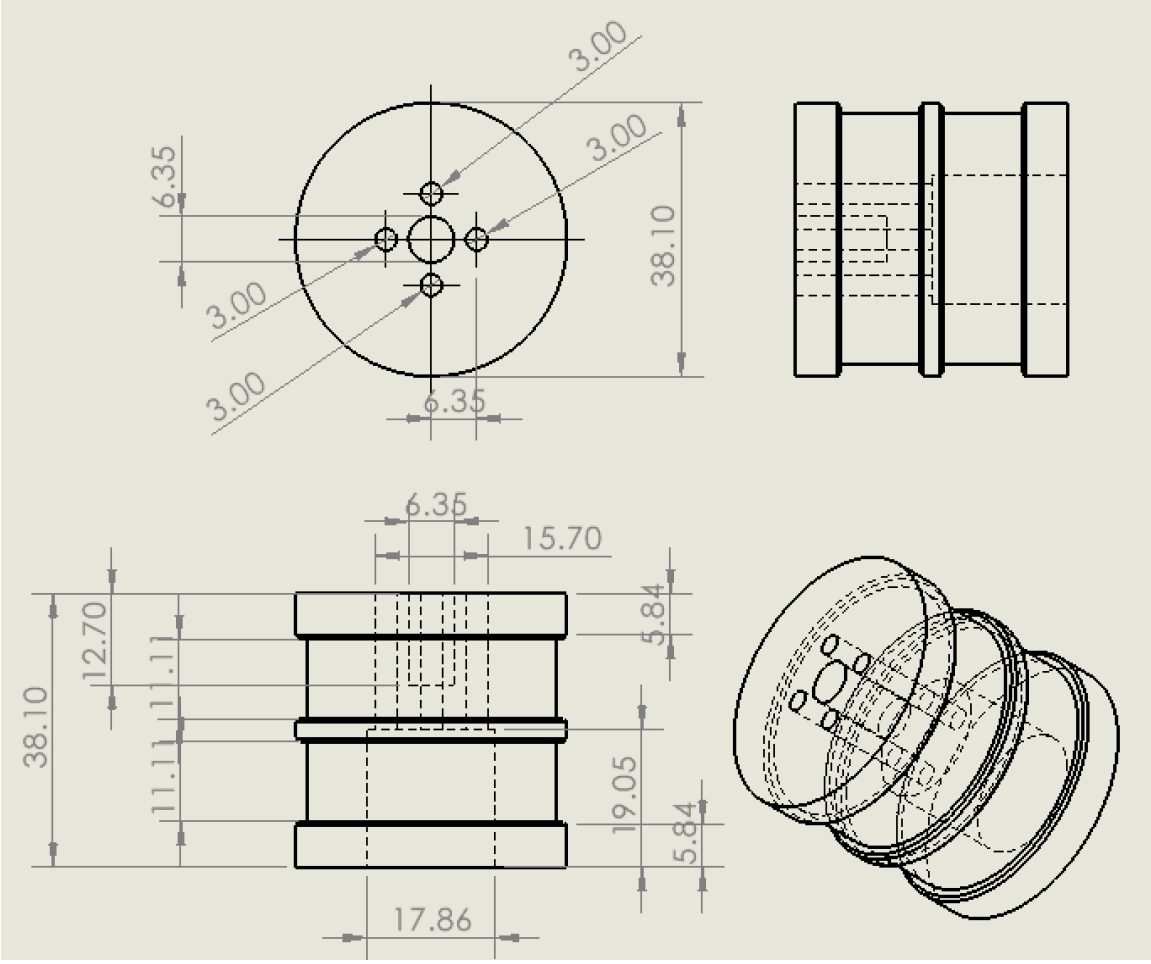

Figure 232: Traction actuator proximal segment connector drawing

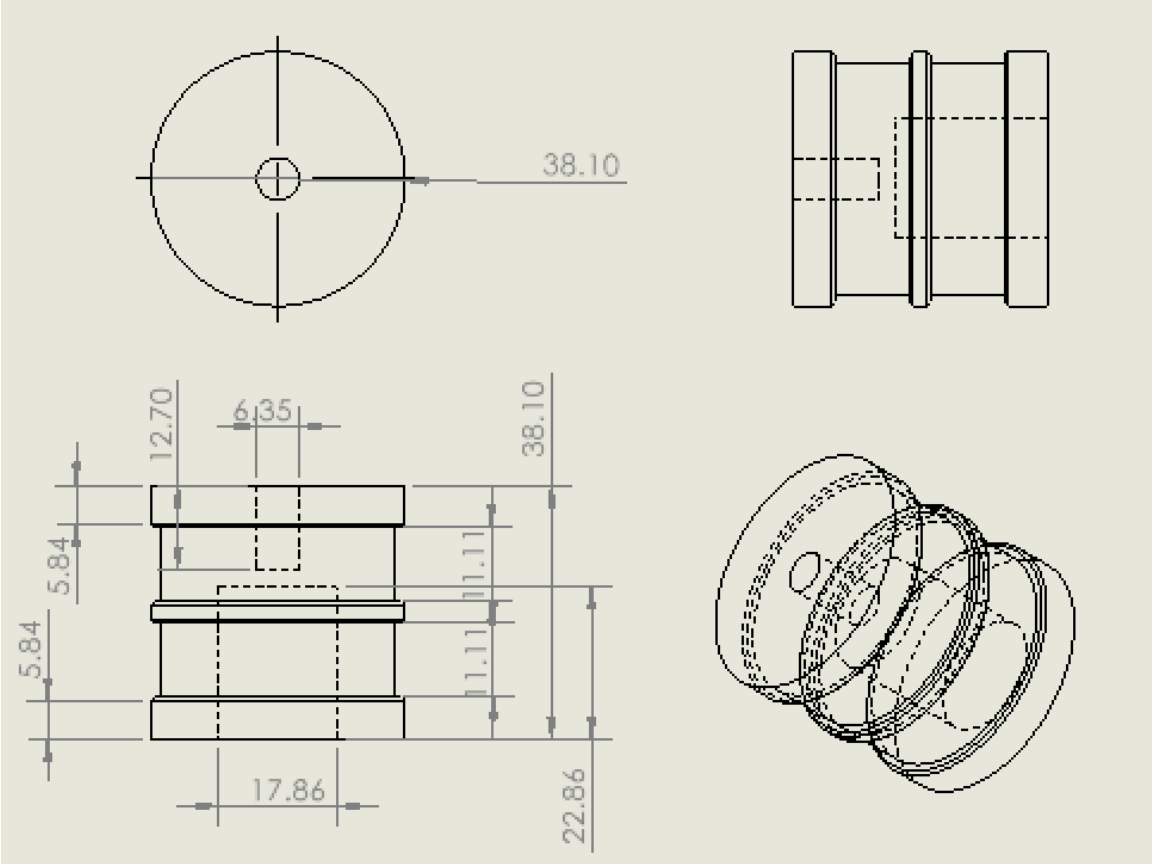

Figure 233: Traction actuator distal segment connector drawing

Appendix J: Comprehensive Contact Length Results for Traction Segment Experiments

Appendix J provides the comprehensive pressure, tube size, and contact length measurements for the traction segment experiments to observe how the contact length varies non-linearly with pressure as the segments expand to contact the tubes.

Table 30: Comprehensive contact length results for traction segment experiments

Actuator	Initial Length of Actuator (mm)	Inside Diameter of Tube (mm)	Initial Outside Diameter of Actuator (mm)	Measured Contact Length (mm)	Pressure (MPa)
1A	84.1	38.1	31.8	0.0	0.113
				82.6	0.142
				77.8	0.164
				82.6	0.201
				87.3	0.209
		44.5		0.0	0.139
				63.5	0.179
				65.1	0.194
				76.2	0.234
				89.7	0.345
		50.8		0.0	0.158
				56.4	0.192
				72.2	0.221
				77.8	0.240
				82.6	0.268
				83.0	0.300
2A	133.4	38.1		0.0	0.072
				131.8	0.099
				131.8	0.123
				135.0	0.147
		44.5		0.0	0.134

				115.9	0.160
				123.8	0.172
				135.0	0.261
		50.8		0.0	0.139
				104.8	0.168
				119.1	0.180
				133.4	0.236
1B	84.1	44.5	38.1	0.0	0.079
				67.5	0.105
				76.2	0.130
				84.2	0.167
				85.7	0.219
				92.1	0.371
		50.8		0.0	0.081
				74.6	0.114
				76.2	0.141
				74.6	0.138
				73.8	0.156
				84.2	0.211
		57.2		0.0	0.108
				41.3	0.146
				69.1	0.169
				73.8	0.176
				73.8	0.196
				81.0	0.244
				88.9	0.318
2B	133.4	44.5		0.0	0.067
				120.7	0.094
				128.6	0.129
				136.5	0.157
		50.8		0.0	0.072
				106.4	0.122
				117.5	0.137
				128.6	0.181
		57.2		0.0	0.137
				107.2	0.155
				123.8	0.179
				138.1	0.229
1C	84.1	50.8	44.5	0.0	0.045
				72.2	0.083

				78.6	0.083
				81.8	0.131
				84.2	0.139
				84.2	0.141
				90.5	0.202
				0.0	0.059
				75.4	0.142
				79.4	0.132
				81.8	0.172
		57.2		0.0	0.121
				69.9	0.141
				76.2	0.165
				77.0	0.190
				92.1	0.240
				0.0	0.063
				125.4	0.091
				128.6	0.107
		50.8		131.8	0.140
				139.7	0.173
				141.3	0.240
				0.0	0.090
				112.7	0.114
2C	133.4			119.1	0.128
				130.2	0.150
				135.0	0.202
		57.2		135.0	0.200
				0.0	0.119
				96.9	0.134
				108.0	0.141
				111.1	0.145
				128.6	0.208

Biosketch

Steven D. Thomalla was born in St. Paul, Minnesota in 1992. He received his BS degree in mechanical engineering from St. Cloud State University in St. Cloud, MN in 2015, his MS degree in mechanical engineering from the University of Minnesota in 2017, and he is expected to receive his PhD degree in mechanical engineering from the University of Minnesota in 2022. During his time at the University of Minnesota, Steven worked as a Lab Supervisor at the Earl E. Bakken Medical Devices Center where he managed the prototyping facility and managed various medical device innovation programs for graduate students, undergraduate students, and industry professionals. Steven also worked as a research assistant in the Mechanical Energy and Power Systems laboratory in the mechanical engineering department where he conducted high-force soft robotics research. Steven spent two semesters as a teaching assistant for the mechanical engineering senior design program, and he has been invited to give medical device innovation and product development focused lectures for undergraduate courses at the University of Minnesota and for device professionals at the Design of Medical Devices Conference in Shanghai, China in 2019. Steven was awarded the Mistletoe Research Fellowship in 2019 where he was able to travel to Tokyo, Japan and engage in a product development project related to neonatal incubators. Steven likes to be involved in a lot of different things. He has worked for 10 years as a direct care staff at ALC Homes in Little Falls, MN where he provides care for vulnerable adults. Steven has also started his own businesses and has dabbled into 3D printing services, Halloween prop Kickstarter campaigns, and other consulting services. Steven has lived his entire life in Minnesota, and he loves to ski, hunt, and spend time outdoors. One of his favorite places to travel is his fishing cottage in northwestern Manitoba, Canada.